Print edition ISSN 2615-5109
Electronic edition ISSN 2621-0541

Publisher:
Center of Technology, Fakultas Teknik, Universitas Hasanuddin

Address:
Engineering Faculty Campus, Hasanuddin University
Jl. Poros Malino km. 6, Bontomarannu
Kabupaten Gowa, Sulawesi Selatan, Indonesia, 92171
Email : epi-ije@unhas.ac.id
Website : cot.unhas.ac.id/journals/index.php/epiije
Telp/Fax : +62-(0)411-58601

EPI International Journal of Engineering

Editor-in-Chief : **Prof. Baharuddin Hamzah**, Hasanuddin University (Makassar, Indonesia)

Associate Editors : **Dr. Faisal Mahmuddin**, Hasanuddin University (Makassar, Indonesia)
Prof. Yoshihiro Narita, Hokkaido University (Sapporo, Japan)

Editorial Board :

- Indonesia
  Prof. Muh. Arsyad Thaha, Hasanuddin University (Makassar, Indonesia)
  Prof. Wahyu Haryadi Piarah, Hasanuddin University (Makassar, Indonesia)
  Prof. M. Ramli Rahim, Hasanuddin University (Makassar, Indonesia)
  Prof. Herman Parung, Hasanuddin University (Makassar, Indonesia)
  Prof. Imran Umar, Hasanuddin University (Makassar, Indonesia)
  Dr. Rhiza S. Sadjad, Hasanuddin University (Makassar, Indonesia)
  Dr. Ganding Sitepu, Hasanuddin University (Makassar, Indonesia)
  Prof. Satriyo Brodjonegoro, Bandung Institute of Technology (Bandung, Indonesia)
  Prof. I Ketut Aria Pria Utama, Surabaya Institute of Technology (Surabaya, Indonesia)
  Dr. Arifuddin Idrus, Gadjah Mada University (Yogyakarta, Indonesia)
  Dr. Ngurah Nitya, Udayana University (Denpasar, Indonesia)
  Dr. Putu Wijaya Sunu, Bali State Polytechnic (Denpasar, Indonesia)
  Dr. Lukiyanto YB, Sanata Dharma University (Yogyakarta, Indonesia)

- Outside Indonesia
  Prof. Erasmo Carrera, Polytechnic University of Turin (Torino, Italy)
  Prof. Mark Ewing, University of Kansas (Lawrence, USA)
  Prof. Danna Ganbat, Mongol University of Science and Technology (Ulaanbaatar, Mongolia)
  Prof. Peter Hagedorn, Technical University of Darmstadt (Darmstadt, Germany)
  Prof. S. Ilanko, University of Waikato (Hamilton, New Zealand)
  Prof. David Kennedy, Cardiff University, (Cardiff, United Kingdom)
  Prof. Woo Il Lee, Seoul National University (Seoul, Korea)
  Prof. Oliver Polit, University Paris Ouest (Paris, France)
  Prof. Vasaka Visoottiviseth, Mahidol University, (Bangkok, Thailand)
  Dr. Jane Louie Fresco Zamora, Weathernews Inc. (Chiba, Japan)
  Dr. Kazunori Abe, Akita University (Akita, Japan)
  Prof. Jun Ando, Kyushu University (Fukuoka, Japan)
  Prof. Shun Chiyonobu, Akita University (Akita, Japan)
  Prof. Naohiro Hozumi, Toyohashi University of Technology (Toyohashi, Japan)
  Prof. Shigeru Kashihara, Nara Institute of Science and Technology (Nara, Japan)
  Prof. Akio Miyara, Saga University (Saga, Japan)
  Dr. Yusuke Mochida, University of Waikato (Hamilton, New Zealand)
  Prof. Prakash Bhandary Netra, Ehime Univ. (Matsuyama, Japan)
  Prof. Yoshiki Ohta, Hokkaido University of Science (Sapporo, Japan)
  Prof. Tsubasa Otake, Hokkaido University (Sapporo, Japan)
  Prof. Nobumasa Sekishita, Toyohashi University of Technology (Toyohashi, Japan)
  Prof. Hideaki Yasuhara, Ehime University (Matsuyama, Japan)

Foreword

On behalf of the editorial team, I would like to express our gratitude and pleasure for the publishing of the EPI International Journal of Engineering (EPI-IJE) Volume 3 Number 1 February 2020. This edition is the beginning edition of the year 2020. However, unlike several previous editions, this edition does not contain any mini-special topic in order to shorten the publication time.

There are 13 manuscripts published in this edition which are divided into 5 topic categories. The first topic category is mechanical and industrial engineering which contains 5 manuscripts. The first manuscript simulated local heat transfer of plate heat exchanger while the second manuscript investigated thermal and hydraulic characteristics of the discrete double inclined ribs at low curvature coil, and the third manuscript studied the multimodal reduction of elastic vibration using super absorbent polymer beads. The last two manuscripts conducted research on heat waste of the biomass egg drying machine and wave power plant for fisherman boats.

The second topic category is electrical and informatics engineering. In this topic, there are two manuscripts that are related to OFDM-IDMA uplink multi-user system for next generation WLAN and water quality system for crab larvae. There are also two manuscripts in the third topic (architecture and urban & regional development engineering topic) which are about the effectiveness of Petobo temporary shelter and characteristics of the Towani Tolotang's Traditional House.

The fourth topic which is naval architecture, ocean, and marine system engineering contains three manuscripts. The first manuscripts in this topic discussed facility development of Maccini Baji port while the second and the last manuscripts performed a study on the optimum resistance coefficient on Catamaran and 6-axis forces and moments transducer for seaplane floaters, respectively. The last topic is geology and mining engineering which contains only one manuscript. The manuscript studied the valuation of environmental impact due to construction mining at Gowa, South Sulawesi.

I appreciated the high-quality manuscripts contribution of all authors in this edition. I also would like to recognize the significant contribution of our associate editor Prof. Yoshihiro Narita for his continuous support even after he has been back to work at a university in Japan. Lastly, I thank all people and institution who has helped the publication of this edition. I hope the published manuscripts will give benefit and positive contribution to the development of science and technology.

Warm regards,

Prof. Baharuddin Hamzah
Editor-in-Chief of EPI-IJE

TABLE OF CONTENTS

<Mechanical and Industrial Engineering >

<Electrical and Informatics Engineering >

EPI International Journal of Engineering
Volume 3, Number 1, February 2020, pp. 1-9
DOI: 10.25042/epi-ije.022020.01

*p*ISSN 2615-5109
*e*ISSN 2621-0541

Consideration on Local Heat Transfer Measurement of Plate Heat Exchanger with the Aid of Simulation

Thiha Tun[a,*], Keishi Kariya[b], Akio Miyara[c]

[a] Graduate School of Science and Engineering, Saga University. Email: michaellin630@gmail.com
[b] Department of Mechanical Engineering, Saga University. Email: kariya@me.saga-u.ac.jp
[c] Department of Mechanical Engineering, Saga University. Email: miyara@me.saga-u.ac.jp

---

Abstract

In this study, the local heat transfer coefficient of boiling and condensation were obtained by an experimental set up using vertical stainless-steel type brazed plate heat exchanger. A series of 8 vertical brazed plates are used as the major components of the test section of experimental set up and are fabricated into layers so that flow channels are formed between the plates through which water and refrigerants are flowing through. The experiments are carried out at the mass flux of 10, 20 and 50 kg/(m^2·s). In order to measure the local heat transfer coefficient, flat stainless-steel plates of 10 mm in thickness are installed attached to the vertical plates onto which the thermocouples are positioned to measure the temperature distributions at the surface of the plates. By performing the experiment, the direction of the heat flux across the plate tends to deviate downward especially at the lower part of the plate due to the non-uniform temperature distributions across the plate. The results are analyzed and validated at the mass flux of 10 kg/(m^2·s) by the aid of the simulation tool by using ANSYS FLUENT 19.1 to estimate the local heat transfer coefficient and the heat flux across the plate. The analysis result shows that the simulation model can assist to track the deviation of the direction of the heat flow from the horizontal direction across the plate and the experimental results of the local heat transfer coefficient have similar trends with that of the simulation results.

Keywords: Boiling; condensation; local heat transfer coefficient; plate heat exchanger; refrigerant

---

1. Introduction

Plate heat exchangers (PHEs)which have an advantage in acquiring larger heat transfer per volume are highly applicable in industrial applications such as refrigeration, heating, cooling, chemical processing, etc [1]–[4]. Additionally, PHEs have benefits in reducing refrigerant charge and lighter structural supports [5], [6]. The structural construction of the PHEs basically consist of a series of thin, rectangular, pressed steel plates which are stacked and pressed together such that several channels are formed between the plates [7], [8]. The formed channels have been alternate passages for hot and cold fluid media streams to exchange heat between the two fluids [1]–[4]. Since PHE generally has larger heat transfer surface area than a shell and tube type heat exchangers, they are widely used in in many industrial and domestic applications in the small to medium size range [9]. Bergles et al. and Kakaç et al. have mentioned that PHEs have the ability in a flexibility in adding and removing the plates for accommodating variable heat loads, capable of variations in geometry and cleanability (e.g. the gasketed-PHE). Several types of plate heat exchangers are applicable, depending on the industrial application. Mainly, plate heat exchangers: gasketed, brazed, welded/semi-welded and shell and plate are categorized into four types in many industrial applications. Brazed plate heat exchangers are compactable and exhibit high performance in heat transfer capability, and for these reasons brazed PHEs are suitable in heating and refrigerating applications such as evaporation or condensation of refrigerants, heat pumps and cooling of water or oil circuits in engines [10]–[12]. They provide higher resistant to corrosion due to the combination of the stainless-steel plates with the copper brazing and can withstand quite high pressures as all the local contact points between the corrugations in the stack are brazed [13]–[16]. On a contrary, the brazed type PHEs cannot be disassembled for cleaning purpose, and thus the application in fouling are limited [17]–[20].

In this study, a brazed type PHE with corrugation angle of 60° were used in the specially fabricated test section. The refrigerant R1234yf and water were used as the two operating fluid media. The experiment was carried out and the heat flux across the plate and the heat transfer coefficient on the surface of the PHE was estimated through the measurement points along the plates. The experimental results were analyzed with the aid of the simulation model implemented in ANSYS FLUENT

---

*Corresponding author. Tel.: +8-191-097-292
Graduate School of Science and Engineering, Department of Mechanical Engineering
1Honjo-machi, Saga-shi, 850-8502, Japan

19.1R1. The input boundary conditions of the simulation model were used from the experimental data and the heat fluxes across the plate and the local heat transfer coefficients of the experimental results were validated with the simulation results. By the assistance of the simulation model, the heat fluxes across the plate tends to deviate downwards at the lower part of the plate can be seen more clearly. And the validation results show that the experimental results and the simulation results undergo the similar trends at the selected measurement points with more or less deviations in the values of heat fluxes across the plate and the local heat transfer coefficient.

2. Experimental Setup and Procedure

The test section consisted of 8 brazed plates is connected to the primary loop through which the refrigerant of R1234yf is circulated by a micro pump. The refrigerant flow rate is adjusted by the rotation speed of the micropump. The inlet hose of the test section is connected to the pre-heater and the after condenser is located at the outlet hose of the test section so that the heated refrigerant from the pre-heater and the test section can be cooled down to the desired sub-cooled conditions before returning back to the circulated pump.

Water is used as pre-heater, after condenser, reservoir, and test section as heat source water in a separate loop. Coriolis flow meter and flow control valve are used as auxiliary equipment to monitor and control the refrigerant flow. After the mass flow rate is measured by the meter, it is heated by the pre-heater, the pressure and temperature are measured by the mixer, and then enters the test section. In addition, the data logger (Keithley Instruments Co., Ltd. switching function) is used to read the output values of thermocouples, pressure transducers, and Coriolis flow meters. The schematic diagram of the experimental set up has been shown in Fig. 1.

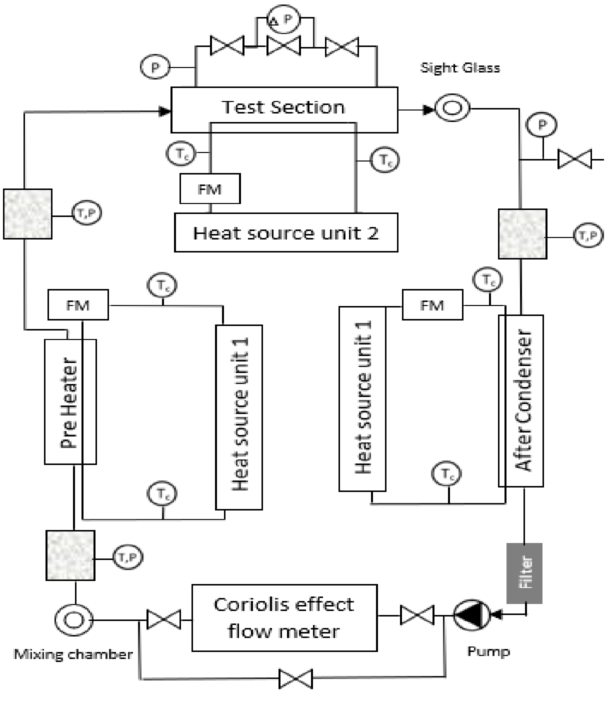

Figure 1. The measurement points distributions of the plate

2.1. *Information on test section and measurement procedure*

The test section, 8 plates in total, are stacked and held together by pressure plate while the refrigerant is flowed into the channel formed by the clearance between the two plates among the plates. The water is forced to flow through the channels lied at the outer sides of the two plates so that the two plates become a heat transfer medium during the process of heat exchange between the two different fluids. A pressure transducer is installed in the test section to monitor the differential pressure between the inlet and outlet of the test section and the overall pressure drop of the test section. In order to measure the local heat transfer coefficient of the heat exchanger plates, 20 thermocouples are set and attached to the surface of the plates to record the temperature distributions at the surface of the plates for both the refrigerant and the heat source water sides of the plates. The measurement points where the thermocouples are set are shown in Fig. 2. The temperature values obtained by the thermocouples are used to calculate the heat flux across the plate and the local heat transfer coefficients.

Table 1 show the geometry of the test section. The dimensions of the plate are 186 mm, 84 mm, and 5 mm respectively. The corrugations pitch, depth and chevron angle are 5.6 mm, 1.5 mm and 60° respectively. The length between the inlet and outlet port center is 136 mm. The locations of the temperature measurement points are located at 14.75, 36.75, 58.75, 80.75, and 102.75 mm vertically from the inlet port of the plate. The horizontal arrangements of the measurement points can be seen in the Fig. 2.

Since the heat flux across the plate and the local heat transfer coefficient cannot be achieved directly from the experimental set up, the data reduction method is used to calculate the heat flux and the local heat transfer coefficient of the plate based on the temperature recorded by the thermocouples.

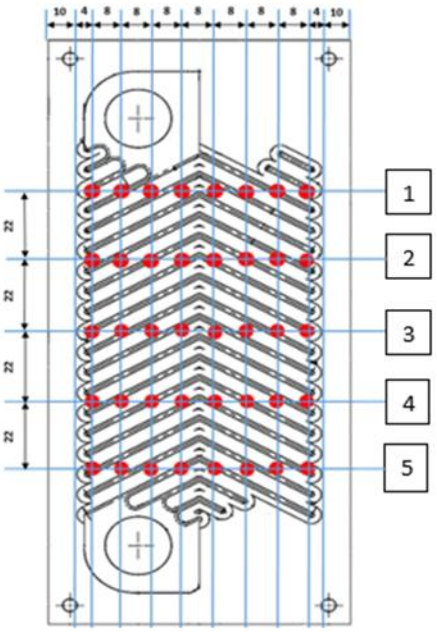

Figure 2. The locations of the measurement points on the plate

Table 1. Geometry and dimensions of the plate

Fluid flow plate length (mm)	117.5
Plate width (mm)	64
Area of the plate (m^2)	0.75
Corrugation type	Chevron
Angle of the corrugation (°)	60
Corrugation pitch (mm)	5.6
Number of plates	8
Number of channels on refrigerant side	1
Number of channels on water side	2

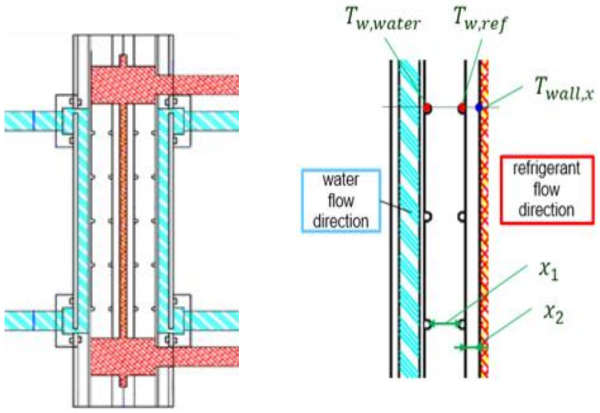

Figure 3. The section view of the test section for the data reduction method calculation

2.2. *Data reduction method*

Consider the process as the steady state one-dimensional heat conduction, the data reduction method is initiated by the governing equation of the conduction heat transfer.

$$\frac{\partial T}{\partial t}+\frac{\partial}{\partial x}\left(\lambda\frac{\partial T}{\partial x}\right)=0 \tag{1}$$

In the conduction heat transfer, the time derivative becomes neglected for the steady state process and the heat flux across the plate in one-dimensional heat transfer (q_x) is

$$q_x=\lambda\left(\frac{T_{w,ref}-T_{w,water}}{x_1}\right) \tag{2}$$

Because of the unavailability of the measurement of the wall surface temperature at the refrigerant side ($T_{w,ref}$), the wall temperature at the refrigerant side is calculated by the following equation.

$$T_{wall,x}=T_{w,ref}+\left(\frac{q_x x_2}{\lambda}\right) \tag{3}$$

By using the value of the wall surface temperature ($T_{wall,x}$), the local heat transfer coefficient, the heat flux per temperature difference (α_x), can be calculated.

$$\alpha_x=\frac{q_x}{T_{sat}-T_{wall,x}} \tag{4}$$

3. Simulation Model and Procedure

Although the heat flux and the local heat transfer coefficient can be calculated based on the experimental data, some important characteristics such as the behavior of the temperature distributions at and across the plate and

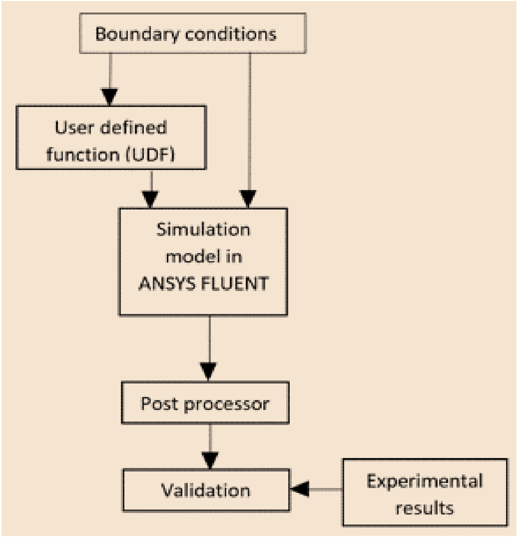

Figure 4. The schematic diagram of the simulation model

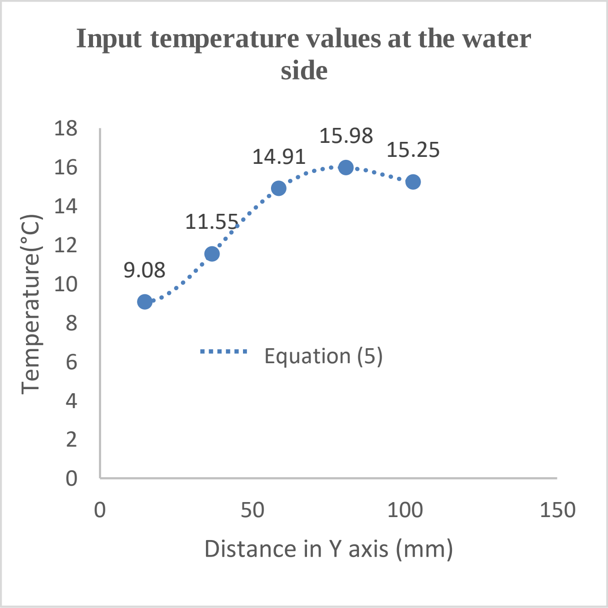

Figure 5. The boundary condition for the water side

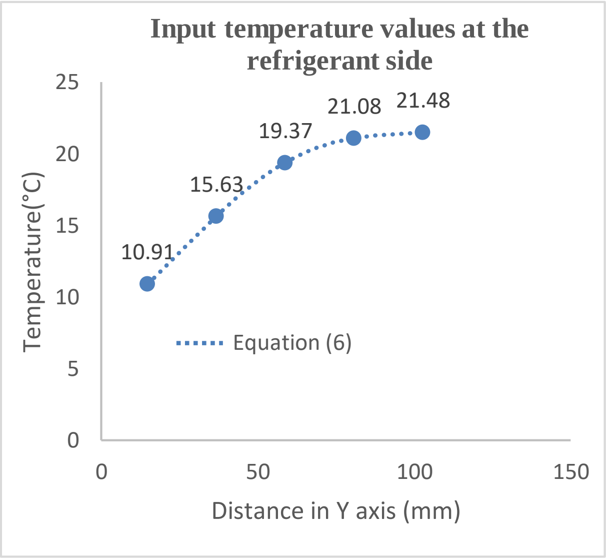

Figure 6. The boundary condition for the refrigerant side

heat flux across of the plate, cannot be evaluated by experimental work alone. For this reason, a simulation model is implemented in ANSYS FLUENT19.1R1. By the assistance of the simulation model, a more detail analysis can be carried out due to the isothermal lines and the directional vectors of the heat flux across the plate. Additionally, the experimental results can also be validated by the results evaluated from the simulated model. Figure 4 illustrates the plans and procedure of the simulation model.

The assumption of the input boundary condition for the simulation model is as follows

- Steady state condition
- No external energy exchange with the surrounding (no external work, no radiation heat absorption)
- Corrugation effect is neglected
- The model is simulated only at the portion where the measuring points are located (i.e.,14.75 to 102.75 mm vertically), and the top and down end sides of the plate is assumed to be adiabatic walls.
- Stainless steel with the thermal conductivity of 16.7 W/(mK) is used as material properties.

A set of temperature values were set at the surface of the wall based on the experimental results at the mass flux of G=10 kg/(m^{2}s) according to the following functions shown in Figs. 5 and 6.

The input boundary condition at the water side was represented by the following function.

$$T(x) = 7.0 \times 10^{-7}x^4 - 0.0002x^3 + 0.0145x^2 - 0.3215x + 11.186 \tag{5}$$

The function mentioned below was applied at the refrigerant side.

$$T(x) = 3.0 \times 10^{-7}x^4 - 5x^3 + 0.0047x^2 + 0.1073x + 8.5297 \tag{6}$$

The boundary conditions at the water and refrigerant sides were scripted in C programming language and imported to ANSYS FLUENT 19.1R1 as user defined functions (UDF).

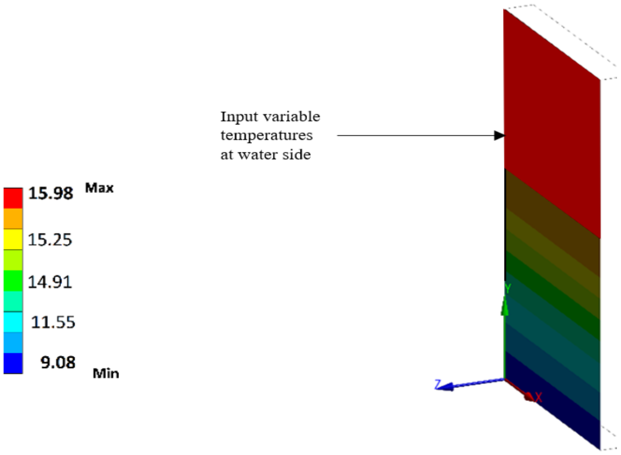

Figure 7. User defined function for the water side

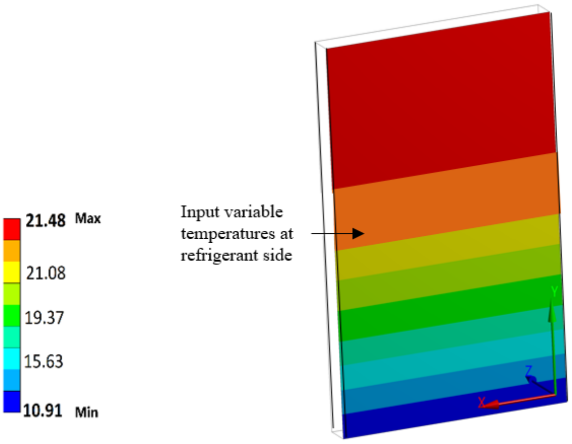

Figure 8. User defined function for the refrigerant side

4. Results and Discussions

With the boundary conditions mentioned above, the temperature distributions and the heat flux were calculated and the local heat transfer coefficient for the condensation mode at the mass flux of 10 kg/(m^2.s) by the ANSYS simulation model and then the validation of the experimental and the simulation results are carried out.

4.1. Contour plot of the temperature distributions of the plate

The directions of the refrigerant and the water was arranged in counter flow with heated water in downward direction and condensing refrigerant flowing downward. Since the heat exchange occurs between the refrigerant and water, the temperature at the water side increased with respect to the travelling distance in vertical direction with the maximum temperature of 15.25°C at the first row of the measuring points at the top side of the plate and the minimum temperature of 9.08°C at the bottom. Whereas, the refrigerant with the temperature of 21.48°C at the measurement point 1, rejected heat gradually when flowing in the downward direction and flowed out with the minimum temperature of 10.91°C from the bottom side. Due to the unequal, non-uniform temperature distributions at the refrigerant and the water side and the lower temperature values at the lower sides of the plate, the isothermal lines are distributed in more or less inclinations across the plate which can be seen in Fig. 9(b). The slopes of the isothermal lines is steeper at the upper side of the plate than the lower side of the plate because of the temperature elevations of the refrigerant side and the water side at the upper side of the plate is larger than that of the elevations of the two sides at the lower side of the plate.

4.2. Contour plot of the total heat flux across the surface of the plate and the heat flux in x- and y-components

As the direction of heat flux is perpendicular to the isothermal lines, the total heat flux across the plate flow more or less horizontally from the refrigerant side to the water side at the upper side of the plate, while at the lower side of the plate, the directions of the total heat flux deviate from its horizontal direction and flow downward from the refrigerant to water side. The magnitude of the maximum total heat flux occurs at the topmost side of the plate with a value of 11.8 kW/m^2 and on the other hand, the minimum total heat flux of 1.36 kW/m^2 appears at the opposite bottommost part at the lower side of the plate. Since the directions of the total heat flux varies gradually from the upper side of the plate with more or less horizontally to the lower side pointing toward the downward directions, the magnitudes of the heat flux in *x*-component, (q_x) have a higher values at the upper side of the plate than the lower side of the plate. The maximum value of the heat flux in the direction of *x* axis is 11.104kW/m^2 at the uppermost side of the plate as shown in Fig. 10. The minimum *x* component heat flux lies at the bottom edge boundary between the refrigerant side and the adiabatic wall with the value of -612.79 kW/m^2.

The negative value of the hat flux in *x* component show that there is a small amount of heat flowing back to the refrigerant side in *x* direction. In opposite to the heat flux in *x* component, the values of the heat flux in *y* direction increases from lower values to the higher values form the upper part to the lower part of the plate. The negative values of the *y* component heat flux mean that the *y* component heat flux have a direction opposite to the *y* axis, i.e., the heat flux tends to flow in the downward direction at the lower part of the plate. The maximum magnitude of q_y is 0.5012kw/m2 at the top upper regions of the plate at the water side and the value of 85.633W/m2 at the upper parts of the refrigerant side. The maximum values of q_y can be found at the lower region of the refrigerant side with the magnitude of -3.2398kW/m2 in downward direction opposite to the *y* axis.

4.3. *Validation of the experimental results and the simulation results*

The validation is carried out at the front and sides of the plate. The horizontal directional heat flux (q_x) at the left and right sides of the plates are calculated by the data reduction methods in Eq. (2) by using the temperatures obtained experimentally. And the obtained heat flux at the sides are compared with the directional heat flux (q_x) from the simulation model. The comparison results show that both the simulation and experimental results show the similar trends at both the left and right sides of the plate but the maximum heat flux of the simulation results is lower than the experimental results with the deviation of 4.7% at the left side and of 4.7% at the right side of the plate respectively. The experimental local heat transfer coefficients at the front face of the plate is calculated based on the Eq. (3) and for the simulation model, the local heat transfer coefficients are calculated at the ANSYS FLUENT post processor based on the horizontal directional heat flux (q_x).

The comparison for the local heat transfer coefficients are proceeded at the measurement points shown in Fig. 2.The comparison results show that the values of the heat transfer coefficients are higher at the middle of the plate than at the two edges for both simulation and experimental data. And the overall trends at the measurement points results in higher values for the experimental data than the simulation data as the directional heat flux calculated by the experimental setup results in higher values than that of the simulation model. The experimental data recorded the peak value of the local heat transfer coefficient of 2.05 kW/(m^{2}K) at the horizontal distance of 44 mm at the measurement point of 1 while the corresponding maximum heat transfer coefficient at the same distance at the same measurement point of the simulation result provides the value of 1.69 kW/m^{2}K with the deviation of 17.3%. The minimum value shown by the experimental result has a value of 0.145 kW/m^{2}K which meets the agreement with the minimum value among all of the simulation results at the same measurement point at the lowest edge of the measurement point of the plate at the distance of 4 mm respectively with the deviation of 28.9%.

Therefore, the overall comparison results between the experimental data and the simulation data concludes that the directional heat flux (q_x) results at the left and right sides of the plate have almost identical trends for the both data whereas there is more or less deviations between the both results in terms of local heat transfer coefficient values at the front face of the plate with similar trends but the larger experimental values of almost every points of measurement are obtained as the results of comparison.

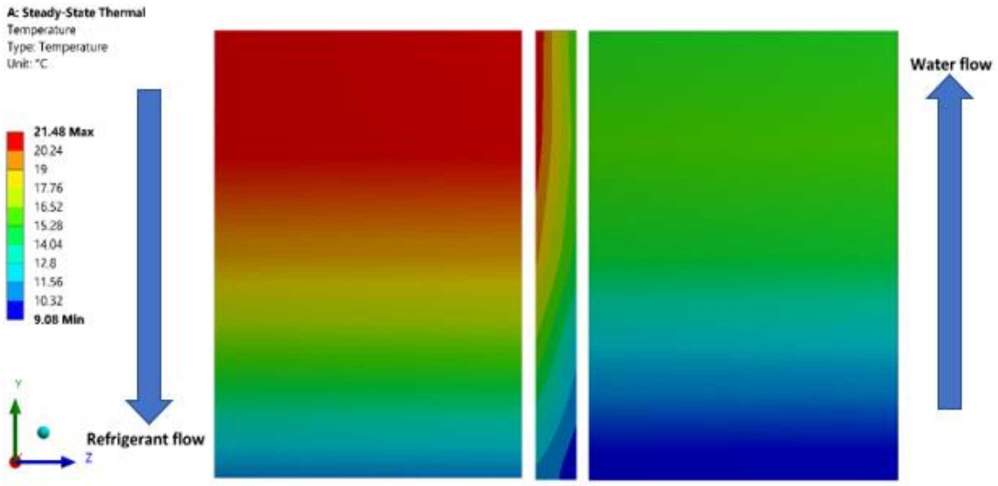

(a) (b) (c)

Figure 9. Contour of the temperature distributions of the plate (a) Refrigerant side, (b) Cross Section, (c) Water side

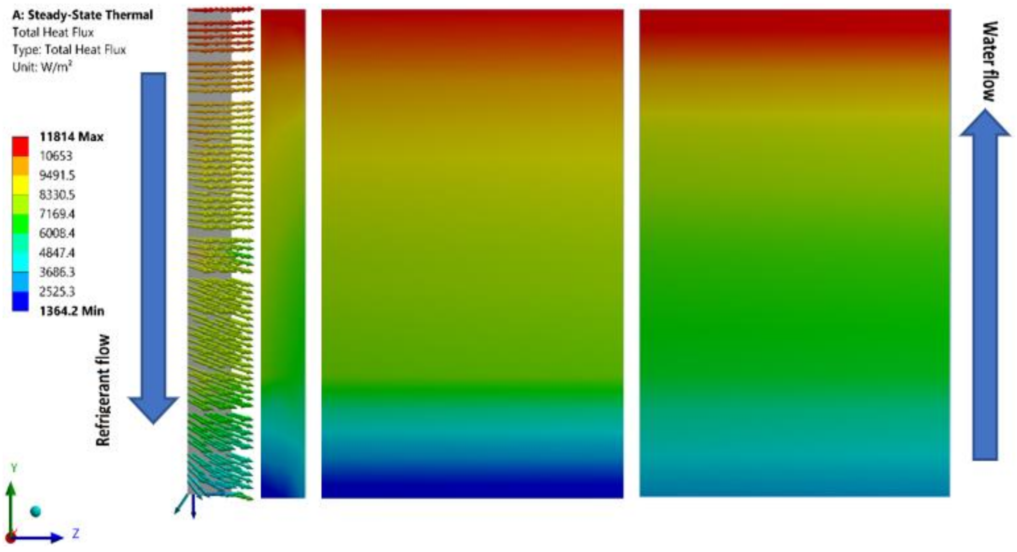

(a) (b) (c) (d)

Figure 10. Contour of the total heat flux of the plate (a) Vector plot, (b) Cross section, (c) Refrigerant side (d) Water side

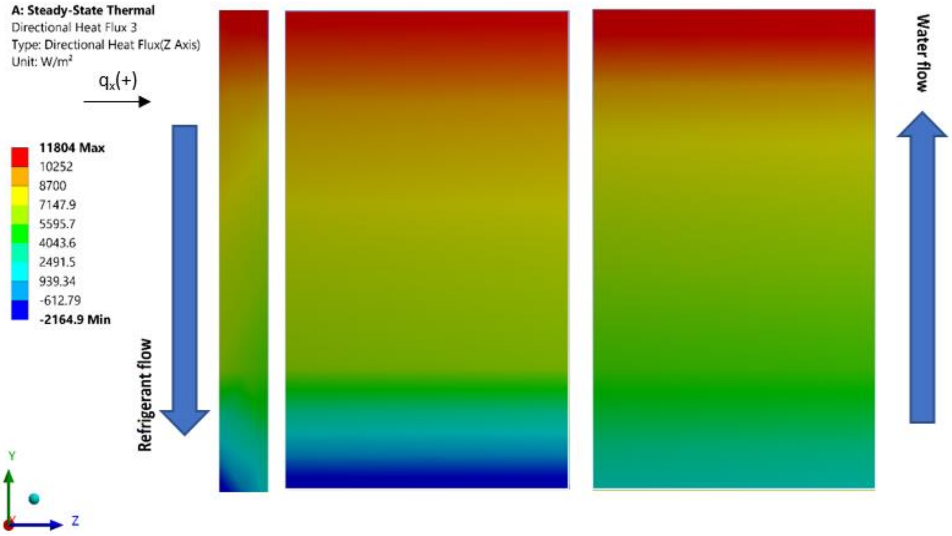

(a) (b) (c)

Figure 11. Contour of the *x* component heat flux(q_x) of the plate (a) Cross Section, (b) Refrigerant side, (c) Water Side

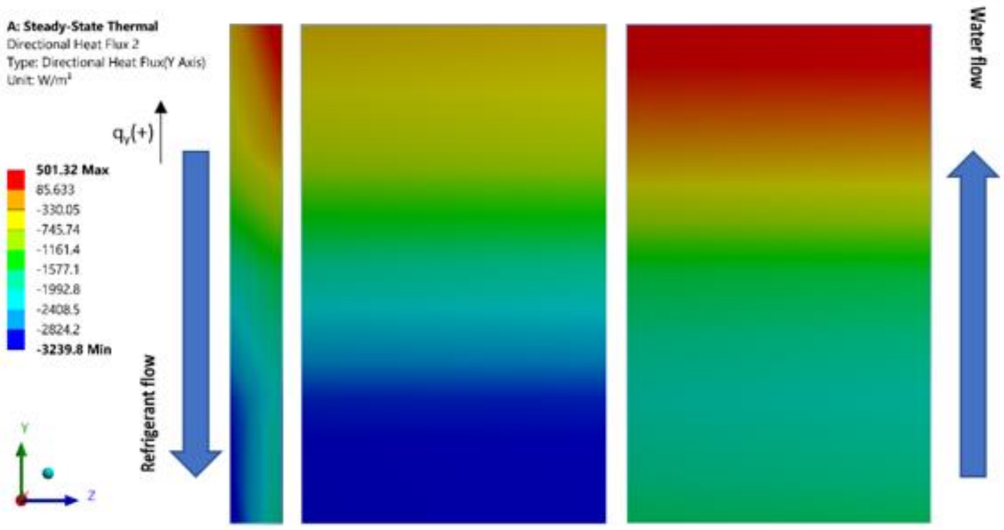

(a) (b) (c)

Figure 12. Contour plot of the *y* component heat flux(q_y) of the plate (a) Cross section, (b) Refrigerant side, (c) Water side

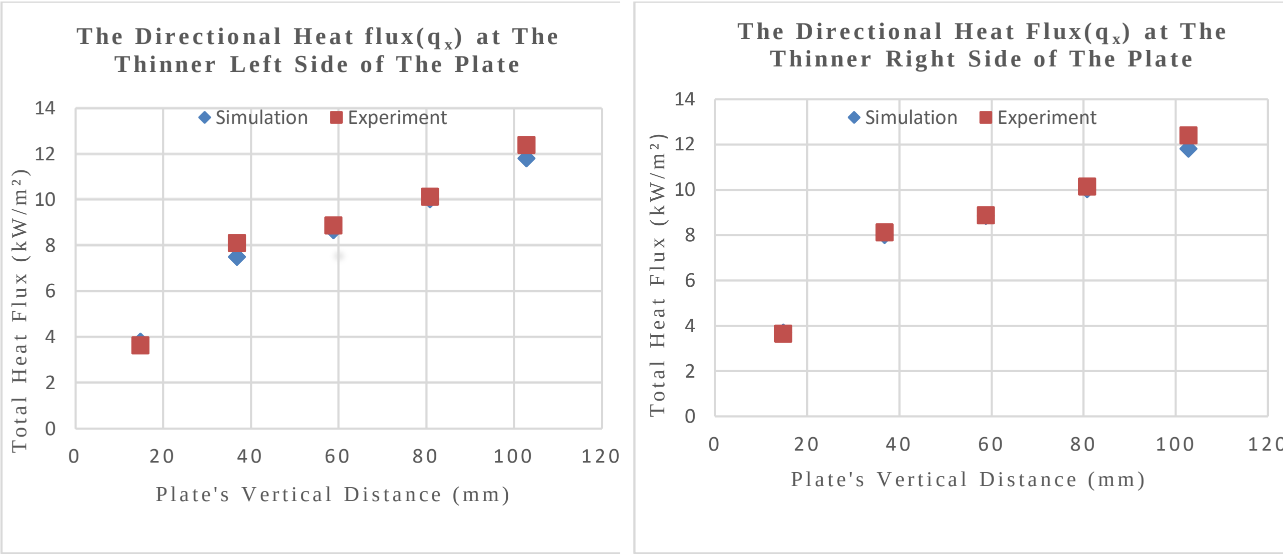

Figure 3. The comparison between the simulation and experimental results at the thinner left and right sides of the plate

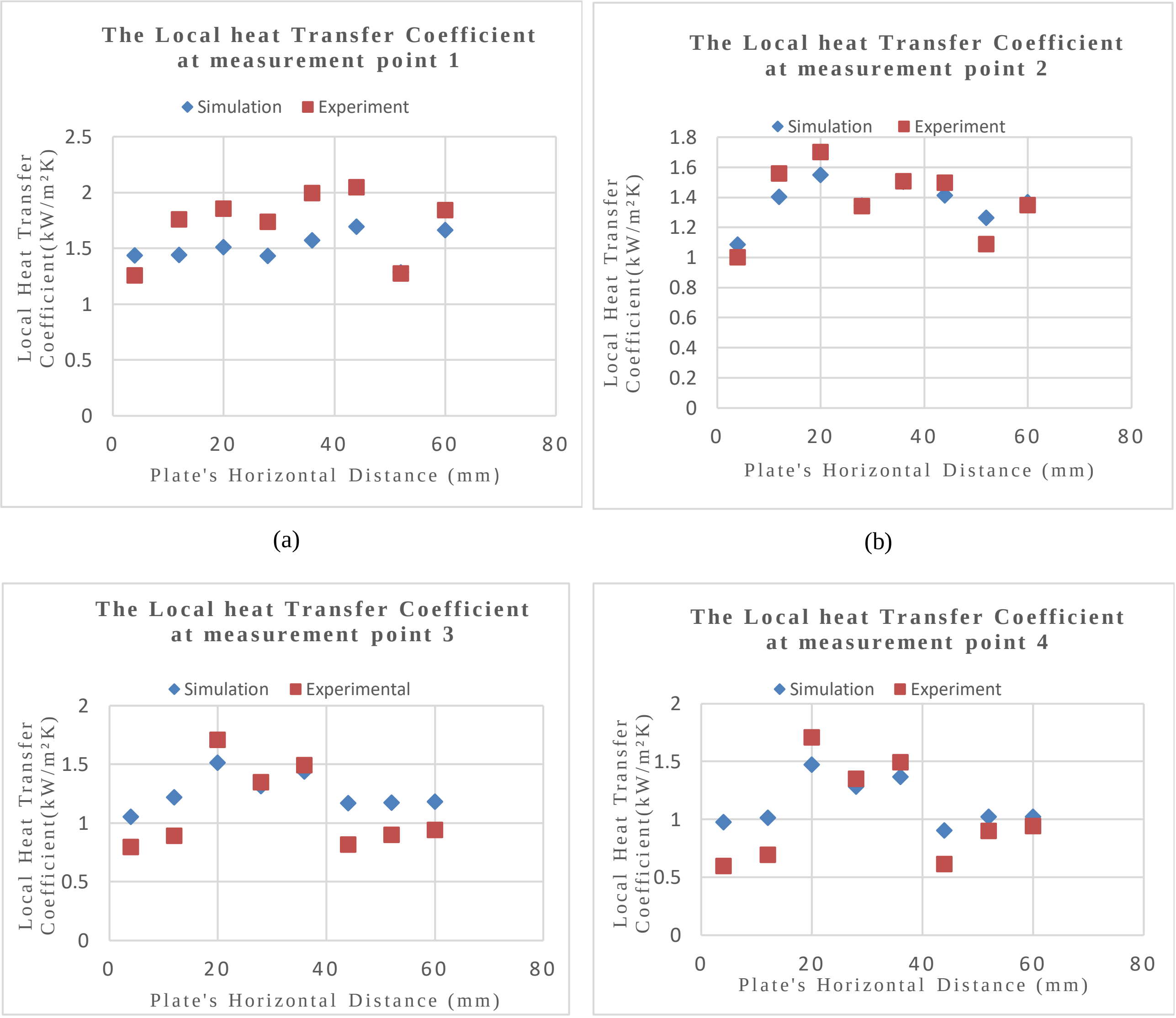

(a)

(b)

(c)

(d)

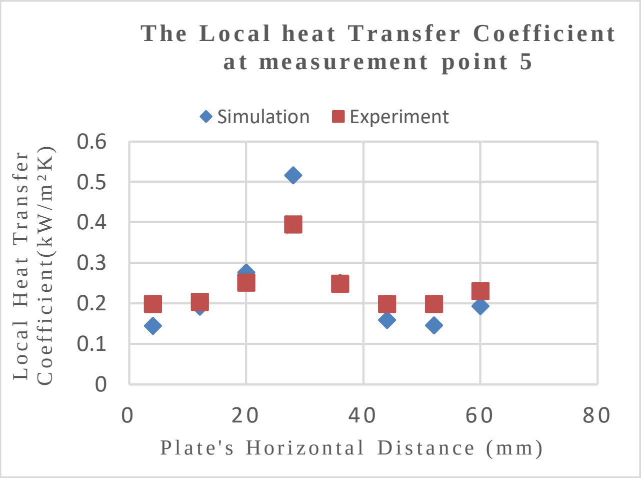

(e)

Figure 4. The Local heat Transfer Coefficient (a) At measurement point 1, (b) At measurement point 2, (c) At measurement point 3, (d) At measurement point 4, (e) At measurement point 5

5. Conclusion

An experimental work was carried for the refrigerant R1234yf with the plate heat exchanger to obtain the local heat transfer coefficients in the PHEs for condensation experiment and the analysis was investigated and validated by the assistance of the simulation model developed in ANSYS FLUENT 19.1 R1 based on the temperature inputs obtained by the experiments. The summary of the analysis is shown below.

- The overall directional vector of the total heat flux across the plate tends to flow from the upper side of the plate to the lower side of the plate and this effect can be seen clearly in the simulation results.
- The validation results of the directional *x* component heat flux at the left and right sides of the plate results in nearly identical trends at the measurement points from top to bottom vertically.
- For the local heat transfer coefficients comparison between the experimental and the simulation data show the similar trends with the experimental values mostly larger than the values received by the simulation model for the selected measurement points at the front face of the plate.

Acknowledgements

The New Energy and Industrial Technology Development Organization (NEDO), Japan supports the sponsorship for this study.

References

[1] M. S. Mahmud, K. Kariya, and A. Miyara, “Local Condensation Heat Transfer Characteristics of Refrigerant R1234ze(E) Flow Inside a Plate Heat Exchanger,” *Int. J. Air-Conditioning Refrig.*, vol. 25, no. 1, 2017.

[2] V. Grabenstein and S. Kabelac, “Experimental Investigations and Modelling of Condensation in Plate Heat Exchangers,” in *International Heat Transfer Conference (IHTC)*, pp. 135–142.

[3] R. L. Amalfi, F. V. Farahani, and J. R. Thome, “Flow Boiling and Frictional Pressure Gradients in Plate Heat Exchangers. Part 1: Review and Experimental Database,” *Int. J. Refrig.*, vol. 61, pp. 166–184, 2016.

[4] R. L. Amalfi, F. Vakili-Farahani, and J. R. Thome, “Flow Boiling and Frictional Pressure Gradients in Plate Heat Exchangers. Part 2: Review and Experimental Database,” *Int. J. Refrig.*, vol. 61, pp. 165–203, 2016.

[5] Z. H. Ayuba, T. S. Khanb, S. Salamb, K. Nawazc, A. H. Ayub, and M. S. Khand, “Literature Survey and a Universal Evaporation Correlation for Plate Type Heat Exchangers,” *Int. J. Refrig.*, vol. 99, pp. 408–418, 2019.

[6] B. Thonon, R. Vidil, and C. Marvillet, “Plate Heat Exchangers: Research and Developments,” *J. Enhanc. Heat Transf.*, vol. 24, no. 1–6, 2017.

[7] X. Tao and C. A. I. Ferreira, “Heat Transfer and Frictional Pressure Drop During Condensation in Plate Heat Exchangers: Assessment of Correlations and a New Method,” *Int. J. Heat Mass Transf.*, vol. 135, pp. 996–1012, 2019.

[8] V. Grabenstein and S. Kabelac, “Experimental and Theoretical Analysis of the Local Condensation Heat Transfer in a Plate Heat Exchanger,” in *Journal of Physics: Conference Series*, 2012, vol. 395.

[9] Y. Jia, C. Wang, Z. Chang, W. Li, and C. Zhang, “Heat Transfer Modelling of Plate Heat Exchanger in Solar Heating System,” vol. 7, pp. 426–447.

[10] O. J. Kwon, B. H. Shon, and Y. T. Kang, “Experimental Investigation on Condensation Heat Transfer and Pressure Drop of a Low GWP Refrigerant R-1233zd(E) in a Plate Heat Exchanger,” *Int. J. Heat Mass Transf.*, pp. 1009–1021, 2019.

[11] D.-H. Han, K.-J. Lee, and Y.-H. Kim, “The Characteristics of Condensation in Brazed Plate Heat Exchangers with Different Chevron Angles,” *J. Korean Phys. Soc.*, vol. 43, no. 1, pp. 66–73, 2003.

[12] R. N. Taktashev and T. S. I. F. A. Yerokhin, “Calculation of Heat Transfer in Case of Freon Condensation in Plate Condenser Channels,” *APRN J. Eng. Appl. Sci.*, vol. 11, no. 1, 2016.

[13] E. M. Djordjević, S. Kabelac, and S. P. Šerbanović, “Heat Transfer Coefficient and Pressure Drop During Refrigerant R-134a Condensation in a Plate Heat Exchanger,” *Chem. Pap.*, vol. 62, pp. 78–85, 2008.

[14] G. A. Longo, A. Gasparella, and R. Sartori, “Experimental Heat Transfer Coefficients during Refrigerant Vaporisation and Condensation Inside Herringbone-type Plate Heat Exchangers with Enhanced Surfaces,” *Int. J. Heat Mass Transf.*, vol. 47, pp. 4125–4136, 2004.

[15] W. S. Kuo, Y. M. Lie, Y. Y. Hsieh, and T. F. Lin, “Condensation Heat Transfer and Pressure Drop of Refrigerant R410a Flow in a Vertical Plate Heat Exchanger,” *Int. J. Heat Mass Transf.*, vol. 48, pp. 5205–5220, 2005.

[16] A. Jokar, S. J. Eckels, M. H. Hosni, and T. P. Gielda, “Condensation Heat Transfer and Pressure Drop of Brazed Plate Heat Exchangers using Refrigerant R134a,” *J. Enhanc. Heat Transf.*, vol. 11, pp. 161–182, 2004.

[17] H. D. Baehr and K. Stephan, *Heat and Mass Transfer*. Berlin: Springer, 1998.

[18] J. G. Collier, *Convective Boiling and Condensation*, 2nd ed. New York: McGraw-Hill, 1981.

[19] V. S. Gullapalli and B. Sundén, “CFD Simulation of Heat Transfer and Pressure Drop in Compact Brazed Plate Heat Exchangers,” *J. Heat Transf. Eng.*, vol. 35, no. 4, pp. 358–366, 2014.

[20] A. K. Tiwari, P. Ghosh, J. Sarkar, H. Dahiya, and J. Parekh, “Numerical Investigation of Heat Transfer and Fluid Flow in Plate Heat Exchanger using Nanofluids,” *Int. J. Therm. Sci.*, vol. 85, pp. 93–103, 2014.

EPI International Journal of Engineering
Volume 3, Number 1, February 2020, pp. 10-20
DOI: 10.25042/epi-ije.022020.02

*p*ISSN 2615-5109
*e*ISSN 2621-0541

Thermal and Flow Characteristics of Discrete Double Inclined Ribs at Low Curvature Coil for GSHP Application

Teguh Hady Ariwibowo[a, *], Keishi Kariya[b] , and Akio Miyara[c]

[a]Graduate School of Science and Engineering, Saga University, Saga, Japan, teguhhady@gmail.com
[b]Department of Mechanical Engineering, Saga University, Saga, Japan, kariya@me.saga-u.ac.jp
[c]Department of Mechanical Engineering, Saga University, Saga, Japan, miyara@me.saga-u.ac.jp

---

Abstract

In this study, the thermal and hydraulic characteristics in low curvature coil with Discrete Double Inclined Ribs (DDIR) were investigated. Water is selected as a working fluid, and flowrate range from 1 to 5 L/min, which is a low flowrate condition. Effect of geometry parameters such as distance between ribs, curvature ribs, and ribs inclination angles was observed. Results obtained by numerical simulations show that the heat transfer in DDIR-coil is 7.7 to 29.11% greater than that in plain coil, while the pressure drop was approximately 12.7 to 89.5% larger than that of plain-coil. A COP improvement factor that is calculated based on energy loss by pressure drop and energy saving by heat transfer enhancement was found to vary between 0.25 and 5.29. Flow visualization shows that there are two vortexes in cross-section at the downstream, and local vortexes arise around the ribs of DDIR-coil, which shows similar pattern and strength to DDIR-straight tube. The vortex makes a long fluid particle path and strengthens the turbulent mixing between the wall and the core flow of the coil. Based on these findings, DDIR-coil is recommended for applications in Slinky Ground Heat Exchangers, especially at low flowrates.

Keywords: CFD, discrete double inclined ribs, low curvature coil, longitudinal vortex

---

1. Introduction

The Ground Source Heat Pump (GSHP) has been proven as an efficient technology in the utilization of geothermal since the end of 1940s. The application of GSHP does not require high geothermal energy and can be installed in many places. This utilization is because soil temperatures have small fluctuations, while ambient air temperatures vary drastically. For example, in winter, air temperatures fluctuate from 0 C to 16 C [1].

Ground Heat Exchanger (GHE) is the primary key in the performance of the GHSP System. Increasing the efficiency of the GSHP system can be done by increasing the efficiency of GHE. Therefore, increasing the efficiency of the GSHP system can be done by increasing the efficiency of GHE by adopting a more advanced geometry. In general, Ground Heat Exchangers (GHE) in the GSHP systems is classified into two, namely the vertical GHE (VGHE) loop and horizontal GHE (HGHE) loop.

Popular HGHE horizontal loop configurations are straight pipe heat exchangers and slinky heat exchangers [1]. This heat exchanger requires a more extensive installation area than that of vertical GHE (VGHE). Based on studies of GHE geometry, slinky GHE is commonly utilized in HGHE application. This GHE has several advantages over vertical heat exchangers, i.e., easy installation, no need for special installation skills, and low installation costs. HGHEs are commonly set up in shallow trenches at a depth of 1 to 2 m from the ground surface.

To improve GHE performance, many researchers changed the tube design, some of which were on VGHE. Fin [2], and groved tube [3] were applied to improve thermal performance of VGHE. However, the modification of the geometry configuration is not commonly found in HGHE, especially the slinky type.

Several studies have been carried out to improve the performance of the slinky HGHE. Wu et al. [4] investigated some curvature coils and central coil intervals. They concluded that the difference in curvature did not show a significant increase in heat transfer extraction. However, a small curvature has a higher heat extraction rate at the same trench length. Central distance intervals increase specific heat extraction. However, increasing the central interval distance decreases the heat extraction at the same trench length. Selamat et al. [5] conducted simulation on the influence of the reclined and standing orientation of the slinky-ground heat exchanger. The results of this study indicate the use of standing orientation can extend the adequate period time by 14%. Ali et al. [6] investigated the effect of standing and

---

*Corresponding author. Tel.: +81-707-648-6605
Graduate School of Science and Engineering, Saga University
Saga, Japan, 840-8502

reclined orientation on the performance of slinky ground heat exchangers. They stated that the increase in heat transfer standing was higher than that of reclined. Standing slinky ground heat exchangers are influenced by deeper soil temperatures besides the amount of black fill material standing is more excellent than reclined slinky ground heat exchangers, which have higher thermal conductivity than the soil at the location.

Slinky GHE type has a low curvature coil. Hardik et al. [7] experimented with the effect of curvature on the coefficient of heat transfer on several types of coil. They claim that large curvature results in high heat transfer dute to strong secondary flow for thermal mixing. The curvature coil performance character has similarities with a straight tube. In low curvature coil, the weak centrifugal force leads to a low-pressure drop and low-heat transfer, especially at low flow rates [8]. Hence, this weakness could be solved by augmentation of coil.

Meng [9] experimented with the first Discrete Double Inclined Ribs (DDIR) straight tube study to improve heat transfer performance in the heat exchanger as his Ph.D. thesis in 2003. The result shows that the ribs could generate longitudinal vortex. Li et al. [10] did an experiment and simulation of the thermal characteristics of the DDIR-tube. They concluded that DDIR-straight tube could increase heat transfer increase from 100% to 120% higher than that of plain tube. However, the pressure drop has also increased from 170% to 250%. Zheng et al. [11] analyzed the thermal and fluid flow performance of DDIR-tubes using numerical analysis. Based on this study, DDIR-tube can increase heat transfer and friction factor 1.58-2.46 and 1.82-5.03 times above than that of smooth tube, respectively.

We conducted preliminary studies on the effect of DDIR on the 2.22 m^{-1} curvature coil [12]–[15]. The result shows that in heat transfer and pressure drop increase in the increase both ribs height and flowrate. High ribs can lead to a more significant distorted vortex of flow structure than that of plain coil. The research shows that DDIR-coil generates two vortexes. This result is the opposite of the use of DDIR-straight tube, which The addition of ribs can increase the amount of vortex. This phenomenon could be caused combine among three flow, i.e., primary flow, secondary flow, and rib-induced flow. However, we do not know which flow and which geometry configurations could enhance heat exchanger performance of DDIR-coil. Based on our best knowledge, there has been no research about the application of DDIR on low curvature coil heat exchanger. The goal of this research is to present a good DDIR-coil design and to obtain the characteristics of heat transfer and fluid flow in several coil configurations for GSHP application.

2. Materials and Methods

2.1 Models descriptions

The illustration diagram of DDIR-coil used in this study is shown in Fig. 1. The coil consists of three parts, namely inlet extension, test section, and outlet extension. In all simulations, the length of the extension both inlet and outlet is 200 mm. This extension is to ensure that flows almost fully developed and eliminates disturbance in the downstream section.

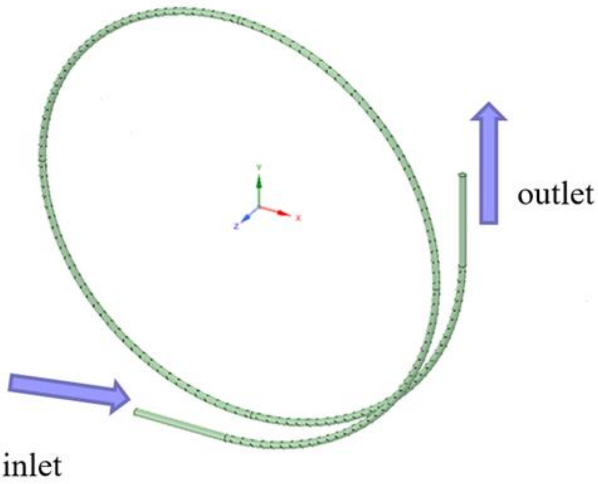

Figure 1. Schematic diagram of the DDIR-coil

The tube inside diameter, tube thickness, coil pitch, number of ribs at one perimeter are 14.46 mm, 0.71 mm, 100 mm, and four pieces, respectively. The geometry configuration of all models can be seen in table 1. The curvature of coil is defined as $\mathrm{C} = 1/R$ where R is the radius of coil. To find out the effect of DDIR-coil on increasing the heat exchanger performance, we also calculate straight-tube, plain-coil, and DDIR-straight tube as a benchmark. Whereas diameter of the coil, angle of ribs, curvature of coil are symbolized as D, α, and C, respectively. Pitch coil, pitch ribs and ribs height are symbolized as P, p and T, respectively.

Table 1. Geometric specifications of the heat exchanger model

Model	**Curvature of coil (m^{-1})**	**Ribs Height (mm)**	**Ribs Angle (°)**	**Ribs Pitch (mm)**	**Axial Length (mm)**
MR-C1	3.33	1	45	22.50	2359
MR-C2	2.66	1	45	22.50	2948
MR-A1	2.22	1	20	22.50	3534
MR-A2	2.22	1	30	22.50	3534
MR-P1	2.22	1	45	33.75	3534
MR-P2	2.22	1	45	45.00	3534
MR-P3/MR-C3/MR-A3	2.22	1	45	22.50	3534
MR-S	-	1	45	22.50	3534
MP-C1	3.33	-	-	-	2359
MP-C2	2.66	-	-	-	2948
MP-C3	2.22	-	-	-	3534

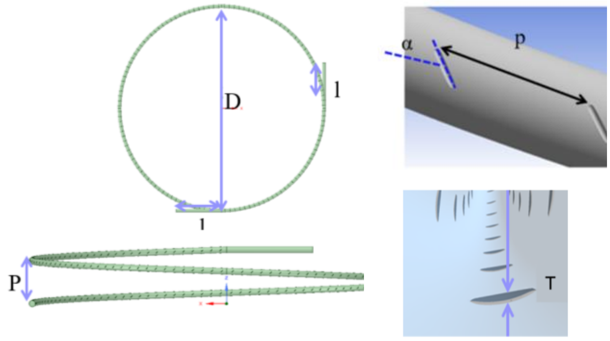

(a) (b)

Figure 2. Structure and configuration of DDIR-coil (a) top view and side of coil, (b) location of ribs inside and outside coil surface

2.2 Governing equations and mathematical methods

The flow simulation utilizes Reynolds averaged Navier-Stokes (RANS) equation. The simulation is assumed as heat transfer, and fluid flow is turbulent, steady-state, and no heat loss to environment. Shear stress tensor κ-ω (SST κ-ω) is a turbulent model that shows an excellent performance in modeling adverse pressure gradient. This model combines κ-ω model in near-wall and κ-ε model in the core flow [16].

The Governing equations are as per the following Continuity equation:

$$\frac{\partial(\rho u_i)}{\partial x_i} = 0 \tag{1}$$

Momentum equation:

$$\frac{\partial(\rho u_i)}{\partial t} + \frac{\partial(\rho u_i u_j)}{\partial x_j} = -\frac{\partial p}{\partial x_i} + \frac{\partial}{\partial x_j}\left(\mu \frac{\partial(u_i)}{\partial x_j} - \rho\overline{u'_i u'_j}\right) \tag{2}$$

Energy equation:

$$\frac{\partial}{\partial x_i}(\rho T) + \frac{\partial}{\partial x_i}(\rho u_i T) = \frac{\partial}{\partial x_i}\left(\frac{\lambda}{c_p}\frac{\partial T}{\partial x_i}\right) \tag{3}$$

Turbulence kinetic energy equation:

$$\frac{\partial(\rho\kappa)}{\partial t} + \frac{\partial(\rho u_i \kappa)}{\partial x_i} = \tilde{P}_\kappa - \beta^*\rho\kappa\omega + \frac{\partial}{\partial x_i}\left((\mu + \sigma_\kappa u_t)\frac{\partial \kappa}{\partial x_i}\right) \tag{4}$$

Specific dissipation rate equation:

$$\frac{\partial(\rho\omega)}{\partial t} + \frac{\partial(\rho u_i \omega)}{\partial x_i} = \varphi\rho S^2 - \beta\rho\omega^2 + \frac{\partial}{\partial x_i}\left((\mu + \sigma_\omega u_t)\frac{\partial \omega}{\partial x_i}\right) + 2(1 - F_1)\rho\sigma_{\omega^2}\frac{1}{\omega}\frac{\partial \kappa}{\partial x_i}\frac{\partial \omega}{\partial x_i} \tag{5}$$

where blending function F_1 is described as follows

$$F_1 = tanh\left\{\left\{min\left[max\left(\frac{\sqrt{\kappa}}{\beta^*\omega y}, \frac{500\upsilon}{y^2\omega}\right), \frac{4\rho\sigma_{\omega 2}\kappa}{CD_{\kappa\omega}y^2}\right]\right\}^4\right\}$$

where

$$CD_{\kappa\omega} = max(2\rho\sigma_{\omega 2}(1/\omega)(\partial\kappa/\partial x_i)(\partial\omega/\partial x_i), 10^{-10})$$

and y is the distance to the adjacent wall. Turbulent eddy viscosity is described by

$$\upsilon_t = \frac{\varphi_1\kappa}{max(\varphi_1\omega, SF_2)}$$

where S is a constant measure of strain rate and F_2 is a second blending function described as follows

$$F_2 = \left\{\left[max\left(\frac{2\sqrt{\kappa}}{\beta^*\omega y}, \frac{500\upsilon}{y^2\omega}\right)\right]^2\right\}$$

The SST model uses a production limiter to prevent turbulence buildup in stagnation areas as follows

$$P_\kappa = \mu_t \frac{\partial u_i}{\partial x_j}\left(\frac{\partial u_i}{\partial x_j} + \frac{\partial u_j}{\partial x_i}\right) \rightarrow \tilde{P}_\kappa = min(P_\kappa, 10.\beta^*\rho\kappa\omega)$$

All constants used, β^*, φ_1, β_1, $\sigma_{\kappa 1}$, $\sigma_{\omega 1}$, φ_2, β_2, $\sigma_{\kappa 2}$, and $\sigma_{\omega 2}$, are a combination of constants calculated based on the $\kappa - \varepsilon$ and $\kappa - \omega$ model. All equations were solved using ANSYS FLUENT 17.2, which is a commercial software based on the finite volume method. For Velocity-Pressure Coupling, the SIMPLE algorithm was utilized. The minimum convergence criterion for the continuity, velocity, and turbulence equation is 10^{-3}, and the energy equation is 10^{-7}.

2.3 Grid generation and independence test

Three-dimensional mesh made using ANSYS Meshing 17.2. The discretized domain uses unstructured-tetrahedral elements, as shown in Fig. 3. To obtain more accurate results, the value of y^+ is less than 1. This setting can make fine quality mesh near the wall and ribs. To find out the accuracy of numerical simulations, we use three sets of grids with 16136244 (coarse), 17779526 (medium), and 20175527 (fine) elements, which were used to test the grid independence test at Re = 4115. In this test, the pressure drop and heat transfer rate were checked. The relative deviations of pressure drop and heat transfer rate were determined based on the value of the fine mesh. Nusselt numbers of coarse, medium, and fine mesh were 71.27, 72.02, and 72.76, respectively. The deviation of Nusslet number from coarse to fine and medium to fine were 2.04 and 1.01 %, respectively. Friction factors of coarse, medium, and fine mesh were 0.08273, 0.08330, and 0.08391, respectively. The deviation friction factors from coarse to fine and medium to fine are 1.39 and 0.71 %, respectively. Therefore, the 20175527-mesh system was chosen quite dense in this study.

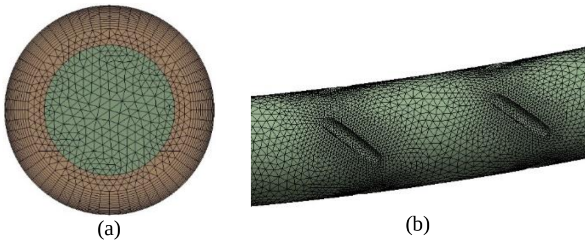

(a) (b)

Figure 3. Mesh system of DDIR-coil: (a) mesh in the cross-section plane of coil, (b) mesh on ribs

2.4 Boundary condition and data reduction

Velocity inlet boundary condition was adopted with uniform velocity, water temperature constant value is 280 K, the pressure outlet boundary condition was utilized. The flow at the wall was assumed as no slip. The wall temperature is assumed to be constant and uniform at 291 K in the inner side of the tube. Outside of the tube was assumed as perfectly insulated, hence no heat loss to surroundings. The tested flow rate is 1 L/min (Re = 1028), 2 L/min (Re = 2057), 3 L/min (Re = 3086), 4 L/min (Re = 4115), and 5 L/min (Re = 5144). The equation of κ in the $\kappa - \omega$ turbulence model uses enhanced wall treatment in wall boundary conditions. This setting means that for all boundary conditions for fine mesh, Low-Reynolds-number treatment was utilized. To find out the strength of vortex, we use swirl strength (λ_{ci}). This method calculates strength of vortex based on the velocity gradient tensor. Swirl strength uses the imaginary portion of the complex eigenvalues of the velocity gradient tensor to describe vortices [17], [18].

The following equation calculates heat transfer rate of the coil

$$Q = \dot{m}c_p(T_o - T_i) \tag{6}$$

where, T_o and T_i are bulk temperature on downstream and upstream crossection, respectively. Calculation of the average heat transfer coefficient is obtained as follows

$$h = \frac{Q}{\int_A \; dA\,\Delta T_m} \tag{7}$$

where, ΔT_m is Logarithmic Mean Temperature Difference (LMTD) and T_w is wall temperature.

$$\Delta T_m = \frac{(T_w - T_o) - (T_w - T_i)}{ln\left(\frac{T_w - T_o}{T_w - T_i}\right)} \tag{8}$$

All water properties are assumed to be constant, so the use of LMTD calculations is valid. Some dimensionless numbers are used in this study as follows

$$Re = \frac{\rho u d}{\mu} \tag{9}$$

$$Nu = \frac{hd}{\lambda} \tag{10}$$

$$f = \frac{\Delta p}{\left(\frac{l}{d}\right)\left(\rho\frac{v^2}{2}\right)} \tag{11}$$

We use the critical Reynolds number calculation in coil, which is proposed by Ito [19]. The critical Reynolds number is shown as follows

$$Re_{cr} = 20000\left(\frac{d}{D}\right)^{0.32} \tag{12}$$

Coefficient of Performance (COP) improvement factor is proposed by Jalaluddin and Miyara [20]. This parameter is to see the improvement of GSHP system due to GHE modification. The COP improvement factor is described as follows

$$\frac{Q_H'}{Q_H} - \frac{V\Delta p}{Q_H}\frac{\Delta p'}{\Delta p} > 0 \tag{13}$$

Where, Q_H, Q_H', V, $\Delta p'$, and Δp are heat transfer rate (W/m), an increase of heat transfer rate (W/m), volumetric flowrate (m^3/s), an increase of pressure drop (Pa/m), and pressure drop (Pa/m), respectively. If left term is larger than 0, it means the performance of GSHP system ground heat increase. The base of COP improvement factor is heat transfer and pressure drop of smooth straight tube on several corelations.

A few Nusselt number and friction factor correlations were used in the turbulent, transition, and laminar regime to determine the heat transfer rate and pressure drop for smooth straight tubes because the Reynolds number in this study was from 1028 to 5144. Critical Reynolds number for ribs pitch variation and ribs angle is 5332. Then, critical Reynold numbers for curvature 2.22, 2.66 and 3.33 m^{-1} are 5332, 5652, and 6071, respectively.

For laminar region, Nusselt number and friction factor were calculated as follows

$$\mathrm{Nu} = 3.66 \tag{14}$$

$$f = \frac{64}{Re} \tag{15}$$

Meanwhile, the calculation of the Nusselt number in the transition region adopted a linear interpolation method of the New Gnileniski Nusslet number [21], which is valid at $2300 < Re < 4000$ and constant wall temperature.

$$Nu = (1-\gamma)Nu_{lam,2300} + \gamma Nu_{turb,4000} \tag{16}$$

where

$$\gamma = \frac{Re - 2300}{2300 - 4000} \tag{17}$$

$Nu_{lam,2300}$ was calculated as follows

$$Nu_{m,T} = \left(Nu_{m,T,1}^3 + 0.7^3 + \left(Nu_{m,T,2} - 0.7\right)^3 + Nu_{m,T,3}^3\right)^{1/3} \tag{18}$$

where,

$$Nu_{m,T,1} = 3.66,$$

$$Nu_{m,T,2} = 1.615\sqrt[3]{Re\,Pr\,d/L},$$

$$Nu_{m,T,3} = \left(\frac{2}{1+22\,Pr}\right)^{1/6} (Re\,Pr\ d/L)$$

then $Nu_{turb,4000}$ was calculated as follows

$$Nu = \frac{(f/8)(Re - 1000)Pr}{1 + 12.7\sqrt{f/8}(Pr^{2/3} - 1)} \left[1 + \left(\frac{d}{L}\right)^{2/3}\right] K \qquad (19)$$

the K factor was described as

$$K = \left(\frac{Pr}{Pr_w}\right)^{0.11}$$

The friction factors in Eq. (18) use Konakov's friction factors as follows

$$f = (1.8\,Log_{10}Re - 1.64)^{-2} \qquad (20)$$

whereas in the transitional regime, Abraham friction factor [22] that is valid Reynold number from 2300 to 4500 are used as follows

$$f = 303\;10^{-12} - 3.6710^{-8}Re^2 + 1.46\;10^{-4}Re - 0.151 \qquad (21)$$

For the turbulent regime, calculation the Nusselt number in Eq. (18) and the friction factor use Petukhov friction factors as follows

$$f = (0.79\,ln\,(Re) - 1.64)^{-2} \qquad (22)$$

3. Results and Discussions

3.1 *Model validation*

We adopted some of the results of experiments conducted by Meng [9] to validate numerical simulations as shown in Fig. 4 and 5. The numerical results were following the experimental results on the f and $Nu/Pr^{1/3}$, Although there were some deviations. The average deviation between simulation and experimental results is 10.6 % for $Nu/Pr^{1/3}$ and 3.9 % for f. This deviation can be caused by the uncertainty of the experimental measurements and the difference between numerical and experimental methods. Accordingly, the numerical method used in the study of heat transfer and pressure drop is reliable.

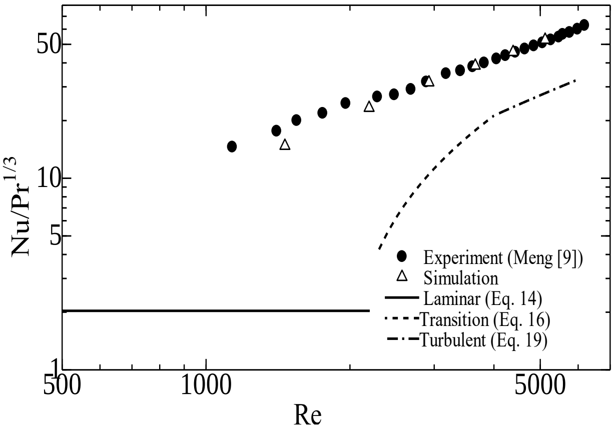

Figure 4. Comparison of $Nu/Pr^{1/3}$ between simulation results and experiment results for the proposed DDIR-straight tube

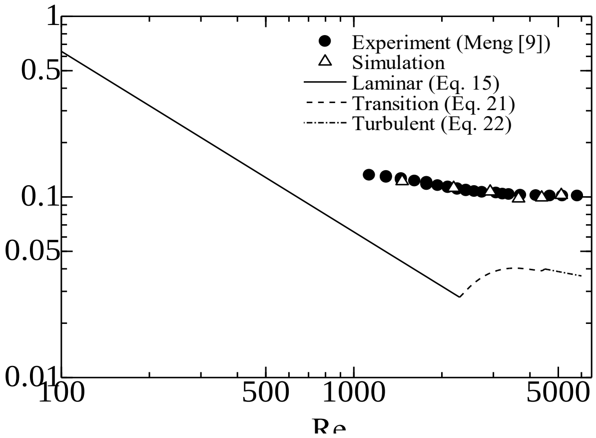

Figure 5. Comparison of friction factors between simulation results and experiment results for the proposed DDIR-straight tube

3.2 *Flow structure and heat transfer*

The behavior of the flow structure on DDIR-coil needs to be examined before discussing the results. The resulting flow analysis is an effective way of describing the flow in the DDIR-coil. Plain-coil is used as a comparison of how significant the effect of DDIR-coil is on the flow structure. Figure 6 shows a three-dimensional flow display in the downstream coil area for Re = 4115. In plain-coil, flow particles tend to occupy an outer side -coil position. The flow is caused by centrifugal force. This centrifugal force also causes some water particles near the wall to move towards the inner side of coil. In general, DDIR-coil produces two vortices when water particles pass through the ribs, namely the front vortex and the rear vortex.

In DDIR-coil, flow particles tend to be distributed almost evenly both at inner side and outer side of coil. The ribs-induced flow is caused by force of the front vortex and rear vortex, which affect the centrifugal coil force. This phenomenon is confirmed by the tendency of water particle flow near the wall from outer side of coil to be distorted to outerside of coil several times when it crosses ribs before finally, the particle flow moves towards the inner side of coil. The path of water particles in DDIR-coil tends to be longer than that of plain-coil. Tangential velocity and streamline observations are a remarkable way to determine the performance of DDIR effects in the flow field.

Figure 7 shows the tangential velocity vector in the downstream coil. In plain-coil, the gradient velocity vector near the wall looks smaller than in DDIR-coil. Besides, the plain-coil location of the stagnation point and separation point tends to have a longer circumferential length than that of DDIR-coil. This tendency is possible because the flow generated by ribs can distort the flow so that it shifts the location of the stagnation point and the separation point. The DDIR-straight tube shows that there are two pairs of vortices in opposite directions. The velocity gradient was significant in the two pairs of vortexes. The stagnation point and flow separation are clearly symmetrical to each other.

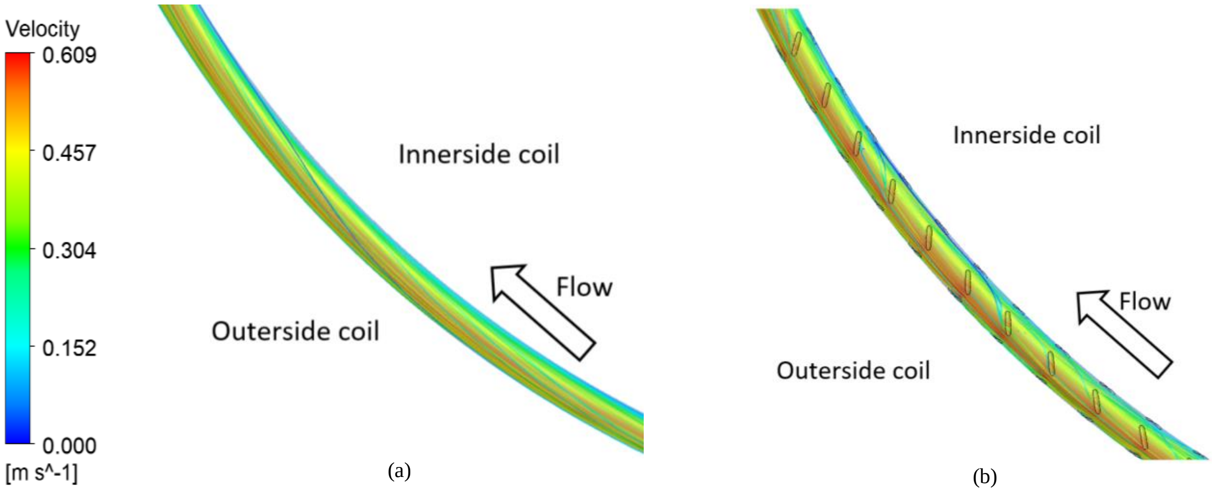

(a) (b)

Figure 6. Limiting 3D isometric view streamline for Re = 4115 (a) MP-C3, (b) MR-C3

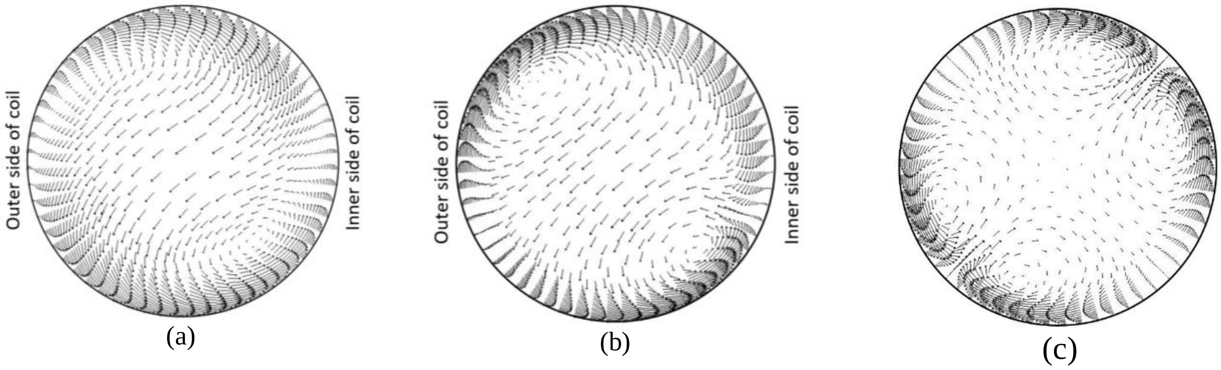

(a) (b) (c)

Figure 7. Tangential velocity vector in outlet test section for Re = 4115 (a) MP-C3, (b) MR-C3, (c) MR-S

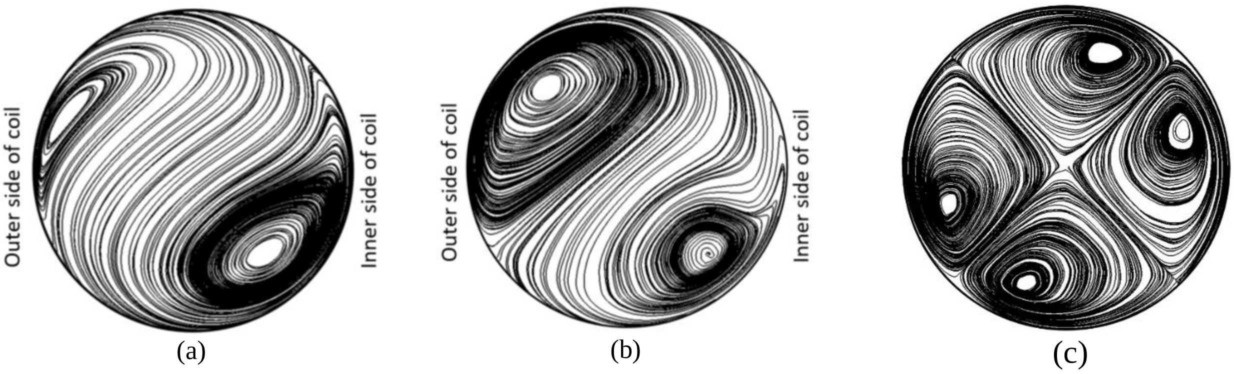

(a) (b) (c)

Figure 8. Streamlines in outlet test section for Re = 4115 (a) MP-C3, (b) MR-C3, (c) MR-S

(a)

(b)

Figure 9. Vortex cores (λ_{ci} = 40s^{-1}) generated for Re = 4115 (a) MR-S, (b) MR-C3

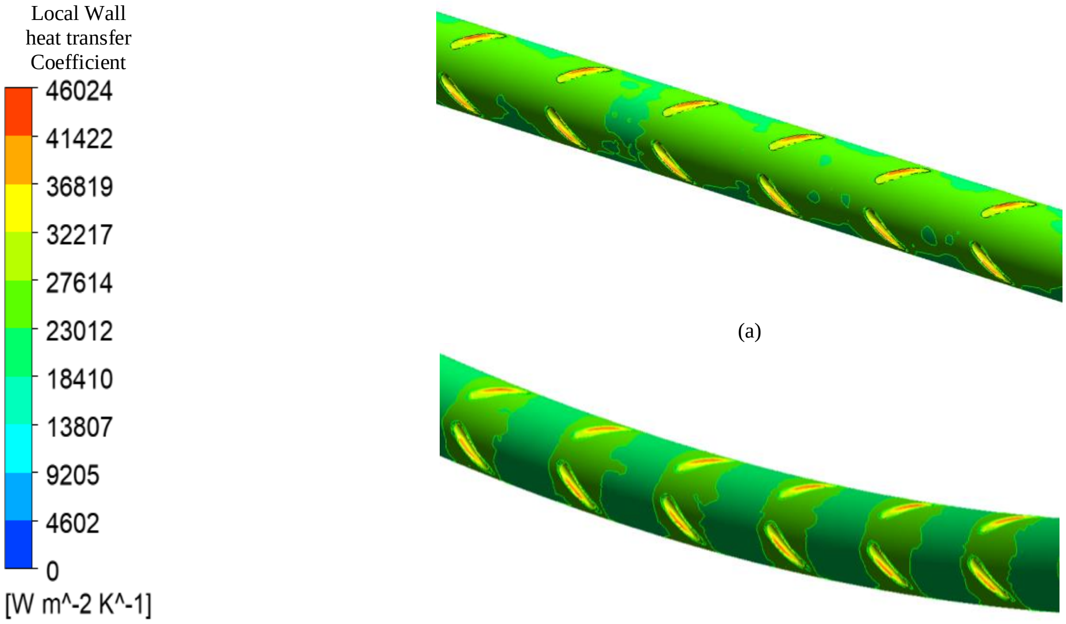

(a)

(b)

Figure 10. Local wall heat transfer coefficient contours on the wall of the test section for Re = 4115 (a) MR-S, (b) MR-C3

Figure 8 shows a streamlined downstream coil. A pair of counter-rotating vortex is produced in both plain-coil and DDIR-coil. Based on research into the application of DDIR on straight tubes, the addition of ribs is accompanied by an increase in the number of longitudinal vortices Zheng et al [11]. This research conduct by using two pairs of V-type ribs on circumferential of tube. The generated vortex should be two pairs. However, in this study, we found one pairs. No additional vortex appears because the vortex generated by the ribs joins the vortex caused by the centrifugal coil force.

This result is confirmed by the size of the vortex seen in the streamline. DDIR-coil tends to have a larger vortex size than that of plain-coil. On the DDIR-straight tube, two pairs of vortexes of similar size and flow patterns that appear dense are seen. This pattern indicates that the DDIR-stright tube pathway particles are longer than that of DDIR-coil and DDIR-plain. The quantitative increment of DDIR-coil in heat transfer and fluid flow can be seen in Fig. 11.

The movement of the ribs-induced vortex with different types of shape is illustrated in Fig. 9. Vortex core visual images are displayed based on iso-surface values of swirling strength of 40s^{-1}. The structure of powerful vortexes is mostly constructed behind the ribs. The structure indicate that the strength of the rear vortex is greater than that of the front vortex. On DDIR-straight tube, the distribution of the vortex appears evenly on each ribs at the same circumferential perimeter. However, on DDIR-coil, the vortex distribution is not the same in every ribs at one circumferential perimeter. This distribution is because the DDIR-straight tube primary flow and the ribs induced flow do not interfere with each other whereas the DDIR-secondary secondary flow and ribs induced flow interfere with each other.

Figure 10 shows the distribution of local heat transfer coefficient for Re = 4115 for DDIR-straight tube and DDIR-coil at the same axial length. It is clear that the heat transfer coefficient of DDIR-straight tube is slightly higher than that pf DDIR-coil on the surface of the ribs, this is because the flow is incident directly onto the surface of the ribs. The local heat transfer coefficient was discovered somewhat higher at the rear ribs due to rear induced vortex. This phenomenon is caused by the strength of the rear vortex higher than that of the front vortex. However, it can be seen clearly that the local heat transfer coefficient is slightly higher in the DDIR-straight tube than that of in the DDIR- coil. DDIR-straight tube produces two flows, primary flow, and ribs induced flow. Meanwhile, DDIR-coil produces three flows, namely primary flow, secondary flow, and ribs-induced flow. Secondary flow and ribs-induced flow probably combine, then weakening the strength of the vortex, hence local heat transfer in DDIR-coil is slightly smaller than that of DDIR-straight tube.

3.3 Rib angle effect

The variation of heat transfer rate, pressure drop and COP improvement factors with different rib angle and flowrate are shown in Figs. 11 (a), (b) and (c). As can be seen, heat transfer and pressure drop increase with increasing flow rate. This increment may be due to increased flowrate that can generate greater windward, leeward, and higher swirl strength. An interesting pattern is shown by an angle of 20^o and 45^o. These two angles show almost a similar performance in both heat transfer and pressure drop in the range flowrate. A more detailed check shows that the 30^o angle has a slightly smaller heat transfer performance than that of the other angles. Whereas the pressure drop showed a more significant increase in each angle of the ribs. The increase in heat transfer is approximately 13.9%-25.15% and the pressure drop increases approximately 26.8%-89.5% over plain-coil. In Figs. 11 (a), (b) and (c), heat transfer rate, pressure drop and COP improvement factor of straight DDIR-straight tube at 45^o ribs angle are also plotted. The straight tube is used as benchmark performance of DDIR-coil at 45^o. As mentioned above, DDIR is more effective in straight tube than coil. However, According to Wu et al. [4] coil is still more suitable for use in ground heat exchangers because the ground heat exchanger is installed in a trench and the coil has higher performance than that of straight tube in the same length of trench.

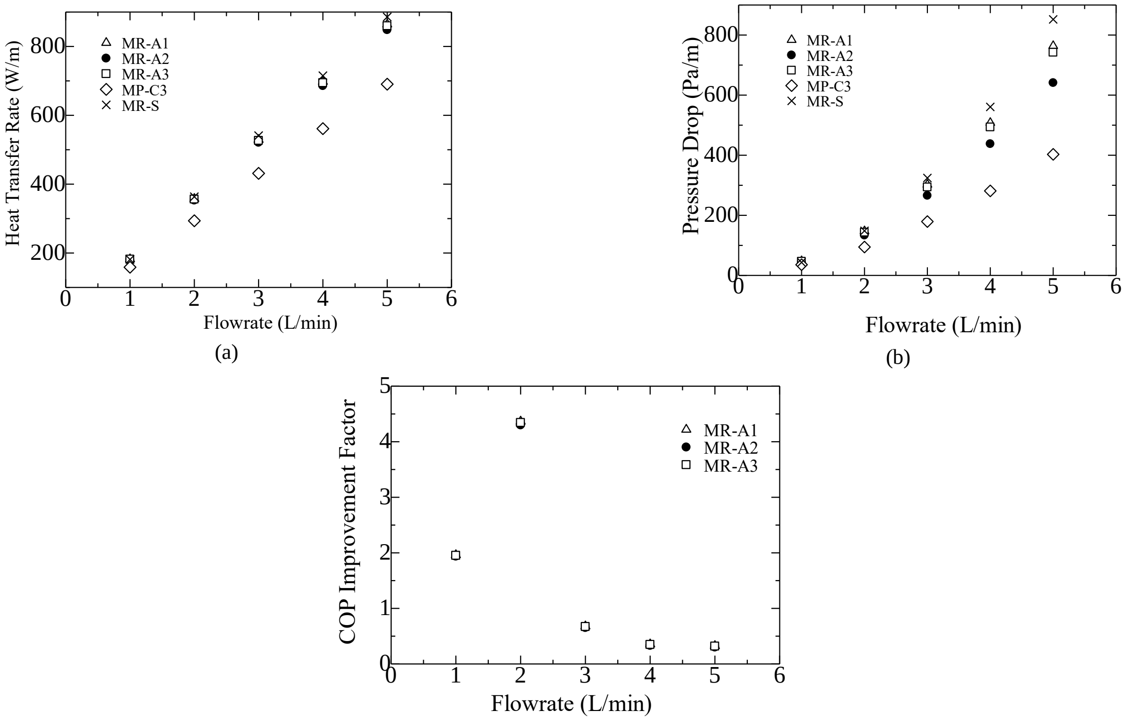

(a)

(b)

(c)

Figure 11. Performance characteristics in angle ribs variation (a) heat transfer rate, (b) pressure drop, (c) COP improvement factor

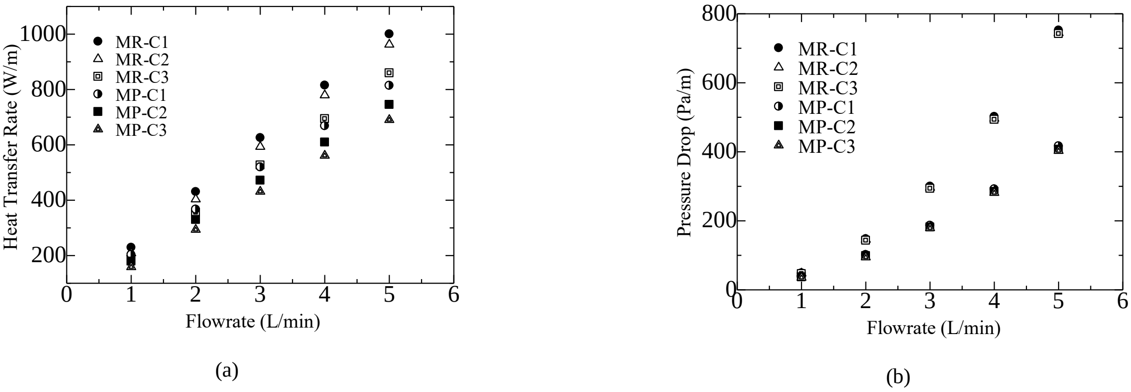

(a)

(b)

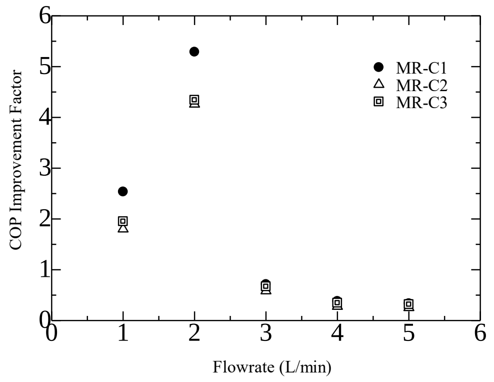

(c)

Figure 12. Performance characteristics in curvature variation (a) heat transfer rate, (b) pressure drop, (c) COP improvement factors

3.4 Curvature effect

Figures 12 (a), (b) and (c) show the effect of the curvature of the DDIR-coil on the performance of heat transfer, pressure drop and COP improvement factors at a rib angle of 45° and pitch rib of 22.5 mm in flowrate from 1 to 5 L/min. The graphs also illustrate plain-coil performance as a benchmark for increasing DDIR-coil performance. Commonly, decrease in curvature on DDIR-coil results in an increase in heat transfer rate and pressure drop. The decrease in curvature appears significantly at the heat transfer rate, but the decrease in pressure drop is very insignificant. The use of DDIR-coil shows more significant than that of plain-coil. The increase in heat transfer rate on curvature 2.22, 2.66, and 3.33 m^{-1} are 12.70-22.85%, 16.27-29.11%, and 14.50-24.51%, respectively. The increment in pressure drop on curvature 2.22, 2.66, and 3.33 m^{-1} are 27.28-80.45%, 28.87-82.81% and 30.83-84.17%, respectively. The value of COP Improvement Factors varies from 0.25-5.29. This trend shows that DDIR-coil provides benefits in terms of energy conservation. Although the heat transfer rate and pressure drop characters increase with the increase in the curvature coil, the COP Improvement factor shows an interesting trend. The highest increase occurred at 2.22 $m^{-1,}$ and the lowest occurred at 2.66 m^{-1}. Dramatic increase and decrease of COP Performance factors in Curvature variations also happen at first flowrate. The COP Improvement Factors tend to change drastically in flow rate 1-3 L/min because the factors are calculated on Eqs. (13)-(21) for straight tube. The trend is triggered mainly flow on the straight tube in the transition regime. Hence, drastic change happens on this area..

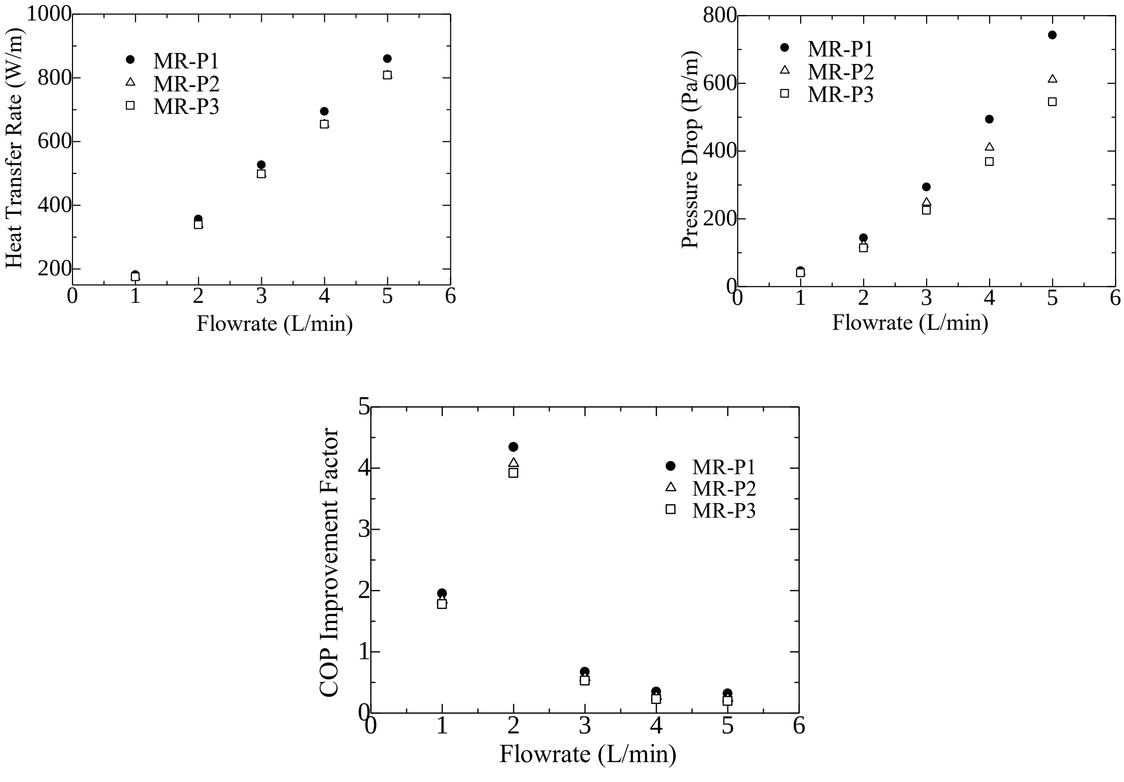

Figure 13. Performance Characteristics in ribs pitch (a) heat transfer rate, (b) pressure drop , (c) COP improvement factor

3.5 Ribs pitch effect

Figures 13(a), (b) and (c) show the effect of pitch ribs on the performance of heat transfer and flow at a rib angle of 45^o and axial coil length of 3533.75 mm. Pitch ribs are calculated based on the axial distance on the center coil. It is clear that the heat transfer rate and pressure drop slightly increased when pitch ribs increased. The reason for this phenomenon is that heat transfer increases more in the downstream ribs than that of upstream ribs, and increment ribs pitch decreases regions in downstream. Heat transfer and pressure drop increase, relative to plain coil, increases by 7.7 - 25.5% and by 12.7 - 84.1 %, respectively

The COP Improvement Factor in pitch ribs varies between 0.19 to 4.34. It can be seen that the value of COP Improvement Factors increases with the decrease in distance between ribs on all flowrates. Significant increase in COP Improvement Factor at a flow rate of 1-2 L / min. Then there is a significant decrease in the flow rate of 2-3 L / min. Then, a decrease occurs slowly at a flow rate of 3-5 L / min. A sudden change in COP Factors that occurs at flow rates of 1-3 L / min occurs due to performance calculations occurring on a straight tube. At this flow rate, the flow is in the transition area so that the heat transfer and pressure drop have increased significantly. However, when it has passed the transition regime, tube performance tends to be more stable and turbulent enough so that straight tube performance approaches coil performance. This characteristic tends to result in a gradual decrease in COP Improvement factors at 3-5 L / min.

4. Conclusion

The results of the research on the effect of DDIR of Low curvature coil on increasing heat transfer, pressure drop, and COP Improvement factors are presented in this paper. The flow structure is described and analyzed. The influence of ribs angle, curvature, and ribs pitch are examined at a specific flowrate range so that the thermal and hydraulic characteristics of DDIR-coil are summarized as follows:

In the flowrate range investigated, DDIR-coil heat transfer increased from 7.7 to 29.11% bigger than that of plain-coil, and the pressure drop increased from 12.7 to 89.5% higher than that of plain-coil. COP Improvement factors approximately vary between 0.25 and 5.29.

The multiple longitudinal vortex arrangement in the DDIR-coil down stream is not apparent when compared to DDIR-straight. However, the Vortex local DDIR in coil is formed and has a strength similar to the vortex local DDIR in straight tube. The combination of secondary flow and ribs induced flow occurs so that the strength of the vortex in DDIR-coil tends to be higher than in plain coil. This phenomenon results in a relatively longer streamline and strong turbulence between the wall area and the core area, which increases heat transfer.

COP Improvement factors increase with decreasing pitch ribs. Ribs angle 20^o results in high COP Improvement Factors. Curvature coil 2.66 m^{-1} produces high COP Improvement Factors. The use of DDIR in low curvature coil / slinky-coil is recommended for practical applications of Ground Heat Exchanger, especially at low flowrate.

Acknowledgements

This research was supported by the "Renewable energy heat utilization technology and development project" of the New Energy and Industrial Technology Development Organization (NEDO), Japan.

References

[1] C. S. Chong, G. Gan, A. Verhoef, R. G. Garcia, and P. L. Vidale, “Simulation of Thermal Performance of Horizontal Slinky-loop Heat Exchangers for Ground Source Heat Pumps,” *Appl. Energy*, vol. 104, pp. 603–610, 2013.

[2] B. Bouhacina, R. Saim, and H. F. Oztop, “Numerical Investigation of a Novel Tube Design for the Geothermal Borehole Heat Exchanger,” *Appl Therm Eng*, vol. 79, pp. 153–162, 2015.

[3] J. Acuña and B. Palm, “Comprehensive Summary of Borehole Heat Exchanger Research at KTH,” in *Proceedings of Conference on Sustainable Refrigeration and Heat Pump Technology*, 2009.

[4] Y. Wu, G. Gan, A. Verhoef, P. L. Vidale, and R. G. Gonzalez, “Experimental Measurement and Numerical Simulation of Horizontal-coupled Slinky Ground Source Heat Exchangers,” *Appl. Therm. Eng.*, vol. 30, pp. 2574–2583, 2010.

[5] S. Selamat, A. Miyara, and K. Kariya, “Numerical Study of Horizontal Ground Heat Exchangers For Design Optimization,” *Renew. Energy*, vol. 95, pp. 561–573, 2016.

[6] M. H. Ali, K. Kariya, and A. Miyara, “Performance Analysis of Slinky Horizontal Ground Heat Exchangers for a Ground Source Heat Pump System,” *Resources*, vol. 56, pp. 1–18, 2017.

[7] B. K. Hardik, P. K. Baburajan, and S. V. Prabhu, “Local Heat Transfer Coefficient in Helical Coils with Single Phase Flow,” *Int. J. Heat Mass Transf.*, vol. 89, pp. 522–538, 2015.

[8] G. Yoo, H. Choi, and W. Dong, “Fluid Flow and Heat Transfer Characteristics of Spiral Coiled Tube: Effects of Reynolds Number and Curvature Ratio,” *J. Cent. South Univ*, vol. 19, pp. 471–476, 2012.

[9] J. Meng, “Enhanced Heat Transfer Technology of Longitudinal Vortices Based on Field-coordination Principle and its Application,” Tsinghua University, 2003. (in Chinese)

[10] X. W. Li, J. A. Meng, and Z. Y. Guo, “Turbulent Flow and Heat Transfer in Discrete Double Inclined Ribs Tube,” *Int. J. Heat Mass Transf.*, vol. 52, pp. 962–970, 2009.

[11] N. Zheng, P. Liu, F. Shan, Z. Liu, and W. Liu, “Numerical Investigations of the Thermal-hydraulic Performance in a Rib-grooved Heat Exchanger Tube Based on Entropy Generation Analysis,” *Appl. Therm. Eng.*, vol. 99, pp. 1071–1085, 2016.

[12] T. H. Ariwibowo, G. Kuriyama, K. Kariya, and A. Miyara, “Numerical Analysis of Thermo-Hydraulic Performance of Discrete Double Inclined Ribs on Low Curvature Coil in Laminar Flow for Ground Source Heat Pump System Application,” in *Proceedings of 15th Asia Pacific Conference on the Built Environment 5R Technology for Building Environment*, 2019.

[13] T. H. Ariwibowo, A. Miyara, and K. Kariya, “Thermal and Hydraulic Performance Simulation of Curved Tube with Discrete Ribs Heat Exchanger for Ground Heat Pump System,” in *Proceedings of 53rd Joint Air Conditioning and Refrigeration Conference*, 2019.

[14] T. H. Ariwibowo, A. Miyara, and K. Kariya, “Consideration of Double Discrete Inclined Ribs in Low Curvature Coil for GSHP System,” *Int. J. Sustain. Green Energy*, vol. 8, pp. 56–64, 2019.

[15] G. Kuriyama, T. H. Ariwibowo, K. Kariya, and A. Miyara, “Heat Transfer and Pressure Drop Characteristics of Curved Tube with Discrete Ribs for Ground Source Heat Exchanger,” in *Proceedings of the 2019 Refrigeration and Air Conditioning Society of Japan Annual Meeting*, 2019. (in Japanese)

[16] F. Menter, M. Kuntz, and R. Langtry, “Ten Years of Industrial Experience with the Sst Turbulence Model,” *Turbul. Heat Mass Transf*, vol. 4, 2003.

[17] V. Holm´en, “Methods for Vortex Identification,” Lund University, 2012.

[18] ANSYS® Academic Research, *Release 17.2, Help System, Fluent User's Guide*. ANSYS, Inc., 2016.

[19] H. Ito, “Friction Factor for Turbulent Flow in Curved Tube,” *J. Basic Eng.*, vol. 81, pp. 123–134, 1959.

[20] Jalaluddin and A. Miyara, “Thermal Performance and Pressure Drop of Spiral-tube Ground Heat Exchangers for Ground-source Heat Pump,” *Appl. Therm. Eng.*, vol. 56, pp. 630–637, 2015.

[21] V. Gnielinski, “On Heat Transfer in Tubes,” *Int. J. Heat Mass Transf.*, vol. 63, pp. 134–140, 2013.

[22] J. P. Abraham, E. M. Sparrow, and W. J. Minkowycz, “Internal-flow Nusselt Numbers for The Low-reynolds-number End of the Laminar-to-turbulent Transition Regime,” *Int. J. Heat Mass Transf.*, vol. 54, pp. 584–588, 2011.

EPI International Journal of Engineering
Volume 3, Number 1, February 2020, pp. 21-29
DOI: 10.25042/epi-ije.022020.03

*p*ISSN 2615-5109
*e*ISSN 2621-0541

Multimodal Reduction of Elastic Vibrations in Plate Structure using Super Absorbent Polymer Beads

Takahiro Tomioka[a,*], Karen Minamisawa[b]

[a]Department of Mechanical Engineering, Faculty of Systems, Science and Technology, Akita Prefectural University. Email:tomioka@akita-pu.ac.jp
[b]Former Department of Machine Intelligence and Systems Engineering, Faculty of Systems, Science and Technology, Akita Prefectural University.

Abstract

This paper deals with multimodal reduction of structural elastic vibrations. Super absorbent polymer beads (SAP beads) have been introduced as a simple damping device inspired by the multimodal vibration reduction effect by passengers on railway vehicles. A series of vibration measurement tests using a 1:10 scale model of railway vehicle floor structure (model underframe) was carried out. The SAP beads which are sold commonly as water retention agent were stacked in a container and applied to the model underframe. From the experiments, multimodal vibration reduction effects have been demonstrated. A drastic difference has been observed when water was added together with SAP beads. To investigate the basic mechanism of the damping effect obtained by the experiments, an analytical model, which consists of multiple masses that are supported at an angle to each other, and its simplified model was proposed and numerical studies were conducted. Some specific combinations of the mass, spring, and damping elements in the model could express the experimental results well, and it has been estimated from the numerical results that each SAP layer act as an un-uniform subsystem.

Keywords: Elastic vibration; damping; multimodal vibration reduction; vibration analysis; viscoelastic material; super absorbent polymer

---

1. Introduction

The elastic vibrations that occur during machine operation tend to become conspicuous particularly in large and/or light-weighted mechanical systems such as the bodies of aircraft or railway vehicles. Generally, several elastic vibration modes are dominant at the same time in those structures, so simultaneous vibration reduction for multiple elastic modes (multimodal vibration reduction) is required to improve the quality and performance of the mechanical system such as maintaining ride quality. Of course, from an industrial application perspective, simple and cost-effective devices are needed. Dynamic vibration absorber (DVA) is a common and popular passive damping device with a simple configuration and established optimal design methods [1].

For railway vehicles, the idea of utilizing underfloor equipment as a DVA has been studied for a long time. Ishikawa and Sato [2] conducted a running test by applying elastically supported mass which imitated underfloor equipment and showed the reduction of the first mode of bending vibration of the carbody. Gong et al. [3] studied to use several kinds of equipment underneath the floor and on the roof as DVAs for different elastic modes of vibration by finite element analysis. However, since an ordinary DVA is a single-mode vibration absorber, a corresponding number of DVAs is necessary for multimodal vibration reduction.

Recently, one of the authors and his colleagues reported passengers' effect on the vibration of light-weighted railway vehicles [4], [5]. Figure 1(a) shows the acceleration power spectrum densities (PSDs) measured on the floor at the window side of the longitudinal center of a Shinkansen train during running at 270 km/h [4]. The peak observed around 10.5 Hz is considered corresponding to vertical elastic vibration mode(s) of the carbody. It can be seen that the peak value is reduced by increasing the number of passengers, whereas the change in the peak frequency is very small. The vibration reduction effect is also observed on the other peaks at least up to 20 Hz. Figure 1(b) compares the PSDs of the carbody loaded with 51 distributed onboard passengers and 5100 kg of iron blocks. Relative to the unloaded carbody, the peak around 10.5 Hz altered differently under passenger and iron block loadings; iron blocks reduced the peak frequency but exerted little effect on the peak value, whereas passengers induced a small frequency shift and a large reduction in the peak value. They show an additional damping effect by passengers, rather than an added mass effect. And the additional damping works on the multiple

---

*Corresponding author. Tel.: +81-184-27-2131
84-4, Tsuchiya-ebinokuchi, Yurihonjo, Akita, Japan, 015-0055

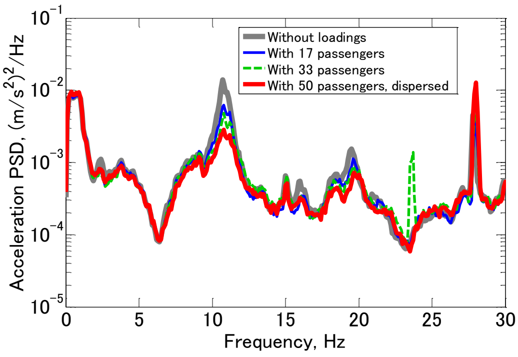

(a) Effect of the number of passengers

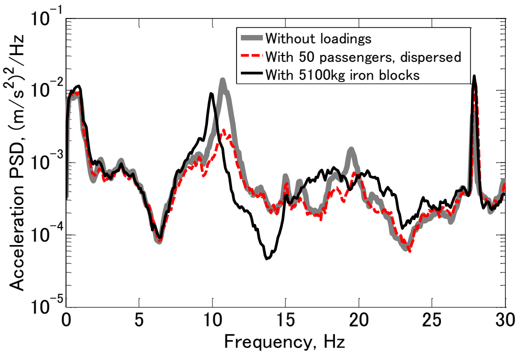

(b) Comparison of PSDs loaded with 50 passengers and 5100 kg of iron blocks on the floor

Figure 1. Acceleration PSDs of a Shinkansen measured during running at 270 km/h [4]. (At longitudinal center, window side on the floor)

elastic vibrations of a running carbody, not on a single mode.

These results suggest that, if the passengers' damping capabilities can be mimicked appropriately, it is expected to realize simple and effective passive vibration reduction devices. Some hints for it are: a human body has many natural frequencies corresponding to the motions of each organ or part, and a human body vibrates in every direction as a viscoelastic body. Based on these ideas, some trials have been carried out such as mounting flexible polyethylene tanks filled with some different kinds of liquid [5] or applying elastic torus filled with water [6], [7]. Their damping performances were confirmed by the excitation tests using actual railway vehicles. Those trials are considered utilizing elastic deformations of the applied objects as DVA.

In this study, super absorbent polymer beads (called SAP beads hereafter) are introduced as a multimodal vibration reduction device considering the viscoelastic characteristics of humans. Vibration measurement tests using a 1:10 scale model of railway vehicle floor structure were conducted, and the damping performance of SAP beads was investigated. Also, an analytical model and its simplified model were proposed to study the basic damping mechanism.

2. Setups for the Experimental Studies

2.1. Test structure and vibration measurement equipment

Figure 2 shows the elastic plate-like structure used in vibration testing in this study. This is a 1:10 scale model of railway vehicle floor structure, so it is called "model underframe" in this paper. The model underframe, which is made of stainless steel, is consisting of a thin plate reinforced by many beams with U-shaped cross-sections arranged like a ladder. Its size is length x width x thickness = 2000 mm x 310 mm x 10 mm and the mass is 10.5 kg. The model underframe was supported by springs (BRIDGESTONE Hybrid Air Damper) at four points like usual railway vehicle carbody and excited using an electro-dynamic exciter (Asahi WaveMaker SL0505) attached at the front end. The response vibration acceleration was measured by piezoelectric accelerometers (PCB 352C65). The excitation force was also measured using a load cell (PCB 208C02). The detailed measurement points on the model underframe are illustrated in Fig. 3. A total of 21 acceleration measurement points was arranged to check the natural modes of the elastic vibration, and the acceleration measured at the center of the model underframe (point f4c) was used to evaluate the vibration reduction effect by SAP beads as described later.

The electrodynamic exciter was driven by a band-limited random signal (a random signal applied by band-pass filter with cut-off frequencies of 10 and 250 Hz), and the duration of excitation was 60 s. The measured acceleration and force signals were recorded as digital data with a sampling frequency of 2048 Hz.

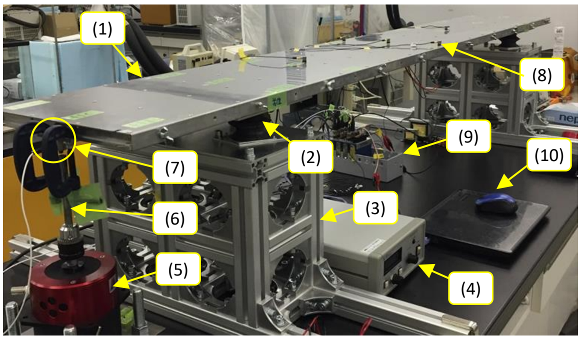

(1) Test structure (model underframe)
(2) Support springs (BRIDGESTONE Hybrid Air Damper EZ EZ9001A)
(3) Pedestal
(4) Exciter console (amplifier and control unit, Asahi APD-050FCA)
(5) Electro-dynamic exciter (Asahi WaveMaker05 SL0505)
(6) Driving rod
(7) Load cell (PCB 208C02)
(8) Accelerometers (PCB 352C65)
(9) Data acquisition unit (NI cDAQ-9189, 9234, 9263)
(10) Control PC

Figure 2. The test structure and the vibration measurement equipment

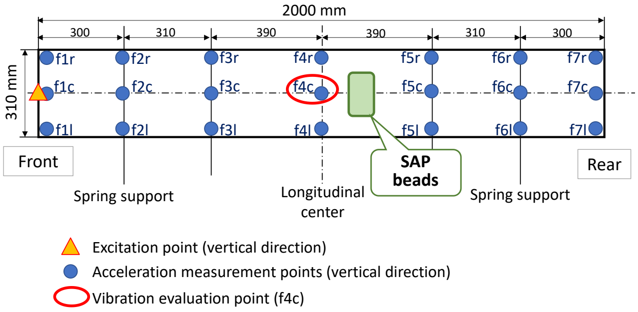

Figure 3. Measurement and excitation points on the model underframe

2.2. Loading conditions using SAP beads

In this study, which is a basic study for the multimodal vibration reduction of the model underframe, SAP beads filled in a container were chosen and examined as a simple multimodal damping device. Figure 4 shows the SAP bead and containers used here. The SAP beads are sold commonly as a water retention agent (substituting natural soil) or fragrance control material, and very easy to purchase. The SAP beads with a size of approximately 15 mm in diameter after soaking were used here. As for the containers of SAP beads, two types made of different materials, plastic (relatively flexible) and stainless steel (SUS; almost rigid), were used. Both of them are common food containers.

The loading conditions for SAP beads in this study are listed in Table 1 together with photographs. Case 1 compares the difference of loading amount of SAP beads in the same container: Case 2 is used to check the container's flexibility upon the damping effect: and Case 3 investigates the effects of water addition. The container filled with SAP beads was attached to the model underframe with thin and strong double-sided tape (NICHIBAN NICETACK NW-K10) at the position shown in Fig. 3.

3. Results of Vibration Measurement Tests

3.1. Test results for the single test underframe

The test results for the single test underframe (without any loadings) are described in this subsection to show its original vibration characteristics.

Figure 5 shows the natural vibration modes of the test underframe itself identified by the measured acceleration data. The modal analysis was carried out by applying the technique based on an ARX (Auto-Regressive eXogenous) model [8]. The thick and thin lines respectively express the deformed and undeformed shape, and the figures with "Hz" are natural frequencies. Five bending modes were obtained below 250 Hz, and no elastic modes with torsional deformation were identified since the excitation point (f1c) was near their nodes. The first bending mode (Fig. 5(a)) is commonly observed in actual railway vehicles.

Figure 6 shows the frequency response functions (FRFs) of acceleration measured at point f4c versus excitation force. Five prominent peaks corresponding to the bending modes shown in Fig. 5 can be observed. Two different curves express the data measured on different days to confirm the repeatability of the experiment under the same conditions.

3.2. Damping capabilities of SAP beads

The damping capability of SAP beads is investigated through the acceleration FRF. The conditions of excitation and FRF evaluation are the same as in Fig. 6.

At first, a comparison was made when different amounts of SAP beads were applied. Figure 7 shows the measured FRFs under the loading condition of Case 1. The gray, blue and red lines show without SAP beads, with 2-layers SAP beads (Case 1A) and with 3-layers SAP beads (Case 1B), respectively. Peak values tend to be reduced as SAP beads are applied, at least with the ones corresponding to the 1st, 2nd, and 4th bending modes. Also, the difference between Case 1A and 1B is observed

(a) A piece of SAP bead

(b) Containers of the SAP beads
Left: plastic (flexible, 45 g),
Right: stainless steel (SUS, almost rigid, 58 g)

Figure 4. SAP bead and its containers used in the experiments

Table 1. Loading conditions for the experiments

Case	Loading conditions (total mass: including container's mass)	Photo
1	A. SAP beads 2-layers (total 297 g) B. SAP beads 3-layers (total 427 g)	A  B 
2	A. SAP beads 3-layers in plastic container (total 427 g) B. SAP beads 3-layers in SUS container (total 440 g)	A  B 
3	A. SAP beads only, 3-layers (total 412 g) B. SAP beads + Water 20 g (total 411 g) C. SAP beads + Water 180 g (total 410 g) D. Water only 365 g (total 410g)	A  B 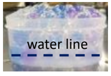 water line C 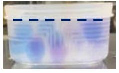 D 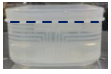

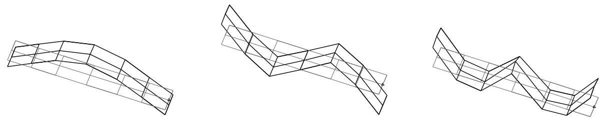

(a) 1st bending (19.0 Hz) (b) 2nd bending (67.0Hz) (c) 3rd bending (125.2 Hz)

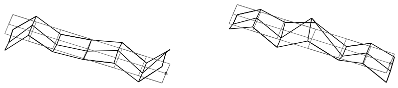

(d) 4th bending (188.2 Hz) (e) 5th bending (233.1 Hz)

Figure 5. Natural vibration modes of the model underframe identified by the excitation test (without loadings)

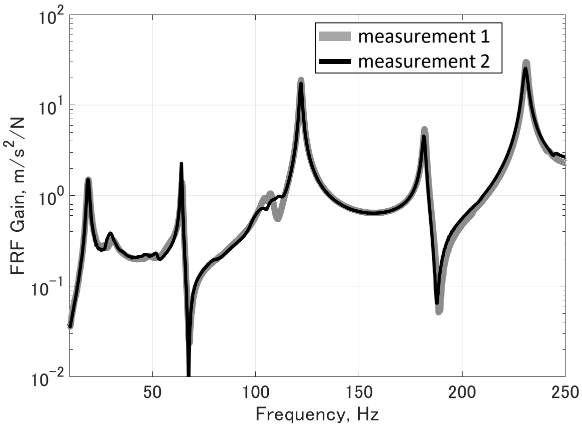

Figure 6. Measured acceleration FRFs versus excitation force at point f4c. (Without loadings; comparison of the data measured on different days)

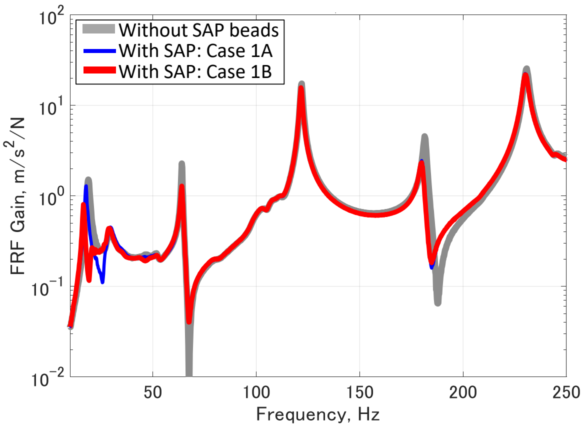

Figure 7. Measured acceleration FRFs versus excitation force at point f4c. (Case 1: effect of amount of SAP beads)

only for the peak near 19 Hz. Figure 8 shows an enlarged view of Fig. 7. The peak shifts towards lower frequency as the amount of SAP beads increases. Each curve with SAP beads also has a trough whose frequency shifts in the same way as the peak.

The vibration reduction by SAP beads seems similar to the DVA effect, particularly about the 1st bending mode (near 19 Hz). If it is so, the mass of SAP beads should work as DVA together with some spring elements. To check whether the container's flexibility act as the spring element, the comparison using different kinds of containers was conducted. Figure 9 shows the results of putting the same amount of SAP beads (382 g) in different containers. The blue and red lines show the results for Case 2A (flexible plastic container) and 2B (rigid SUS container), respectively. These FRF curves are nearly overlapping, indicating that the container's flexibility does not act as a spring element for the DVA effect by SAP beads, at least up to 250 Hz.

Figure 10 shows the results for Case 3. A drastic reduction in the higher frequency region can be observed when water was added. On the other hand, as shown in Fig. 11, the effect by adding water is not so large on the peak around 19 Hz. These data indicate that the mechanism of the vibration reduction effect by SAP beads may be different in low and high-frequency regions.

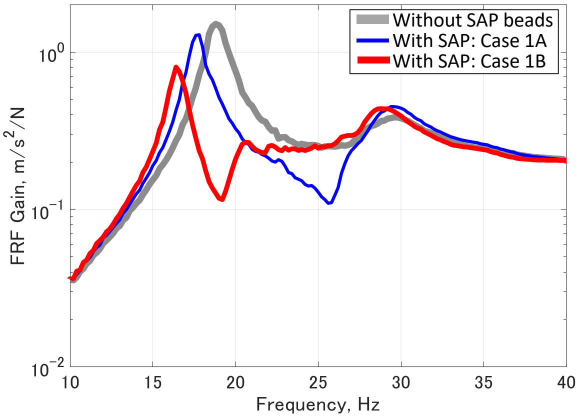

Figure 8. Enlarged view of Fig. 7

4. Numerical Studies with Simple Analytical Models

4.1. Vibration analysis model for the test structure with SAP beads

Multimodal vibration reduction by SAP beads have been observed through the experiments as described in the former section. Some interesting results were obtained such as phenomena similar to a DVA (Figs. 7, 8) and changes by adding water (Figs. 10, 11). The latter one showed a different tendency in the low and high-frequency regions.

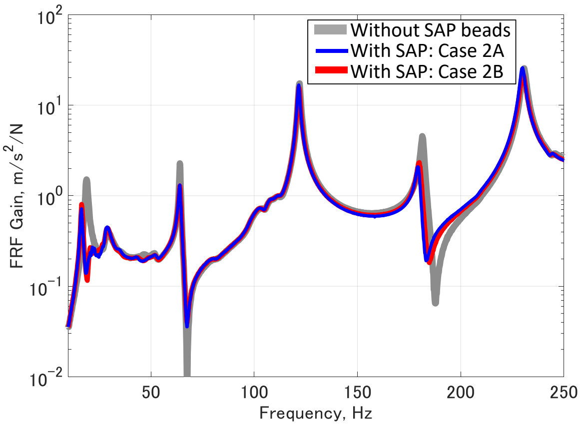

Figure 9. Measured acceleration FRFs versus excitation force at point f4c. (Case 2: effect of container's flexibility)

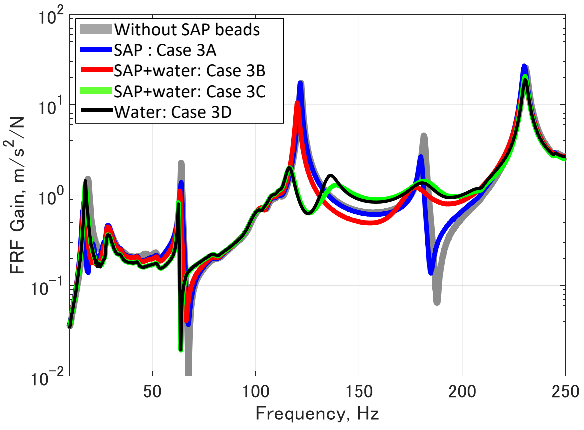

Figure 10. Measured acceleration FRFs versus excitation force at point f4c. (Case 3: effect of adding water)

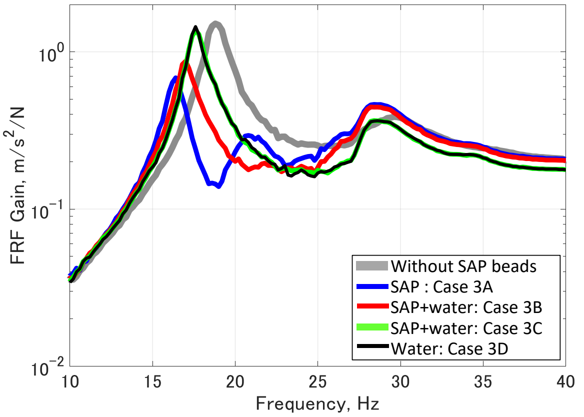

Figure 11. Enlarged view of Fig. 10

To investigate the basic mechanism of the damping capability by SAP beads, some simple analytical models are introduced here, and numerical calculations are conducted. From the experimental results, characteristic changes were observed in the measured FRF curves at the peak near 19 Hz. The proposed analytical models target the frequency region where this mode is dominant.

Figure 12 shows the proposed vibration analysis models. The mass m_0 denotes the main system (the model underframe, here), m_{pq} (p=1,2,3, q=1,2 for p=1,3, q=1,2,3 for p=2) express the mass of SAP beads of p-th layer, x_0 and x_{pq} denote displacement of m_0 and m_{pq}, respectively, $F(t)$ is the harmonic excitation force applied to m_0 concerning time t with circular frequency ω, and j is the imaginary unit. $\tilde{k}_{pq}$ denotes equivalent complex spring to support m_{pq} consisting of ordinary spring k_{pq} and viscous damping c_{pq}. Note this expression is supposing the analysis in the frequency domain for the steady-state response against harmonic excitation at ω. Also, since each SAP bead is supported each other in oblique direction rather than directly above (see the photos in Table 1), the supporting angles θ_{pq} are taken into account in the supporting springs $\tilde{k}_{pq}$. In the numerical study described later, the basic mechanism of the damping ability is investigated by adjusting these parameters. In this paper, the parameter adjustment is carried out by trial and error method comparing the numerical and experimental results.

The kinetic and potential energies for the system with a 3-layer SAP model can be written as follows.

$$
\begin{aligned}
T &= \frac{1}{2}m_0\dot{x}_0{}^2 + \frac{1}{2}m_{11}\dot{x}_{11}{}^2 + \frac{1}{2}m_{12}\dot{x}_{12}{}^2 \\
&\quad + \frac{1}{2}m_{21}\dot{x}_{21}{}^2 + \frac{1}{2}m_{22}\dot{x}_{22}{}^2 + \frac{1}{2}m_{23}\dot{x}_{23}{}^2 \\
&\quad + \frac{1}{2}m_{31}\dot{x}_{31}{}^2 + \frac{1}{2}m_{32}\dot{x}_{32}{}^2
\end{aligned} \tag{1}
$$

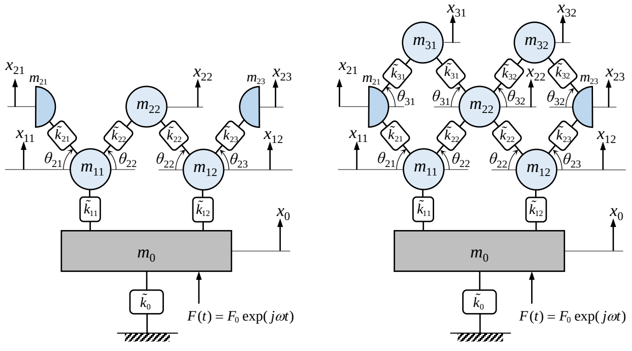

(a) With 2-layer SAP model

(b) With 3-layer SAP model

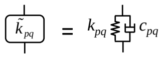

$$\tilde{k}_{pq} = k_{pq} + j\omega c_{pq}$$

(c) Equivalent spring model

Figure 12. Proposed vibration model of test structure with 2-layer and 3-layer SAP models

$$
\begin{aligned}
V &= \frac{1}{2}\tilde{k}_0 x_0{}^2 + \frac{1}{2}\tilde{k}_{11}(x_{11}-x_0)^2 + \frac{1}{2}\tilde{k}_{12}(x_{12}-x_0)^2 \\
&\quad + \frac{1}{2}\tilde{k}_{21}\sin^2\theta_{21}(x_{21}-x_{11})^2 + \frac{1}{2}\tilde{k}_{22}\sin^2\theta_{22}(x_{22}-x_{11})^2 \\
&\quad + \frac{1}{2}\tilde{k}_{22}\sin^2\theta_{22}(x_{22}-x_{12})^2 + \frac{1}{2}\tilde{k}_{23}\sin^2\theta_{23}(x_{23}-x_{12})^2 \\
&\quad + \frac{1}{2}\tilde{k}_{31}\sin^2\theta_{31}(x_{31}-x_{21})^2 + \frac{1}{2}\tilde{k}_{31}\sin^2\theta_{31}(x_{31}-x_{22})^2 \\
&\quad + \frac{1}{2}\tilde{k}_{32}\sin^2\theta_{32}(x_{32}-x_{22})^2 + \frac{1}{2}\tilde{k}_{32}\sin^2\theta_{32}(x_{32}-x_{23})^2
\end{aligned} \tag{2}
$$

where T and V indicate the kinetic and the potential energies, respectively, dot ($\dot{}$) expresses derivative with respect to t. By applying following Lagrange's equation,

$$\frac{d}{dt}\left(\frac{\partial T}{\partial \dot{\mathbf{x}}}\right) + \frac{\partial V}{\partial \mathbf{x}} = \mathbf{F} \tag{3}$$

the equations of motion can be obtained as follows.

$$\mathbf{M}\ddot{\mathbf{x}} + \tilde{\mathbf{K}}\mathbf{x} = \mathbf{F} \tag{4}$$

where

$$
\begin{aligned}
&\mathbf{x} = [x_0(t)\ x_{11}(t)\ x_{12}(t)\ x_{21}(t)\ x_{22}(t)\ x_{23}(t)\ x_{31}(t)\ x_{32}(t)]^T \\
&\mathbf{F} = [F(t)\ 0\ 0\ 0\ 0\ 0\ 0\ 0]^T
\end{aligned}
$$

and $\mathbf{M}$ and $\tilde{\mathbf{K}}$ are the mass and the complex equivalent stiffness matrices, respectively. Considering steady-state response to harmonic excitation, $\mathbf{x}$ and $\mathbf{F}$ can be written as,

$$
\begin{aligned}
&\mathbf{x} = [X_0\ X_{11}\ X_{12}\ X_{21}\ X_{22}\ X_{23}\ X_{31}\ X_{32}]^T e^{j\omega t} = \mathbf{X}e^{j\omega t} \\
&\mathbf{F} = [F_0\ 0\ 0\ 0\ 0\ 0\ 0\ 0]^T e^{j\omega t} = \mathbf{F}_0 e^{j\omega t}
\end{aligned}
$$

where $\mathbf{X}$ and $\mathbf{F}_0$ express the time-independent components of the response displacement and the input force. By solving the Eq. (4) at specified ω, the response at the frequency versus input force magnitude can be calculated and $\mathbf{X}$ expresses the frequency response function (FRF) of displacement when unit input force (F_0=1) is applied. The obtained displacement FRF vector has eight elements (eight degrees of freedom; 8DOF) corresponding to the model with the 3-layer SAP model shown in Fig. 12(b). For the case with a 2-layer SAP model, the above-mentioned formulation procedure is the same, just by omitting the values for the third layer (the values with p=3). To compare the numerical results with measured ones in acceleration FRF, $\left|\omega^2\mathbf{X}(\omega)\right|$ for unit input force will be calculated in the next subsection.

These analysis models seem to have interesting features by the effects of supporting angle, mass distribution, the balance of supporting springs, etc., however, for simplicity, the following assumptions are introduced in this paper.

$$
\begin{cases}
m_{11} = m_{12},\ \ m_{21} = m_{23} = m_{22}/2,\ m_{31} = m_{32}, \\
\tilde{k}_{11} = \tilde{k}_{12},\ \tilde{k}_{21} = \tilde{k}_{22} = \tilde{k}_{23},\ \tilde{k}_{31} = \tilde{k}_{32}, \\
\theta_{21} = \theta_{22} = \theta_{23},\ \theta_{31} = \theta_{32}
\end{cases} \tag{5}
$$

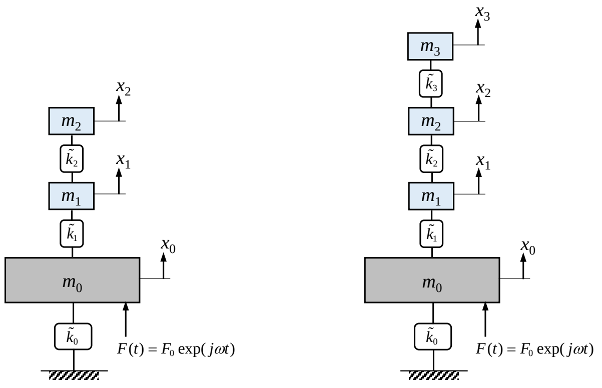

(a) With 2DOF SAP model (b) With 3DOF SAP model

Figure 13. Simplified vibration model of test structure with 2DOF and 3DOF SAP models equivalent to Fig. 12 under the assumptions of Eq. (5)

Under these assumptions, those models become equivalent to the 3DOF (with 2DOF SAP model, for the case with 2-layer SAP model) and 4DOF (with 3DOF SAP model, for the case with 3-layer SAP model) simple models as shown in Fig. 13. And the elements of the equations of motion (4) can be reduced as follows.

$$\mathbf{M} = \begin{bmatrix} m_0 & & & 0 \\ & m_1 & & \\ & & m_2 & \\ 0 & & & m_3 \end{bmatrix},$$

$$\tilde{\mathbf{K}} = \begin{bmatrix} \tilde{k}_0 + \tilde{k}_1 & -\tilde{k}_1 & 0 & 0 \\ -\tilde{k}_1 & \tilde{k}_1 + \tilde{k}_2 & -\tilde{k}_2 & 0 \\ 0 & -\tilde{k}_2 & \tilde{k}_2 + \tilde{k}_3 & -\tilde{k}_3 \\ 0 & 0 & -\tilde{k}_3 & \tilde{k}_3 \end{bmatrix}$$

There are following relations between these two models.

$$\begin{cases} m_{11} + m_{12} = 2m_{11} \equiv m_1, \\ m_{21} + m_{22} + m_{23} = 2m_{22} \equiv m_2, \\ m_{31} + m_{32} = 2m_{31} \equiv m_3, \\ \tilde{k}_{11} + \tilde{k}_{12} = 2\tilde{k}_{11} \equiv \tilde{k}_1, \\ \tilde{k}_{21} \sin^2 \theta_{21} + 2\tilde{k}_{22} \sin^2 \theta_{22} + \tilde{k}_{23} \sin^2 \theta_{23} = 4\tilde{k}_{22} \sin^2 \theta_{22} \equiv \tilde{k}_2, \\ 2\tilde{k}_{31} \sin^2 \theta_{31} + 2\tilde{k}_{32} \sin^2 \theta_{32} = 4\tilde{k}_{32} \sin^2 \theta_{32} \equiv \tilde{k}_3 \end{cases}$$

4.2. Numerical results and discussions

Numerical calculations were carried out to investigate the basic mechanism of the damping effects by SAP beads. The calculations were focusing on the peak around 19 Hz observed in the experiments. Its peak height seems not so prominent according to the measurement results shown in section 3; however, this peak is corresponding to the first bending mode of the model underframe which is one of the major targets to be reduced in actual railway vehicles. Besides, the peak height is strongly influenced by the excitation conditions, so the first bending mode may be more prominent under other excitation conditions.

The parameters for the main component were chosen as shown in Table 2 by referring to the actual condition of the model underframe. For SAP beads, the parameters listed in Table 3 were applied. The masses of the SAP were decided as 0.3 kg and 0.42 kg for SAP 2-layer and 3-layer cases, respectively. The spring and damping coefficients were determined heuristically by comparing the calculated acceleration FRFs with experimental results. The values in Table 3 are for the models in Fig. 13. The parameter values for the corresponding (equivalent) model shown in Fig. 12 are also listed in Tables A1-A6 in Appendix A.

Figure 14 shows the numerical results of acceleration FRFs of m_0 versus input force when the subsystem with two different 2DOF systems was applied. This calculation was intended to check the applicability of the 2DOF subsystem model in the case for the 3-layer SAP is applied. The spring constants k_1=8.4x10^3 N/m and k_2=25.2x10^3 N/m were selected for both the 2DOF SAP model. These are respectively equivalent to k_{11}=4.2x10^3 N/m and k_{22}=2k_{11} in the model of Fig. 12(a) under the assumption of Eq. (5), with all supporting angles are set to 60 degrees. (The detailed parameter values for the model in Fig. 12(a) are listed in Tables A1 and A2.) The masses were adjusted to express two and three-layer SAP cases, respectively. By using these parameters, the 2DOF SAP models have natural frequencies of 25.506 Hz (the 2-layer case) and 21.556 Hz (the 3-layer case), respectively. Comparing these FRF calculation results with the corresponding experimental results shown in Fig. 8, it can be found that the blue line agrees well with each other. So it is considered that the measured result with 2-layers of SAP beads can be represented by the 2DOF SAP model, and the trough frequency observed in the FRF corresponds to one of the natural frequencies of the additional system. On the other hand, some differences are observed in the red line such as; in Fig. 14, the peak around 17 Hz is higher than Fig. 8 and there is another peak around 23 Hz which doesn't exist in Fig. 8. These may indicate the 2DOF SAP

Table 2. Calculation parameters for the main component.
(Assuming the 1st bending mode of the model underframe)

variable	unit	value
m_0	kg	10
k_0	N/m	14.2517x10^4
c_0	Ns/m	71.6284
ζ_0	-	0.03
f_0	Hz	19.0

Table 3. Calculation parameters for the 2DOF and 3DOF SAP models

Intended experimental condition		Case 1A	Case1B	Case1B	Case 1B Case 3A	Case 3B	Case 3C
variable	unit model	SAP 2DOF (Fig. 13(a))	SAP 2DOF (Fig. 13(a))	SAP 3DOF (Fig. 13(b))	SAP 3DOF (Fig. 13(b))	SAP 3DOF (Fig. 13(b))	SAP 3DOF (Fig. 13(b))
m_1	kg	0.15	0.21	0.15	0.195	0.195	0.195
k_1	N/m	8.4x10^3	←	←	←	←	12.0x10^3
c_1	Ns/m	3.55	4.20	←	4.05	10.12	12.09
ζ_1	-	0.05	←	←	←	0.125	←
m_2	kg	0.15	0.21	0.15	0.195	0.195	0.195
k_2	N/m	25.2x10^3	←	12.6x10^3	←	←	25.2x10^4
c_2	Ns/m	7.53	8.91	5.32	8.59	←	27.15
ζ_2	-	0.05	←	←	←	←	←
m_3	kg	-	-	0.12	0.03	←	←
k_3	N/m	-	-	12.6x10^3	540	5400	←
c_3	Ns/m	-	-	4.76	0.493	1.56	←
ζ_3	-	-	-	0.05	0.05	←	←
Total additional mass	kg	0.3	0.42	0.42	0.42	0.42	0.42
Numerical result		Fig. 14-16 (blue line)	Fig. 14 (red line)	Fig. 15 (red line)	Fig. 16 (red line) Fig. 17 (blue line)	Fig. 17 (red line)	Fig. 17 (green line)
Description		2DOF SAP model for SAP 2-layer Case	Applicability check of the 2DOF SAP model for 3-layer Case	Nearly uniform distribution of m_{pq} and k_{pq}	Un-uniform distribution of m_{pq} and k_{pq}	Effect of water addition by adjusting the 3DOF SAP model	

model is inappropriate to represent the SAP 3-layers case. Note that the small peak around 30 Hz seen in the experimental results is supposed to a rigid mode that the model underframe vibrates over supporting springs without elastic deformation, which is out of focus of the numerical models here.

The red line in Fig. 15 shows a result when the 3DOF SAP model is used to represent the 3-layer SAP case. The gray and blue lines are the same as Fig. 14. On the red line, the spring constants for k_1 is equal to the 2DOF SAP model, and k_2=k_3=12.6x10^3 N/m are applied here, which correspond to k_{22}=k_{31}=k_{11}=4.2x10^3 N/m in Fig. 12(b). The assumptions in Eq. (5) and all supporting angles are 60 degrees are used again. (See Appendix Table A3.) The mass values are set m_1=m_2 and m_3=0.8m_2. These 3DOF SAP model settings are intended to presume the elasticity and mass density of SAP are nearly uniform, however rather large disagreement with Fig. 8 is observed over the 2DOF model in Fig. 14.

Figure 16 shows the case that the 3DOF SAP model is used and un-uniform distributions are assumed for m_{pq} and k_{pq} with m_{11}=m_{22}=0.0975 kg, m_{32}=0.015 kg, k_{11}=4.2x10^3 N/m, k_{22}=2k_{11}, k_{31}=180 N/m. Other parameters and assumptions are the same as Figs. 14 and 15. (See Appendix Table A4.) The red curve in this figure seems well to express the experimental result shown in Fig. 8. This may suggest that the top layer of SAP beads stacked in more than 3-layers act as smaller mass and spring elements than the layers below. This may also relate to the stacking condition, that is, as shown in Table 1, the top layer beads were loosely surrounded by the container in the experiments. In the red line, there is a trough near 25 Hz. This is caused by the DVA effect of the motion of the 3DOF SAP model, where m_1 and m_2 are in phase, and m_3 is out of phase, according to the numerical result.

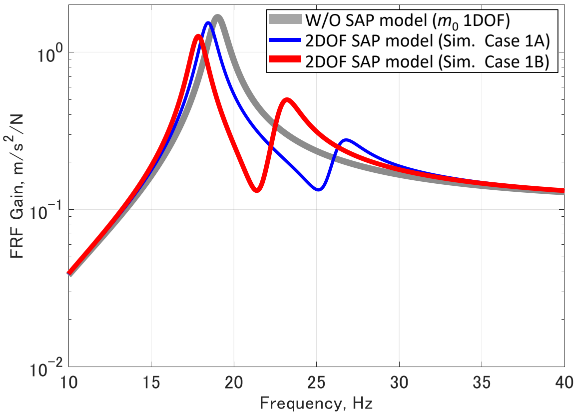

Figure 14. Numerical results of acceleration FRF intended to simulate the experiments for Case 1. (2DOF SAP model is applied for the Case 1B)

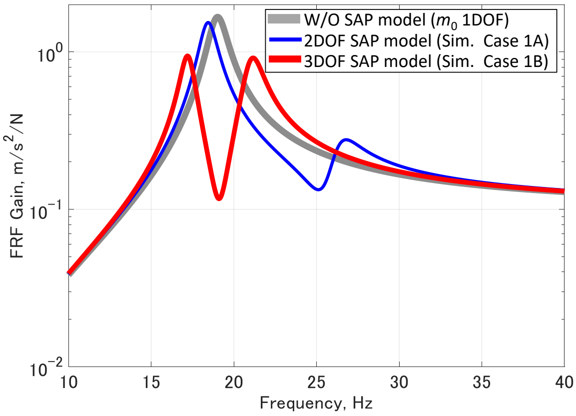

Figure 15. Numerical results of acceleration FRF intended to simulate the experiments for Case 1. (3DOF SAP model with nearly uniform distributions of m_{pq} and k_{pq} are applied for the Case 1B)

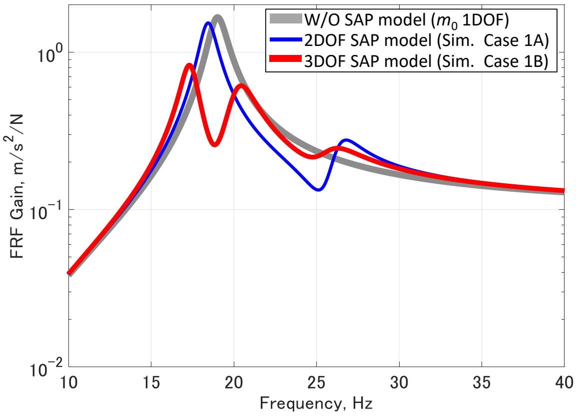

Figure 16. Numerical results of acceleration FRF intended to simulate the experiments for Case 1. (3DOF SAP model with un-uniform distributions of m_{pq} and k_{pq} are applied for the Case 1B)

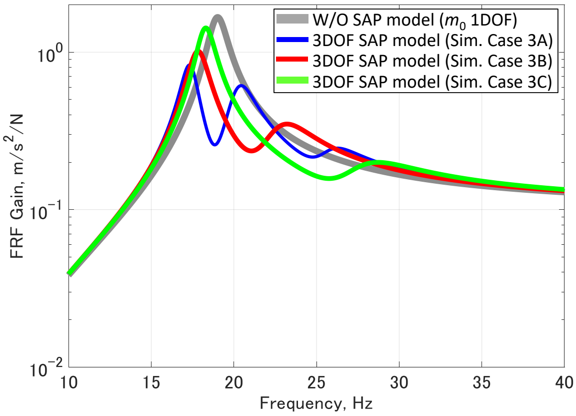

Figure 17. Numerical results of acceleration FRF intended to simulate the experiments for Case 3

The numerical results by adjusting the 2nd and 3rd layer of the 3DOF SAP model intended to simulate the effect of water addition are shown in Fig. 17. The red line in this figure was applied the 10 times value in k_3 and the 2.5 times in ζ_1, respectively than the 3-layer SAP model (blue line; which is the same with the red line in Fig. 16). In the green line, 20 times value was applied in k_2 and about 1.4 times in k_1. By comparing them with the experimental result shown in Fig. 10, the tendency of the peak change seems well agree. This may mean the added water effects equivalent to enlarge the spring constants of the 3rd and 2nd layers greatly. The values for water-added conditions for the corresponding model in Fig. 12(b) are shown in Tables A5 and A6.

Since the analytical model used here was very simple, further investigations will be needed to understand the detailed damping mechanisms by SAP beads and water. However, some interesting hints about them have been obtained through the numerical study.

5. Conclusions

In this study, to realize multimodal reduction of elastic vibrations in mechanical systems, super absorbent polymer beads (SAP beads) have been introduced as a simple damping device inspired by the multimodal vibration reduction effect by passengers on railway vehicles. A series of vibration measurement tests using a 1:10 scale model of railway vehicle floor structure (model underframe) was carried out. The SAP beads which are sold commonly were stacked in ordinal food container and applied to the model underframe. Also, an analytical model consisting of multiple masses supported at an angle to each other and its simplified model were proposed and numerical calculations were conducted to investigate the damping mechanisms. The results obtained in this work are summarized as follows.

- SAP beads have multimodal vibration reduction ability on the elastic vibration of the model underframe.
- The container's flexibility doesn't affect the damping effect at least up to 250 Hz for the experimental condition in this study. This means the damping ability comes from the viscoelastic characteristics of SAP beads themselves.
- A drastic reduction in higher frequency region can be observed when water was added together with SAP beads, indicating the vibration reduction mechanism may be different in low and high-frequency regions.
- According to the numerical investigation, it has found that some specific combinations of the mass, spring, and damping elements in the proposed analytical model could express the experimental results well and the basic mechanism of the damping effect for the lower frequency region is the DVA effect by SAP beads. Also, each SAP layer is estimated to act as an un-uniform subsystem for the cases with 3-layer SAP beads and with water.

Acknowledgements

This work was supported by JSPS KAKENHI Grant Number JP18K04024.

References

[1] J. P. Den Hartog, *Mechanical Vibrations*, 3rd ed. McGraw-Hill Book Company, 1947.

[2] R. Ishikawa and Y. Sato, “Decrease of Vehicle Body Bending Vibration by Dynamic Damper,” in *Proceedings of the 68th JSME Spring Annual Meeting*, 1991, vol. C, pp. 531–533. (in Japanese)

[3] D. Gong, J. Zhou, W. Sun, Y. Sun, and X. Zhanghui, “Method of Multi-mode Vibration Control for the Carbody of High-speed Electric Multiple Unit Trains,” *J. Sound Vib.*, vol. 404, pp. 94–111, 2017.

[4] T. Tomioka and T. Takigami, “Experimental and Numerical Study on the Effect due to Passengers on Flexural Vibrations in Railway Vehicle Carbodies,” *J. Sound Vib.*, vol. 343, pp. 1–19, 2015.

[5] T. Tomioka, T. Takigami, and K. Aida, “Experimental Investigations on the Damping Effect due to Passengers on Flexural Vibrations of Railway Vehicle Carbody and Basic Studies on the Mimicry of the Effect with Simple Substitutions,” *Veh. Syst. Dyn.*, vol. 55, pp. 995–1011, 2017.

[6] T. Tomioka, S. Tachikawa, and Y. Akiyama, “Development of Torus-shaped Elastic Body as a Vibration Absorber for Flexural Vibration in Railway Vehicle Carbody and Its Experimental Validation Using Commuter-type Vehicle,” *Mech. Eng. J.*, vol. 4, 2017.

[7] T. Tomioka, S. Tachikawa, Y. Akiyama, and K. Aida, “Reduction of Flexural Vibration of Railway Vehicle Carbody by Using Elastic Torus (Validation of Vibration Reduction Effect Using Actual Railway Vehicle and Numerical Investigations on the Vibration Reduction Mechanism),” *Trans. JSME*, vol. 83, pp. 16–00342, 2017.

[8] T. Tomioka, T. Takigami, and K. Aida, “Modal Analysis of Railway Vehicle Carbodies Using a Linear Prediction Model,” *J. Syst. Des. Dyn.*, vol. 3, pp. 918–931, 2009.

Appendix A. The detailed values for the model shown in Fig. 12 equivalent to the numerical calculations in 4.2

The parameter values for the model in Fig 12 equivalent to the numerical study (by the model shown in Fig. 13) under the assumption of eq. (5) are summarized in Table A1-A6.

Table A1. Parameter values for the SAP models for Case 1A in the 2DOF SAP model and the equivalent model

2DOF SAP model (subsystem) shown in Fig. 13			Equivalent parameter values in the model shown in Fig. 12 to the 2DOF SAP model		
variable	unit	value	variable	unit	value
m_1	kg	0.15	$m_{11}(=m_{12})$	kg	0.075
k_1	N/m	8.4x10^3	$k_{11}(=k_{12})$	N/m	4.2x10^3
c_1	Ns/m	3.55	$c_{11}(=c_{12})$	Ns/m	1.77
ζ_1	-	0.05			
m_2	kg	0.15	$m_{22}(=2m_{21}=2m_{23})$	kg	0.075
k_2	N/m	25.2x10^3	$k_{21}(=k_{22}=k_{23})$	N/m	8.4x10^3
c_2	Ns/m	7.53	$c_{21}(=c_{22}=c_{23})$	Ns/m	1.67
ζ_2	-	0.05	$\theta_{21}(=\theta_{22}=\theta_{23})$	deg.	60
Total additional mass	kg	0.3	Total additional mass	kg	0.3
Natural frequencies of the 2DOF subsystem		25.506, 96.327 Hz			
Numerical result		Fig. 14-16 (blue line)			

Table A2. Parameter values for the SAP models for Case 1B in the 2DOF SAP model and the equivalent model.

2DOF SAP model (subsystem) shown in Fig. 13			Equivalent parameter values in the model shown in Fig. 12 to the 2DOF SAP model		
variable	unit	value	variable	unit	value
m_1	kg	0.21	$m_{11}(=m_{12})$	kg	0.105
k_1	N/m	8.4x10^3	$k_{11}(=k_{12})$	N/m	4.2x10^3
c_1	Ns/m	4.20	$c_{11}(=c_{12})$	Ns/m	2.10
ζ_1	-	0.05			
m_2	kg	0.21	$m_{22}(=2m_{21}=2m_{23})$	kg	0.105
k_2	N/m	25.2x10^3	$k_{21}(=k_{22}=k_{23})$	N/m	8.4x10^3
c_2	Ns/m	8.91	$c_{21}(=c_{22}=c_{23})$	Ns/m	1.98
ζ_2	-	0.05	$\theta_{21}(=\theta_{22}=\theta_{23})$	deg.	60
Total additional mass	kg	0.42	Total additional mass	kg	0.42
Natural frequencies of the 2DOF subsystem		21.556, 81.411 Hz			
Numerical result		Fig. 14 (red line)			

Table A3. Parameters values for the SAP models for Case 1B in the 3DOF SAP model and the equivalent model: in case with nearly-uniform distributions of m_{pq} and k_{pq}.

3DOF SAP model (subsystem) shown in Fig. 13			Equivalent parameter values in the model shown in Fig. 12 to the 3DOF SAP model		
variable	unit	value	variable	unit	value
m_1	kg	0.15	$m_{11}(=m_{12})$	kg	0.075
k_1	N/m	8.4x10^3	$k_{11}(=k_{12})$	N/m	4.2x10^3
c_1	Ns/m	4.20	$c_{11}(=c_{12})$	Ns/m	2.10
ζ_1	-	0.05			
m_2	kg	0.15	$m_{22}(=2m_{21}=2m_{23})$	kg	0.075
k_2	N/m	12.6x10^3	$k_{21}(=k_{22}=k_{23})$	N/m	4.2x10^3
c_2	Ns/m	5.32	$c_{21}(=c_{22}=c_{23})$	Ns/m	1.77
ζ_2	-	0.05	$\theta_{21}(=\theta_{22}=\theta_{23})$	deg.	60
m_3	kg	0.12	$m_{31}(=m_{32})$	kg	0.06
k_3	N/m	12.6x10^3	$k_{31}(=k_{32})$	N/m	4.2x10^3
c_3	Ns/m	4.76	$c_{31}(=c_{32})$	Ns/m	1.59
ζ_3	-	0.05	$\theta_{31}(=\theta_{32})$	deg.	60
Total additional mass	kg	0.42	Total additional mass	kg	0.42
Natural frequencies of the 3DOF subsystem		19.117, 56.326, 83.207 Hz			
Numerical result		Fig. 15 (red line)			

Table A4. Calculation parameters used in the SAP models for Case 1B and 3A in the 3DOF SAP model and the equivalent model: in case with un-uniform distributions of m_{pq} and k_{pq}.

3DOF SAP model (subsystem) shown in Fig. 13			Equivalent parameter values in the model shown in Fig. 12 to the 3DOF SAP model		
variable	unit	value	variable	unit	value
m_1	kg	0.195	$m_{11}(=m_{12})$	kg	0.0975
k_1	N/m	8.4x10^3	$k_{11}(=k_{12})$	N/m	4.2x10^3
c_1	Ns/m	4.05	$c_{11}(=c_{12})$	Ns/m	2.10
ζ_1	-	0.05			
m_2	kg	0.195	$m_{22}(=2m_{21}=2m_{23})$	kg	0.0975
k_2	N/m	12.6x10^3	$k_{21}(=k_{22}=k_{23})$	N/m	4.2x10^3
c_2	Ns/m	8.59	$c_{21}(=c_{22}=c_{23})$	Ns/m	2.86
ζ_2	-	0.05	$\theta_{21}(=\theta_{22}=\theta_{23})$	deg.	60
m_3	kg	0.03	$m_{31}(=m_{32})$	kg	0.015
k_3	N/m	540	$k_{31}(=k_{32})$	N/m	180
c_3	Ns/m	0.493	$c_{31}(=c_{32})$	Ns/m	0.164
ζ_3	-	0.05	$\theta_{31}(=\theta_{32})$	deg.	60
Total additional mass	kg	0.42	Total additional mass	kg	0.42
Natural frequencies of the 3DOF subsystem		18.838, 25.301, 84.671 Hz			
Numerical result		Fig. 16(red line) Fig. 17(blue line)			

Table A5. Calculation parameters used in the SAP models for Case 3B in the 3DOF SAP model and the equivalent model: in case with un-uniform distributions of m_{pq} and k_{pq}.

3DOF SAP model (subsystem) shown in Fig. 13			Equivalent parameter values in the model shown in Fig. 12 to the 3DOF SAP model		
variable	unit	value	variable	unit	value
m_1	kg	0.195	$m_{11}(=m_{12})$	kg	0.0975
k_1	N/m	8.4x10^3	$k_{11}(=k_{12})$	N/m	4.2x10^3
c_1	Ns/m	10.12	$c_{11}(=c_{12})$	Ns/m	5.06
ζ_1	-	0.125			
m_2	kg	0.195	$m_{22}(=2m_{21}=2m_{23})$	kg	0.0975
k_2	N/m	12.6x10^3	$k_{21}(=k_{22}=k_{23})$	N/m	4.2x10^3
c_2	Ns/m	8.59	$c_{21}(=c_{22}=c_{23})$	Ns/m	2.86
ζ_2	-	0.05	$\theta_{21}(=\theta_{22}=\theta_{23})$	deg.	60
m_3	kg	0.03	$m_{31}(=m_{32})$	kg	0.015
k_3	N/m	5400	$k_{31}(=k_{32})$	N/m	1800
c_3	Ns/m	1.56	$c_{31}(=c_{32})$	Ns/m	0.52
ζ_3	-	0.05	$\theta_{31}(=\theta_{32})$	deg.	60
Total additional mass	kg	0.42	Total additional mass	kg	0.42
Natural frequencies of the 3DOF subsystem		21.329, 67.189, 89.048 Hz			
Numerical result		Fig. 17 (red line)			

Table A6. Calculation parameters used in the SAP models for Case 3C in the 3DOF SAP model and the equivalent model: in case with un-uniform distributions of m_{pq} and k_{pq}.

3DOF SAP model (subsystem) shown in Fig. 13			Equivalent parameter values in the model shown in Fig. 12 to the 3DOF SAP model		
variable	unit	value	variable	unit	value
m_1	kg	0.195	$m_{11}(=m_{12})$	kg	0.0975
k_1	N/m	12.0x10^3	$k_{11}(=k_{12})$	N/m	6.0x10^3
c_1	Ns/m	12.09	$c_{11}(=c_{12})$	Ns/m	6.05
ζ_1	-	0.125			
m_2	kg	0.195	$m_{22}(=2m_{21}=2m_{23})$	kg	0.0975
k_2	N/m	25.2x10^4	$k_{21}(=k_{22}=k_{23})$	N/m	8.4x10^4
c_2	Ns/m	27.15	$c_{21}(=c_{22}=c_{23})$	Ns/m	9.05
ζ_2	-	0.05	$\theta_{21}(=\theta_{22}=\theta_{23})$	deg.	60
m_3	kg	0.03	$m_{31}(=m_{32})$	kg	0.015
k_3	N/m	5400	$k_{31}(=k_{32})$	N/m	1800
c_3	Ns/m	1.56	$c_{31}(=c_{32})$	Ns/m	0.52
ζ_3	-	0.05	$\theta_{31}(=\theta_{32})$	deg.	60
Total additional mass	kg	0.42	Total additional mass	kg	0.42
Natural frequencies of the 3DOF subsystem		26.541, 70.405, 258.123 Hz			
Numerical result		Fig. 17 (green line)			

EPI International Journal of Engineering
Volume 3, Number 1, February 2020, pp. 30-33
DOI: 10.25042/epi-ije.022020.04

*p*ISSN 2615-5109
*e*ISSN 2621-0541

The Characterization of Thermoelectric Generator in Utilizing the Heat Waste of the Biomass Egg Drying Machine

Sudarmanto Jayanegara[a,*], Zuryati Djafar[b], Zulkifli Djafar[c], Nasaruddin Azis[d], Wahyu Haryadi Piarah[e]

[a]Department of Mechanical Engineering, Hasanuddin University. Email: jayanegarasudarmantogmail.com
[b]Department of Mechanical Engineering, Hasanuddin University. Email: zuryatidjafar@unhas.ac.id
[c]Department of Mechanical Engineering, Hasanuddin University. Email: zulkiflidjafar@unhas.ac.id
[d]Department of Mechanical Engineering, Hasanuddin University. Email: nasruddinazis@unhas.ac.id
[e]Department of Mechanical Engineering, Hasanuddin University. Email: wahyupiarah@unhas.ac.id

Abstract

This research was conducted to determine the character of the TEG module as a source of electrical energy in utilizing heat in the chimney wall of an egg rack drying machine that uses rice husk as engine furnace fuel. The test is carried out by utilizing heat on 2 pieces of chimney (upper chimney and lower chimney) separated by a Heat Exchanger (HE) with a furnace blower speed of 2600 rpm and environmental blower speed of 2800 rpm with the amount of thermoelectric used as many as 44 units. The results show that the TEG module in the upper chimney obtained temperature difference (ΔT), voltage difference (ΔV) and power (P) respectively ΔT 38.75 °C; ΔV 3.68 Volts; P 0.796 Watt and for the lower chimney respectively ΔT 73.25 ° C; ΔV 12.26 Volts; P 2.446 Watt.

Keywords: Characterization; egg rack dryer; TEG; temperature difference; voltage difference

1. Introduction

The electricity for humans in modern era is an irreplaceable need. Every activity undertaken is inseparable from the roles of electrical energy in order to facilitate all work. In Indonesia, electricity production tends to use fossil energy, especially coal, oil, and natural gas as its main raw material. But on the other hand, fossil energy is non-renewable energy whose nature will run out. Especially for petroleum fuels, it is estimated that it will run out no later than the end of the 21st century and coal is predicted to run out approximately 200 to 300 years to come [1].

The total electricity generated by renewable energy in 2011 was 21.8 TWh or around 12% of the total electricity supplied at 183.2 TWh. Coal-fired, natural gas, and oil-fired power plants are PLN's foundation in producing electricity. All three resources are accounted for nearly 80% of the total electricity generated [2].

Several renewable energy sources can be used to generate electricity, including: First, power plants with macro capacity that usually utilize water, steam, gas, nuclear, and others. Second, power plants with micro capacity, one of which utilizes thermal energy [3]. The heat energy, among others, comes from sunlight and objects that release heat, such as irons, motor vehicle exhausts, heating stoves, drying machines, and so on. Although the power plant is only micro-capacity, the maximum use in the long run can help conserve the use of electricity generated by macro-capacity power plants. Macro-capacity power plants should only be used to meet the needs of high-power electricity. Meanwhile, for the fulfillment of small-scale electricity, such as lighting lamps, can utilize micro-capacity power plants.

Micro-capacity power plants can generally utilize renewable energy sources where one source is heat energy. In this paper, the source of heat energy is obtained from the surface of the egg rack drying machine chimney. The egg rack drying machine, aside from being used as a dryer, can also be used as a source of electrical energy by converting wasted heat energy into electrical energy.

2. Literature Review

Thermoelectric technology is one alternative energy source in overcoming the energy crisis from year to year [4]. This technology is a solid-state technology that is not moving and environmentally friendly [5], [6].

---

*Corresponding author. Tel.: +62 852-8404-1817
Jalan Poros Malino km. 6 Bontomarannu
Gowa, Sulsel, Indonesia

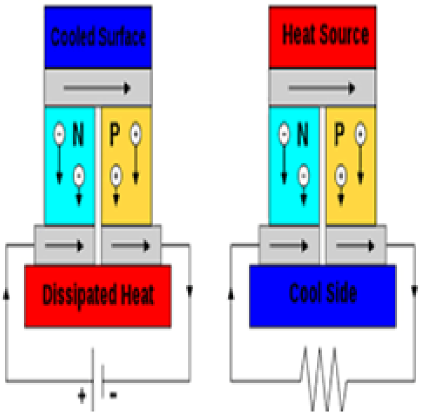

Figure 1. Mechanism of the Seebeck effect [14]

Thermoelectric Generator (TEG) is a type of power plant that is based on the principle of the Seebeck effect that was first discovered by scientist Thomas Johan in 1821 [7]–[9].

The Seebeck effect is that if two metal materials (usually semi-conductors) which are interconnected are in an environment with a temperature difference then the material will produce a difference in voltage or electromotive force [10]. In Fig. 1, type n semiconductor will produce negative potential on the cold side and positive potential on the remaining heat so that electrons will move from positive to negative potentials, while the p-type semiconductor is vice versa [11]–[13]. The resulting voltage is proportional to the temperature difference between the two materials. The greater the temperature difference, the greater the voltage produced.

The egg rack is a container that functions to store and arrange the eggs produced by the chickens so that they do not easily crack and facilitate the sales transaction process [14]. The process of drying the egg rack (after printing) can use two methods namely with the help of sunlight and using a drying machine [15]. The egg rack drying machine with a rice husk stove serves as a substitute for the drying process in the rainy season [16].

3. Research Methodology

In this paper, the research is focused on the utilization of waste heat on the surface of the chimney. Where the chimney is divided into 2 parts. The lower side is in direct contact with the furnace and the upper-side is separated by the Heat Exchanger (see Fig. 2). The equipment used was at one of PT. Rak Nusantara, one of the producers of egg racks in Batu Lappa, Wattang Pulu Subdistrict, Sidenreng Rappang District (3055 '22 "LS and 1190 54" 39.3 "BT).

Figure 2 is the design of testing equipment where the sampling points are in the upper chimney and the lower chimney. Aluminum plates with a thickness of 3 mm are placed in the upper chimney and the lower chimney as a TEG module holder which functions to utilize wasted heat to produce electricity. In this test, 8 TEG modules for the upper chimney and 36 TEG modules for the lower chimney that are installed spread out with an electric series circuit (Figs. 3 and 4). Heatsink cooler and fan are mounted on top of the TEG module which serves to dissipate heat on the cold side so that the temperature difference can be more maximal.

The output voltage of the TEG module is measured by using a multimeter after a while getting heat flow from the aluminum plate. Measuring the temperature of the hot side (Th), cold side (Tc) and voltage (ΔV) of the TEG module is done with an interval of 5 minutes for 120 minutes (the burning process) and then carried out measurements with an interval of 5 minutes for 60 minutes (Process without burning). The data obtained is then recorded in the observation table.

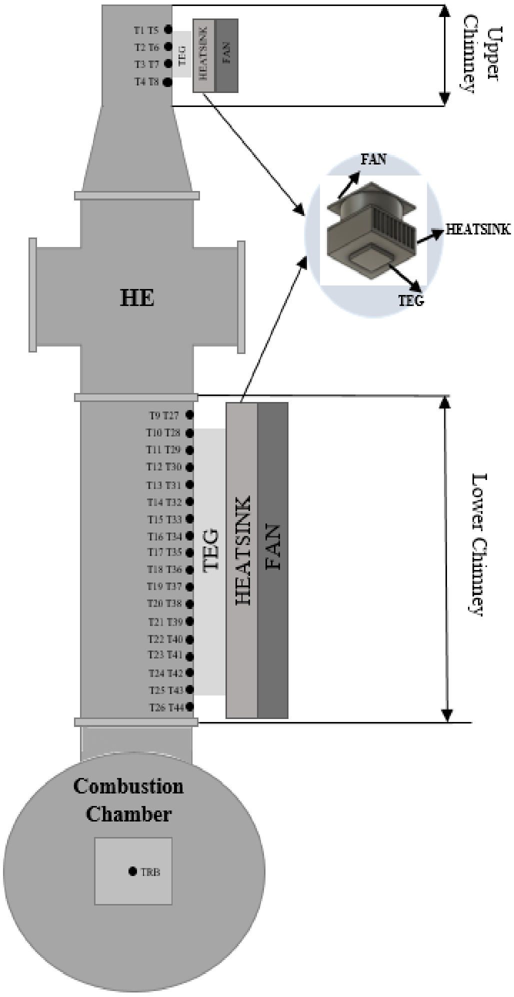

Information:

- Combustion Temperature (TRB) measurement point
- Lower Chimney Temperature measurement points (T_9 to T_{44})
- Upper Chimney Temperature measurement points (T_1 to T_8)

Figure 2. Test equipment design

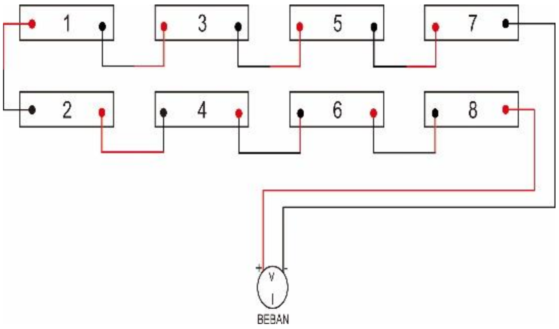

Figure 3. The upper chimney electric series (8 TEG)

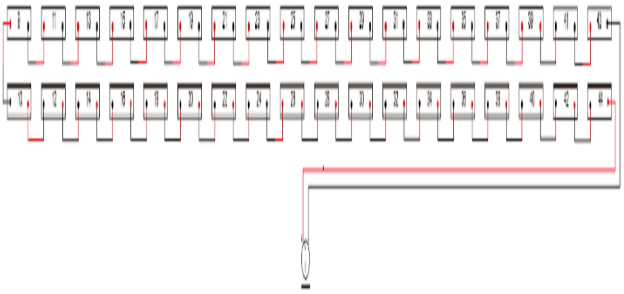

Figure 4. The lower chimney electric series (36 TEG)

Voltage generated from thermoelectric modules due to temperature differences will cause an electric current. The electric current equation can be stated in the following equation [17], [18]

$$I = \frac{\alpha \Delta T}{R_i + R_L} = \frac{\alpha \left(T_h - T_c\right)}{R_i + R_L} \qquad (1)$$

where

I = Electric currect flowing in circuit (A)

R_i = Thermoelectric module internal resistance (Ω)

R_L = External resistance (Ω)

$\Delta T = T_h - T_c$

$$\alpha = \frac{\Delta V}{(\Delta T)}$$

while the rate of heat transfer (Qh) from the heat source on the hot side surface (T_h) to the cold side surface (T_c) is as follows [15]

$$Qh = \left(\alpha \; I \; T_h\right) + k\left(T_h - T_c\right) \qquad (2)$$

where k is the module thermal conductivity (W/m °C). The output power (P) produced against the external load [17] and the efficiency (η) of the Thermoelectric Generator is as follows [19].

$$P = I^2 R_L \qquad (3)$$

$$\eta = \frac{P}{Q_h} \qquad (4)$$

4. Result and Discussion

4.1. Historical graphs of hot and cold temperatures

Figure 5 shows the history of the average temperature of the hot side and the average temperature of the cold side of the upper chimney and the lower chimney which has increased since the initial minutes of burning until the 120th minute (end of the burning process) with values of 113.5 °C respectively. (TUCh on average), 74.75 °C (TUCc on average), and 210.92 °C (TLCh on average), 137.67 °C (TLCc on average). Furthermore, it has decreased to near the ambient temperature in the 180th minute. This is due to the burning process occurs continuously over time until the fuel (rice husk) runs out. Furthermore, it can be seen that the temperature of the lower chimney has a higher value compared to the upper chimney because the position of the lower chimney is just above the burning chamber (furnace).

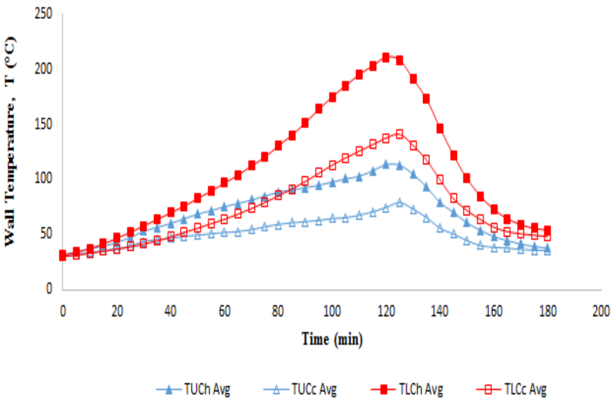

Figure 5. $T_H avg$ and $T_C avg$ in the upper and lower chimney of the TEG module

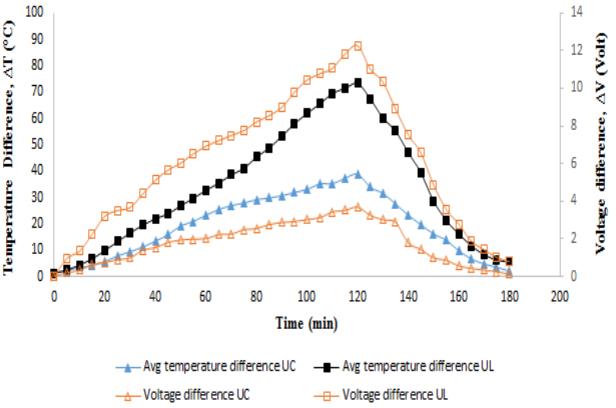

Figure 6. Average ΔT and ΔV in the upper chimney and lower chimney of the TEG module

4.2. Graph of the average temperature difference and voltage difference

In Fig. 6, it can be seen that the difference in average temperature in the upper and lower chimneys reaches a peak in the 120th minute with values of 38.75 °C for UC and 73.25 °C for LC. While the voltage with each is 3.68 Volts for UC and 12.26 Volts for LC. The difference in voltage obtained along with the temperature difference at each chimney an increase.

4.3. Graph of heat absorbed

Figure 7 shows the heat absorbed in the upper chimney and the lower chimney for the TEG module which has increased since the initial minutes of combustion until the 120th minute with values respectively 38.69 Watt for UC and 293.66 Watt for LC. Furthermore, it decreased in the 180th minute. This was also affected by the thermal conductivity of an aluminum plate and heat transfer.

4.4. Electric power graph

In Fig. 8 it can be seen if the power generated in the upper and lower chimneys reaches their peak in the 120th minute with values of 0.179 Watt for UC and 2.445 Watt for LC respectively. Furthermore, it decreases in the 180th minute until the total power can no longer be produced.

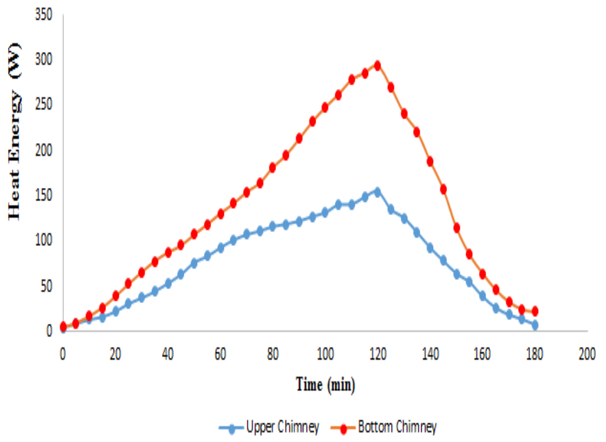

Figure 7. QH in the upper chimney and the lower chimney of the TEG module

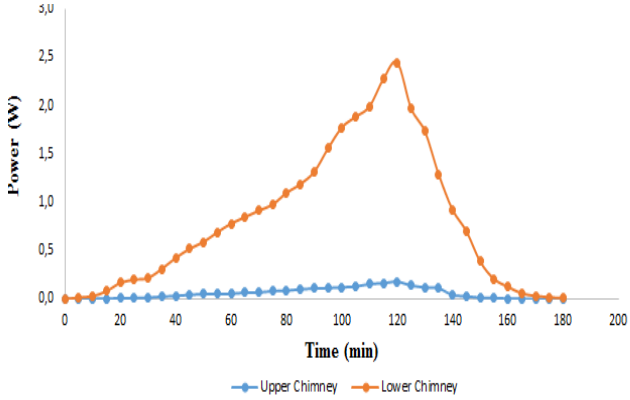

Figure 8. Electric power (P) in the upper and lower chimney of the TEG module

4.5. TEG module Efficiency Graph

Figure 9 shows that the efficiency of the upper chimney and the lower chimney has peak values of 0.12% and 0.83%, respectively. The efficiency value is still relatively small. This is because the TEG used is of low quality (Non-Branded).

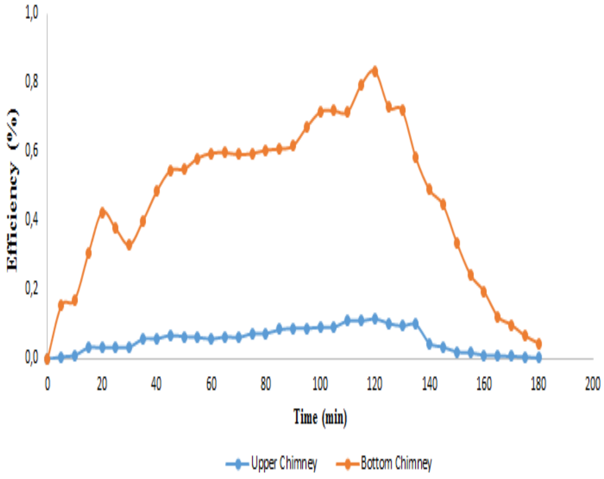

Figure 9. Efficiency (η) in the upper chimney and lower chimney of the TEG module

5. Conclusion

The test results show that with 8 modules thermoelectric element generator (TEG) in the upper chimney and 36 TEG modules in the lower chimney which are arranged in series can produce an output voltage with a maximum temperature difference of each ΔV 3.68 Volts; ΔT 38.75 ° C for the upper chimney, and ΔV 12.26 Volts; ΔT 73.25 ° C for the lower chimney. The potential power that can be produced is 0.179 W (UC) and 2.445 W (LC). This research is very good and effective as a future prospect to help in saving and using electricity in the future.

Reference

[1] A. Pudjanarsa and D. Nursuhud, *Energy Conversion Machine*, 2nd ed. Yogyakarta: ANDI, 2008.

[2] Center of Data and Information of Energy and Mineral Resources, *Study of Indonesian Energy Outlook*. Kementerian Energi dan Sumber Daya Alam, 2012.

[3] Center of Data and Information of Energy and Mineral Resources, *Study of Supplying and the Utilization of Migas, Batubara, EBT dan Listrik*. 2017.

[4] S. Nugrah, A. Aziz, and R. I. Mainil, “The Testing of Thermoelektric Generator (TEG) with Heat Source Electric Heater 60 Volt Using Cold Water at Environment Temperature,” *J. Online Mhs. Fak. Tek. Univ. Riau*, vol. 4, no. 2, 2017.

[5] Y. Prasetyo *et al.*, “Characteristic of Thermoelectric TEC Varies Type With Variation Load Resistor,” *J. Energi dan Teknol. Manufaktur*, vol. 2, pp. 36–41, 2019.

[6] M. A. Pradana and M. Widyartono, “Prototipe Pembangkit Listrik Termoelektrik Generator Menggunakan Penghantar Panas Aluminium, Kuningan dan Seng,” *J. Tek. Elektro*, vol. 9, pp. 251–258, 2020.

[7] K. Khoiriyah, Mustaqimah, A. S. F. Al Maliin, M. T. Maaulana, and N. I. Kamal, “Design and Characteristic of Thermoelectric Generator by using Solar Energy,” in *Prosiding Seminar Nasional Fisika (SINAFI)*, 2018.

[8] M. Ilham, Rizki, M. A. Nurdin, S. E. M. Putra, Hanani, and R. Hidayat, *Module 3 Thermoelectric*. ITB, 2013.

[9] R. Abrar, M. R. Fauzi, and B. Istana, “Optimization of Waste Heat Utilization in Biomass Gasification Furnaces as Electricity Generators,” in *Simposium Nasional Teknologi Terapan (SNTI) 2*, 2014.

[10] S. Klara and Sutrisno, “Utilization of Diesel Engine Exhaust Gas Heat as Electrical Energy,” *Res. J. Mar. Technol.*, vol. 14, no. 1, 2016.

[11] H. Simatupang, *Characteristics Thermoelectric for Solar Power Plants with Water Cooling*. Yogyakarta: Mechanical Engineering Study Program, Science and Technology Faculty, 2019.

[12] Sugiyanti and S. Siswantoro, “Utilization of Heat in LPG Gas Stoves for Electric Energy Charge Using a Thermoelectric Generator,” *J. Technol.*, vol. 7, no. 2, pp. 100–105, 2014.

[13] G. Min and D. M. Roe, *Handbook of Thermoelectric, Peltier Devices as Generator*. Florida: CRC Press LLC, 1994.

[14] H. A. Liemana, D. Lestariningsih, and L. Agustinne, “Automatic Carton Egg Tray Drying System above the Cart,” *Widya Tek.*, vol. 6, no. 2, pp. 152–162, 2007.

[15] P. Kurniasih, “Business Feasibility of Making Egg Packaging Products from Waste Paper in West Sumatra,” *For. Soc. Econ. Res.*, vol. 10, no. 3, pp. 152–172, 2013.

[16] B. Syarifuddin, *Analysis of the Effectiveness of a Heat Exchanger on an Egg Rack Dryer Machine with a Rice Husk Fired Furnace*. Makassar: Fakultas Teknik Universitas Hasanuddin, 2018.

[17] H. J. Goldsmid, “Introduction to Thermoelectricity,” *Springer Ser. Mater. Sci.*, vol. 121, 2010.

[18] N. Putra, W. N. Septiadi, H. Rahman, and R. Irwansyah, “Thermal Performance of Screen Mesh Wick Heat Pipes with Nanofluids,” *Therm. Fluid Sci. 40*, pp. 10–17, 2012.

[19] R. Saleha, N. Putra, S. P. Prakoso, and W. N. Septiadi, “Experimental investigation of thermal conductivity and heat pipe thermal performance of ZnO nanofluids,” *Int. J. Therm. Sci.*, vol. 63, pp. 125–132, 2013.

EPI International Journal of Engineering
Volume 3, Number 1, February 2020, pp. 34-38
DOI: 10.25042/epi-ije.022020.05

*p*ISSN 2615-5109
*e*ISSN 2621-0541

Analysis of Potentials of Wave Power Plant for Fisherman Boats in Selayar Islands

Asrianto[a], Luther Sule[b], Nasaruddin Asis[c]

[a]Department of Mechanical Engineering, Hasanuddin University. Email:anto199491@gmail.com
[b]Department of Mechanical Engineering, Hasanuddin University. Email:luther.sule@yahoo.co.id
[c]Department of Mechanical Engineering, Hasanuddin University. Email:nasruddinazis@unhas.ac.id

---

Abstract

This research aims to determine the design of ocean wave power generation equipment for fishing boats in Selayar Islands and to determine how much power is generated by ocean wave power generation equipment. The results showed that the power generated with an arm length of 2 meters with a wave height of 0.1 - 0.6 meters adjusted to the up and down of the arms produced 71.7 W, 83.72 W, 168.28 W, 240.4 W, 277.64 W and 483.2 W. Whereas an arm length of 4 meters with a wave height can reach 0.1 - 1 meter producing power of 35.76 W, 59.75 W, 72.24 W, 84.35 W, 144.51 W, 471.51 W, 596.64 W, 606 W, 642.83 W, and 800.58 W.

Keywords: Electric alternators; fishing boats, ocean waves

---

1. Introduction

Indonesia as an archipelago country with an area of 1,904,556 km^2 consisting of; 17,508 islands, 5.8 million km^2 of ocean and 81,290 million km of beach length, the potential of ocean energy, especially ocean waves, is very potential to be empowered as a new and renewable alternative primary energy especially for power generation. With a long coastline, wave energy potential is very significant and if used properly [1], it can be a very large source of energy. The practical potential of Indonesian wave energy is estimated at around 17,989 MW [2].

Astronomically, the Selayar islands are located between 5° 42 '- 7° 35' south latitude and 120° 15 '- 122° 30' east longitude. Based on its geographical position, the Selayar islands have boundaries: North - Bulukumba Regency, East - Flores Sea, West - Flores Sea and Makassar Strait, South - East Nusa Tenggara Province. Selayar Islands has an area of 10,503.69 km^2 with 1,357.03 km^2 of land area and sea area of 9,146.66 km^2 [3].

Fishermen in Selayar Islands Regency use lifter nets powered by an average of 3-4 engines: 3 main engines push the boat and 1 engine to turn on lights that attract fish. This second engine is usually powered by diesel. Consistent diesel consumption can cause an energy crisis. The energy crisis occurred as a result of increasing scarcity of crude oil and increasing energy demand. A breakthrough in alternative and renewable energy sources is increasingly needed [4]. An alternative energy source that might be a solution to this looming crisis is the ocean waves that have long been known as enormous energy sources [5], [6].

Several ocean wave power generation systems have been developed by various researchers in the world, including ocean wave power station oscillating system, water wave power plant with buoy system, ocean wave power plant with crank system, etc.

From several published studies discussing the topic of power plants using ocean wave energy in many regions throughout the world, inspired the authors to design an oscillation of wave energy power plants that can be installed on fishing boats in the fishing village of Selayar islands regency.

2. Literature Review

2.1. Ocean waves

Sea wave is the movement of the rise and fall of water in the direction perpendicular to the surface of the seawater that forms a curve or graph sinusoidal. The wind that moves its power to the surface of the water, causing ripples, the strains/hills and turns into sea waves or waves [7]. Ocean waves have potential and kinetic energy that can be calculated with the equation from Kim Neilsen. By using this equation we can get some energy contained in high tidal waves [8].

---

*Corresponding author. Tel.: +62 823-9658-0889
Jalan Poros Malino km. 6 Bontomarannu, Gowa
South Sulawesi, Indonesia 92171

The equation for ocean wave potential energy is:

$$E_w = \frac{1}{4} \cdot \rho \cdot g \cdot a^2 \cdot \lambda \tag{1}$$

The power that can be generated from the energy of sea waves in coastal waters in Indonesia can be obtained by using the following equation:

$$P_w = \frac{\frac{1}{4} \cdot \rho \cdot g \cdot a^2 \cdot \lambda}{T} \tag{2}$$

where

P_w = Sea Wave Power
ρ = Seawater Density
α = Amplitude of Ocean Waves *H/2*
g = Acceleration of Gravity
λ = Wavelength
T = Wave Period

Sea waves are sea water propagations that fluctuate up and down due to being generated mainly by winds in deep sea generation areas. In general, the shape of ocean waves in nature is very complex and difficult to describe systematically because it is not linear, three-dimensional, and has a different height and wave period. Ocean waves are generated by wind (wind waves), the force of the sun and moon (tides), volcanic eruptions or earthquakes in the sea (tsunami) [9].

The shape and propagation of waves that vary and are irregular greatly affect the characteristics of the waves that occur in these waters. In addition to changes in height, length and speed of waves also occur other phenomena such as silting, refraction, diffraction and reflection before the wave breaks. Wave siltation is the process of decreasing the wave height due to changes in depth where the wave velocity decreases and consequently there is also a refraction because the direction of motion of the wave peaks follows the contour shape of the ocean depth. Refraction is emphasized on the change in wave height due to the bending of the wave peak direction. While diffraction is the process of moving towards a protected area, causing waves [10].

The wave arrival period can be calculated using the equation suggested by Nielsen [11] in Utami [12] as follows:

$$T = 3.55 \times \sqrt{H} \tag{3}$$

where

T = period of wave (s)
H = wave height (m)

By knowing the estimated period of the wave arrival, then we can calculate the wave length and velocity with the equation according to Ross [13] in Utami [12] as follows:

$$\lambda = 5.12 \times T^2 \tag{4}$$

where :

λ = wavelength (m)
T = period of wave (s)

2.2. Alternator

The application of the concept of electromagnetic induction is used in dynamos or generators. This tool converts mechanical or kinetic energy into electrical energy. The working principle of a dynamo or generator is of two kinds, including:

- The coil rotates in a magnetic field.
- The magnet rotates between several coils.

When the coil is rotated between the magnetic poles so that it cuts the magnetic field lines, the coil will receive a magnetic flux of varying magnitude. Changes in magnetic flux can cause induction emf. Kinetic energy on the dynamo or generator can be obtained from the rotation of the wheels, wind, and waterfalls. In general, based on the current generated, the dynamo or generator can be divided into two types, namely AC (alternating current) and DC (direct current). In a dynamo, there is a rotating part called a rotor, while the stationary part is called a stator [14].

3. Research Methodology

3.1. Time and place of research

This research was conducted from January to December 2019 in the waters of the western Selayar Islands, Selayar Islands Regency. About the Analysis of Wave Power Generation for fishing boats in the Selayar Islands. The design tools used in the study are as follows:

Figure 1 shows the oscillating wave energy power plant design on a fishing boat. The design consists of parts such as:

a. Alternator
b. Freewheel
c. Chain
d. V-belt
e. Pully
f. buoy mechanism
g. Bearing
h. Spring

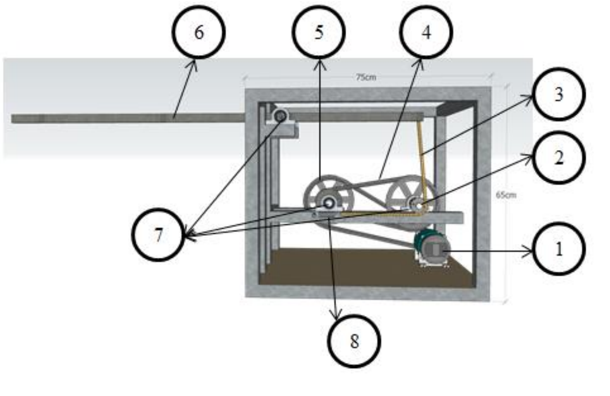

Figure 1. Sea wave power plant

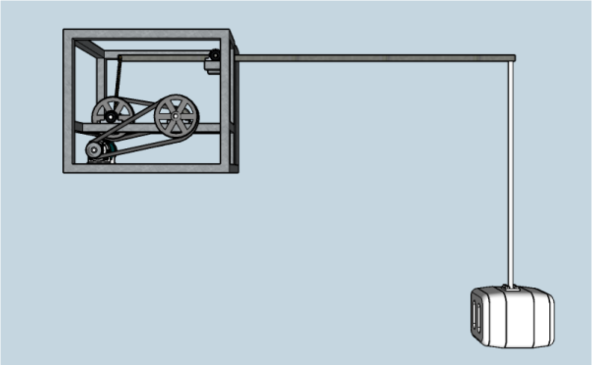

Figure 2. Side view of the equipment

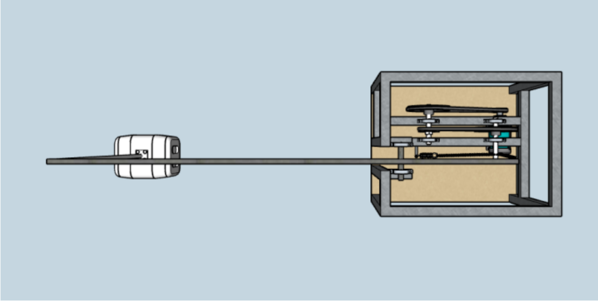

Figure 3. Top view of the equipment

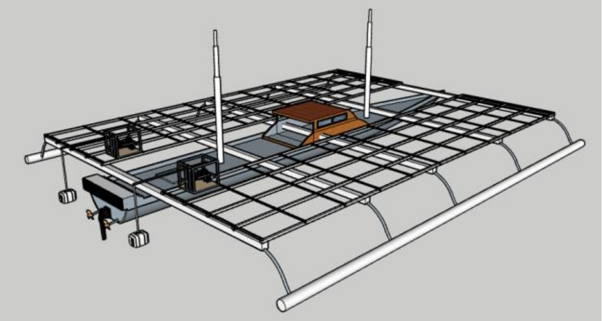

Figure 4. Equipment position on the boat

Technical calculations are needed to get the value of sea wave power which is a comparison to get the value of efficiency from ocean wave power plant. The amount of power produced by each is calculated as:

$$T = 3.55 \times \sqrt{H} \tag{5}$$

$$\lambda = 5.12 \times T^2 \tag{6}$$

$$P_w = \frac{\frac{1}{4} \cdot \rho \cdot g \cdot a^2 \cdot \lambda}{T} \tag{7}$$

$$\eta = \frac{P_\alpha}{P_w} \times 100\% \tag{8}$$

3.2. Testing method

- The alternator is connected to the battery according to the set sequence so that the alternator can charge.
- Put the charging indicator light on the battery
- Move the arm on the sea wave power plant in accordance with the frequency of the ocean waves.
- Measure the rpm of the alternator pully using a tachometer and the power coming out of the alternator with a digital multimeter.
- Take note of the rpm and voltage generated after moving the arm of a sea wave power plant.

3.3. Data analysis

The data analysis technique used in this study is a quantitative data analysis technique with descriptive statistics using equations. The data obtained are tabulated in tabular form and interpreted in graphical form which will then become a reference in making a description.

4. Results and Discussion

Sea wave data used are sea waves in the waters of the western islands of Selayar islands. The data can be seen in Table 1. Figure 5 is the tool used for testing in research data collection.

4.1. Example calculations

Taken from significant maximum mean sea wave height data.

a. Density of seawater = 1030 kg /m^3
b. Maximum average wave height = 1 meter
c. Acceleration of gravity = 9.8 kg.m / s
d. Wave period = $T = 3.55 \times \sqrt{H}$ where H is the wave height.
e. Period for maximum wave height;

- $T = 3.55 \times \sqrt{1}$
- $T = 3.55\ s$

Table 1. Sea wave height in the waters of the western islands of Selayar Island

2018 Month	Average Sea Wave Height (m)	Maximum Wave Height (m)
January	0.75-1.0	1.0 - 2.0
February	0.75-1.0	1.0 - 2.0
March	0.5-.075	1.0 - 1.25
April	0.1-0.5	0.5 - 0.75
June	0.5-0.75	0.75 - 1.0
July	0.5-0.75	0.75 - 1.0
August	0.5-0.75	1.0 - 1.25
September	0.5-0.75	1.0 - 1.25
October	0.5-0.75	1.0 - 1.25
November	0.1-0.5	0.75 - 1.0
December	0.1-0.5	0.75 - 1.0

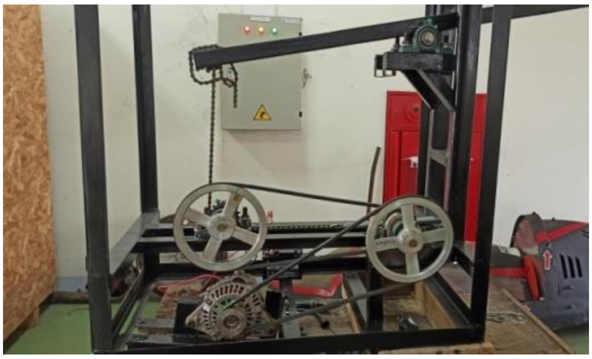

Figure 5. Sea wave power generation equipment

f. Wavelength = $\lambda = 5.12 \times T^2$ then

g. Wavelength for maximum wave height

- $\lambda = 5.12 \times 3.55^2$
- $\lambda = 64.5\ meter$

h. Sea wave amplitude = $\frac{H}{2}$ = = 0.5 meters $\frac{1}{2}$

Solution:

The equation for ocean wave potential energy is:

$$E_w = \frac{1}{4} \cdot \rho \cdot g \cdot a^2 \cdot \lambda \tag{9}$$

Power that can be generated from the energy of sea waves in coastal waters in Indonesia can be obtained by using the equation:

$$P_w = \frac{\frac{1}{4} \cdot \rho \cdot g \cdot a^2 \cdot \lambda}{T} \tag{10}$$

Then,

$$P_w = \frac{\frac{1}{4} \cdot 1030\ \frac{kg}{m^3} \cdot 9.8\ \frac{m}{s^2} \cdot 0.5^2\ m \cdot 64.5\ m}{3.55\ s}$$

$$= 45849.5\ watt$$

The power generated from the tool for a 1 meter wave height with an arm length of 4 meters is 800.58 watts, so the efficiency is

$$\eta = \frac{P_\alpha}{P_w} \times 100\% \tag{11}$$

Then, the efficiency is

$$\eta = \frac{800.58}{45849.5} \times 100\%$$

$$= 1.746\%$$

4.2. Variation in arm length of 2 meters

Figure 6 shows the number of rotations (n) the tool can produce, with wave height (S1) and variations in arm length of 2 meters. At a wave height of 0.1 - 0.6 m, it can produce 301.5 rpm, 395.5 rpm, 487.6 rpm, 540 rpm, 675 rpm, and 758.5 rpm. The mass of the buoy used at 2 meters arm length is 5 kg. Thus, it can be concluded that the higher the wave, the more rotation that can be produced by the instrument. In addition, it can also be influenced by the length of the arm.

Figure 7 shows the amount of power produced (P), with wave height and arm length variation of 2 meters. At a minimum wave height of 0.1 - 0.6 m, each produces 71.7 W, 83.72 W, 168.28 W, 240.4 W, 277.64 W and 483.2 W waves respectively. can affect the amount of power. In addition, the number of turns on the alternator pully also greatly affects the amount of power that can be generated. From the following graph we can see an increase in power generated based on rpm.

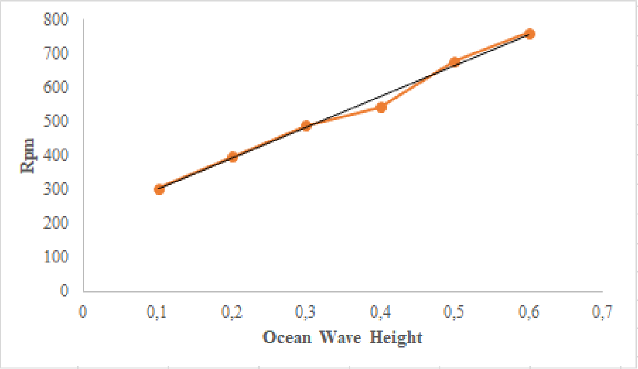

Figure 6. Wave height (m) and alternator pulley rotation (rpm) arm length of 2 meters

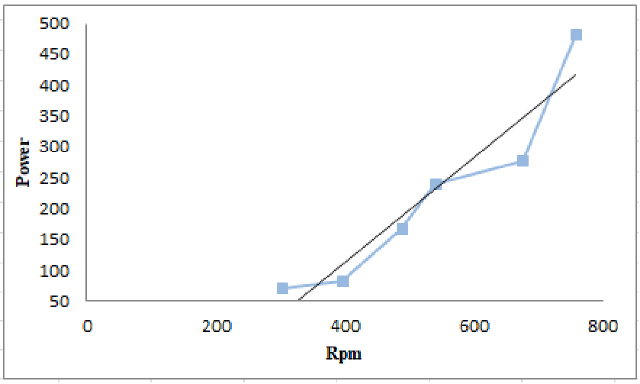

Figure 7. Rpm and power generated (P)

4.3. Variation in arm length of 2 meters

Figure 8 shows the number of rounds (n) that a sea wave power plant can produce, with wave height and variations in arm length of 4 meters. At a wave height of 0.1-1 m, it can produce 194.4 rpm, 329.4 rpm, 356.2 rpm, 375.3 rpm, 447 rpm, 688.2 rpm, 710 rpm, 1023.2 rpm, 1105 rpm, and 1194.2 rpm. It can be concluded that the higher the wave, the more rotation the instrument can produce. The resulting Rpm is different from the arm length of 2 meters when it is tested. The buoy mass used at the arm length of 4 meters is 3 kg. this shows that arm length also affects the buoy mass.

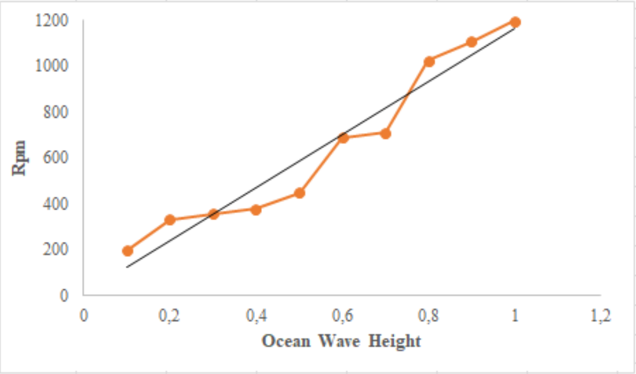

Figure 8. Wave height (m) and alternating pully alternator (rpm) arm length 4 meters

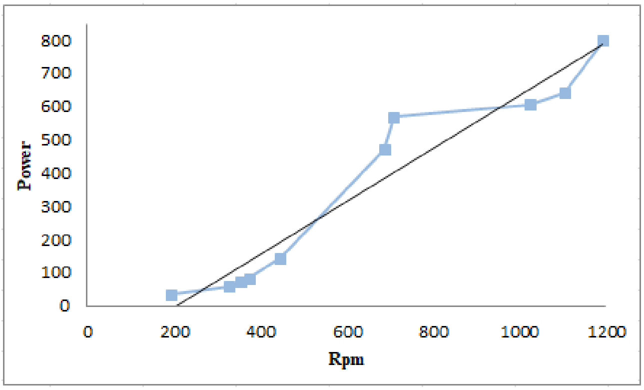

Figure 9. Rpm and power generated (P)

Figure 9 shows that the power generated (P) with wave height and arm length variation is 4 meters. At a minimum wave height of 0.1 - 1 m, it produces 35.76 W, 59.75 W, 72.24 W, 84.35 W, 144.51 W, 471.51 W, 596.64 W, 606 W, 642.83 W and 800.58 W. Wave height can affect the magnitude of the power. In addition, the length of the arm also affects the power generated by the tool. the number of turns on the alternator pully also greatly influences the amount of power that can be generated. From the following graph we can see an increase in power.

5. Conclusion

The results showed that, the power generated with an arm length of 2 meters with a wave height of 0.1 - 0.6 meters adjusted to the ups and downs of the arms produced 71.7 W, 83.72 W, 168.28 respectively W, 240.4 W, 277.64 W and 483.2 W. Whereas an arm length of 4 meters with a wave height can reach 0.1 - 1 meter producing power of 35.76 W, 59.75 W, 72.24 W, 84.35 W, 144.51 W, 471.51 W, 596.64 W, 606 W, 642.83 W and 800.58 W.

References

[1] A. Zamri, Yusri, Asmed, E. Adril, and J. W. Soedarsono, *Four Pendulum Systems Ocean Wave Power Plant*. Padang State Polytechnic, 2014.

[2] D. Anggraini, M. I. Al Hafiz, A. F. Derian, and Y. Alfi, “Quantitative Analysis of Indonesia Ocean Wave Energy Potential Using Oscillating Water Column Energy Converter,” *Int. J. Sci. Technol.*, vol. 1, no. 1, pp. 228–239, 2015.

[3] Selayar Regency Statistics Agency, *Selayar Islands Regency in Figures 2017*. Selayar, 2017.

[4] D. N. Sugianto, Kunarso, M. Helmi, and I. Alifdini, “Wave Energy Reviews in Indonesia,” *Int. J. Mech. Eng. Technol.*, vol. 8, no. 10, pp. 448–459, 2017.

[5] M. A. Marfai, D. W. Tyas, I. Nugraha, A. Fitriatul’Ulya, and W. Riasasi, “The Morphodynamics of Wulan Delta and Its Impacts on the Coastal Community in Subdistrict Buildings, Demak Regency, Indonesia,” *J. Environ. Prot. (Irvine,. Calif).*, vol. 7, pp. 60–71, 2016.

[6] F. D. Wijaya, Sarjiya, and M. R. P. Sugita, “Optimizing Tri-Core Permanent-Magnet-Linear-Generator DirectDrive Wave-Energy-Conversion System Design for Sea Wave Characteristics in South Coast Yogyakarta,” *Int. J. Electr. Comput. Eng.*, vol. 7, no. 2, pp. 610–618, 2017.

[7] A. Mandiharta, *Study of Potential Development of Tidal Energy as Alternative Energy*. Elelctrical Engineering Study Program, Engineering Faculty, Udayana University, 2007.

[8] B. Murdani, *Design Analysis of Sea Wave Power Plant with Oscillating Water Column System at Baron Beach*. Jakarta, 2008.

[9] M. M. Danial, *Coastal Engineering*. Bandung: Alfabeta, 2008.

[10] W. A. Pratikto *et al.*, *Coastal Protection Structures*. Surabaya: Marine Engineering, Sepuluh November Technology Institute, 2000.

[11] K. Nielsen, “On the Performance of Wave Power Converter,” in *Int. Sym. Util.of Ocean Waves*, 1986.

[12] S. R. Utami, *Study of the Potential Sea Wave Power Generation Using the Oscillating Water Column (OWC) System in Thirty Indonesian Water Areas*. Electrical Engineering Department, Engineering Faculty, Indonesia University, 2010.

[13] D. Ross, *Energy from the Waves*, 2nd ed. Perganon Press, 1980.

[14] B. Lu’Lu’, *An Experimental Study on the Effect of Konis Angle Variations on the Pendulum Motion Pattern and Resurrection Voltage in a Konis Pendulum System Wave Power Generation (PLTGL-SB) Power Simulator*. Surabaya: Sepuluh November Institute of Technology, 2011.

EPI International Journal of Engineering
Volume 3, Number 1, February 2020, pp. 39-45
DOI: 10.25042/epi-ije.022020.06

*p*ISSN 2615-5109
*e*ISSN 2621-0541

OFDM-IDMA Uplink Multi-user System with Scalable Latency for Next Generation WLAN

Leonardo Lanante Jr[a,]*, Nguyen Tran Thi Thao[b], Yuhei Nagao[c], Hiroshi Ochi[d]

[a]Graduate School of Computer Science and Systems Engineering, Kyushu Institute of Technology. Email: leonardo@cse.kyutech.ac.jp
[b]Graduate School of Computer Science and Systems Engineering, Kyushu Institute of Technology. Email: nguyen@dsp.cse.kyutech.ac.jp
[c]Graduate School of Computer Science and Systems Engineering, Kyushu Institute of Technology. Email: nagao@dsp.cse.kyutech.ac.jp
[d]Graduate School of Computer Science and Systems Engineering, Kyushu Institute of Technology. Email: ochi@dsp.cse.kyutech.ac.jp

---

Abstract

In this paper, we propose an Interleave-Division Multiple Access (IDMA) based uplink multi-user system for next generation WLAN. By minimizing the latency through accurate detection per iteration, we were able to design a receiver architecture that meets the latency demands of current IEEE 802.11 WLAN. To do this, the proposed system utilizes a novel algorithm for simplified LLR calculation of the soft input soft output demapper needed in the IDMA first stage detection. The proposed system has a maximum of 34.8 bits/s/Hz spectral efficiency for a single spatial stream and can support up to 8 users in a single 20MHz channel. We compare the proposed system to a reference OFDMA system and show its advantages in terms of diversity, flexibility and BER performance.

Keywords: 802.11ax; IDMA; uplink multi-user access

---

1. Introduction

Interleave Division Multiple Access (IDMA) is a special form of Code Division Multiple Access (CDMA) where instead of unique spreading codes, the receiver differentiates each STA by their unique interleaving patterns. This leads to a low complexity receiver which grows linearly with the number of parallel stations (STAs) supported [1].

IDMA has several other advantages over uplink multiple access schemes such as orthogonal frequency division multiple access (OFDMA) and CDMA. These includes higher spectral efficiency and insensitivity to clipping distortion [2]–[4]. In addition, because all users utilize all subcarriers at the same time, there is no need for scheduling avoiding extra overhead, computational complexity and latency [5]. At the simplest case, the hardware complexity of the IDMA transmitter is very similar to a regular OFDMA or multicarrier CDMA transmitter. The IDMA transmitter however utilizes multiple interleaver patterns if the system supports multilayer transmission. The receiver on the other hand is recursive and requires deep memory hardware requirements. In [6], the author demonstrated the feasibility of implementing IDMA in current LSI technology.

IDMA has been previously proposed for cellular networks as an upgrade to the 3rd generation WCDMA system. In [7], the authors proposed a single carrier multi-layer IDMA system for 3GPP long term evolution (LTE) systems. This system features direct enhancement of throughput and reliability from the previous CDMA based system. In [5], the performance of the multicarrier version of IDMA is analyzed in cellular environment.

This paper focuses on the design of an IDMA based uplink multi-user system in IEEE 802.11 Wireless LAN (WLAN). Currently, the 802.11 standardization of the next generation WLAN called IEEE 802.11ax has introduced a long desired uplink multi-user access feature to improve the system efficiency [8].

In [9], a preliminary proposal was presented in the IEEE TGax discussing the feasibility of the IDMA approach in IEEE 802.11 systems. The main problem that needs to be addressed in designing an IDMA based system in a random access network with bursty transmission is the latency. The 802.11 standard defines various interframe spaces (IFS) that need to be met by all STA to prevent collisions and maintain smooth operation. With IDMA however, each iteration consists of an interleaving and deinterleaving process causing huge latencies much higher than the defined IFS.

In this paper, we detail a latency adaptive receive algorithm first reported in [10] that only needs a few iterations to produce high reliable bit estimates. This algorithm utilizes a maxlog soft input soft output detector for the initial stage and a simple despreading operation in the second stage. Due to the high accuracy first stage, not only is the receiver iterations can be stopped at any number of iteration, the algorithm also works very well with very

---

*Corresponding author.
680-4 Kawazu, Iizuka-shi, Fukuoka City,
Japan

high order QAM modulation such as 64QAM and 256QAM without any requirement of minimum spreading factor and parallel number of users for convergence. High spectral efficiency operation however needs to be supported by diversity mechanisms such as maximal ratio combining of multiple receive antenna signals.

In order to minimize the hardware complexity, we also re-use a lot of existing IEEE 802.11 blocks such as channel coding, and constellation mapper/soft output demapper pair. While outside the scope of this paper, block re-use opens up the possibility of an OFDMA-IDMA hybrid multiple access system which adds more flexibility with regards to resource scheduling.

To reduce the bloat of the paper considering the enormous combinations of modes of operation, we only consider a single spatial stream system operating at one 20MHz channel. The extension to both multi-stream and higher bandwidth operation should be straightforward following the concepts discussed in this paper.

The rest of the paper proceeds as follows. In section 2, we discuss the current 802.11 architecture including a straightforward extension to OFDMA. Section 3 then describes the proposed IDMA architecture in detail. In section 4, we derive the proposed multi-user detection algorithm used in the orioised system. Numerical simulation results are then shown in section 5. Lastly, we conclude this paper in section 6.

2. IEEE 802.11 Architecture

In this section, we describe the 802.11 WLAN architecture. While there are technically a number of physical layer (PHY) options defined in the standard, only the OFDM PHY has become relevant in recent years. Up to the latest standard including the 802.11ac ammendments, the 802.11 PHY consists of an OFDM system with 312.5kHz subcarrier spacing (i.e. 64 subcarriers for 20MHz bandwidth) and guard interval of either 800ns or 400ns duration.

2.1. Transmitter

The block diagram of the 802.11 transmitter is shown in Fig. 1. The binary input signal is first scrambled to avoid long sequences of 1's or 0's which could degrade the performance of the system. The scrambled signal is then encoded using a convolutional encoder. Note that as an alternative, IEEE 802.11 devices can use low density parity check code (LDPC) and in this case the proceeding interleaver is no longer needed. After interleaving, the bits are then mapped according to the chosen modulation order. After modulation, OFDM modulation is performed using the inverse discrete fourier transform (IDFT), and guard interval inserter. Finally, windowing and TX filtering are done in order to reduce the signal spectral sidebands which may cause interference to other systems.

Figure 1. IEEE 802.11 WLAN transmitter architecture

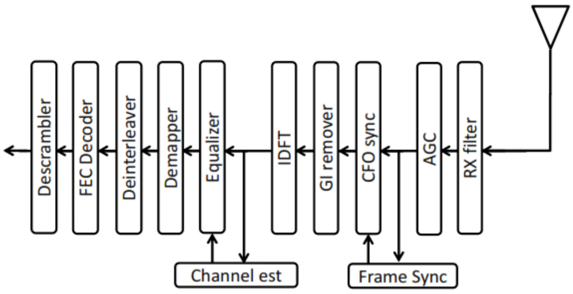

Figure 2. IEEE 802.11 WLAN receiver architecture

2.2. Receiver

Aside from the time and frequency synchronization, the receiver is completely the reverse of the transmitter as shown in Fig. 2. The receive filter is done to reduce the effect of noise and interference outside the receive bandwidth. The output is then used to adjust the automatic gain control as well as carrier frequency offset compensation. These processes are done in the time domain and can be implemented either sequentially or joint. After this, the receiver is now ready to perform frequency domain processing. It first removes the guard interval and then applies discrete fourier transform(DFT) to obtain the frequency domain symbols. When receiving long training symbols, the channel estimation block works by computing the channel coefficients such that when the receiver is at the point of receiving the actual data symbols, the equalizer can use the previously computed channel estimates. These channel estimates will be used by the equalizer throughout the duration of the packet. After equalization, the receiver will perform demapping and deinterleaving before doing FEC decoding. The FEC decoder is usually the Viterbi decoder when convolutional encoder is employed in the transmitter. Finally, descrambling is done to obtain the originally transmitted data bits.

2.3. Reference OFDMA system

As of March 2015, the 802.11 task group ax (TGax) has adopted the use of OFDMA for the next generation of WLAN standard. While still in the early stage, latest development requires the reduction of the subcarrier spacing from 312.5kHz to 78.125kHz resulting in a quadrupled symbol duration and number subcarriers [8]. Using this, we designed a reference uplink OFDMA system to compare our proposed IDMA system.

Table 1. Reference OFDMA system specification

Parameter	Value
FFT point	256
Data pilot/Null subcarriers	232/8/16
MCS	0-8
Number of UL MU slots	8
FEC	BCC/Viterbi Algorithm
Interleaver	Block Interleaver
OFDM symbol duration	16us
Guard Interval	3.2us
Max MU Throughput	87 Mbps

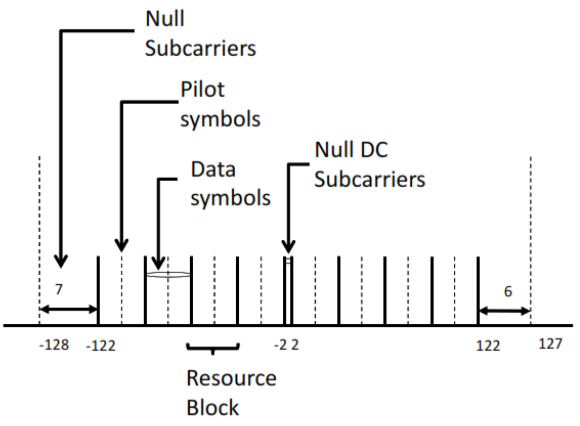

Figure 3. Proposed system multi-user frequency design

Aside from the frequency design, the transceiver architecture of 802.11ax devices will differ from current 802.11ac devices in the use of the subcarriers. In the 802.11ax devices, each STA will have the capability to utilize only a portion of the subcarrier set. For this reason, the number of parallel users transmitting at one time is a major design parameter.

We follow a straightforward resource block allocation as described in Fig. 3. In this figure, the case where the set of subcarriers is divided into 8 resource blocks with one resource block occupying 29 data subcarriers and 1 pilot subcarrier is shown. In this setting, the resource block is approximately 2.5MHz. Note that while finer resource blocks result in increased MU diversity, it will also result in a much higher complexity as well as complexity in user scheduling. In section 5, we also consider the case when the resource block bandwidth is 10MHz for comparison. There are a total of 16 null subcarriers consisting of 13 guard band subcarriers and 3 null DC subcarriers. For simplicity, the pilot subcarrier is placed at the center of the resource block. Table 1 shows the rest of the system parameters of the reference OFDMA PHY architecture. Unless otherwise specified, the remainder of the paper assumes the parameters in Table 1.

For the interleaver, we follow the same block interleaver design as in the 802.11 standard but with modified parameters applied independently to each resource block. Depending on the resource scheduling strategy of the access point (AP), it can allot multiple resource blocks to one STA at a time.

3. IDMA system

3.1. Design criteria

The proposed IDMA WLAN system specification is shown in Table 2. This specification is very similar to the reference OFDMA system except for the interleaver type and the maximum throughput. Because each STA can use all the available subcarriers at once, the theoretical maximum throughput is much higher than that of OFDMA. However, in order to support this high throughput at realistic receive signal strength, diversity techniques must be employed such as space time block coding (STBC) or receive maximum ratio combining (MRC).

As mentioned in the Introduction, the main problem in implementing IDMA in the current 802.11 system is the latency. While there are many interval constraints defined in the standard, we concentrate on the short IFS (SIFS) which is defined as the amount of time required for the receiver of a frame to process the received frame and to respond with a response frame such as the acknowledge (ACK) frame. For 802.11 OFDM PHY, this is set at 16us. Hence, the receiver must be able to finish receive processing within 16us with a realistic operating clock frequency. Considering additional delays from the transmit path as well as the MAC processing delay, it is a good rule of thumb to aim around 10μs as receive processing delay. As detailed in section 4, the latency of the proposed system fits well with this constraint.

3.2. IDMA transmitter

The proposed IDMA transmitter differs from the 802.11 transmitter with the addition of spreading and the patterns used in the interleaver. The spreading can be thought of as part of the FEC encoder in a general system but to be more specific, we define the FEC encoder as the current 802.11 FEC encoder while the spreader is a repetition coder which can be modified depending on the total number of bits sent. In the IDMA and turbo coding literature, the choice for the convolutional encoder is one of the recursive type because this has better performance in iterative decoding when the *a posteriori* probability (APP) decoder is inside the iteration loop. But since this will cause a very high latency to implement, we opt for a simpler iteration loop where only the repetition decoder is placed inside the iteration loop. Another advantage of having this sacrifice in terms of complexity is that we can re-use the Viterbi decoder already present in legacy 802.11 systems.

In this paper, we do not make any optimization with regard to the interleaver except that it is generated randomly. The set of 8 interleaver patterns used by the participating 8 STAs are pre-generated and stored in both AP and STAs. The specific interleaver used by one client depends on its index assigned by the AP during association.

Table 2. Proposed IDMA system specification

Parameter	Value
FFT point	256
Data pilot/Null subcarriers	232/8/16
MCS	0-8
Number of UL MU slots	8
FEC	BCC/Viterbi Algorithm
Interleaver	Random Interleaver per user
OFDM symbol duration	16us
Guard Interval	3.2us
Max MU Throughput	696 Mbps

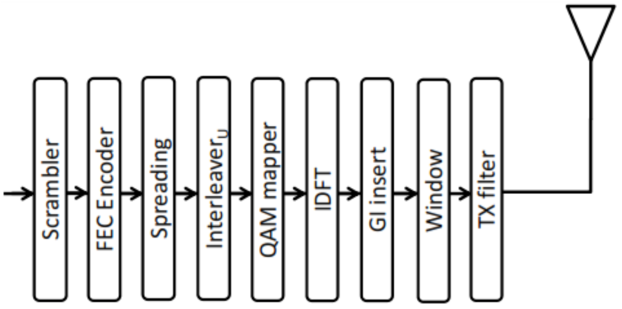

Figure 4. Proposed IDMA transmitter architecture

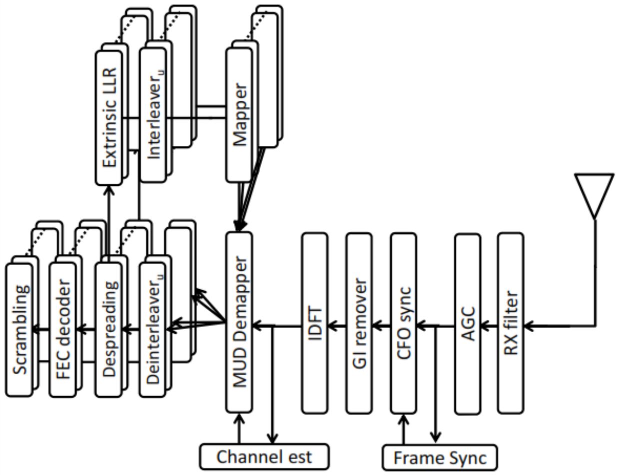

Figure 5. Proposed IDMA receiver architecture

3.3. IDMA receiver

Often, the receiver architecture for a standardized system need not to be described in detail to give the designer as much freedom as possible. However, in order to prove the feasibility of the proposed system in a WLAN environment, we show a specific receiver implementation with good performance, complexity and latency. The receiver architecture is shown in Fig. 5. Note that blocks are very similar to a regular 802.11 receiver until the multi-user detection (MUD) which marks the start of the IDMA processing.

4. Multi-user Detection

Let the receive signal after OFDM demodulation be

$$y(j)=\sum_{n=1}^{N}h_n(j)x_n(j)+a(j) \tag{1}$$

where $x_n(j)$ represents the transmit symbol sent by STA n in the j_{th} subcarrier, h_n is the channel coefficient from STA n to the AP, and lastly a is the zero mean complex Gaussian noise sample with variance σ^2 in the receiver. The quadrature modulated symbol x comes from the set A containing all the possible symbols from a specific quadrature amplitude modulation (QAM) constellation. The goal of the MUD is to detect x_n for n = 1,...,N given y and noisy estimates of h.

In [1], the authors defined a series of elementary operations to obtain a rough estimate of x by assuming that the sum of the signals of a number of users will result in a gaussian like signal with a pdf of

$$P\left(y\middle|x=\left\{\alpha\middle|\alpha\in A\right\}\right)=\frac{1}{\sqrt{2\pi Var\left(\zeta_n(j)\right)}}\times \exp\left(\frac{\left(y(j)-\left(h_n\alpha+E\left(\zeta_n(j)\right)\right)\right)^2}{2Var\left(\zeta_n(j)\right)}\right) \tag{2}$$

where

$$E\left[\zeta_n(j)\right]=E\left[y(j)\right]-h_nE\left[x_n(j)\right] \tag{3}$$

$$Var\left[\zeta_n(j)\right]=Var\left[y(j)\right]-\left|h_n\right|^2Var\left[x_n(j)\right] \tag{4}$$

denotes the new mean and variance of the noise which includes the interference from other users. With random interleaving and sufficiently high number of users, the central limit theorem makes this assumption very accurate.

Obtaining the likelihood ratio from (2) is straightforward using [11] where the same low complexity soft demapper employed in many 802.11 systems was first proposed.

In (3), the variable $E[x_n(j)]$ refers to the soft symbol estimate of $x_n(j)$. The soft symbol estimate can be obtained from the extrinsic information $\epsilon(x_{n,k}(j))$ using the expression $E[x_n(j)] = \tanh(\epsilon(x_{n,k}(j))/2)$ for BPSK signals. Note that the extrinsic information $\epsilon(x_n(j))$ is the feedback information of the previous iteration providing new information about the estimates of the symbols of each users.

In the first iteration, there is no extrinsic information causing the estimate of $E[x_n(j)]$ to be very inaccurate. Through the decoder which may consist of a combination of despreader and an APP decoder, increasingly accurate estimate of $E[x_n(j)]$ are produced. Even with little actual noise, the receiver needs more than 4 iterations to obtain an acceptable bit error rate (BER) [2]. Another drawback with this method is that due to the inaccurate first estimate, the method is limited to low order QAM modulated symbols such as BPSK and QPSK due to the non-linearity of the soft-demapper operation for higher order QAM.

In order to lessen the number of iterations and reduce latency, it is necessary to obtain an accurate result right from the first iteration. To do this, we employ joint maximum likelihood estimation of the transmitted bits for all users. Let

$$x_{\sim n}=\left[x_1 \quad \ldots \quad x_{n-1} \quad x_{n+1} \quad \ldots \quad x_N\right] \tag{5}$$

and

$$h_{\sim n}=\left[h_1 \quad \ldots \quad h_{n-1} \quad h_{n+1} \quad \ldots \quad h_N\right] \tag{6}$$

we then define the conditional probability distribution function

$$P\left(y\middle|x_n=\left\{\alpha\middle|\alpha\in A\right\},x_{\sim n}\right)=\frac{1}{\sqrt{2\pi\sigma^2}} \exp\left(\frac{\left(r(j)-\left(h_n\alpha+h_{\sim n}^{H}x_{\sim n}\right)\right)^2}{2\sigma^2}\right) \tag{7}$$

following [12], the LLR can be computed using

$$\lambda\left(x_{n,k}(j)\right)=\log\frac{\sum_{\alpha\in S_{n,k}^{(1)}}\left(y(j)\middle|x(j)=\alpha\right)}{\sum_{\alpha\in S_{n,k}^{(1)}}\left(y(j)\middle|x(j)=\alpha\right)} \tag{8}$$

$$=\log\frac{\sum x_{\sim n}\left(\sum_{\alpha\in S_{n,k}^{(1)}}\left(y(j)\middle|x(j)=\alpha\right)Px_{\sim n}\right)}{\sum x_{\sim n}\left(\sum_{\alpha\in S_{n,k}^{(0)}}\left(y(j)\middle|x(j)=\alpha\right)Px_{\sim n}\right)} \tag{9}$$

where

$$P\left(x_{\sim n}\right)=\Pi_{n_i=1,n_i\neq n}^{N}P\left(x_{n_i}\right) \quad (10)$$

and *k* is the bit index of the symbol transmitted by STA *n*.

We then define the metrics

$$m_o\left(x_{n,k}\left(j\right)\right)=\min_{\alpha\in S_{n,k}^{(0)}},x_{\sim n}\left|y\left(j\right)-h_n\alpha-h_{\sim n}^{H}x_{\sim n}\right|^2+ 2\sigma 2\log\left(P\left(x_{\sim n}\right)\right) \quad (11)$$

$$m_1\left(x_{n,k}\left(j\right)\right)=\min_{\alpha\in S_{n,k}^{(1)}},x_{\sim n}\left|y\left(j\right)-h_n\alpha-h_{\sim n}^{H}x_{\sim n}\right|^2+ 2\sigma 2\log\left(P\left(x_{\sim n}\right)\right) \quad (12)$$

It is easy to show that using the approximation $\log\sum_j \exp\left(z_j\right)\approx z_j$, (8) can be rewritten as

$$\lambda\left(x_{n,k}\left(j\right)\right)=m_o\left(x_{n,k}\left(j\right)\right)-m_1\left(x_{n,k}\left(j\right)\right) \quad (13)$$

Note that the above method can be likened to a soft decision version of a joint hard detection in an interference channel and hence will have good BER performance even at one iteration given a high enough signal to noise ratio. Further iterations will result in performance near AWGN capacity.

4.1. *Extrinsic LLR*

After an initial estimate of the transmitted symbols for all STAs, the decoding of each STA's transmit sequence is done. For every STA *n*, the receiver performs deinterleaving expressed as

$$\tilde{\lambda}\left(x_{n,k}\left(j\right)\right)=\pi_n^{-1}\left(\lambda\left(x_{n,k}\left(j\right)\right)\right) \quad (14)$$

which is followed by the channel decoder.

As seen in Fig. 5, the feedback loop of the IDMA receiver does not include the actual channel decoder (i.e. Viterbi decoder). The first reason for this is to reduce hardware complexity because this avoids the need of a soft output channel decoder such as an APP decoder or soft output Viterbi algorithm. The next reason is this allows us to reduce the latency of the system by implementing a parallel interleaver instead of a serial one.

Given the deinterleaved MUD output $\tilde{\lambda}\left(x_{n,k}\left(j\right)\right)$, the despread output is

$$T_{n,k}\left(i\right)=\sum_{n_r=0}^{N_r-1}\tilde{\lambda}\left(x_{n,k}\left(n_r+jN_r\right)\right) \quad (15)$$

Without the channel decoder, the extrinsic LLR can be calculated as

$$\in\left(x_{n,k}\left(j\right)\right)=\pi_n\left(T_{n,k}\left(i\right)-\lambda\left(x_{n,k}\left(j\right)\right)\right) \quad (16)$$

$$=\pi_n\left(\sum_{nr=0}^{Nr-1}\pi_n^{-1}\left(\lambda\left(x_{n,k}\left(n_r+iN_r\right)\right)\right)\right)-\lambda\left(x_{n,k}\left(j\right)\right) \quad (17)$$

Finally, the extrinsic LLR information is used to compute the feedback variable $P(x_{-n})$ according to

$$P\left(x_n\right)=\tanh\left(\in\left(x_{n,k}\left(j\right)\right)/2\right) \quad (18)$$

and (10).

4.2. *Summary and latency analysis*

Each iteration of the proposed MUD involves the following processes:

1) Soft Demapper
2) Deinterleaver
3) Despreader
4) Extrinsic LLR computation
5) Interleaver
6) Feedback variable update

From the receive signal *y*, the first process involves computing a first estimate of each STAs data bits using (11-13) to obtain $\lambda(x_{n,k}(j))$. This process is simply many parallel arithmetic computations and latencies are only due to pipelining. The next step is the deinterleaver shown in (14) which due to the memory operations involved would need a maximum of 2048 cycles for 256 FFT size and spreading factor of 8. The next step is the despreader as expressed in (15) and is an accumulator operation that has negligible latency. For the computation of the Extrinsic LLR shown in (17), another interleaver operation which again would need 2048 cycles in the highest supported spreading factor is required. Lastly, the feedback update variable in (10) and (18) when implemented using a lookup table will also have negligible latency.

As evident in the explanation above, the main contributor of the latency is the interleaver and deinterleaver pair performed in every iteration. Using a nominal operating frequency of 640MHz, we plot the latency vs. the number of iterations in Fig. 6. In this figure, it is readily seen how the latency linearly increase for every iteration and spreading factor (SF). For the specified maximum SF of 8, the proposed system can only process the signal with 2 iterations while still meeting the target deadline. While the latency results may look very pessimistic, we would like to note that the increase in latency per iteration can be reduced directly by applying parallel interleavers which would tradeoff hardware complexity of the interleaver to meet the required latency.

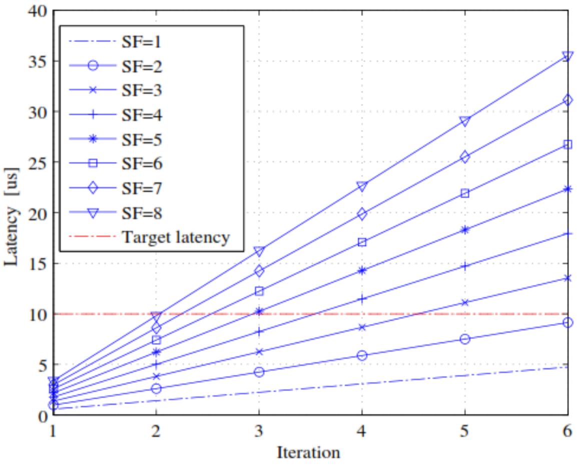

Figure 6. Latency vs Iteration of iterative IDMA receivers

5. Simulation Results

In order to show the performance of the proposed system, as well as to confirm the soundness of the chosen design architecture, we perform simulations comparing our reference OFDMA architecture with the proposed IDMA architecture. The default simulation parameters are listed in Table 3.

Figures 7 and 8 show the performance of the proposed system compared with OFDMA uplink transmission. In this simulation, the total bitrate is fixed to 7.3Mbps by setting all the STA's modulation and coding scheme (MCS) to 0. MCS's definitions follow the 802.11ac standard and are all listed in Table 4.

For OFDMA, the number of subcarriers is divided equally between the number of STAs such that for N STAs, each STA will have a data rate of 7:3/N Mbps. For IDMA, because all the subcarriers are used by all STAs at the same time, we use a spreading factor equal to N to match the data rate of the reference OFDMA system. In the following simulation results, there are two versions of the OFDMA system, one is without frequency resource scheduling and the other is with ideal frequency resource scheduling denoted in the figures as OFDMA-ideal. Ideal frequency resource scheduling requires perfect channel state information (CSI) at the transmitter prior to the transmission of the scheduling frame and the actual uplink MU transmission.

In Fig. 7, we simulate the performance of IDMA and OFDMA when there are only two resource blocks whose bandwidth is 10MHz each. This implementation is the easiest to implement but suffers from poor diversity gain. In this simulation, there are a total of 4 active STAs competing for the two available resource blocks. In the ideal OFDMA case, the AP allots to the STA whose channel has the highest energy on a particular resource block. On the other hand, the regular OFDMA case as well as the IDMA case allots the resource blocks to a random active STA. As seen in the figure, the performance of the proposed system has clear advantage to OFDMA with random frequency allocation but has worse performance against OFDMA with perfect scheduling by about 3dB.

Table 3. Simulation parameters

Packet Size	500 Octets
Channel Model	TGac Channel B
Spreading Factor	2, 8
Number of Users	2, 8
MSC	0-8
Power Allocation	None
IDMA iterations	4
Monte Carlo Iterations	1000
Analog RF Impairments	All off

Table 4. MCS parameters

MSC	Modulation	Coding Rate	Data Rate [Mbps]
0	BPSK	1/2	7.3
1	QPSK	1/2	14.5
2	QPSK	3/4	21.8
3	16-QAM	1/2	29.0
4	16-QAM	3/4	43.5
5	64-QAM	2/3	58.0
6	64-QAM	3/4	65.3
7	64-QAM	5/6	72.5
8	256-QAM	3/4	87.0

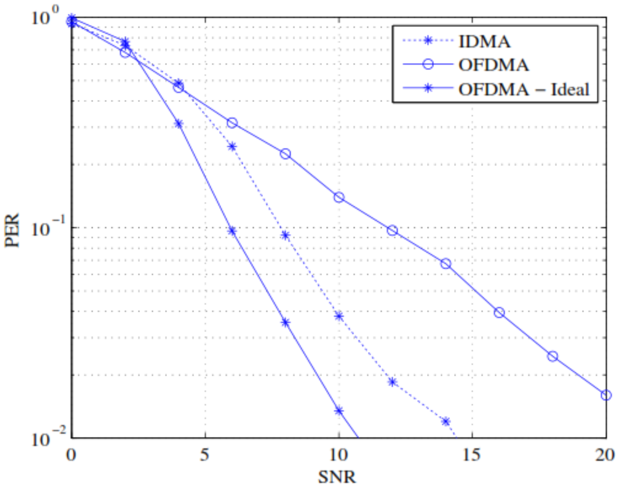

Figure 7. Average PER of proposed algorithm compared to reference OFDMA system. Total STAs = 4, Total Resource Blocks = 2

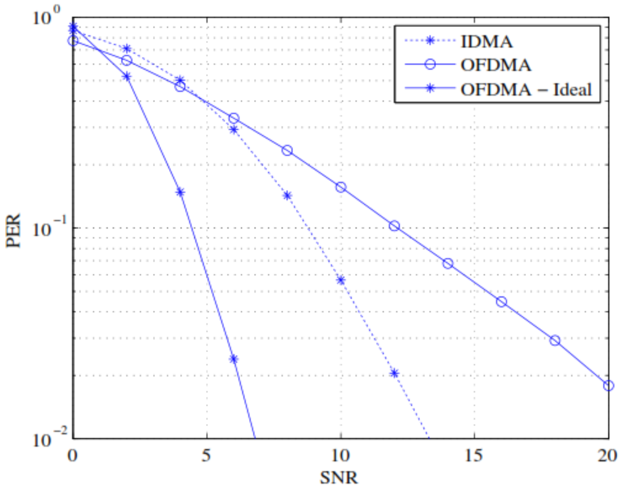

Figure 8. Average PER of proposed algorithm compared to reference OFDMA system. Total STAs = 16, Total Resource Blocks = 8

In Fig. 8, we perform the same simulation with resource block bandwidth of 2.5MHz for a total of 8 resource blocks that can be allotted to 8 STAs in parallel. In this case, the total number of active STAs is 16 which is again twice the number of resource blocks available. As the bandwidth of the resource blocks decreases, the diversity gain of OFDMA with perfect scheduling is increasing. On the other hand, with random scheduling, the fact that each STA experiences flat fading is not compensated by any multi-user diversity gain making the overall performance degradation worse. The performance of IDMA is almost unchanged regardless of the number of STAs present in the system.

From the above results, the benefit of the proposed system is clearly due to the lack of scheduling overhead. This effect is substantial considering that ideal scheduling would need the AP to poll all STAs one at a time.

In Fig. 9, we examine the effect of the number of IDMA iterations in the performance of the proposed system. In this simulation, we consider a system that can accommodate 8 parallel STA transmission. Again, we fix the data rate to 7.3 Mbps by adjusting the spreading factor accordingly. In the figure, it can be seen that the

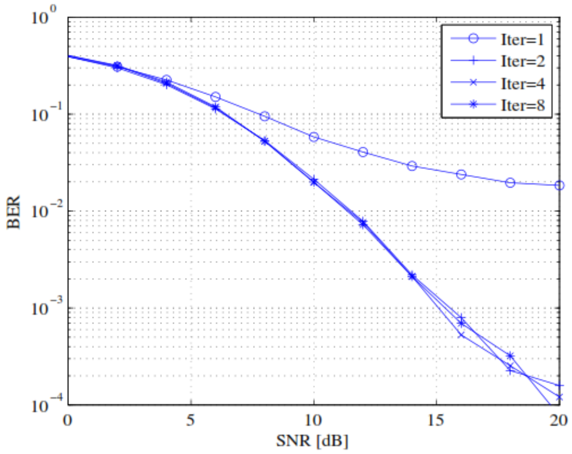

Figure 9. Effect of IDMA iterations, *N=8*

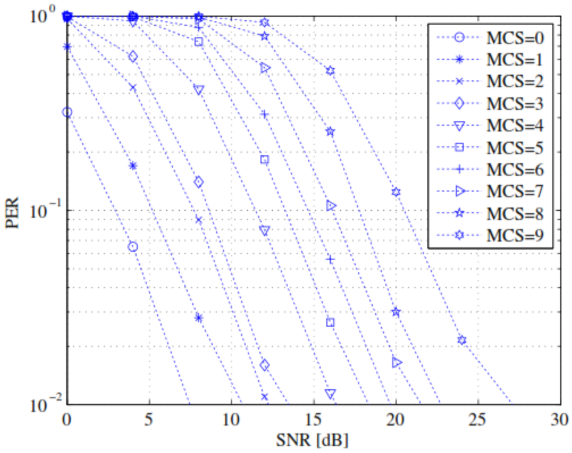

Figure 10. Performance of the proposed IDMA system with various MCS

performance of the proposed system only needs at least 2 iterations to obtain good BER performance.

Lastly, we simulate the performance of the proposed system in various MCS's. The advantage of the proposed system is that aside from the option to control the system performance by changing the MCS, it can also adjust spreading factor and the number of streams per user based on any available STA information such as CSI or long term PER statistics. In Fig. 10, the packet error rate (PER) of the proposed system across all MCSes for $N = 2$ STAs is shown. We employed 2 IDMA iterations and a spreading factor of 8. As the graphs show, the proposed system can easily provide the maximum MCS of 9 for 2 users without any scheduling at about 21dB of SNR for a 10% PER.

6. Conclusions

In this paper, the performance of an OFDM-IDMA system for next generation uplink multi-user system was presented. This system has very high compatibility with the current 802.11ac system and with a reference straightforward extension to an OFDMA system. This makes it possible to operate IDMA on top of OFDMA given some conditions are met. These conditions include the ability to allot resource blocks to multiple users and the ability for the AP to instruct a specific interleaver pattern to associated STAs. The proposed system utilizes almost all of the currently existing IEEE 802.11ac blocks which while not optimal, reduces additional complexity for implementing OFDM-IDMA. Simulation results reveal that it only needs around 2 iterations to provide good BER performance for both high and low scattering channel environments. Finally, we showed simulation results showing the ability of the system to support the maximum MCS of the 802.11ac system.

References

[1] L. Ping, "Interleave-division Multiple Access And Chip-by-chip Iterative Multi-user Detection," *IEEE Commun. Mag.*, vol. 43, no. 6, p. S19S23, 2005.

[2] L. Ping, L. Liu, K. Wu, and W. K. Leung, "Interleave Division Multipleaccess," *IEEE Trans. Wirel. Commun*, vol. 5, no. 4, pp. 938–947, 2006.

[3] D. Hao and P. A. Hoeher, "Iterative Estimation and Cancellation of Clipping Noise for Multi-Layer IDMA Systems," in *7th International ITG Conference*, 2008, pp. 1–6.

[4] K. Kusume, G. Bauch, and W. Utschick, "IDMA vs. CDMA: Analysis and Comparison of Two Multiple Access Schemes," *Wirel. Commun. IEEE Trans.*, vol. 11, no. 1, pp. 78–87, 2012.

[5] T. Matsumoto, Y. Hatakawa, and S. Konishi, "Performance Analysis of Interleave-division Multiple Access for Uplink in Multi-cell Environment," in *The 7th Wireless Communications and Mobile Computing Conference (IWCMC)*, 2011, pp. 376–381.

[6] S. Yoshizawa, Y. Hatakawa, T. Matsumoto, S. Konishi, and Y. Miyanaga, "Hardware Implementation of an Interference Canceller for IDMA Wireless Communications," in *International Symposium on Intelligent Signal Processing and Communications Systems (ISPACS)*, 2013, pp. 645–650.

[7] P. A. Hoeher and X. Wen, "Multi-Layer Interleave-Division Multiple Access for 3GPP Long Term Evolution," in *IEEE International Conference on Communications*, 2007, pp. 5508–5513.

[8] R. Stacey, "Specification Framework for TGax," *https://mentor.ieee.org/802.11/dcn/15/11-15-0132-0200ax-spec-framework.docx*, 2015.

[9] S. Yoshizawa, L. Lanante, and H. Ochi, "OFDM-IDMA Uplink Communication," *https://mentor.ieee.org/802.11/dcn/14/11-14-0095-00-0hew-ofdmidma-uplink-communication.pptx*. 2014.

[10] T. T. N. Tran, L. Lanante, Y. Nagao, and H. Ochi, "Higher Order QAM Modulation for IDMA System," *IEICE Technical Report*, vol. 114, no. 49. 2015.

[11] F. Tosato and P. Bisaglia, "Simplified Soft-output Demapper for Binary Interleaved COFDM with Application to HIPERLAN/2," in *IEEE International Conference on Communications*, 2002, vol. 2, pp. 664–668.

[12] W. Tianbin and P. A. Hoeher, "Superposition Mapping With Application In Bit-interleaved Coded Modulation," in *International ITG Conference on Source and Channel Coding (SCC)*, 2010, pp. 1–6.

EPI International Journal of Engineering
Volume 3, Number 1, February 2020, pp. 46-49
DOI: 10.25042/epi-ije.022020.07

*p*ISSN 2615-5109
*e*ISSN 2621-0541

Design of Water Quality Monitoring System for Crab Larvae using IOT

Wahyudi Sofyan[a,*], Muhammad Niswar[b], Andani Achmad[c]

[a]Department of Electrical Engineering, Hasanuddin University, Makassar, Indonesia. Email: wahyudisofyan09@gmail.com
[b]Department of Electrical Engineering, Hasanuddin University, Makassar, Indonesia. Email: mniswar@gmail.com
[c]Department of Electrical Engineering, Hasanuddin University, Makassar, Indonesia. Email: andani@unhas.ac.id

---

Abstract

Abstract Water quality is one of the determining factors in maintaining survival and growth of crab larvae, therefore we need a tool that can monitor water quality which includes temperature parameters, pH and salinity in real-time and online in crab larva culture. This system consists of several sensor nodes with the main component being Arduino Uno which is connected by several sensor nodes as a publisher and Raspberry Pi 3 (RPi3) board as a broker. Data from each sensor node will be sent to brokers with different topics - and stored in a database using a wireless network. The application system used with the MQTT (Message Queue Telemetry Transport) protocol uses a red node. The Red node will display data of each sensor node in the form of a gauge and graph. In this study, a water quality monitoring system was designed and developed. This tool uses the MQTT (Message Queue Telemetry Transport) protocol to display sensor node data in real-time.

Keywords: Crabs; high mortality; larvae; monitoring; MQTT protocol; node-red application

---

1. Introduction

Crab is food that has a high level of nutrition, this makes crab a source of export commodities. However, currently there is population degradation caused by overfishing and is not balanced with the level of demand. With these conditions, it is necessary to follow up in increasing the population of crabs, by conducting cultivation. But now crab cultivation is still using traditional methods, where farmers find a serious problem, especially in the level of water quality that is used does not have clear standards so that the impact on the minimum ratio of the number of larvae harvests.

Water quality monitoring is very necessary to determine the water conditions needed by larvae to maintain the viability of larvae from the zoea 1 larva stage to megalopa. Research by Sun et al. shows that the development of zoea 1 to 1 day young crabs require 15-18 days at 22-25ºC. Meanwhile according to Bryars & Havenhard (2006) shows that at the constant temperature needed is 22.5 ºC and 25 ºC [1] and the ideal level of salinity is 30-35 ppt [2]. This shows that water quality is a serious concern in producing crab culture, especially at the larval stage. But now farmers are still using conventional systems to monitor water quality and collect data on water samples used and then analyze them in the laboratory. This process requires a long time and expensive labor.

Based on this, the author raised the title of IOT (Internet of Things) based water quality monitoring system using the MQTT (Message Quequing Telemetry Transport) protocol to provide information on water quality data with parameters of temperature, pH and salinity that can be used as a reference for cultivation by means of the easy and economical price.

2. Experimental Program

2.1 Monitoring system

The design of the monitoring system uses temperature sensors, pH and salinity in Fig. 1. Each sensor node has its own topic and sensor data will be sent through a network system with the MQTT (Message Queue Telemetry Transport) protocol shown in Fig. 2. This research uses the following instrumentation:

1. Software
   a. Node-Red
   b. Mosquitto (Python)
   c. Java Script
   d. C/C++ (Arduino)
2. Hardware
   a. Asus AMD A10 Quad Core X4 (2.5 GHz)
   b. Monitor 14”
   c. Arduino Uno R3
   d. Raspberry Pi V3
   e. Temperature Sensor DS18B20 Water Proof
   f. Ph-4502C Sensor
   g. Salinity/Conductivity K1.0 Sensor

---

*Corresponding author. Tel.: +62-877-0359-5628
Jl. Poros Malino, Borongloe, Bontomarannu,
Kabupaten Gowa,
Sulawesi Selatan 92171

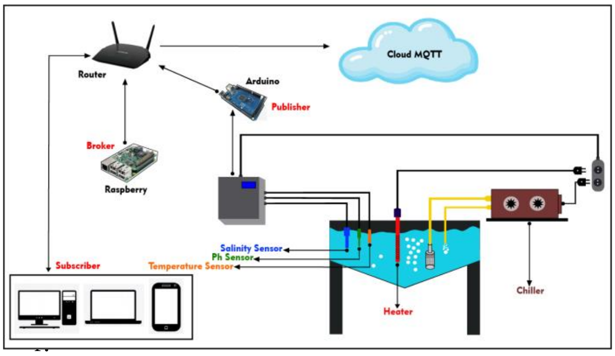

Figure 1. Monitoring system model

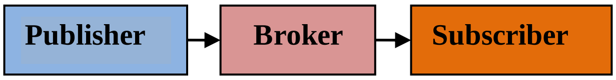

Figure 2. MQTT protocol model

2.2. Model description

The design model for this monitoring system consists of 3 sensors namely temperature sensor, Ph and salinity which are in the box and connected to Arduino Uno in this case is a publisher, and connected with Raspberry Pi as a broker. For reading data each sensor will be displayed in the form of a website and can be accessed using a device that is connected to a network system.

In general, the MQTT protocol for delivering messages from server to client or vice versa using low resources [3]. The system model of this research method can be described as follows.

2.3. Internet of Things

In general, the Internet of Things (IoT) is the concept of connecting several devices used to communicate or exchange data connected through the internet. The concept of IoT has been widely used in several objects and implemented almost in all sectors of life. Some assumptions predict that by 2020 in 50 billion objects will be connected to the Internet [4].

For the internet of things, in this study by connecting several nodes including Arduino Uno as the main node to process sensor data and send it to Raspberry Pi to be displayed to application services. The process of sending sensor data via a wireless router communication whose address communication is registered at Arduino Uno.

2.4. Temperature sensor

In this study water temperature sensors are used. Where this temperature sensor has analog and digital outputs. The use of temperature sensors has upper and lower limits, but for water temperature it is very necessary to maintain. Where the use of water temperature sensors is used analog output, temperature sensors are basically analog but can be converted in digital form [5] with DC input range 3.3 - 5 V. Temperature data will be sent to the Raspberry Pi with a temperature topic that will be displayed by node-red application with gauge and graph models. Every data change on this sensor is set every 5 minutes to get a good temperature data range.

In the crab larvae, the optimum temperature needed is 30^0C, which shows the highest average survival rate of 43.18 ± 7.32% [6]. By utilizing a temperature monitoring system, the temperature conditions relating to water quality in crab larvae can be maintained.

2.5. pH sensor

For the pH sensor in this study, the output used is analogous to DC input 5V. Data for the pH sensor will be sent to the Broker on the topic of pH with a time itemization every 5 minutes and the data will be displayed in the form of a percentage gauge and graph and saved to a local database of the raspberry pi.

The condition of water pH is one of the factors that influence the survival rate of crab larvae. The overall survival rate at each pH is 7.5 ± 0.1, 8.0 ± 0.1 and 8.5 ± 0.1 is 6.28 ± 0.12%, 6.76 ± 00.91% and 5.59 ± 0.53% [7].

2.6. Salinity sensor

In this research, salinity sensors have analog outputs that work to measure the salt content in larvae holding water with a capacity of 300 liters. The best growth of zoea to crab megalopa is treatment A, ie zoea which is maintained with water salinity ranging from 32-34 ppt.

The growth of the type of crustase is determined by a series of molting (skin change) processes from zoea1 to megalopa and even to adult crab. Normally the growth of crab larvae through 4 zoea stages and 1 megalopa stage that requires maintenance for 8-10 days, then from megalopa metamorphosis to crablet [8]. Salinity sensor data readings will be sent to Raspberry Pi with a gauge and graph percentage.

2.7. Raspberry Pi V3

Raspberry Pi is a small computer, it uses many different types of processors. Raspberry can install several versions of Linux, the operating system that appears and feels very much like Windows. Raspberry Pi is also used to surf the internet, to send emails to write letters using a word processor, but you can also do even more [9]. In this study, the tool that functions as a broker that communicates with Arduino Uno as a publisher is Raspberry Pi V3. Where raspberry Linux operating system has been installed with the mosquito library so that the data from Arduino in the form of sensor data can be received in the form of topics. Each topic that is sent will be displayed with certain time duration and sensor data is saved to the local database at any time in the previous settings. The database used in this case is MySQL which is connected to each sensor node sent by arduino.

Flow-based programming tool to help IoT developers integrate various I/O components with the Application Program Interface (API) and IoT services. Node-RED uses node.js so that it can run on a network or in the cloud. Now there are thousands of flows and nodes available in the NodeRED library so that connections can be made with many devices and services. Node-RED consists of Node.js-based runtime that directs to a web browser to access the flow editor. Through the web browser, the application can be created by dragging the available nodes in the palette to the workspace and then making a series.

3. Result And Discussion

3.1 Temperature water quality

Temperature is one of the factors that can influence the life of crab larvae about increasing or decreasing larval survival [10]The effect of temperature also has an impact on the length of change in metamorphosis, after feeding patterns and feed nutrients [11]. The results of the implementation of this design produce water temperature conditions in crab larvae ranging from an average of 29^0C-to 30^0C by recording data in the morning, afternoon and night by taking data every 5 minutes for reading and sending sensor data. Every data in 5 minutes will be saved into the database according to a predetermined time schedule. With a temperature sensor, monitoring can be done at any time as shown in Fig. 3.

3.2 pH water quality

For the pH sensor used, where the sensor reading data does not change too much on the water quality conditions in the larvae tub. This is because in larvae tanks for 200 liters capacity, the water is replaced every day by using the sipon model. And the data obtained for the pH sensor is ± 7.43. With a pH sensor, monitoring can be done at any time as shown in Figure 4.

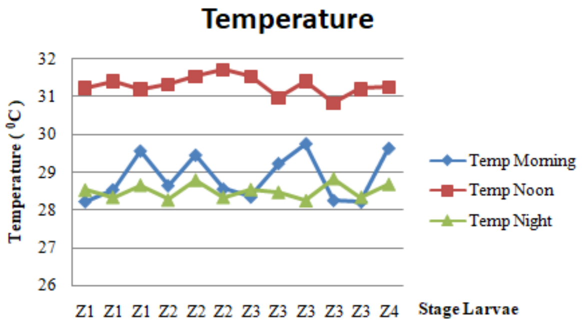

Figure 3. Water temperature conditions in crab larvae

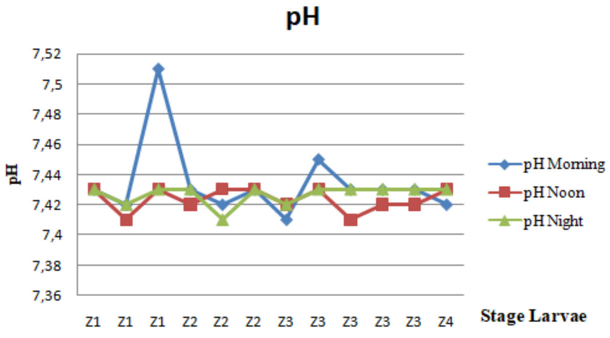

Figure 4. Water pH conditions in crab larvae

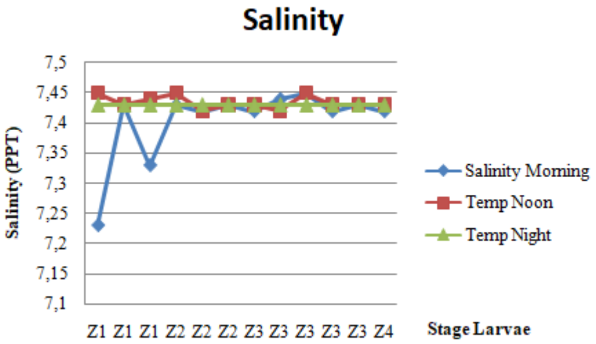

Figure 5. Water Salinity conditions in crab larvae

3.3 Salinity water quality

In this study, the traffic conditions obtained were not too many changes, namely in the number 34.30 ppt. Because the location of the crab larvae is in an indoor location. So that salinity does not show a high increase. With a salinity sensor, monitoring is carried out with conditions not showing an increase or decrease in salinity as shown in Fig. 5.

3.4 Application monitoring

Each reading of the data of each sensor has been processed by Arduino Uno, so the data for each sensor is displayed in the form of a percentage gauge and a graph with a specified time interval. In this application, data reading is done in real-time to determine the state of water quality directly. The application display can be displayed by accessing the existing IP address on the Raspberry Pi connected to Arduino Uno and for the addressing conditions of the IP done dynamically on a wireless connection.

The pictures in Figs. 5-8 shows the percentage of each sensor in the website application using node-red which is one application that supports the MQTT protocol. To display the percentage, as shown above, flow-based is needed to compile and execute data that will be received through the publisher.

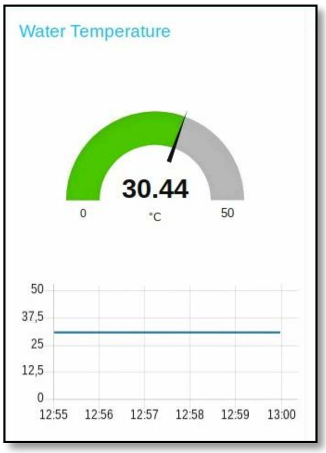

Figure 6. Model percentage of temperature sensors

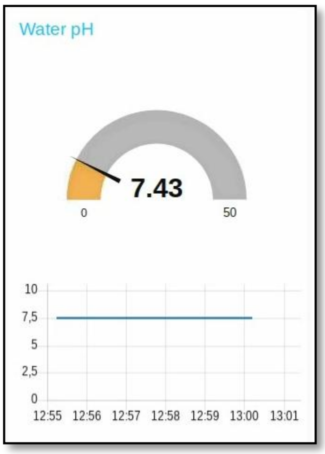

Figure 7. Model percentage of pH sensors

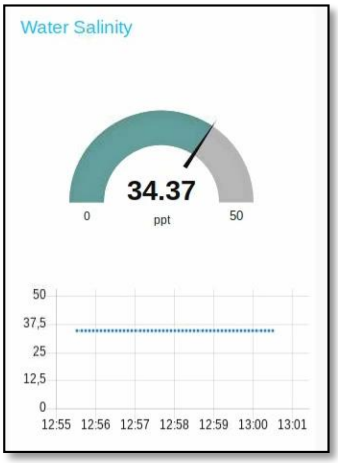

Figure 8. Model percentage of salinity sensors

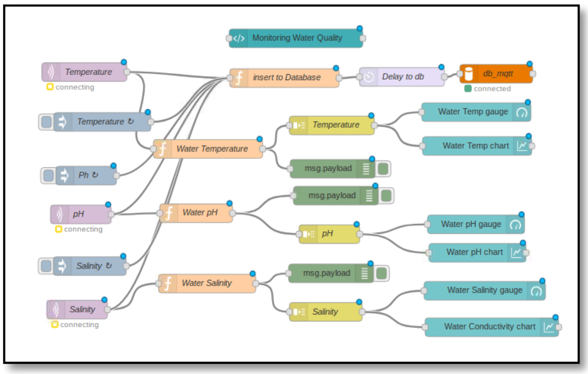

Figure 9. Flow node red

For each percentage displayed, it is designed in advance by making a flow at each node and must be connected. For each sensor, topic is listed in the flow node-red function. As in Fig. 9.

4. Conclusion and Future Work

The water quality monitoring system in crab larvae is very helpful for farmers in accessing water quality data through the internet. The monitoring system in this study only uses three sensors as parameters and each sensor data will be saved to the internal database of Raspberry Pi V3. The time interval every 5 minutes of taking sensor data makes the water quality data can be measured properly, and can be used as study material to determine the ideal water quality in crab larvae.

Acknowledgement

The author would like to thank C-BEST JICA for helping to fund this research.

References

[1] M. Ikhwanuddin, M. N. Azra, M. A. D. Talpur, A. B. Abol-Munai, and M. L. Shabdin, “Optimal Water Temperature and Salinity for Production of Blue Swimming Crab, Portunus pelagicus 1st Day Juvenile Crab,” *Aquac. Aquarium, Conserv. Legis. Int. J. Biolux Soc.*, vol. 5, no. 1, 2014.

[2] S. D. Brown and T. M. Bert, “The effects of temperature and salinity on molting and survival of Menippe adina and M. mercenaria (Crustacea, Decapoda) postsettlement juveniles,” *Mar. Ecol. Prog. Ser. Mar. Ecol. Prog. Ser.*, vol. 99, pp. 41–49, 1993.

[3] P. G. Krishna, K. S. Ravi, V. S. S. S. Kumar, and M. V. S. N. S. Kumar, “Implementation Of Mqtt Protocol On Low Resourced Embedded Network,” *Int. J. Pure Appl. Math.*, vol. 116, no. 6, 2017.

[4] A. Wijaya and M. Rivai, “Monitoring dan Kontrol Sistem Irigasi Berbasis IoT Menggunakan Banana Pi,” *J. Tek. ITS*, vol. 7, no. 2, 2018.

[5] S. Surya and S. S. Chauhan, “Water Level Indicator with Temperature Sensor,” *IOSR J. Electr. Electron. Eng.*, vol. 10, no. 3, pp. 65–71, 2015.

[6] M. Ikhwanuddin, T. Hayimad, A. Ghazali, S.-S. A. Halim, and S. A. Abdullah, “Resistance Test at Early Larval Stage of Blue Swimming Crab, Portunus Pelagicus,” *Songklanakarin J. Sci. Technol.*, vol. 38, no. 1, pp. 83–90, 2016.

[7] R. Ravi and M. K. Manisseri, “The effect of different pH and photoperiod regimens on the survival rate and developmental period of the larvae of Portunus pelagicus (Decapoda, Brachyura, Portunidae),” *Iran. J. Fish. Sci.*, vol. 12, no. 2, pp. 490–499, 2013.

[8] B. Susanto, “Growth, Survival Rate and Performance of Zoea-Megalopa of Blue Swimming Crab (Portunus Pelagicus) by Lowering Salinity,” *J. Perikan. (J. Fish. Sci.)*, vol. 9, no. 1, pp. 154–160, 2007.

[9] H. Chaudhari, “Raspberry Pi Technology: A Review,” vol. 2, no. 3, 2015.

[10] C. Reiber and G. F. Birchard, “Effect of temperature on metabolism and hemolymph pH in the Crab Stoliczia abotti,” *J. Therm. Biol*, vol. 18, no. 1, pp. 45–92, 1993.

[11] B. Susanto, I. Setyadi, M. Marzuqi, M. Syahidah, and I. Rusdi, “Pengaruh Pemberian Pakan yang Berbeda Terhadap Pertumbuhan dan Sintasan Benih Rajungan Portunus sp,” Gondol Bali, 2003.

EPI International Journal of Engineering
Volume 3, Number 1, February 2020, pp. 50-58
DOI: 10.25042/epi-ije.022020.08

*p*ISSN 2615-5109
*e*ISSN 2621-0541

The Effectiveness of Petobo Temporary Shelter

Asiana Rahmawati[a,*], Mohammad Mochsen[b], Abdul Mufti Radja[c]

[a]Department of Architecture, Faculty of Engineering, Hasanuddin University, Makassar. Indonesia. Email: asianarahmawati@pm.me
[b]Department of Architecture, Faculty of Engineering, Hasanuddin University, Makassar, Indonesia. Email: sirmochsen@gmail.com
[c]Department of Architecture, Faculty of Engineering, Hasanuddin University, Makassar, Indonesia. Email: muftiradja@gmail.com

---

Abstract

Temporary shelter (huntara) is one of the government's solutions in undertaking victims after a disaster. Shelter of Petobo is one of the temporary shelters built by the government in the aftermath of the disaster in Palu City in September 28th, 2018. Petobo shelter was built in October and occupied in December. This shelter has a capacity of 70 units. 1 unit of the shelter is measured 26.4m x 12m, it consists of 12 rooms, 4 bathrooms, 4 toilets, a laundry room, and a shared kitchen. The shelter consists of 840 room cubicles with room sizes of 3.6m x 4.8m. After being occupied, some residents said that the shelter they lived in was very small, with family members of more than 3 people, the space for occupants was very limited so that some residents made changes to their residential units. This study evaluates Petobo shelter with BNPB and UNHCR Standards, and examines occupant perceptions about the effectiveness of Petobo shelter in terms of physical building requirements which consist of safety, health, comfort, and convenience. This research was conducted in Palu City, Central Sulawesi. The type of this research is evaluation, using survey methods to measure the value of several variables. The data obtained were analyzed using descriptive statistical techniques. The results of this study indicate that the Petobo shelter is in accordance with BNPB and UNHCR standards, but according to the occupants' perception it is less effective in terms of the physical requirements of the building, which consists of safety, health, comfort, and convenience as a post-disaster refugee residence.

Keywords: Conformity; effectiveness; perceptions of occupants; temporary shelter

---

1. Introduction

According to the Law of the Republic of Indonesia Number 24 of 2007, Disaster is an event that threatens and disrupts people's lives caused by natural and non-natural factors, resulting in fatalities, environmental damage, property losses, and psychological impacts [1]. On September 28, 2018 an earthquake occurred in Palu City and its surroundings. The impact of the earthquake resulted in many deaths, as well as destroyed buildings and infrastructure [2]. Besides having to lose family and relatives, they also have to move or flee to a safe place. This has become a sensitive issue for the government in dealing with disasters.

One of the government's solutions in dealing with disasters is to build temporary shelters. The development of shelters is intended as one of the recovery efforts that bridges the transition period between the emergency response phase and the reconstruction period [3]. This is expected to alleviate the suffering of victims of disasters in the city of Palu. The shelters in Palu City were built by the Ministry of PUPR. The shelter can become a standard for those who want to assist in the provision of shelter in Palu and its surroundings [4]. The Indonesian Institute of Sciences (LIPI) revealed, so far the Indonesian government does not yet have a standard for the shelter for victims of natural disasters. Petobo shelter is one of the shelters in Palu City. This shelter is ± 10 Ha wide. Petobo shelter was built in October 2018, and began to be occupied in December 2018. Petobo shelter has a capacity of 70 units. 1 unit of shelter measuring 26.4m x 12m, consisting of 12 rooms, and supporting facilities such as 4 bathrooms, 4 toilet, laundry room, and shared kitchen. Petobo shelter consists of 840 rooms that can accommodate 4200 people, where 1 household gets 1 room with a maximum capacity of 5 people.

The residents of the Petobo shelter said that the shelter they lived in was very small, the size of each room is only 3.6m x 4.8m with family members of more than 3 people, the space was very limited, and this was one of the problems in the Petobo shelter. Another problem is that many residents of the shelters make changes in their housing units, by adding more spaces independently. Furthermore, some of the residents of the shelter also build other huts around Petobo shelter, and the unit they got is only used as storage for goods. Based on these phenomena, the problem can be formulated, namely: how the effectiveness of the Petobo shelter as a place for post-disaster refugees in Palu City according to residents' perceptions.

---

*Corresponding author. Tel.: +6282290490332
Perumahan Nurul Baidah D1/5,
Gowa, Sulawesi Selatan

2. Literature Review

2.1. Temporary shelter

Temporary shelters are different from emergency shelters and permanent shelters. Temporary shelters are impermanent shelters and do not have to meet all the criteria of permanent shelters, but on the other hand, temporary shelters must also meet the minimum living needs of their users for one-two years [5]. Thus, specific criteria are needed in designing the basic concepts of temporary shelter. Due to it is in term of temporary, the method of construction and design of this shelter must be designed effectively and efficiently.

2.2 Feasibility of temporary shelter

It must be ensured that temporary shelter aid is appropriate to accomplish the needs of affected communities and the occupancy standards. The concept of "ineligibility of shelter" can be applied to all types of shelters, from emergency shelters to permanent shelters. It is important to remember that shelter is a process. A residence is considered appropriate only if the residents have access to basic services such as education and health, as well as the opportunity to undertake livelihood activities in the settlement or community. According to the Ministry of Social, to determine what is feasible or not, there are several important points that must be considered, namely safe from further risks, environmentally friendly, appropriate resilience, in accordance to local culture, appropriate facilities, access to services, and in accordance to climate [6].

2.3 Effectiveness of temporary shelter

Effectiveness is one concept that has a very important meaning, but the reality is difficult to define with certainty. The reason is there are many concepts related to the sense of effectiveness. The word 'effective' comes from English, which is effective, that means successful or something done successfully. According to Hidayat [7] mentioning effectiveness is as a measure that states how far the target (quantity, quality, and time) has been achieved.

According to Kelman in Ero [8], effectiveness is part of the evaluation, to test and assess whether the undertaken policy actions (programs) produce impacts which achieves the main goals. In other words, effectiveness can also be a measure of success in achieving goals. The development process generally starts from the planning, implementation, and evaluation stages, so effectiveness is included in the evaluation stage. The shelter was supposed to be built as a place to evacuate affected communities after the disaster, and can help ease their burden, thus they can live properly. The perception of residents living in temporary shelters determines the effectiveness of the shelter as a post-disaster refugee's site.

In the Law of the Republic of Indonesia number 28 of 2002 concerning building construction [9], each building must accomplish administrative and technical requirements in accordance with the function of the building. Temporary shelter serves for after-disaster refugees. In order for temporary shelters to be functioned effectively, according to the Law of the Republic of Indonesia number 28 of 2002, temporary shelters must achieve the building technical requirements of safety, health, security, and convenience.

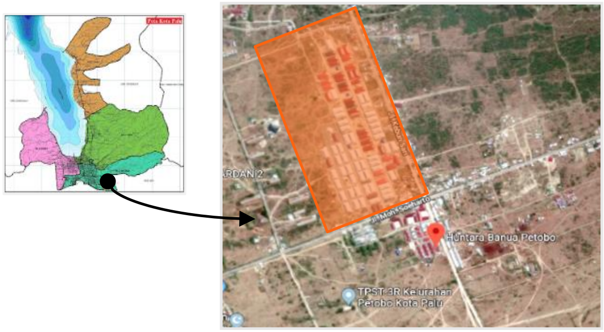

Figure 1. Location of the shelters in the city of Palu [10]

3. Research Methods

3.1. Research sites

The research location is a place to conduct research activities to obtain data from respondents. The research location (see Fig. 1) is located in Petobo shelter located on Jalan Kebun Sari, Village of Petobo, Sub-district of South Palu, Palu, and Central Sulawesi Province.

3.2. Types of research

The type of this research is quantitative with 2 methods, namely evaluation and survey. To answer the appropriateness of Petobo shelter with BNPB and UNHCR standards, the method used is evaluation. Weiss argues that evaluation research is applied research, which is a systematic way to find out the effectiveness of a program, policy, or other object under study if it is compared to the objectives or standards set [11].

3.3. Population and sampling techniques

The target population is the head of the family or family members who are considered to be able to represent to answer questions from researchers. The total population of this study was 840 households. In this study, researcher used simple random sampling because the population is considered homogeneous, and sampling members of the population are carried out randomly without regarding to strata. To determine the number of samples, based on existing population, the sample of this study used Yamane formula [12]. The number of samples needed to answer the effectiveness of temporary shelters in the Petobo shelter is 89 households.

3.4. Data collection technique

To have this research more focused, and based on the problem formulation that has been described, the data collection techniques used namely: observation, study of literature, documentation, and questionnaires.

3.5. Data analysis technique

Data analysis is classifying data based on variables and types of respondents, tabulating data based on variables from all respondents, and doing calculations to answer the problem formulation [12]. Data analysis techniques in this study using statistics.

Analysis of the efficacy data in question is an evaluation to test and assess whether Petobo shelter has an impact in accordance with the main objectives, where the purpose of the shelter as a post-disaster refugee site. To measure this, it is used a level to describe how the shelter building units provided for disaster victims. The data obtained in the form of respondents' answers which are then categorized by score using Likert scale measurement [12], where (3) = effective, (2) = less effective, (1) ineffective. Next, calculate the percentage and score of each using a formulation.

4. Discussion

Petobo shelter can be said to be effective if the shelter can achieve the building technical requirements. The perception of the residents of the shelter determines the effectiveness of the shelter as a post-disaster refugee site. There are 4 variables to measure the effectiveness of temporary shelter, among others.

4.1 Safety

Safety in question in this study is the safety requirements of shelter building includes building location, building structure shelters ability to withstand loads during an earthquake, and security in shelters in tackling a fire hazard.

Safety, in this study, refers to the requirements of the shelter building including the location of the building, the ability of the building structure to withstand the load during an earthquake, and security in the shelter in overcoming the fire hazard. Residents' perceptions to assess the location of the shelter, can be seen in the results of a questionnaire as shown in Fig. 2.

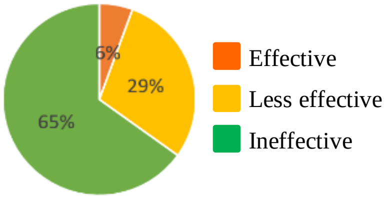

Figure 2. Result of the questionnaire of the shelter's location

Table 1. The result of the assessment of the shelter location based on the residents' perception

Assessment			respondents	Category (%)	variable score
shelter locations	Category	Weight			
Feel safe in the shelter location	Effective	3	5	5.6	15
Feel less safe and have no other choice	Less effective	2	26	29.3	52
Feel insecure and fear of forthcoming disaster	Ineffective	1	58	65.1	58
amount			89	100	125
The effectiveness of variable = 125 / (89 x 3) x 100%					47%

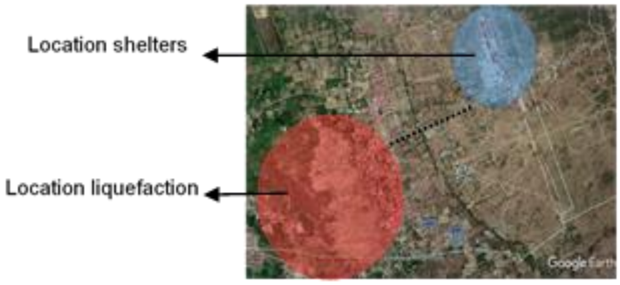

Figure 3. The distance to the location of shelters Petobo liquefaction

From Table 1 above, the residents of Petobo shelter answered that the location of the shelter is currently unsafe. This is because the location of the shelter is only ± 1 km from the former location of liquefaction (see Fig. 3), the residents of the shelter are still traumatized by the disaster that befell them. Many residents want to move out from this location, but they have no choice but to stay in the shelter.

The ability of building structures to withstand loads during an earthquake is one of the building's safety requirements. The perception of residents is needed to assess the capability of the building structure of a shelter. The results of the questionnaire can be seen in Fig. 4.

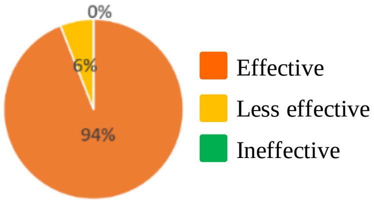

Figure 4. The results of the questionnaire capability building structure

Table 2. Results of analysis o the shelter structure ability assesment based on the residents' perception

Assessment			respondents	Category (%)	Score Variable
Shelter Structures Capability	Category	Weight			
There was no damage to the structure during the stay and earthquakes	Effective	3	84	94.3	249
There is a non-structural damage during the stay and earthquakes	Less effective	2	5	5.7	10
damage to the structure so that the shelters uninhabitable	Ineffective	1	0	0	0
Amount			89	100	259
The effectiveness of variable = 259 / (89 x 3) x 100%					98%

Figure 5. Mild steel structure in Petobo shelter

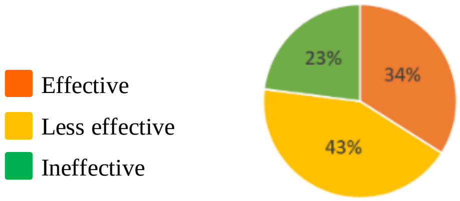

Figure 6. Results of the questionnaire of fire safety

Table 3. Result of the analysis of fire safety assessment based on the residents' perception

Assessment			respondents	Category (%)	Score Variable
Distance of Firebreak	Category	Weight			
Distance between residential ± 8 m	Effective	3	30	33.7	90
Distance between residential ± 5 m	Less effective	2	38	42.6	76
Distance between the adjacent residential ± 3 m	Ineffective	1	21	23.7	21
Amount			89	100	187
The effectiveness of variable = 187 / (89 x 3) x 100%					70%

From Table 2, most of the residents of the shelter said that the ability of shelter building structure is effective enough to withstand the load. Petobo shelter structure using mild steel with disassembly models (see Fig. 5). When an earthquake occurs, the structure remains sturdy and only a fraction of the shelters which suffered from minor damage, but the shelter is still habitable.

Fire safety in shelters, in this study, is the distance between residences there is a firebreak (vacant land to prevent fire expansion). Residents' perceptions are needed to assess security in the shelters in dealing with fire hazards. The results of the questionnaire can be seen in Fig. 6.

From Table 3, the residents of the shelter answered that the fire safety in the shelter was quite effective. This is because the distance between the residences is varied. Petobo shelter site was designed using a grid layout with a rectangular area separated by a road, where the width of the road is 8 meters (see Fig. 7). While respondents who answered less effective and ineffective because their shelter units are facing each other and the distance is close to each other, it is about 3-5 meters (see Fig. 8).

Figure 7. Shelter Petobo separated by road

Figure 8. Petobo that face each other shelters

Table 4. Safety of shelter building of Petobo

No.	**Indicators of Safety of Shelter Building**	**level of Effectiveness (%)**	**Category**
1	Shelter Location	47%	Less effective
2	The ability of the structure from earthquake	98%	Effective
3	fire safety	70%	Effective
	***Average* Effectiveness**	72%	Effective

The results of analysis of the effectiveness of the shelter building Assessment Summary based on the resident's perception are shown in Table 4.

4.2 Health

Health, in this study, is referred to the requirements of the shelter building, including the, lighting system, and sanitation. Residents' perceptions are needed to assess the availability of openings in the shelter unit as air exchange. The results of the questionnaire can be seen in Fig. 9.

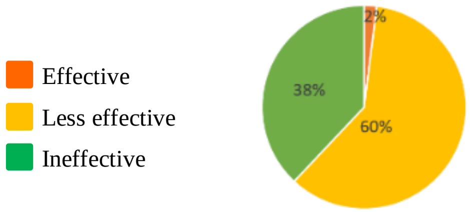

Figure 9. Results of air conditioning system questionnaire

Table 5. Results of analysis of air conditioning availability assessment in the shelter based on theresidents' perception

Assessment			respondents	Category (%)	variable score
Availability of Air Conditioning	Category	Weight			
Achieve the needs of residents	Effective	3	2	2.2	6
Less achieve the needs of residents	Less effective	2	53	59.6	106
Does not achieve the needs of residents	Ineffective	1	34	38.2	34
Amount			89	100	146
The effectiveness of variable = 146 / (89 x 3) x 100%					55%

Figure 10. View of Shelter building of Petobo

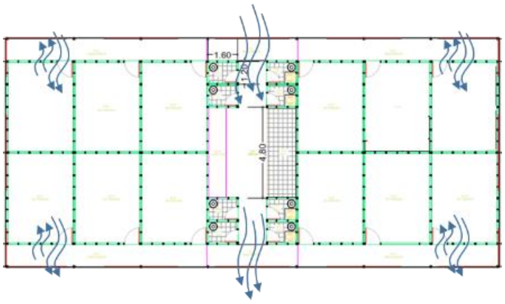

Figure 11. Air exchange in shelter units of Petobo

From Table 5, it can be seen that the residents of the shelter said that the availability of openings in the shelter units are less effective for air exchange. This is due to the design of openings layout such as doors, windows, and vents at the shelter units (see Fig. 10). Occupancy openings are located on one side of the room, where openings on the same side make the air come in the room through the same side as the air is out. This makes the air exchange in the residential units less than optimal.

Air exchange at supporting facilities located in the central part of the shelter is also less effective (see Fig. 11), because the positions of the opposite openings are the same size. This makes the air exchange inside lower. Besides, the location of the toilet and public bathroom adjacent to the residential unit makes the residents less comfortable because of the smell of the toilet.

Lighting systems in the building must have openings for natural lighting, and have a light source for artificial lighting. The residents' perception is needed to assess the availability of lighting in the shelter building. The results of the questionnaire can be seen in Fig. 12.

From Table 6, the residents of the shelter answered that the availability og lighting system at Petobo shelter is effective. This is due to the fact that residents of the shelter feel that they had enough natural light enter the shelter unit through the openings such as doors, windows, and vents. Some residents in the shelter also answered less effective because the light entering the room is excessive, causing glare, but there are treatments of the residents to minimize glare in buildings (see Fig. 13) by using curtains, and some are using canopy with improvised material.

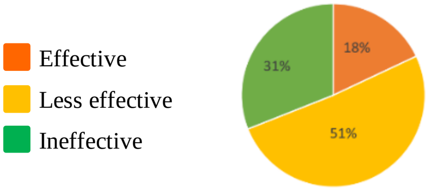

Figure 12. Results of the lighting system questionnaire

Table 6. The Results of analysis of the lighting availability assessment based on residents' perception

Assessment			**frequency**	**Category (%)**	**variable score**
Availability of Lighting	Category	Weight			
Achieve needs of residents	Effective	3	56	62.9	168
Less achieve the needs of residents	Less effective	2	22	24.7	44
Does not meet the needs of residents	Ineffective	1	11	12.4	11
amount			89	100	223
The effectiveness of variable = 223 / (89 x 3) x 100%					83%

Figure 13. Minimize the light entering the shelter unit

.

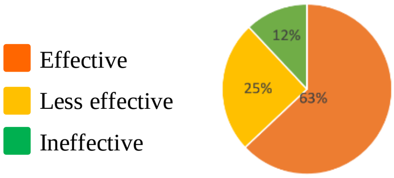

Figure 14. The results of the sanitation system questionnaire

Table 7. Result of analysis of the sanitation system assessment based on residents' perceptions

Assessment			**respondents**	**Category (%)**	**variable score**
Availability of sanitation in shelters	Category	Weight			
avhieve the availability of sanitation	Effective	3	16	18	48
Less achieve availability of sanitation	Less effective	2	45	50.6	90
Does not achieve the availability of sanitation	Ineffective	1	28	31.5	28
Amount			89	100	166
The effectiveness of variable = 166 / (89 x 3) x 100%					62%

Building health also includes sanitation. To reach the sanitation system requirements in the buildings, the shelter must be equipped with a clean water supply system, sewage and garbage system. Residents' perceptions are needed to assess the availability of sanitation system. The results of the questionnaire can be seen in Fig. 14

Based on the Table 7, residents of the shelter answered that the availability of sanitation system in Petobo shelter is less effective for the needs of residents. This is due to the sanitation system in the shelter, namely the availability of clean water for bathing and drinking, and the waste water disposal system is very lack. The source of clean water in Petobo shelter is a wellbore, which uses an indirect system and a solar cell (see Fig. 15).

As for the waste water disposal system in Petobo shelter, not all the units in Petobo shelter have drainage. Besides, the liquid and solid waste disposals are put together towards septitank (see Fig. 16), thus some septitanks in the units are overflowed and leak.

Figure 15. Solar cell in shelter of Petobo

Figure 16. The liquid waste disposal pipe

Table 8. Health building of Petobo shelters

No.	Indicators of Shelter Building Health	level of Effectiveness (%)	Category
1	Air conditioning system	55%	Less effective
2	lighting system	83%	Effective
3	Sanitation system	62%	Less effective
	***Average* Effectiveness**	67%	Less effective

The assessment of the health effectiveness of a building based on the residents' perception is shown in Table 8.

4.3 Convenience

In this study, convenience means the comfort of the space, the availability of space to fulfill the needs of the residents, the comfort of privacy in carrying out activities in the shelter building, and the level of comfort is determined by a condition that does not result to the user and the function of the building being disturbed by vibration or noise both from within the building and its environment. The convenience of space in the shelter must consider the dimensions of space, and the number of users. The results of the questionnaire can be seen in Fig. 17.

Based on the Table 9, the residents of the shelter answered that the space comfort in Petobo shelter is less effective. This is because the area of the shelter units is not proportional for the number of residents. On average residents who have 3 or more family members feel uncomfortable staying in the shelter. Many residents add more spaces to their residential units (see Fig. 18), with remains of liquefaction materials.

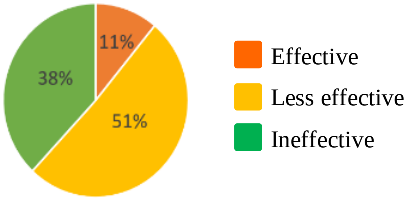

Figure 17. The results of the questionnaire comfort space

Table 9. Results of the analysis of comfort ratings based on perception occupant space

Assessment			**respondents**	**Category (%)**	**variable score**
Comfort space	Category	Weight			
Space suit guests'	Effective	3	10	11.2	30
Less space suit guests'	Less effective	2	45	50.6	90
Does not meet the comfort of the space	Ineffective	1	34	38.2	34
Amount			89	100	154
The effectiveness of variable = 154 / (89 x 3) x 100%					57%

Figure 18. The addition of space in the units of Petobo shelter

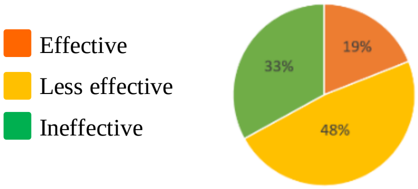

Figure 19. Results of the availability of space questionnaire

Table 10. Result of analysis of space availability assessment based on the residents' perception

Assessment			**respondents**	**Category (%)**	**variable score**
The availability of space in shelters	Category	Weight			
Achieve the needs of residents	Effective	3	17	19.1	51
Less achieve the needs of residents	Less effective	2	43	48.3	86
Does not achieve the needs of residents	Ineffective	1	29	32.6	29
Amount			89	100	166
The effectiveness of variable = 166 / (89 x 3) x 100%					62%

The requirements of the comfort at the shelter are also influenced by the availability of space. The results of the questionnaire of 89 respondents can be seen in Fig. 19.

Residents of the shelter answered in Table 10 that the availability of space in Petobo shelter is not effective. For the availability of bathrooms, toilets, and laundry rooms in residential areas, residents already feel quite effective. Whereas, for shared kitchens, many residents do not use it. The reason is because the kitchen provided is small for users of 12 families. Then, the kitchen that is not used according to its function, eventually, is converted into residents parking (see Fig. 20).

Privacy is also one of the comfort requirements at the shelter. The privacy, in this study, is referred to the reviewed from the layout of the room. The results of the questionnaire can be seen in Fig. 21.

From Table 11, the residents of the shelter answered that the privacy in Petobo shelter is ineffective or non-existent. This is due to the absence of a public toilet distribution for men and women. Thus, it is vulnerable to sexual harassment in public facilities in the shelter unit. In addition, many residents limit their occupancy as a form of privacy (see Fig. 22).

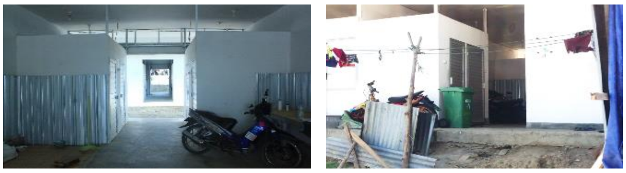

Figure 20. Transformation of kitchen function in Petobo Shelter

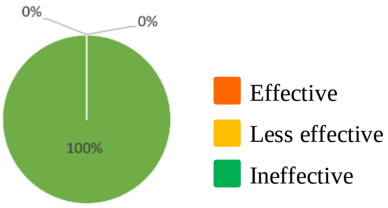

Figure 21. The results of the questionnaire privacy space

Table 11. Result of analysis of the privacy space assessment based on the residents' perception

Assessment			respondents	Category (%)	variable score
Privacy in shelters	Category	Weight			
Achieve privacy of residents	Effective	3	0	0	0
Less achieve the privacy of residents	Less effective	2	0	0	0
Does not achieve the privacy of residents	Ineffective	1	89	100	89
Amount			89	100	89
The effectiveness of variable = 89 / (89 x 3) x 100%					33%

Figure 22. Privacy in Petobo shelter

Convenience at the shelter is also determined by a situation that does not result in the user being disturbed by vibrations or noise arising either inside or outside the building. The results of the questionnaire can be seen in Fig. 23.

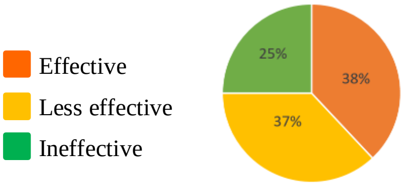

Figure 23. The results of the questionnaire noise

Table 12. Result of analysis of noise based on the residents' perception

Assessment			frequency	Category (%)	variable score
Noise	Category	Weight			
Not noisy in at shelter	Effective	3	0	0	0
Less noisy at shelterr	Less effective	2	40	44.9	80
Very noisy at shelter	Ineffective	1	49	55.1	49
Amount			89	100	166
The effectiveness of variable = 166 / (89 x 3) x 100%					48%

Figure 24. Build up the the boundaries at the residence unit Petobo Shelter

Table 13. comfort of the shelter building of Petobo

No.	Indicators of comfort of Shelter Building	Level of Effectiveness (%)	category
1	Comfort of space	57%	Less effective
2	The availability of space	62%	Less effective
3	Privacy	33%	Less effective
4	Noise	48%	Less effective
	Average	50%	Less effective

From Table 12, it can be said that the residents feel very noisy at the shelter of Petobo. This is because the covering material of the wall and floor do not muffle the sound. That is why if people walk or children run around the shelter unit, it will cause noise. One of the methods used by the residents to reduce noise is to build up boundaries between their residences and others (see Fig. 24). The Effectiveness of comfort of shelter building based on the residents' perception is shown in Table 13.

4.4 Easiness

Easiness, in this study, refers to the requirements for the simplicity of building of Petobo shelter, including the ease of connection to, from, and inside the buildings, availability of facilities, accessibility that is easy, safe, and convenient, including for persons with disabilities and the elderly. Residents' perceptions are needed to assess circulation in the shelter. The results of the questionnaire can be seen in Fig. 25.

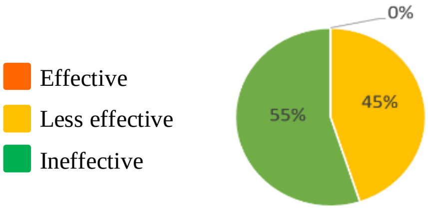

Figure 25. Result of the Ease of relationship to, from, and within building questionnaire

Table 14. Result of the analysis of ease of relationship to, from, and within the building based on the residents' perception

Assessment			respondents	Category (%)	variable score
Circulation	Category	Weight			
Easy, safe and convenient	Effective	3	34	38.2	102
Less easy, safe and convenient	Less effective	2	33	37.1	66
uneasy, unsafe and inconvenient	Ineffective	1	22	24.7	22
Amount			89	100	190
The effectiveness of variable = 190 / (89 x 3) x 100%					71%

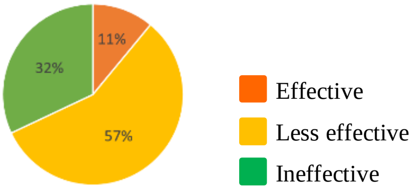

Figure 26. The results of the questionnaire facilities and accessibility

From Table 14, it can be concluded that most of the residents of the shelter answered that the ease of contact to, from, and inside the building at Petobo shelter is effective. The requirements of building facilities also include the provision of facilities and accessibility that are easy, safe, and cconvenient, including for people with disabilities and the elderly. The perception of residents is needed to assess the facilities and accessibility that is easy, safe, and convenient at the shelter. The results of the questionnaire can be seen in Fig. 26.

Table 15. Result of analysis of facilities and accessibility assessment based on the residents' perception

Assessment			**Respondents**	**Category (%)**	**variable score**
Ease of the building for people with disabilities and elderly	Category	Weight			
Achieve the easiness	Effective	3	10	11.2	30
Lessachieve the easiness	Less effective	2	51	57.3	102
Does not achieve the easiness	Ineffective	1	28	31.5	28
Amount			89	100	160
The effectiveness of variable = 160 / (89 x 3) x 100%					60%

From Table 15, most of the residents of the shelter answered the ease of accessibility for people with disabilities and the elderly in Petobo shelter is less effective. This is due to the lack of access for people with disabilities. Some residents provide their own stairs to help ascend to the residential unit (see Fig. 27).

The effectiveness of the convenience of building shelter based on the residents' perception is shown in Table 16. Based on the analysis and discussion above about the effectiveness of temporary shelter in terms of the physical requirements of the building, including safety, health, comfort, and convenience, it is summarized as follows shown in Table 17.

Figure 27. Stairs to help ascend to the residential units

Table 16. Convenience of shelter building of Petobo

No.	Indicators of convenience of the building	level of effectiveness (%)	category
1	accessibility	71%	Less effective
2	provision of facilities	60%	Less effective
	Average	66%	less effective

Table 17. Comfort of shelter building of Petobo

No.	Effectiveness indicator shelter	Level of effectiveness (%)	Category
1	Safety	72	Effective
2	Health	67	Less effective
3	Convenience	50	Less effective
4	Easiness	66	Less effective
Average Index 255/4 x 100%		62%	Less effective

From the analysis and discussion in the table above, it can be concluded that the effectiveness of shelter Petobo terms of the perception of shelter occupants to safety, health, comfort, and convenience by 62%, where the category is less effective. So the temporary dwelling Petobo less effective as a container or a refugee after the disaster because does not meet the physical requirements of the building. Less effective in terms of safety because of the location of shelters Petobo. In terms of health is less effective because the system penghawaan in shelters less and also the management of liquid and solid wastes are put together. In terms of comfort, less effective due to lack of space makes discomfort, so that residents add space in their dwelling units. In addition layout of the rooms and lack of privacy between spaces. In terms of convenience.

From the analysis and discussion in the table above, it can be concluded that the effectiveness of Petobo shelter based on the residents' perception in terms of safety, health, concenience, and easiness is 62%, which is less effective. Therefore, the temporary shelter of Petobo is less effective as a place for refugees after a disaster because it does not achieve the physical requirements of the building. In term of safety is less effective because of the location of Petobo shelter. In term of health, it is less effective because of the lack of adequate ventilation in the shelter unit and also the integrated management of liquid and solid waste disposal system. In term of convenience, it is less effective due to the lack of space creating inconvenience, so that residents add more spaces to their residential units. Besides, the layout of the room affects on the absence of privacy between spaces. In term of easines, it is less effective because there are no facilities that can support people with disabilities and the elderly such as stairs.

5. Conclusions and Suggestion

5.1 Conclusions

The effectiveness of Petobo shelter based on the the residents' perception is 62%, which is in less effective category. Thus, the temporary shelter of Petobo is less effective as a place for refugees after a disaster because it does not achieve the physical requirements of buildings such as safety, health, convenience, and easiness. In term of safety, it is less effective because of the location of Petobo shelter. In term of health, it is less effective because of the lack of adequate ventilation in the shelter and also the integrated management of liquid and solid waste disposal system. In term of convenience, it is less effective due to the lack of space creating inconvenience, so that residents add more spaces in their residential units. Besides, the layout of the room affects the lack of privacy betweesn spaces. In term esiness, it is less effective because there are no facilities that can support people with disabilities and the elderly such as stairs.

5.2 Suggestions

Based on the results of the study, suggestions that can be made to improve the effectiveness of temporary shelter are as follows:

a. It needs further evaluation related to the location of the shelters that are adjacent to the liquefaction location.
b. It is better for having privacy between sexes for the convenience of residents, and to reduce the potential for crime at the shelter.
c. It is necessary to plant vegetation at the shelter area to reduce heat and filter out dust.
d. Although the temporary shelter is only inhabited in a short period of time, it is necessary to pay attention to the need for clean water sources, liquid and solid waste storage, supporting facilities such as parking, security posts, and guardrail.
e. Temporary shelter design needs to pay attention to the convenience for elderly residents and people with disabilities.

References

[1] House of Representative of Indonesia Republic, *Law of the Republic of Indonesia Number 24 on Disaster Management*. 2007. (in Bahasa)

[2] BNPB, “Loss and Damage Disaster Impacts in Central Sulawesi Reached 13.82 Trillion Rupiah,” 2018. [Online]. Available: https://www.bnpb.go.id/. [Accessed: 15-Jun-2019].

[3] F. S. Affisa, “Effectiveness of Temporary Shelter Region as Post-Disaster Recovery Media Merapi Refugees 2010 (Case Study on Temporary Shelter Region Plosokerep, Gondangpusung, Banjarsari and Gondanglegi),” Graduate School of UGM, 2013. (in Bahasa)

[4] Pu-net, “The Ministry of PUPR Targets 699 shelters Unit Completed End of February 2019,” 2019. [Online]. Available: https://www.pu.go.id/berita. [Accessed: 17-Aug-2019]. (In Bahasa)

[5] A. J. Forouzandeh, M. Hosseini, and M. Sadeghzadeh, “Guidelines for Design of Temporary Shelters After Earthquakes Based On Community Participation,” in *The 14th World Conference on Earthquake Engineering (WCEE)*, 2008.

[6] Social Ministry of the Republic Indonesia, *Free Shelter for Humanity*, Asean. Jakarta: Fabian Prideaux, 2019.

[7] W. A. Tantu, “Evaluation of Damage to Roads and Road Maintenance Management Effectiveness on Line Traffic West South Sulawesi (Case Study Roads Pare-Pare Boundary South West),” Graduate School of Hasanuddin University, 2009. (in Bahasa)

[8] Ero, “Effectiveness Analysis pembagunan Konaweha River Bridge Toll-Mowila Wawolemo Southeast Sulawesi Province Vicinity of Improved Accessibility,” Graduate School of Hasanuddin University, 2008. (in Bahasa)

[9] House of Representative of Indonesia Republic, *Law of the Republic of Indonesia Number 28 of 2002 on Building*. Jakarta.

[10] Palu City Statistics Center, “Maps of Palu City,” 2018. [Online]. Available: https://palukota.bps.go.id/. [Accessed: 17-Aug-2019].

[11] Sugiyono, *Research Methods Evaluation (Approach Quantitative, Qualitative, and Combination)*. Bandung: Alfabeta, 2018. (in Bahasa)

[12] Sugiyono, *Research Methods Combined (Mixed Methods)*. Bandung: Alfabeta, 2018. (in Bahasa)

EPI International Journal of Engineering
Volume 3, Number 1, February 2020, pp. 59-68
DOI: 10.25042/epi-ije.022020.09

*p*ISSN 2615-5109
*e*ISSN 2621-0541

Characteristics of Micro Spatial Patterns, Functions and Meanings of the *Towani Tolotang's* Traditional House

Husnirrahman Jamaluddin.[a,*], Afifah Harisah[b], Ria Wikantari[c,]

[a]Department of Architecture, Engineering Faculty, Hasanuddin University, Makassar, Indonesia. Email: husnirrahman.jamal@yahoo.com
[b]Department of Architecture, Engineering Faculty, Hasanuddin University, Makassar, Indonesia. Email: ifahhussein@yahoo.co.id
[c]Department of Architecture, Engineering Faculty, Hasanuddin University, Makassar, Indonesia. Email: rwikantaria@gmail.com

Abstract

The architecture of *Towani Tolotang's* traditional house has characteristics that represents the identity, activities, social and cultural values of the community. The *Towani Tolotang* people strongly maintain the relationship of togetherness and unity shown by the architecture of traditional houses. This study discussed and examined the characteristics of micro spatial patterns, functions, and meanings of the *Towani Tolotang's* traditional house. The study was conducted in Amparita Village, Sidrap Regency, South Sulawesi. The discussion on the architecture of the traditional house of *Towani Tolotang* was carried out by applying the naturalistic phenomenological method. This type of research is qualitative with the process of collecting data through participatory observation, in-depth interviews, and document studies. Data analysis was performed using descriptive qualitative, describing in accordance with the natural situation. The results of the study revealed that there were two spaces in the spatial pattern of *Towani Tolotang's* traditional house being the characteristics different from Bugis's houses in general. They were *tamping* and special rooms. The function of the space was similar to the Bugis's house in general, except the two spaces. *Tamping* was functioned as a place to receive guests with the status of ordinary people, and the special room was used as a place for ritual and taking prayer for the people of *Towani Tolotang*. Every space in the *Towani Tolotang's* traditional house has its own meaning, included *tamping* which means respect for the traditional leader and special room which means the sacred space.

Keywords: House function and meaning; micro spatial pattern; Towani tolotang; traditional house

1. Introduction

As with other Archipelago ethnics, each ethnic in South Sulawesi has diverse cultural characteristics. Cultural diversity in the Bugis community appears in traditional houses. One of the Bugis community groups that still fosters and maintains the architectural characteristics of their traditional houses is the *Towani Tolotang* community. There are two groups of *Towani Tolotang* social strata, namely ordinary people and *Uwa'* (community leader).

The traditional house of *Towani Tolotang* has its uniqueness seen in the form of round pillars and rooms with no chairs. So both the house owner and the guest just sit on the floor. *Uwa's* house (traditional stakeholders) has a large living room because guests usually come in large numbers. The existence of *tamping* is also seen in the interior of the house, the difference in floor height which distinguishes the social strata or the position of ordinary people and *Uwa'*, the lower floor for ordinary people, and the higher floor for Uwa'.

The traditional house of *Towani Tolotang* still has the shape and characteristics of Bugis's houses in general. But, the uniqueness or identity in detail about *Towani Tolotang's* traditional house has not been known surely by the community. Not only in its form and function, but also its relation to worldview is not fully understood. Related to this, it can be obtained that the people of Sidrap in general and the *Towani Tolotang* community themselves do not know the meaning behind the symbols of the architecture of their traditional houses.

The architecture of the *Towani Tolotang's* traditional house related to social cultural views or values of life has not been specifically discussed by previous researchers. Likewise, studies that discuss traditional houses by looking at their relevance to social patterns, traditions, home space functions and community life values have not been reviewed. On the other hand, it is important to study in order to see the structural relationship between the *Towani Tolotang's* traditional house and social activities and community values systems. Related to this, the author raised the architecture of the traditional house *Towani Tolotang* as an object of study. The focus of this study was on three problem statements namely how the micro spatial

---

*Corresponding author. Tel.: +6285299999737
BTN Pao-Pao Permai Blok E2 No. 2,
Gowa, Sulawesi Selatan

pattern is, how the function is and how the meaning of space in the traditional house of the *Towani Tolotang* community is in Amparita, Sidrap Regency.

2. Literature Review

2.1. Traditional houses concept

Traditional houses are further developments from ordinary houses into typical houses such as the king's house, houses of worship and so on. Home is a human work in three important dimensions in life; the house creates an "imaginary space" in a tangible space that can be used, as a place that limits "something" to the world around it, and aims to make humanity the "main part" of the surrounding environment [1].

The cultural change is seen in the changes of behavior and activity. Those then manifest in the physical form of the building. Implicitly, there is a relationship between behavior and the shape of the building in two ways. First, the shape of the building is the physical manifestation of behavior patterns, including desires, motivations and feelings. Second, that if a form has been built, then it will affect behavior and lifestyle [2].

2.2. Traditional architecture

According to Amos Rapoport in the book House Form and Culture [2], traditional architecture is an architectural work that grows from popular architecture with all kinds of traditions and optimizes or utilizes local potentials. For example, material, technology and knowledge. Because traditional architecture greatly optimizes the potential or local culture, a building with a traditional concept takes environmental sustainability into account so it is also a sustainable architecture. Traditional architecture was discovered by trial and error by the people themselves.

Rapoport also added that architectural work was created not only to carry the symbol or to be used solely as a place to live but it contains deeper meaning than just as a shelter for humans. In traditional society, architecture is always associated with religious things. Religious matters, something that is considered sacred are the main considerations in the preparation of architectural patterns.

2.3. Spaces

A field that is developed will turn into space. Space in a three-dimensional concept has length, width and height. Space consists of points (where several fields meet), lines (where the two fields intersect) and fields (as boundaries of space), so that shapes are created. Form is the main feature that shows a space, determined by the appearance and relationship between fields that explain the boundaries of space. A space can be solid (space has mass), or empty space (space is inside or limited by fields). The visual characteristics are (1) appearance (the result of a certain configuration of surfaces and sides of a shape), (2) dimensions (determining proportions and scale), (3) color (affecting the visual weight of a shape), (4) texture (affects the quality of reflection of light on the surface of the shape), (5) position (relative position of a shape to the environment), (6) orientation (determines the direction of view), (7) visual inertia (degree of concentration and stability of a form; inertia of a shape depends on the geometry and its orientation relative to the base plane). These visual characteristics will always be influenced by the perspective or perspective of the observer, the distance of the observer to the shape, the lighting conditions, and the visual environment that surrounds the shape [3].

2.4. Spatial pattern

Architecture not only takes the form and appearance of a building, but also includes the space where each activity takes place. The need for public and private spaces is one of the determinants in the formation of spatial patterns or structures.

Space occurs because of the relationship between humans and the objects they see, and the relationship is not only determined by sight, but is also influenced by smell, hearing, and touch. Most human activities occur outdoors. Outer space occurs by limiting nature, separated from nature by giving a "frame", so it is not nature itself that can expand infinitely. Outer space also means as a man-made outer environment with a specific purpose, it can be said of a space as part of nature. The part that is limited by the "frame" when we look inward, then the space inside the "frame" is referred to as positive space, in which there are functions, intentions and human will. Outer space is limited by two areas, namely floors and walls or space that occurs using two limiting elements [4].

2.5. Function

In architecture-interior, use and image become very important in creating the atmosphere of space. Building in the form of inanimate objects does not mean soulless. The house built is a human home. Therefore it is something that is actually always being breathed on by human life, character, lust and ideals. The house represents the image of the builder [5].

In the context of use which refers to profit, the use of pleasure, comfort and security, the main function of a house is as a residential space that accommodates domestic activities. In essence, architectural-interior works are valued for giving satisfaction to social and personal needs, used in a number of ways that are useful or functioning for human life [6].

2.6. Meaning

In relation to the taxonomy of meaning, C.K. Ogden and I.A. Richards, in The Meaning of Meaning, identified at least 23 'meanings' of the word 'meaning'. There are fundamental differences in the use of the concept 'meaning' in various scientific fields. The meaning in aesthetic context is different from the meaning of meaning in symbolic context. Phenomenology uses the word meaning in terms of 'essence' or 'essence' of something; psychoanalysis uses the word meaning to explain 'will' and 'desire'; then aesthetics use it to explain the specific emotional levels involved in a work; hermeneutics sees meaning as a product of the interpretation of a text; symbolic relates to the unique relations between an object and the 'world'; and semiotics uses the term meaning to explain the 'concept' (signified) behind the sign [7].

3. Research Methods

3.1. Type of research

In this qualitative study, the role of researchers was as a key instrument in collecting and interpreting data. Data collection tools used direct observation, interviews and document studies. Triangulation with inductive methods was used to check the validity and reliability of the data. The results of qualitative research emphasize more on meaning than generalization [8].

Research on the architecture of *Towani Tolotang's* traditional house, especially micro spatial patterns, functions and their meaning are relevant with qualitative research because they meet the characteristics of it. This was indicated in the in-depth data disclosure through interviews, observations and document reviews of what the informants were doing, arranging and functioning the space in the houses of the *Towani Tolotang* community.

The method used in this research is the naturalistic phenomenology method. Phenomenology is a thought that not only looks at everything from the outside but tries to explore the meaning of what is behind the phenomenon [9].

The phenomenological method seeks to illustrate the meaning of the life experiences of several individuals regarding the concept of the phenomena they experience, where adherents of phenomenology try to study the structure of consciousness in individual experiences.

Based on the above understanding, with this research, the researcher intended to obtain all information regarding the traditional houses of the *Towani Tolotang* community, especially the micro spatial patterns, functions and reasons. All facts, desires, prejudices, which were obtained by interacting directly with informants namely the *Towani Tolotang* community who were then used in analyzing the phenomena that occurred. This research was conducted in May until July 2019.

3.2. Research objects

The object of research is something that is of concern in a study, the object of this study is the target in research to get answers and solutions to problems that occur. As for Sugiyono explained the understanding of the object of research is a scientific target to obtain data with specific goals and uses about something objective, valid and reliable about a thing (certain variables) [10].

The object under study was the traditional house of *Towani Tolotang* which was the residence of the Tolotang community leader called *Uwa'*. This research focused on the concept of micro-spatial pattern of functions and meaning of traditional houses. In the *Towani Tolotang* community there are two classes of social strata, namely ordinary people and *Uwa'* (community leader). The *Towani Tolotang* community has several *Uwa'*, but in this study the researchers purposely selected eight *Uwa's* houses that had the most influence on the community as samples. Those *Uwa'* has many adherents and was considered an elder by the *Towani Tolotang* community. Of the eight *Uwa's* houses to be investigated, only five *Uwa'* were willing to provide information about their traditional house using interview and documentation methods.

3.3. Data collection techniques

a. Observation, the observation technique used was unstructured observation studies. At the beginning of a study, it is possible that the observer does not have a clear idea of certain aspects that require focus. In observing events as they are can also be part of the plan in many qualitative studies (qualitative study). In that case, the observer will note practically everything that is observed. Such studies are unstructured observational studies.

b. The interview is part of a qualitative method. In this study the authors used in-depth interview techniques. In-depth interview is the process of obtaining information for research purposes by way of question and answer face to face between the interviewer and the respondent or interviewee, with or without using interview guides where the interviewer and the informant are involved in relative social life long time ago [11]. The special feature of this in-depth interview is its involvement in the life of the key person.

c. Document study is a data collection method that is not addressed directly to the research subject. Document study is a type of data collection that examines various kinds of documents that are useful for analysis material. Some data was obtained from the Amparita Village office and the Religious Affairs Office of Amparita, as well as the community leader of *Towani Tolotang*.

3.4. Data analysis techniques

a. Data Reduction, was the process of selecting, focusing on simplifying, extracting, and transforming rough data arising from written records in the field. Where after researchers obtained data, feasibility should first be assessed by selecting which data was really needed in this study.

b. Display (Data Presentation), the presentation of data was limited as a collection of arranged information that was adjusted and clarified to facilitate researchers in mastering data and not immersed in a pile of data.

c. Conclusions was the final stage in the research process to give meaning to the data that had been analyzed. The data processing process began with structuring field data (raw data), then reduced in the form of unification and data categorization.

3.5. Data validity check

The validity of the data is the truth of the data can be trusted because of the consistency of the procedure and the neutrality of its findings and decisions [12]. The validity tests of the data seem carried out is the credibility test (degree of trust), then using the inspection technique that is triangulation.

In this study, researchers used triangulation techniques with sources and methods. In the technique of triangulation with sources, the researcher compared the results of interviews obtained from each source or research informant: the community, customary officials, or '*panrita bola*' of traditional house of *Towani Tolotang* as a comparison to check the truth of the information obtained. In addition, researchers also checked the degree of trust through triangulation techniques with methods, namely by checking the results of research with different data collection techniques: interviews, observations, and document studies so that the degree of data confidence can be valid.

4. Discussion

4.1. Specific review of research locations

The *Towani Tolotang* community has a traditional leader or stakeholder, namely *Uwa'*. Based on the results of data collection at the study site, information was obtained that some of *Uwa'*s houses 'which had the most influence on the community, namely *Uwa'* which had many adherents and were considered as elders by the *Towani Tolotang* community. These *Uwa'* were chosen based on their status in the society which has a high position in the sense that they are descendants of the previous *Uwa'*, then have the courage to act, are honest, just, wise and authoritative, and are chosen based on the decision of the custom assembly.

In this study, the researchers were directed to eight of *Uwa'*s houses which had the most influence on the community, but of the eight *Uwa'* only five were willing to share information using interview and documentation methods. The five *Uwa'* are *Uwa'* Tadang, *Uwa'* Eja, *Uwa'* Jappi, *Uwa'* Sikki, and *Uwa'* Cina'.

Figure 1. Map of *Uwa'* Point House in Amparita

The a map of *Uwa'*s house point in Amparita Village, can be seen in Fig. 1. The *Uwa'*s House which is willing to be interviewed marked in orange, while the *Uwa'*s House which is not willing marked in purple.

Based on observations at the research location, only five *Uwa'* were willing to be interviewed and to provide information about the *Towani Tolotang's* traditional house. Their houses were then used as samples to get the characteristics of the micro spatial pattern, function and meaning of the *Towani Tolotang's* traditional house.

a. *Uwa'* Tadang (Sample 1)

Figure 2 is a view and space in the house of Uwa' Tadang. Figure 3 is the vertical relationship pattern of *Uwa'* Tadang's house, which starts from the *awa bola* (under the house), then goes up to the *ale bola* (the body of the house), then goes up to the *rakkeang* (attic).

Figure 2. *Uwa'* Tadang's House

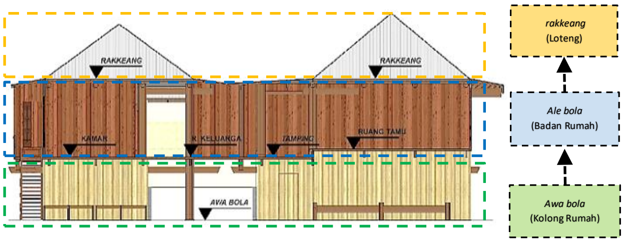

Figure 3. Vertical Relationship Pattern of *Uwa'* Tadang's House

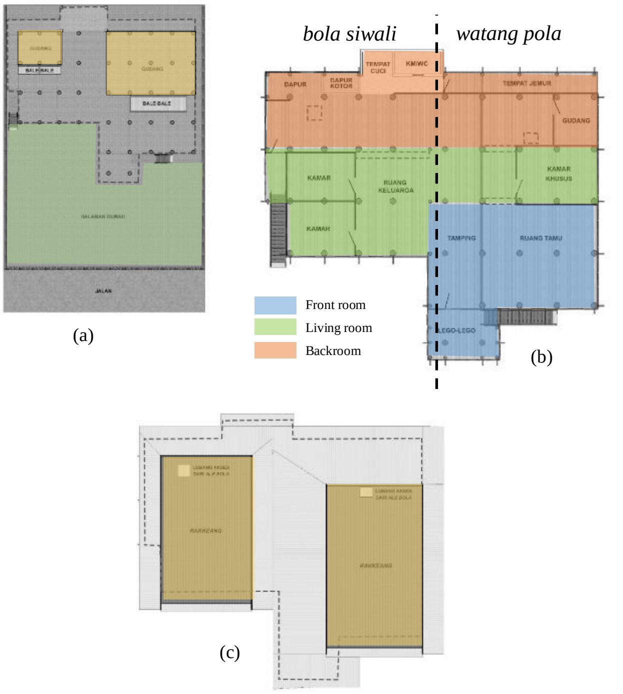

Figure 4. Horizontal Relations Pattern of *Uwa'* Tadang's House
(a) *awa bola*, (b) *ale bola*, (c) *rakkeang*

Shown in Fig. 4, part (a) is the spatial pattern of *Uwa'* Tadang's house, where there is a yard area marked in green, then underneath the house is a warehouse for farming equipment and other tools marked in orange.

Part (b) is the zoning and spatial pattern of *Uwa'* Tadang's house. *Uwa'* Tadang's House consists of *watang pola* and *bola siwali*. In the house there are three zones, the first of which is blue front, consisting of *lego-lego* as a place to wait for guests, living room and *tamping*, where the position of *tamping* is lower than the room guests are intended as a tribute to the customary holders, because ordinary people can only sit on the *Tamping*. Then the green color is the middle part, consisting of the bedroom, family room and special room as a place of ritual and pray, where the special room is placed right on the *possi bola* (home center), the position of the *bola* is one of the sacred and considered sacred parts of the house, so this room is also considered sacred. Then the red color is the back, consisting of a warehouse, kitchen, bathroom/toilet, washing place, and a clothesline.

Part (c) is the layout pattern of *rakkeang* (attic) of the house of *Uwa'* Tadang's used for storing harvests. The house is marked in orange.

b. *Uwa'* Eja (Sample 2)

Figure 5 shows a view and space in the house of *Uwa'* Eja. Figure 6 shows is the vertical relationship pattern of *Uwa'* Eja's house, which is the same as the previous *Uwa'*s house which was preceded by *awa bola* (under the house), then up to the *ale bola* (body of the house), then up to *rakkeang* (attic).

In Fig. 7, part (a) is the spatial pattern of *Uwa'* Eja's house, where there is a yard area marked in green, then underneath the house there is a warehouse for farming equipment and other tools marked with orange color.

Part (b) is the zoning and spatial pattern of *Uwa'* Eja's house. The *Uwa'* Eja's house only consists of *watang pola* and has no *bola siwali*, in the house there are three zones, the first of which is the blue color in the front, consisting of *lego-lego* as a place to wait for guests, living rooms and *tamping*, where *tamping* positions are more lower than the living room is intended as a tribute to the customary holder, because ordinary people can only sit on *tamping*. Then the green color is the middle part consisting of a special room as a place of ritual and praying, where the special room is placed right on the *possi bola* (center of the house), the *possi bola* is one of the sacred parts of the house, so this room is also considered sacred. Then the red color is the back, consisting of the family room, storeroom, kitchen, bathroom/ toilet, washing area, and clothesline.

Section (c) is the spatial layout pattern (attic) of *Uwa'* Eja's house which is used to store the harvest. In that house the shelves are marked in orange.

Figure 5. *Uwa'* Eja's House

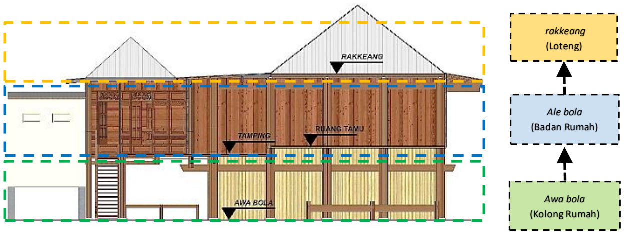

Figure 6. Vertical Relationship Pattern of *Uwa'* Eja's House

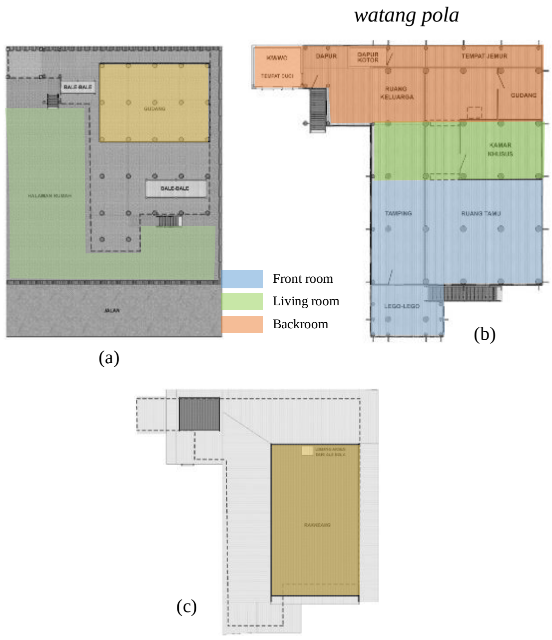

Figure 7. Horizontal Relations Pattern of *Uwa'* Eja's House
(a) *awa bola*, (b) *ale bola*, (c) *rakkeang*

c. *Uwa'* Jappi (Sample 3)

Figure 8 is a view and space in the house of *Uwa'* Jappi. Figure 9 is a vertical relationship pattern of *Uwa'* Jappi's house, which is the same as the previous *Uwa'*s house which was preceded by *awa bola* (under the house), then up to the ale ale (home body), then up to *rakkeang* (attic).

In Fig. 10 above part (a) is the spatial pattern of *Uwa'* Jappi's house, where there is a yard area marked in green, then underneath the house is a storage room for farming equipment and other tools marked in orange.

Section (b) is the zoning and spatial pattern of *Uwa'* Jappi's house. *Uwa'* Jappi's house consists of *watang pola* and *bola siwali*, in the house there are three zones, the first of which is blue as the front area, consisting of *lego-lego* as a place to wait for guests, living room and *tamping*, where the position of *tamping* is lower than the living room is intended as a tribute to the customary holders, because ordinary people can only sit on the *tamping*. Then the green color is the middle part consisting of a special room as a place of ritual and praying, where the special room is placed right on the *possi bola* (center of the house), the *possi bola* is one of the sacred parts of the house, so this room is also considered sacred. Then the red color is the back, consisting of the family room, storeroom, kitchen, bathroom / WC, washing area, and clothesline.

Figure 8. *Uwa'* Jappi's House

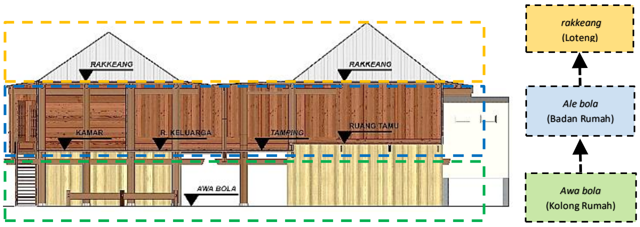

Figure 9. Vertical Relationship Pattern of *Uwa'* Jappi's House

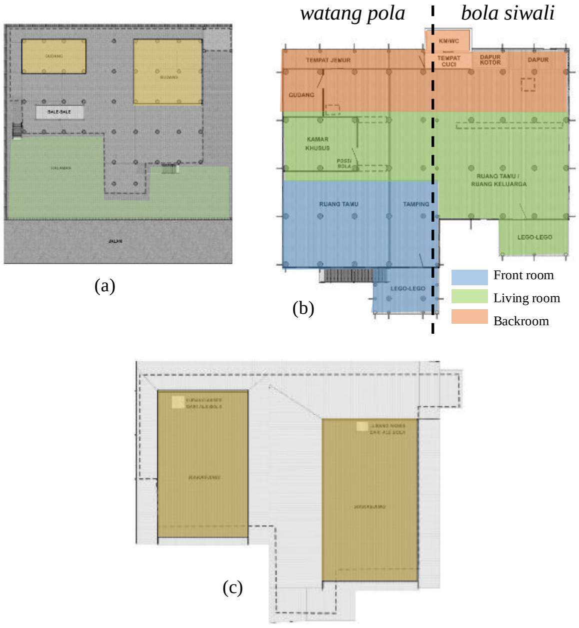

Figure 10. Horizontal Relations Pattern of *Uwa'* Jappi's House
(a) *awa bola*, (b) *ale bola*, (c) *rakkeang*

Section (c) is the spatial pattern of the *Rakkeang* (attic) of *Uwa'* Jappi's house which is used to store the harvest. The house is marked in orange.

d. *Uwa'* Sikki (Sample 4)

Figure 11 is a view and space in the house of *Uwa'* Sikki. Figure 12 is the vertical relationship pattern of *Uwa'* Sikki's house, which starts from the *awa bola* (under the house), then goes to the *ale bola* (body of the house), then goes up to the *rakkeang* (attic).

Figure 11. *Uwa'* Sikki's House

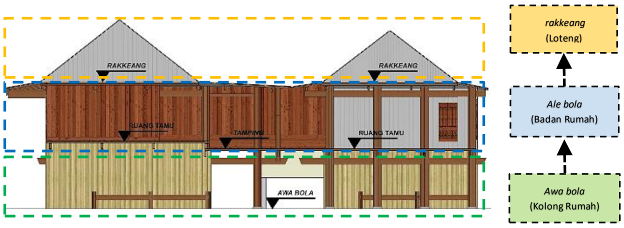

Figure 12. Vertical Relationship Pattern of *Uwa'* Sikki's House

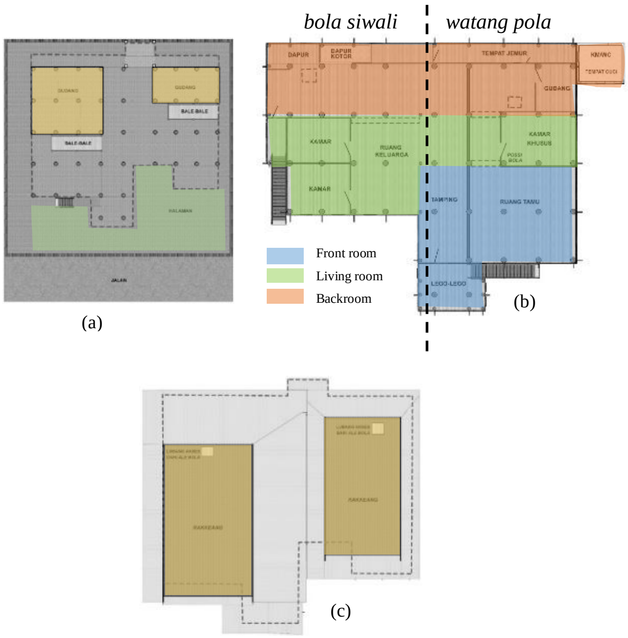

Figure 13. Horizontal Relations Pattern of *Uwa'* Sikki's House
(a) *awa bola*, (b) *ale bola*, (c) *rakkeang*

In Fig. 13 part (a) is the spatial pattern of *Uwa'* Sikki's house, where there is a yard area marked in green, then underneath the house is a storage room for farming equipment and other tools marked in orange.

Section (b) is zoning and spatial pattern of *Uwa'* Sikki's house. *Uwa'* Sikki's house consists of *watang pola* and *bola siwali*. In the house there are three zones, the blue one is the front, consisting of *lego-lego* as a place to wait for guests, living room and *tamping*, where the position of *tamping* is lower than the living room is intended as a tribute to the customary holders, because ordinary people can only sit on the *tamping*. Then the green color is the middle part consisting of a special room as a place of ritual and praying, where the special room is placed right on the *possi bola* (center of the house), the *possi bola* is one of the sacred parts of the house, so this room is also considered sacred. Then the red color is the back, consisting of the family room, storeroom, kitchen, bathroom/WC, washing area, and clothesline.

Figure 14. *Uwa'* Cina's House

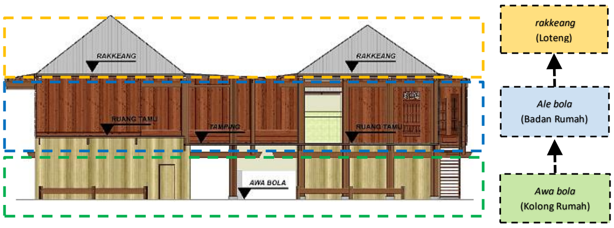

Figure 15. Vertical Relationship Pattern of *Uwa'* Cina's House

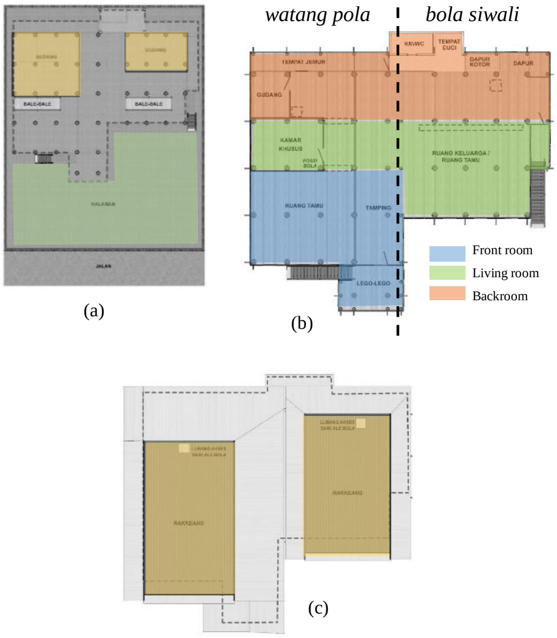

Figure 16. Horizontal Relations Pattern of *Uwa'* Cina's House
(a) *awa bola*, (b) *ale bola*, (c) *rakkeang*

Part (c) is the layout pattern of the *rakkeang* (attic) of *Uwa'* Sikki's house which is used to store the harvest. In that house the shelves are marked in orange.

e. *Uwa'* Cina' (Sample 5)

Figure 14 is a view and space in the house of *Uwa'* Cina'. Figure 15 is the vertical relationship pattern of *Uwa'* Cina's house, which starts from the *awa bola* (under the house), then goes to the *ale bola* (body of the house), then goes up to the *rakkeang* (attic).

Figure 16 part (a) is the spatial pattern of *Uwa'* Cina's house, where there is a yard area marked in green, then underneath the house is a storage room for farming equipment and other tools marked in orange.

Part (b) is the zoning and spatial pattern of *Uwa'* Cina's house. The *Uwa'* Cina's house consists of *watang pola* and *bola siwali*. In the house there are three zones, the first of which is the blue color in the front, consisting of *lego-lego* as a place to wait for guests, living rooms and *tamping*, where *tamping* positions is lower than the living room is intended as a tribute to the customary holder, because ordinary people can only sit on *tamping*. Then the green color is the middle part consisting of a special room as a place of ritual and praying, where the special room is placed right on the *possi bola* (center of the house), the *possi bola* is one of the sacred parts of the house, so this room is also considered sacred. Then the red color is the back, consisting of the family room, storeroom, kitchen, bathroom / WC, washing area, and clothesline.

Part (c) is the layout pattern of the *rakkeang* (attic) of *Uwa'* Cina's house which is used to store the harvest. In that house the shelves are marked in orange.

In the five sample images above, it can be seen the spatial pattern in the *Towani Tolotang* traditional house, vertically all samples have the same pattern because indeed the *Towani Tolotang* traditional house is a stilt house. The pattern starts from the *awa bola* (under the house), then goes up to the *ale bola* (the body of the house), then goes up to the *rakkeang* (attic).

Horizontally, the spatial pattern of the *Towani Tolotang* traditional house as a whole from the sample also has the same pattern. Starting from the *awa bola* (under the house) both in the *watang pola* and *bola siwali* there is a yard and a warehouse to store farming equipment.

In the ale section of *ale bola* or body of the house as a whole of the sample also has the same pattern. In the *Watang pola* or the main house, starting from the front there are *lego-lego* as a place to wait before entering the house, then entering the house there is a living room and *tamping*, then there is a special room right on the *possi bola*, then at the rear there is a warehouse, buffer, bathroom/toilet and washing area, as well as a clothesline. On the *bola siwali* or side / additional house consisted of several rooms and family gathering rooms, but there were also those who do not make rooms in the *bola siwali*, only left empty in order to receive more guests when there are traditional activities. There was a slight difference, in the sample 2 *Uwa'* Eja's house there was no *bola siwali*, then in sample 1 *Uwa'* Tadang's house and sample 3 *Uwa'* Jappi house, the *bola siwali* position is in the south while in sample 4 *Uwa'* Sikki's house and sample 5 *Uwa'* Cina's house the *bola siwali* position was in the north. Although different positions, the spatial pattern of *Towani Tolotang's* traditional houses from the whole sample remains the same.

At the top of the house there is a *rakkeang* or attic that is commonly used to store crops, to access it is made a hole in the ceiling of the house. Both *watang pola* and *bola siwali* have *rakkeang*. All of the samples have the same pattern in the *watang pola* and *bola siwali*.

Overall, based on observations, direct observations and interviews with customary leader (*Uwa'*), that all *Towani Tolotang's* traditional houses have the same house form. There is a slight difference in the location or position of the *bola siwali*. However, according to *Uwa'*, there are no specific rules or provisions regarding the rotation or direction of the house, everything is adjusted from the site and surrounding environment. Then there is also the *Uwa'* house 'which does not have a *bola siwali* because they lack of land to build and also that they live close to other families such as their parents or siblings. For the spatial planning patterns in the *Towani Tolotang's* traditional house, everything is almost the same. There is a slight difference in the living room, there are some *Uwa'* houses which do not add rooms to the *bola siwali* with the reason to get more space when there are traditional activities and invite many guests or families.

4.2. *Characteristics of Micro spatial patterns, functions and meanings in the Towani Tolotang's traditional house.*

Table 1 presents a characteristics of micro spatial patterns, functions and meanings of the *awa bola* (underneath) *Towani Tolotang's* traditional house. In the table there are zoning spaces that indicate the position and nature of space, there are also classifications that indicate the characteristics or specific properties of space. In the table can be seen that there are two spaces as characteristics of the house: yard and farm equipment storage. Then in the table there is a description of the function and meaning of each space.

Table 1. Characteristics of micro spatial patterns, functions and meanings on *awa bola* (under the house) of *Towani Tolotang's* traditional house

No.	Room	Zoning	Classification		Function	Meaning
			C	S		
1.	Yard	Public	✓		used as a place to park family's or guest's vehicle.	-
2.	Warehouse	semi-Public	✓		used as a place to store farming equipment and other working tools.	-

C : Characteristics
S : Specific

In Table 2 the characteristics of micro spatial patterns, functions and meanings are summarized on the ale ale (house body) of *Towani Tolotang's* traditional house. In the table there are zoning spaces that indicate the position and nature of space, and there are also classifications that indicate the characteristics or specific properties of space. In the table can be seen that there are nine spaces that become the characteristics: *lego-lego*, *tamping*, living room, family room, special room, warehouse, kitchen, bathroom/toilet and washing area and clothesline, then there is one specific room, namely bedroom because there is *Uwa'* house that does not have a bedroom for his own reasons. In *Towani Tolotang's* traditional house, there are two spaces as characteristics that have differences with the Bugis's houses in general, *tamping* and special rooms. *Tamping* is used as a place to receive regular community guests. There is difference in height between *tamping* and the living room. Every *Towani Tolotang's* traditional house also has a special room as a place of ritual and prayers, where the special room is placed right on the *possi bola* (center of the house), the *possi bola* is one of the sacred and considered sacred parts of the house, so this room is also considered sacred. Then in the table there is a description of the function and meaning of each space.

Table 2. Characteristics of micro spatial patterns, functions and meanings on *ale bola* (the body of the house) of *Towani Tolotang's* traditional house

No.	Room Name	Zoning	Classification		Function	Meaning
			C	S		
1.	*Lego-lego*	Public (Front room)	✓		Places to wait for guests who will come to visit or where guests wait until the host comes out to entertain.	*Lego-lego* is there because at the *Towani Tolotang's* traditional house, each new guest or ordinary community must get permission before entering and not indiscriminately entering the house.
2.	Living room	semi-Public (Front room)	✓		as a room to receive honored guests or close family, sometimes also used for tudang sipulung activities.	- No chair or table in the living room means a sense of togetherness and intends to further kinship. - The position of the living room is higher than *tamping* to distinguish the position of *Uwa'* and its people, meaning respect for customary leaders.
3.	*Tamping*	semi-Public (Front room)	✓		A place to receive guests with the status of ordinary people in the *Towani Tolotang* community.	The position of *tamping* is lower than the living room, ordinary people can only sit on *tamping*, the behavior of people on functioning *tamping* is a meaningful symbol as a people's appreciation to their leader (*Uwa'*).
4.	Room	Privat (Living room)		✓	As a room for resting and sleeping, it is usually used for *Uwa'* and girls or children of *Uwa'* who are married who still live with their parents.	-
5.	Family room	semi-Public (Living room)	✓		as a family gathering room and also used to relax.	-
6.	Special room	Privat (Living room)	✓		used as a place of ritual and pray for the people of *Towani Tolotang*.	special room is placed right on the *possi bola* (center of the house), *possi bola* is one part of the house that is sacred and considered sacred, so this room is also considered sacred.
7.	Warehouse	Privat (Living room)	✓		used for storing household goods and equipment.	-
8.	Kitchen	Service (Back room)	✓		used for cooking activities for women, but also a place to store kitchen equipment.	the kitchen is always placed in the back of the house because it is privacy and many activities of woman are there.

9.	Bathroom / TOILET, Washing area	Service (Back room)	✓		used for clean-up, defecate and shower. There is also a washing area on the front or side,	-
10.	Drying area	Service (Back room)	✓		used for drying clothes or other equipment.	-

C : Characteristics
S : Specific

Table 3. Characteristics of micro spatial patterns, functions and meanings on *rakkeang* (attic) of *Towani Tolotang's* traditional house

No.	Room Name	Zoning	Classification		Function	Meaning
			C	S		
1.	*Rakkeang (loteng)*	Privat	✓		used as a place to store crops such as rice, corn and other objects.	*Towani Tolotang's* belief that *rakkeang* is considered as the world above or close to the sky and the creator so that it is considered sacred.

C : Characteristics
S : Specific

Table 3 is a characteristics of micro spatial patterns, functions and meanings of the *Towani Tolotang's* traditional house. In the table there are zoning spaces that indicate the position and nature of space. There are also classifications that indicate the characteristics or specific properties of space. In the table, it can be seen that there is one room being the characteristics, namely *rakkeang* (attic), a place to store harvests. Then in the table there is a description of the function and meaning of space.

5. Conclusions and Suggestions

5.1. Conclusion

The first, *Towani Tolotang's* traditional house is in the form of a stilt house like Bugis's houses in general, so that the vertical spatial pattern of *Towani Tolotang's* traditional house is vertically started from *awa bola* (under the house), then goes up to *ale bola* (home body), then goes up to *rakkeang* (attic).

The characteristics of the micro spatial pattern of the *Towani Tolotang's* traditional house horizontally is in the *awa bola* (under the house). There are two spaces: the house yard and the warehouse. Then in the *ale bola* (home body) is divided into three parts, namely *lontang risaliweng* (front room), *lontang ritengnga* (front room) and *lontang rilaleng* (back room). In *lontang risaliweng* (front room) there are three spaces namely *lego-lego*, *tamping,* and living room. In *Lontang ritengnga* (living room) there are three rooms, namely bedroom, family room, and special room, but the bedroom is specific because there are some *Uwa'* houses that do not use the bedroom for some reasons. In the *lontang rilaleng* (back room) there are four rooms namely warehouse, kitchen, bathroom/toilet and washing area, as well as a clothesline. Then the very top of the house is a *rakkeang* (attic). In *Towani Tolotang's* traditional house there are two spaces as characteristics that make it different from the Bugis's houses in general: *Tamping*, a place to receive ordinary guests which is different in height with the living room, and the existence of a special room as a place of ritual and pray.

The second matter concerns the function of space in the traditional house of *Towani Tolotang*. Every room in the *Towani Tolotang's* traditional house has a general function like the Bugis's houses in general. However, there are two rooms that have a special function in the *Towani Tolotang's* traditional house, namely the *tamping* which has a function as a place to receive guests with ordinary community status in the *Towani Tolotang* community. Then there is a special room that is used as a place of ritual and pray for the people of *Towani Tolotang*.

The third matter concerns the meaning of space in *Towani Tolotang* traditional house. In *Towani Tolotang* traditional house, not all rooms have special meanings, but there are six rooms that have their own meaning related to the spatial planning. Space that has a special meaning, namely; 1) *lego-lego*, in the *Towani Tolotang's* traditional house, there are *lego-lego* where every new guest or ordinary community must get permission and not just enter the house; 2) *tamping*, *tamping* position is lower than the living room because ordinary people in the *Towani Tolotang* community are only allowed to sit in *tamping*, the behavior of the people on functioning *tamping* is a meaningful symbol as a people's appreciation to their leader (*Uwa'*); 3) the living room, does not have a chair or table that has a sense of togetherness and intends to establish more kinship; 4) special room, this room is placed right on the *possi bola* (center of the house), *possi bola* is one of the sacred parts of the house and is considered sacred, so this room is also considered sacred; 5) kitchen, this space is always placed at the back of the house because it is privacy and there are many activities for women; and 6) *rakkeang*, the *Towani Tolotang* community's belief that *rakkeang* is considered to be the world above or near the sky and the creator so that its nature is considered sacred.

5.2. Suggestions

Based on the results of research that has been done, suggestions that can be submitted in this study are as follows:

1. *Towani Tolotang's* traditional house architecture is the brainchild of the *Towani Tolotang* community, especially in Amparita which must be preserved as part of regional culture as well as one of the diversity and cultural richness of the Indonesian people.
2. The implied values in the *Towani Tolotang* traditional house should be used as guidelines to maintain and strengthen solidarity for the *Towani Tolotang* community.

In this research, it is undeniable that there are still many shortcomings so it is deemed necessary to be developed further and more in-depth studies on the *Towani Tolotang* traditional house from other aspects and perspectives that can be carried out.

References

[1] D. Sumintardja, *Kompedium Sejarah Arsitektur*, 1st ed. Bandung: LPBM, 1975.

[2] A. Rapoport, *House, Form and Culture*. New Jersey: Prentice-Hall, Inc., 1969.

[3] Ching and D. K. Francis, *Bentuk*, *Ruang dan Susunannya*. Jakarta: Erlangga, 1999.

[4] S. Gunadi, *Merencana Ruang Luar*. Surabaya: ITS, 1984.

[5] Mangunwijaya, *Wastu Citra*. Jakarta: PT. Gramedia, 1992.

[6] Feldman and E. Burke, *Art as Image and Idea*. New Jersey: Prentice-Hall, Inc., 1967.

[7] Piliang and Y. Amir, “Pluralitas Bahasa Rupa: Membaca Pemikiran Primadi Tabrani,” *J. Ilmu Desain*, vol. 1, no. 1, 2006.

[8] Moleong and J. Lexy, *Metodologi Penelitian Kualitatif*. Bandung: PT. Remaja Rosda Karya, 2000.

[9] Wirawan, *Evaluasi: Teori*, *Model*, *Standar*, *Aplikasi*, *dan Profesi*, Depok. Pt. Raja Grafindo Persada, 2012.

[10] Sugiyono, *Metode Penelitian Kuantitatif*, *Kualitatif*. Bandung: CV. Alfabeta, 2017.

[11] Sutopo, *Metodologi Penelitian Kualitatif*. Surakarta: UNS, 2006.

[12] Moleong and J. Lexy, *Metodologi Penelitian Kualitatif*. Bandung: PT. Remaja Rosda Karya, 2007.

EPI International Journal of Engineering
Volume 3, Number 1, February 2020, pp. 69-73
DOI: 10.25042/epi-ije.022020.10

*p*ISSN 2615-5109
*e*ISSN 2621-0541

Study on Facility Development of Maccini Baji Port as a Minor and Hub Port for Small Island Connectivity

Akbar[a], Misliah[b], Andi Siti Chairunnisa[c], Suandar Baso[d,*]

[a]Department of Naval Architecture, Engineering Faculty, Hasanuddin University. Email: akbarmakmur80@gmail.com
[b]Department of Naval Architecture, Engineering Faculty, Hasanuddin University. Email: misliahidrus@yahoo.co.id
[c]Department of Naval Architecture, Engineering Faculty, Hasanuddin University. Email: andi.chairunnisa@yahoo.co.id
[d]Department of Naval Architecture, Engineering Faculty, Hasanuddin University. Email: s.baso@eng.unhas.ac.id

Abstract

Maccini Baji port as minor port is a hub of small islands connectivities in Pangkejene and Kepulauan Regency, South Sulawesi. It has strategic role to serve cargo and passenger ship from not only small islands in Pangkejene and Kepulauan Regency but also from outside such as Papua, Maluku, and Nusa Tenggara Timur. Correspondingly, Maccini Baji port has faced the fluctuated increase of visited ships from 2011 to 2018 based on forecasting result by using stepwise and regression methods and has a good potential to be developed especially for cement cargo. This study describes analysis on port facility performance of Maccini Baji and its development. The research result has shown the berth occupancy ratio (BOR) of Maccini Baji port in 2022 will reach 61%. This has become a primarily point to consider in lengthening berth of Maccini Baji port. Therefore, the port berth of Maccini Baji should be lengthened 272 meters where existing berth length is 225 meters. In addition, basin and anchorage area will be also developed where the dimensions of turning basin will be 6 meters in depth, 121.8 meters in diameters, and its area will be 116 m^2. The dimensions of anchorage area will be 6 metres in depth, and 105.9 meters in radius and its area will be 35.21 m^2. Based on SWOT analysis, some aspects will be considered to succesfully develop Maccini Baji port such as geographic location, port facility improvement, increas of service capacity and facility efficiency, development of hinterland area, local government participation.

Keywords: Maccini Baji port; minor port; port development; port facility; small island connectivity

1. Introduction

The port is a node of the sea-to-land transportation system which is an economic unit whose role is to stimulate the growth and development of trade or the economy consisting of storage, distribution, processing, marketing, and others. Inland waterways and maritime transport network consist of two equally important elements i.e. links and nodes. For an efficient and reliable functioning of the transport network both elements must be equally developed and harmonized [1]. Correspondingly, port has a strategic role in enhancing the resources distribution and the port role today exceeds the simple function of services to ships and cargo. Apart from their role as the traditional sea, ports are a good location for value-added logistics but also for other related services including industrial, trade, financial, and even leisure and property development activities. Thus, the port system not only serves as an integral component of the transport system, but also is a major sub-system of the broader production, trade and logistics systems [2].

The enhancements or developments of ports have been done significantly and their required in-depth studies. Palmer investigated the main current trends affecting seaport development [3]. Similarly, several studies of port development have been done such investigation seaports, dry ports, and development corridors and its implication for regional development in India [4]. Dwarakisha and Salim studied the role of ports in the development of a nation [5]. Balasubramanian investigated the adverse effects of port development on coastal ecology and community in Ennore [6].

Regardless, the development of small size ports should be considered because a number of small size of ports in developing country are big and nowadays its function has a big essential and important. However, there are often thought to be playing a secondary part where their logistics and socio-economic role are still largely undefined and underestimated in literature and in policies. Moreover, their visibility is limited and their voice often weak [7]. Kuntoji G. and Rao S. has been reviewed the development of minor ports to improve the economy of developing country [8]. Based on these dicussion above, the development of small sized port is rarely discussed and

---

*Corresponding author. Tel.: +62 852 55625397
Jl. Poros Malino, Borongloe, Bontomarannu, Kabupaten Gowa, Sulawesi Selatan 921119

studied. Therefore, the study regarding the development of small sized port is widely needed to make more intrepretations.

In present study describes the development of Maccini Baji port where the port's facilities are in extremely poor condition and capacity limitations. Despite having poor conditions, the calling ships in Maccini Baji port are increasing in 2011 to 2018. By those reasons, Maccini Baji port has been improved its operations as a minor port and hub for small island connectivity by lengthening its berth port due to over berth occupancy.

One of small sized ports in South Sulawesi is Maccini Baji port which is located in Pangkajene and Kepulauan Regency with latitude longitude coordinates 4°46' and 119°29'. The location of Maccini Baji port is shown in Fig. 1. Based on the minister of transportation's decree No. KP 432/2017, the hierarchy of Maccini Baji port is set as a local feeder port.

2. Research Methodology

The present study discusses the facility development of a minor and hub port for small island connectivity. Here, the case study was addressed to Maccini Baji port. In order to obtain research results, several methods and steph have been systematically done as discussed below.

2.1. Data collection

Some data were collected and observed related with the development of Maccini Baji port (Fig. 1) such as socio demography, economic, hinterland, population, Gross Regional Domestic Product (GRDP), and land-use planning and others in Pangkejene and Kepulauan Regency. The data of trip generation were observed including ship type, people and cargo movement. Moreover, land transportation network, facilties and operation service of Maccini Baji port were observed as well.

2.2. Analysis step

The number of calling ships in Maccini Baji port was predicted and projected by using linear regression and stepwise models. This was investigated from 2011 to 2018 by using linear regresion model to show a tendency of the number calling ship in icreasing year. Furthermore, this was projected by using stepwise model from 2011 to 2034 taking into account population and GRDP. Here, linear regression and exponential growth were used also to compare their results based on the *coefficient* of *determination (*R squared).

Figure 1. The map of Maccini Baji port location in Pangkejene and Kepulauan Regency

Given data set of n statistical units, a linear regression model assumes that the relationship between the dependent variable and the independent variable. The model has the form as follow:

$$Y= a + bX \text{ ....(1)}$$

where Y is the dependent variable, X is the independent variable, b is the slope of the line (coefficient) and a is the Y-intercept (coefficient). Correspondingly, the utilization of port facility in Maccini Baji port was assessed using Berth Occupancy Ratio (BOR) formula to achieve reguired standardized level and optimum throughput related with available data and forecasting results. Then, the assessment result was verified by using port performance indicator of UNCTAD requirement. The berth port length was simulated by using some assumptions based on ship dimension and space need between ship related with forecasting results. Berth occupancy ratio shows the port service level which can be defined generally as given:

$$\text{BOR} = (T_0/T_t) \times 100\% \text{ .... (2)}$$

$$\text{BOR} = (n_s \times Ls + 10 \times n_t)/(L_b \times 24 \times d) \times 100\% \text{......(3)}$$

where, T_0 is total time which quay wall is occupied from berthing to un-berthing (vessel turnaround time) in the proposed time span. T_t is total time which quay wall is able to service in the proposed time span (working times). Moreover, n_s is a number of ships

Port facilities that are needed have been analyzed based on berth port, fairway/channel etc. The berth length is determined based on IMO regulation as given by:

$$L_p = L_{oa}\,(n + 1) + 10\%\, L_{oa} \text{ ....(4)}$$

where L_p is jetty length, L_{oa} is length overall of a ship, and n is a number of ships.

A number of ships that are moored in jetty could be calculated by using formula as follow:

$$A = (Cs \times BT)/(OT \times \text{BOR})\text{.......................................(5)}$$

where Cs is ship number for service (ship/year), BT is berthing time (hour/ship), BOR is berth occupancy ratio (Eq. 2), and OT is port operation time per year (hour).

2.3. Strategy for port development

In order to evaluate and develop Maccini Baji port, a strategy planning was made by using Strenghts, weaknesses, opportunities, and threats (SWOT) analysis. The internal and external factors that affect on Maccini Baji port were identified and assessed. Then, Maccini Baji port was determined its position and competition in creating a port strategic framework. The SWOT analysis is a square with each of the four areas making up one quadrant (I, II, III, and IV).

3. Results and Discussions

3.1. Existing facilities in Maccini Baji port

Table 1 shows the main facilities in Maccini Baji port. Recently, Maccini Baji port has no equipment to support loading-unloading activity from and/to dock, therefore, loading/unloading is still handled by human.

Nowadays, Maccini Baji port serves pioneer sea transportation which is organized by the Indonesia Government in providing operating subsidies to the pioneer fleet. The pioneer Papua Dua serves routes namely Liukang Tangayya between Balo-Baloang Island, Matalaang Island, Sapuka Island, and Sailus Island and Badas port in Nusa Tenggara Barat. On the other hand, sail-boat machine (Pelra) dominantly transport cement to Kaimantan Island. A number trip per year is 21 to 26 times and requires operation time 11 to 14 days.

Correspondingly, Maccini Baji port also has a mooring facility for wooden boats that serve transportation between islands araound Liukang Tupabbiring Utara. Table 2 shows calling ships from 2011 to 2018 which almost increased per year. However, it decreased in 2013 and 2016 and significantly increased in 2014, 2015, and 2018.

Table 1. Main facilities in Maccini Baji port

Type of Facility	Description
Dock	
-Concrete dock	Length = 225 mm, width = 8 mm
-Passenger Pontoon Pier	Length = 20 mm, width = 10 mm
Concrete Pier Trestle	Length = 250 mm, width = 6 mm
Gangway Terminal Passenger	Length = 125 mm, width = 4 mm
Causeway	Length = 190 mm, width = 6 mm
Warehouse of Deviations	Total = 3 units, area = 400 m^2
Stacking Field	Area = 253 m^2
Passenger Terminal	Amount = 1 Unit, Area = 300 m^2
Fire Fighting Facilities	Amount = 1 Unit, Area = 100 m^2
Equipment Maintenance Facilities	Amount = 1 Unit, Area = 200 m^2

Table 2. The calling ship number per year in Maccini Baji port

Year	Calling ship (set)
2011	332
2012	362
2013	343
2014	443
2015	599
2016	548
2017	580
2018	650

3.2. The performance of Maccini Baji port

Here, the performance of Maccini Baji port was analized taking into account the utiliztion of berth port, basin and anchorage area.

BOR of Maccini Baji port was analyzed based on ralated data, forecasting result of calling ship, and dock usage rate in evary year. In 2019, the berth lenght of Maccini Baji port is 225 meters and it could moore four ships in assuming 40.6 meters ship length, berthing time (BT) 24 hours, and 10 meters for space between ship. Referring to those assumptions, BOR was obtained 50% and this shows that BOR is still not optimum.

Meanwhile, the BOR of Maccini Baji port from 2019 to 2021 will reach 61% with four moored ships and space between ship as assumed similar with previous assumptions. This BOR shows higher magnitude than BOR standard given by UNCTAD requirement. This means that berth condition will be utilized fully and this will also affect on queue for other ships in case there is not berth development. For this reason, the berth port must be lenghtened.

Correspondingly, the forecasting of calling ship will increase from 2018 to 2034 and it will affect on berth utilization. However, BOR of Maccini Baji port will reach 61% in 2022, therefore, the berth of Maccini Baji port must be lengthened. As known, the existing berth lenght of Maccini Baji port is 225 m and it will be then lenghtened becoming 272 m or additing length 47 m to meet its BOR. In addition, the berth length in 272 m will also cover until 2034.

Moreover, other port facities were analized their utilization such as turning basin and anchorage area as well. Regarding to berth development, the basin and anchorage area will be developed as well. Therefore, the dimensions of turning basin will be 6 meters in depth, 121.8 meters in diameters, and its area will be 116 m2. In additions, the dimensions of anchorage area will be 6 metres in depth, and 105.9 meters in radius and its area will be 35.21 m2.

3.3. Strategy for the development of Maccini Baji port

In order to develop Maccini Baji port, the internal and external factors that effect on its port perfomance were indentified firstly as shown in Table 3 and 4. Then, the weight, rating, and score each element of internal and external factors was determined and obtained by questionnarie.

As explained on section methodology, the analysis that used in determinating the development of Maccini Baji port is SWOT method. Table 3 and 4 show the weight, rating, and score for each internal factor and external factor. The score of strength factor in internal factors shows higher comparing with weakness factor and this means that the internal factor has a sufficient strong or good potential for developing Maccini Baji port. The avergared total score of internal factors is 2.43.

Table 3. SWOT Matrix for the internal factors of Maccini Baji port

Internal Factors	Weight	Rating	Score
Strength			
1. Increasing the number of calling ship	1	3	3
2. Good strategic location as a hub for small island	1	4	4
3. Having regional area development	1	2	2
		Subtotal	9
Weakness			
1. Poor loading and unloading equipments	0	2	0
2. Limited depth basin and anchorage area	1	3	3
3. Less people mobility	1	2	2
4. High cost and time for port development	1	3	3
		Subtotal	8
Total Score			17
Average			2.43

Table 4. SWOT Matrix for the enternal factors of Maccini Baji port

External Factors	Weight	Rating	Score
Opportuny			
1. Having market share potential as a hub small islands	1	4	4
2. Goverment supporting for development	1	2	2
3. Having big population in island cluster, Pangket Regency	1	4	4
		Subtotal	10
Threat			
1. Advance technology development without high level of aexpertise	0.5	2	1
2. Regulation for serving large ship size	1	3	3
		Subtotal	4
Total Score			14
Average			2.8

On the other hand, the score of oppurtunity factor in external factor is higher also comparing with threat factor and this means that the oppurtunity of Maccini Baji port could minimize the threat which is faced now and next future. This situation has become proper for developing Maccini Baji port. The averaged total score of external factors is 2.80.

The position of internal and external factors in SWOT matrix for Maccini Baji port is in quadrant I where the opportunity and strenght factors are dominant. Therefore, Maccini Baji port could be developed for anticipating the increase of the calling ship in the future.

Maccini Baji port is experiencing significantly the increase of calling ship number, as well as it has a startegitc location as a hub for small islands. This has a potential of market share, regional area development, and government support.

The above discussion highlighted that the development of Maccini Baji port will be focused on service of loading-unloading activities and port facilities. This development is also as overhead capital to improve transportation service, economy production and distribution. Correspondingly, the followings are some aspects that will be considered in development startegy:

1. The geographic location of the ports is logistically most favorable.
2. Taking advantage of existing facilities and improving facility.
3. Increasing the capacity of service and facility efficiency.
4. Development of hinterland area.
5. Participating local government in developing Maccini Baji port.

4. Conclusions

Currently, the calling ships in Maccini Baji port was increasing significantly from 2011 to 2019 and this will affect that BOR of Maccini Baji port will reach 61% in 2022, however the existing facilities of Maccini Baji port are in extremely poor condition and capacity limitations. The study on the facility development of a minor port which is addressed to Maccini Baji port was successfully done.

Several main points will be concerned to develop Maccini Baji port as follows:

a. The berth will be lenghtened becoming 272 m or additing length 47 m from existing lenght to meet its increased BOR.

b. The basin and anchorage area will be also developed where the dimensions of turning basin will be 6 meters in depth, 121.8 meters in diameters, and its area will be 116 m2. The dimensions of anchorage area will be 6 metres in depth, and 105.9 meters in radius and its area will be 35.21 m2.

c. Based on SWOT analysis, some aspects will be considered to succesfully develop Maccini Baji port such as geographic location, port facility improvement, increas of service capacity and facility efficiency, development of hinterland area, local government participation.

References

[1] S. Jovanovic *et al.*, "Port Infrastructure and Industrial Development: Status of Port Infrastructure Development along the Danube," 2017.

[2] UNCTAD, "Assessment of a Seaport Land Interface: An Analytical Framework," 2004.

[3] S. Palmer, "Current Port Trends in an Historical Perspective," *J. Marit. Res.*, pp. 99–111, 1999.

[4] A. H. Kidwai and G. Kuzur, "Seaports, Dry Ports and Development Corridors: Implication for Regional Development in Globalising India," 2015.

[5] G. S. Dwarakisha and A. M. Salim, "Review on the Role of Ports in the Development of a Nation," in *International Conference on Water Resources, Coastal and Ocean Engineering, Aquatic Procedia 4*, 2015, pp. 295–301.

[6] B. Balasubramanian, "Challenges Towards Sustainable Port Development in India: The Adverse Effects of Port Development on Coastal Ecology and Community in Ennore, a case study," 2018.

[7] M. Simona, “A Cluster Initiative: Small and Medium Sized Ports as Hubs for Smart Growth and Sustainable Connectivity,” *Interreg IVA 2 Seas Programme, 2 Seas Magazine*, 2014.

[8] G. Kuntoji and S. Rao, “A Review on Development of Minor Ports to Improve the Economy of Developing Country,” in *International Conference on Water Resources, Coastal and Ocean Engineering Aquatic Procedia 4*, 2015, pp. 256–263.

EPI International Journal of Engineering
Volume 3, Number 1, February 2020, pp. 74-83
DOI: 10.25042/epi-ije.022020.11

*p*ISSN 2615-5109
*e*ISSN 2621-0541

Prediction of an Optimum Total Resistance Coefficient on Catamaran using Design of Experiment (DOE) Incorporated with CFD Approach

Ahmad Fitriadhy[a,*], Sun Yin Lim[b], Adi Maimun[c]

[a]School of Ocean Engineering, University Malaysia Terengganu. Email: naoe.afit@gmail.com
[b]School of Ocean Engineering, Universiti Malaysia Terengganu. Email: suyin101095@gmail.com
[c]Department of Aeronautics, Automotive and Ocean Engineering. University Technology Malaysia. Email: adi@utm.my

---

Abstract

In the presence of complex hydrodynamic interferences between two demihulls on a catamaran ship has been prone to have a reliable prediction to her optimum total resistance. To achieve this, the author presents a Computational Fluid Dynamic (CFD) modelling incorporated with Design of Experiment (DOE) approach. Several parameters such as effect of Froude number (F_r) with respect to various lateral separation ratios (S/L) of the catamaran have been taken into account. Here, the optimum total resistance coefficient (C_T) has been mainly set within the range of S/L ratio $0.2 \leq S/L \leq 0.4$ associated with Froude number $0.56 \leq F_r \leq 0.66$. The primary objective function of this optimization model has led towards minimizing a drag force and increased a lift force with respect to the above S/L ratios. In general, the simulation results had seemed quantitative similarity values for the optimum F_r of 0.6589, 0.6599 and 0.6596 with S/L ratios of 0.2, 0.3 and 0.4, respectively. In the case of F_r = 0.56, the optimum S/L ratios of 0.2993 and 0.3988 have resulted in insignificant reduction of C_T by 0.62% and 0.32% as compared to S/L of 0.3 and 0.4, respectively. Similarly, the optimum S/L ratios of 0.2750 and 0.3750 with F_r = 0.66 have led to reduce by 0.14% and 0.46% as compared to S/L of 0.3 and 0.4, respectively. This CFD simulation results are very useful as preliminary data for the optimised ship resistance, which is mainly required to predict a ship powering in the early design stage.

Keywords: Catamaran; Froude number; lateral separation ratio; optimization; total resistance coefficient

---

1. Introduction

A catamaran is a multi-hulled vessel featuring two parallel hulls of equal size. Catamaran's native nature accords some advantages such as speed, carrying capacity [1] better stability and hydrodynamic performance [2], [3]. Yet, catamaran ships encounter less resistance due to presence of lower draft as compared to demi hull ship [4].

Correspondingly, substantial amount of research has been carried out in late year to review the resistance characteristics of catamaran. This is necessary because resistance behavior of the catamaran is clearly different when compared to the demi hull ships [5], [6]. The effect of lateral separation ratio (S/L) between two demi hulls have revealed that the change of the lateral distance between two demi hulls on the catamaran contributed a significant effect to the resistance components [7]–[9]. This is supported by investigation of A. Fitriadhy that different S/L ratio having the significant different values of total resistance coefficient. His research showed that as Fr number increasing from 0.47 to 0.66, there are a significant loss of the total resistance coefficient. The unfavorable Froude number predominantly occurred at F_r = 0.47 regardless of S/L, which directly corresponds to arise in the peak total resistance coefficient [10], [11]. Hence, this region $0.47 \leq F_r \leq 0.66$ had become a great interest of area to be study. It is evident that a significant reduction in resistance could be achieved by finding the optimum position of stagger [12]. Experimental work in towing tank is relatively time-consuming, expensive and impractical for various resistance test configurations. Furthermore, optimization scheme unable to be achieve in towing work. But it is possible to be carried out with Computational Fluid Dynamic (CFD) as published by Anantha [13]. It is clear that a reliable CFD approach has become necessary at gaining more accurate predictions of the total resistances in various lateral separation ratios. However, an increase of speed results in proportionally increase in her resistance. Therefore, a prediction of optimum resistance for catamaran has become primary requirement towards obtaining a better efficiency associated with lower operating cost.

This paper presents an optimization modelling simulation to obtain an optimum Froude number with

---

*Corresponding author. Tel.: +609-668-3856
Universiti Malaysia Terengganu
Kuala Terengganu, Malaysia, 21030

respect to various S/L ratio and also to obtain the optimum S/L ratio on a rounded catamaran using Design of Experiment (DOE) approach incorporated with Computational Fluid Dynamic. This method has been possibly applied to deal with assessment of the optimum S/L ratio, which results in lesser total resistance coefficient for prescribed speed. Several parameters such as effects of the lateral separations ratio (S/L) between 0.2 to 0.3, 0.3 to 0.4 and its corresponding total resistance coefficient of a rounded hull catamaran form in calm water over a range of Froude number have been taken into account in the simulation. Here, a commercial CFD software of ANSYS FLUENT 18.0 is used with the coupling of parameter.

2. Governing Equations

ANSYS FLUENT models the numerical solution of the Reynolds Averaged Navier-Strokes Equations (RANSE) along with the Volume of Fluid (VOF) method for simulating the free surface flow. The k-epsilon (k-ε) turbulence model has been used in viscous flow code for meshing the computational domain. Besides, inflation layer was treated as the interface between air and water, to accurately capture the boundary layer region for any wall-bounded turbulent flows.

2.1. Total resistance prediction of a ship

In FLUENT, the total force component along the specified force vector $\vec{a}$ on a wall zone is computed by summing the dot product of the pressure and viscous forces on each face with the specified force vector. The terms in this summation represent the pressure and viscous force components in the direction of the vector $\vec{a}$

$$F_a = \vec{a}.\vec{F}_P + \vec{a}.\vec{F}_V \tag{1}$$

where, F_a is the total force component, $\vec{a}$ is the specified force vector, $\vec{F}_P$ is the pressure force vector and $\vec{F}_V$ is the viscous force vector [14]. William Froude is known as the pioneer on the prediction of ship resistance using a model which is far smaller than the real ship [15]. The total resistance of a ship is expressed in Eq. (2) as the sum of the frictional resistance (R_F) and the residual resistance or known as the pressure resistance (R_P).

$$R_T = R_F + R_P \tag{2}$$

where the coefficient of the total resistance according to ITTC [16] is expressed as

$$C_T = \frac{R_T}{0.5 \times \rho \times WSA \times {V_S}^2} \tag{3}$$

where, R_T is the dimensional total resistance, ρ is the water density, WSA is the wetted surface area of the ship and V_S is the forward ship speed.

2.2. Volume fraction equation

The tracking of the interface between the air and water phases is accomplished by the solution of a continuity equation for the volume fraction of two phases. For the q^{th} phase, this equation has the following form

$$\frac{1}{\rho_q} = \left[\frac{\partial}{\partial t}\left(\alpha_q\rho_q\right) + \nabla.\left(\alpha_q\rho_q\vec{v}_q\right) = S_{\alpha_q} + \sum_{p=1}^{n}\left(\dot{m}_{pq} - \dot{m}_{qp}\right)\right] \tag{4}$$

where $\dot{m}_{qp}$ is the mass transfer from phase q to phase p and $\dot{m}_{pq}$ is the mass transfer from phase p to phase q [17]. The volume fraction equation is solved through implicit time discretization. ANSYS FLUENT's standard finite-difference interpolation schemes, QUICK, Second Order Upwind and the Modified HRIC schemes, are used to obtain the face fluxes for all cells, including those near the interface.

2.3. Turbulence model

In this CFD simulation, we propose the Realizable k-ε Model, which is available In FLUENT solver. The term "realizable" means that the model satisfies certain mathematical constraints on the Reynolds stresses, consistent with the physics of turbulent flows. The modeled transport equations for k and ε in the realizable k-ε model are

$$\frac{\partial}{\partial t}(\rho k) + \frac{\partial}{\partial x_j}(\rho k u_j) = \frac{\partial}{\partial x_j}\left[\left(\mu + \frac{\mu_t}{\sigma_k}\right)\frac{\partial k}{\partial x_j}\right] + G_k + G_b\text{-}\rho\varepsilon\text{-}Y_M + S_k \tag{5}$$

In these equations, G_k represents the generation of turbulence kinetic energy due to the mean velocity gradients, G_b is the generation of turbulence kinetic energy due to buoyancy, Y_M represented the contribution of the fluctuating dilatation in compressible turbulence to the overall dissipation rate [18].

Cell meshing size is one significant point that should observed. Thus, first cell height for inflation need to be estimated, depends on the local Reynolds number, which is computed based on the wall variable y^+. Y^+ is a dimensionless parameter illustrating local Reynolds number in the near wall region. In this study, the authors choose $y^+ = 8$ for low Fr number and $y^+ = 50$ for high Fr number.

$$y^+ = \frac{pU_{fric}y_{wall}}{\mu} \tag{6}$$

where U_{fric} is the friction velocity, $U_{fric} = \sqrt{\frac{\tau_{wall}}{\rho}}$, $\tau_{wall} = \frac{C_f\rho {V_S}^2}{2}$ and $C_f = \frac{0.026}{Re^{1/7}}$.

2.4. Optimization

Optimizing a design with multiple objective functions is needed in this paper. These situations can be described in general mathematical forms as follows. The design variables are denoted by:

$$\vec{X} = [x_1, x_2, x_3, \ldots, x_n] \in D^n \tag{7}$$

where n represents total number of design variables and $D^n = n$ – dimensional design space, and defined by:

$$x_{i,min} \leq x_i \leq x_{i,max}, i = 1,2,3, \ldots .n \tag{8}$$

Optimization of a ship hull from a resistance point of view forms a non-linear optimization problem [19]. There are two objectives here. The first one is to optimize an output variable (C_T) which is influence by input variable (Fr number). The second one is to optimize an output variable (C_T) which is influenced by input variable (S/L ratio).

2.4.1. Design of experiment using central composite design

Central Composite Designs, also known as Box-Wilson Designs, are a five-level fractional factorial design that is suitable for calibrating the quadratic response model [20]. Face-centered CCDs is chosen in this study. The five-level coded values of each factor are represented by

$$[-\alpha, -1, 0, +1, +\alpha] \tag{9}$$

where $[-1, +1]$ corresponds to the physical lower and upper limit of the explored factor space. It is obvious that $[-\alpha, +\alpha]$ establishes new "extreme" physical lower and upper limits for all factors. The value of α varies depending on design property and number of factors in the study [20].

Face-centered CCDs are a special case of Central Composite Designs in which $\alpha = 1$. As a result, the face-centered CCDs become a three-level design that is located at the center of each face formed by any two factors. Figure 1 is a geometrical representation of a face-centered CCD of three factors [20].

2.4.2. Response surface types using genetic aggregation

The Genetic Aggregation response surface's selection of the best response surface is based on a genetic algorithm generating populations of different response surfaces solved in parallel. The fitness function of each response surface is used to determine which one yields the best approach. It takes into account both the accuracy of the response surface on the design points and the stability of the response surface (cross-validation) [21]. The Genetic Aggregation response surface can be written as an ensemble using a weighted average of different meta models:

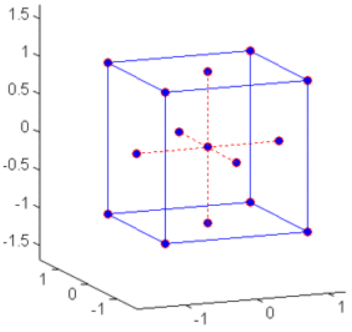

Figure 1. Central composite design for face-centered.

$$\hat{y}_{ens}(x) = \sum_{i=1}^{N_M} w_i \cdot \hat{y}_i(x) \tag{10}$$

where $\hat{y}_{ens}$ is prediction of the ensemble, $\hat{y}_i$ is prediction of the $i\text{-}th$ response surface, N_M is number of meta models used, $N_M \geq 1$ and w_i is weight factor of the $i\text{-}th$ response surface. DesignXplorer minimizes the Root Mean Square Error (RMSE) of the Design Point on $\hat{y}_{ens}$ to estimate the best weight factor values.

$$RMSE(\hat{y}_{ens}) = \sqrt{\frac{1}{N}\sum_{j=1}^{N}\left(y(x_j) - \hat{y}_{ens}(x_j)\right)^2} \tag{11}$$

where x_j is j^{th} Design Point, $y(x_j)$ is output parameter value at x_j and N number of Design Points.

3. Simulation Condition

The hull geometry has been imported into ANSYS Workbench, which was generated from CAD software. The principal dimension of the catamaran model in Fig. 2 is given completely in Table 1.

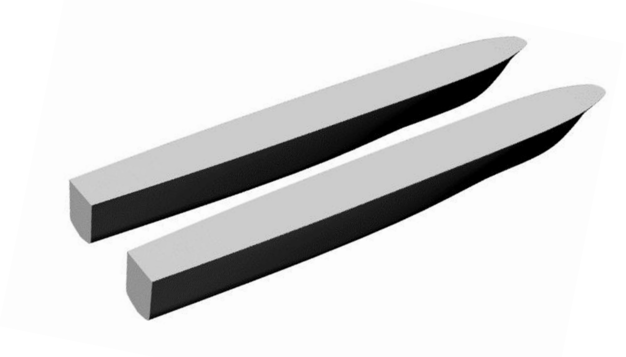

Figure 2. Rounded hull catamaran model

Table 1. Principle dimension of a rounded hull catamaran model

Description	Demi hull	Catamaran
Length (m)	1.3720	1.3720
Breadth (m)	0.12300	-
Draught (m)	0.0780	0.0780
Wetted Surface Area, WSA (m^2)	0.2510	0.5020
Volume (m^3)	0.0072	0.0144
Displacement (kg)	7.2220	14.444
Vertical Center of Buoyancy (m)	0.0490	0.0490

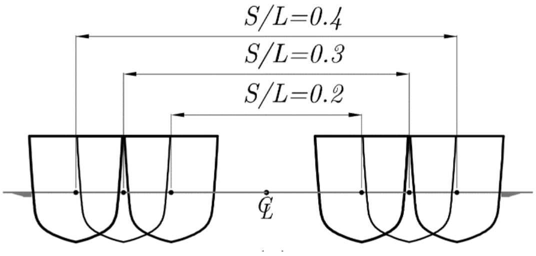

Figure 3. Simulation conditions on predicting total resistances on the catamaran due to effect of S/L.

Table 2. Matrix of simulation

Matrix of CFD Simulation		Froude Number
S/L	0.2	0.19, 0.28, 0.37, 0.47, 0.56 and 0.66
	0.3	
	0.4	

3.1. Simulation parameter

Several parameters such as effects of the lateral separations ratio (S/L) against various Froude number (Fr) from 0.19 to 0.66 were taken into account as shown in Fig. 3. The details of simulation parameters are summarized in Table 2. Computational domain and meshing generation.

Referring to Table 3, pressure inlet and outlet are set to open channel flow with free surface and bottom level defined. Some assumptions were made for mathematical model settings such as catamaran speed is constant and the water surfaces are calm without waves. Interpolation scheme used for pressure is PRESTO due to there are strong body forces present. Volume fraction used is modified HRIC to overcome difficulties in interface tracking because of their overly diffusive nature.

The domain (Fig. 4) must be sufficiently large in the horizontal direction to prevent the influence of flow by boundaries. It provides computational efficiency where less nodes and elements are required to achieve high solution accuracy [22]. Meshing cell used in this case is purely tetrahedral meshes with 10 prism layers (Fig. 5) as it is relatively complex geometries [23]. Besides, the free-surface flow requires a fine grid. Inflation is required here. The authors apply the symmetrical computational domain model considering on less computational time.

Table 3. Boundary setting conditions

Description	Distance with respect to origin point	Type	Description
X_{max} (Inlet)	1.0 L_{pp}	Pressure inlet	Open channel
X_{min} (Outlet)	3.0 L_{pp}	Pressure outlet	Open channel
Y_{min} (Side)	1.5 L_{pp}	Stationary wall	Zero viscous stress
Y_{max} (Side)	1.5 L_{pp}	Stationary wall	Zero viscous stress
Z_{min} (Bottom)	1.5 L_{pp}	Moving wall	Vessel speed
Z_{max} (Top)	0.5 L_{pp}	Stationary wall	Zero viscous stress

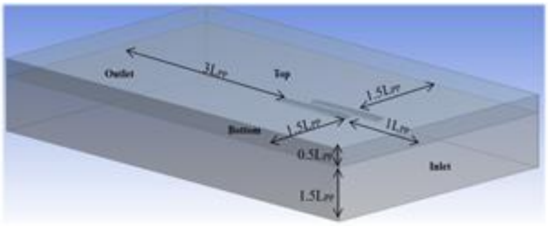

Figure 4. Domain dimension and boundary conditions

Figure 5. Tetrahedral meshes and 10 prism layers as inflation

Table 4. Mesh independence study

Number of Elements	Resistance, $R_T(N)$	Percentage of Difference (%)
145,853	15.208	-
288,802	14.023	8.45
572,421	13.102	7.21
1,152,100	12.421	5.48
2,288,364	11.836	13.9
4,583,156	11.815	0.18

Mesh independence study is performed to ensure that the total resistance conformed to convergence and mesh-independence criteria. Table 4 illustrates a summary of ship resistance calculations, using different number of elements. In this study, 2,288,364 (or approximately 2.3 million) elements in the simulation, satisfies the mesh-independence criterion.

4. Results and Discussions

As seen in the following figures (Figs. 7-9), the CFD simulations on predicting resistance on rounded hull catamaran had been successfully carried out at various Froude number with S/L ratios. The simulation results are appropriately discussed in sub-sections 4.1, 4.2 and 4.3, respectively.

4.1. Effect of Froude number (Fr) on catamaran

Figure 6(a) shows that the increase of F_r was proportional to the total resistance (R_T) on the catamaran, where a maximum increment of about 135% occurred asF_r increased from 0.19 to 0.28. The detailed results of the resistance prediction for the catamaran is summarized in Table 5. The results correspond to the fact that increase of wave crest and trough near the body of hull [10]. At F_r 0.47, the catamaran reached the highest total resistance coefficient. The result was found to be similarly to the work previously reported by Papanikolaou and Dafnias [24], where F_r around 0.45 was identified as an unfavourable Froude number for the catamaran resistance.

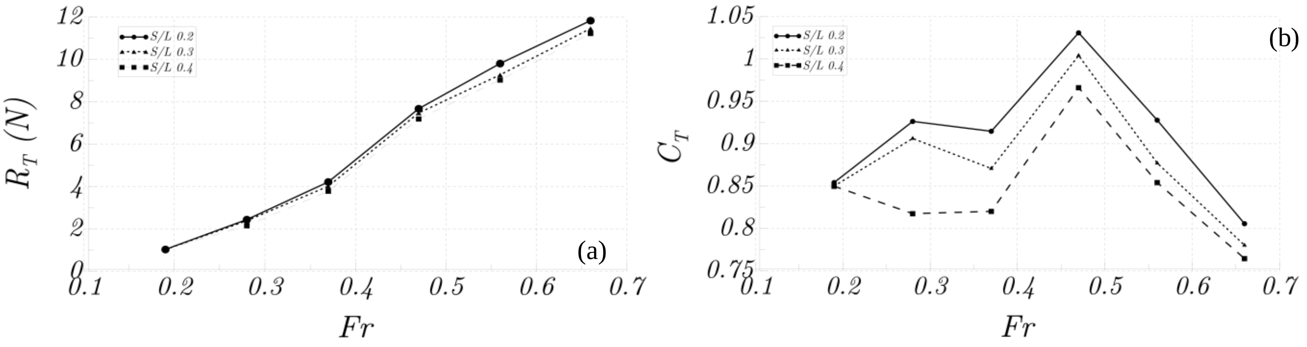

Figure 6. Total resistance for catamaran with S/L = 0.2 to 0.4 at various Froude numbers

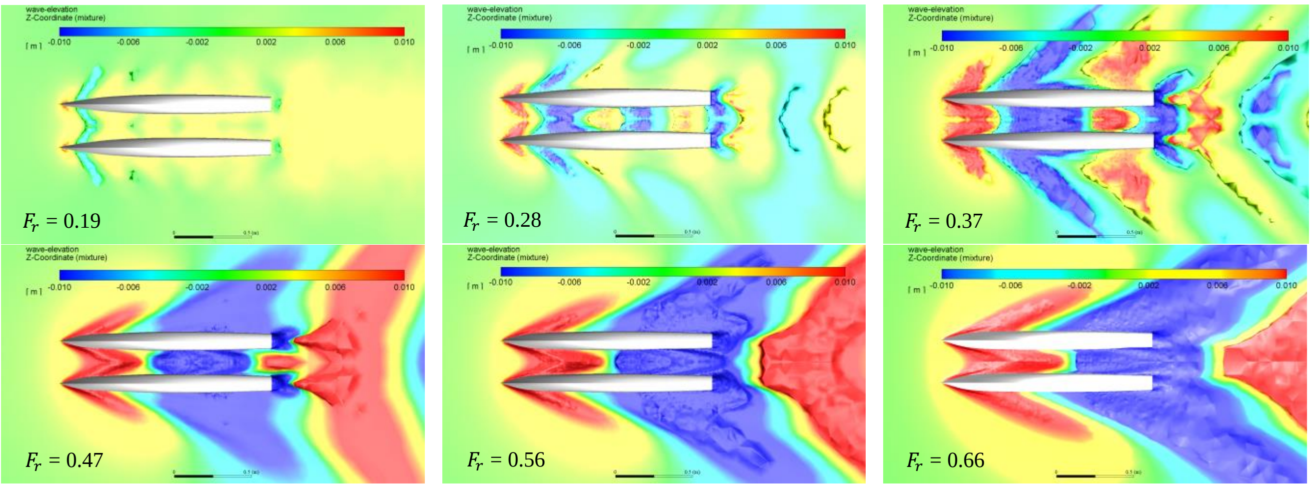

Figure 7. Wave pattern characteristics of catamaran (S/L = 0.2)

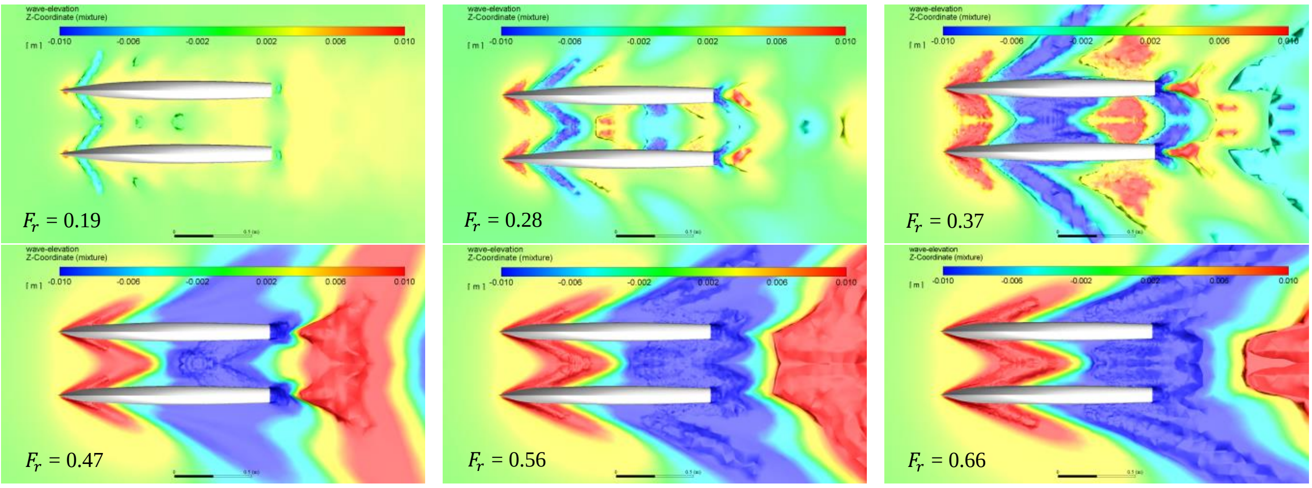

Figure 8. Wave pattern characteristics of catamaran (S/L = 0.3)

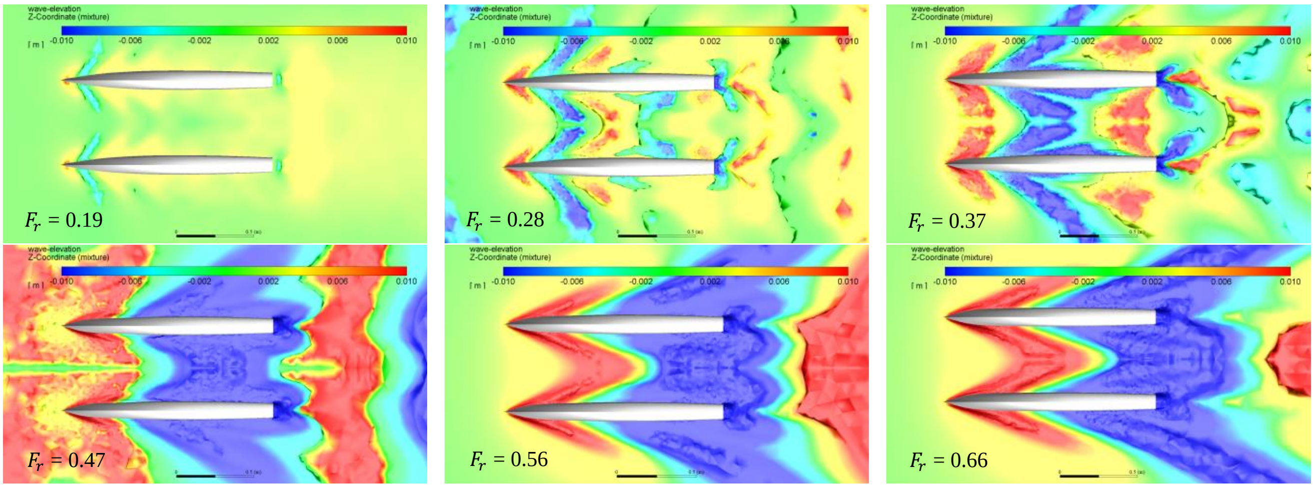

Figure 9. Wave pattern characteristics of catamaran (S/L = 0.4)

Table 5. Total resistance coefficient at S/L 0.2 to 0.4

S/L	Froude No.	$R_T(N)$	Discrepancy of R_T	C_T	Discrepancy of C_T
	Fr	CFD	%	CFD	%
0.2	0.19	1.04006	-	0.00854	-
	0.28	2.44924	135.49	0.00926	8.43
	0.37	4.22312	72.43	0.00915	-1.26
	0.47	7.67966	81.85	0.01031	12.68
	0.56	9.81270	27.78	0.00928	-10.00
	0.66	11.83626	20.62	0.00806	-13.16
0.3	0.19	1.03500	-	0.00850	-
	0.28	2.39603	131.50	0.00906	6.60
	0.37	4.02042	67.80	0.00871	-3.91
	0.47	7.47984	86.05	0.01004	15.30
	0.56	9.27706	24.03	0.00877	-12.63
	0.66	11.46229	23.55	0.00780	-11.05
0.4	0.19	1.03472	-	0.00850	-
	0.28	2.16170	108.92	0.00818	-3.80
	0.37	3.78697	75.18	0.00820	0.32
	0.47	7.19772	90.07	0.00966	17.79
	0.56	9.03499	25.53	0.00854	-11.58
	0.66	11.23205	24.32	0.00765	-10.50

4.2. Lateral separation ratio (S/L) on catamaran

Regardless of lateral separation ratios, the results showed the subsequent increase of Froude number from 0.47 to 0.66 was proportional to the total resistance coefficient as displayed in Fig. 6(b). As the lateral separation ratios increases, the corresponding total resistance and total resistance coefficient decreases. The result was found to be similarly to the work previously reported by A. Fitriadhy [6], [10], Molland [8], Subramanian and Sahoo [9], where increasing of S/L ratio will decrease the total resistance [25], [26]. This occurred mainly due to the less contribution of wave interference and viscous effects between the two demihulls [10].

4.3. Optimization of Fr number in various S/L ratio

As we can see that from subsection 4.2, total resistance coefficient reaches the highest peak for F_r = 0.47 regardless of S/L ratio. After F_r = 0.47, total resistance coefficient decrease significantly in the range of F_r 0.47 to 0.66 (Table 5). The lower the speed of the vessel, it is expected that fuel consumption and ship emissions are also reduced [25]. Hence, we are interested to obtain an optimized F_r for each S/L ratio from the range 0.2 to 0.4. We will perform Design of Experiment (DOE) from F_r 0.47 to F_r 0.66. The existing F_r will be 0.47, 0.56 and 0.66. The number of design points need to be carefully determined based on the number of input factors and their ranges as well as the response model accuracy [27]. Hence, 2 design points will be added in between the existing F_r as shown in Table 6.

Response surface is performed, thus minimum and maximum calculated values appeared among the 8 design points. Optimization is then carried out with the objective to obtain an optimized F_r that have total resistance and also total resistance coefficient that lesser than the value of F_r = 0.66. As the trend for total resistance coefficient declined from F_r = 0.47 to F_r = 0.66. Somehow there is a point that between those ranges, there is a lower C_T compared to F_r = 0.66. Table 7 below shows the comparison of total resistance coefficient for the optimized F_r with respect to F_r = 0.66 for various S/L. The computed wave patterns characteristics for the catamaran with optimized F_r compared to existing F_r = 0.66 are presented below in Fig. 10.

Table 6. Additional design points for F_r = 0.47 to 0.70 for various S/L

S/L	**F_r**	**Total Resistance, R_T**	**Total Resistance Coefficient, C_T**	**Discrepancy of C_T (%)**
0.2	0.47	7.67965580	0.010309358	-
	0.50	8.35270580	0.009907698	-3.90
	0.53	9.12483220	0.009632937	-2.77
	0.56	9.81270200	0.009278935	-3.67
	0.60	10.5472960	0.008688088	-6.37
	0.63	11.1728106	0.008347702	-3.92
	0.66	11.8362646	0.008057724	-3.47
	0.70	12.9357172	0.007828527	-2.84
0.3	0.47	7.47984400	0.010041126	-
	0.50	8.16363880	0.009683433	-3.56
	0.53	8.66383060	0.009146266	-5.55
	0.56	9.27707560	0.008772445	-4.09
	0.60	10.1522756	0.008362700	-4.67
	0.63	10.7705714	0.008047171	-3.77
	0.66	11.4622898	0.007803135	-3.03
	0.70	12.3832724	0.007494194	-3.96
0.4	0.47	7.19771800	0.009662393	-
	0.50	7.86430400	0.009328372	-3.46
	0.53	8.51746600	0.008991751	-3.61
	0.56	9.03499320	0.008543530	-4.98
	0.60	9.83548880	0.008101754	-5.17
	0.63	10.4989298	0.007844216	-3.18
	0.66	11.2320536	0.007646398	-2.52
	0.70	12.0684222	0.007303651	-4.48

Table 7. Optimized F_r with its corresponding total resistance coefficient for various S/L

S/L	F_r	Total Resistance, R_T	Total Resistance Coefficient, C_T	Discrepancy of C_T (%)
0.2	0.6589	11.7956312	0.008055673	-
	0.6600	11.8362646	0.008057724	0.0250
0.3	0.6599	11.4603770	0.007803015	-
	0.6600	11.4622898	0.007803135	0.0015
0.4	0.6596	11.2088390	0.007639852	-
	0.6600	11.2320536	0.007646398	0.0860

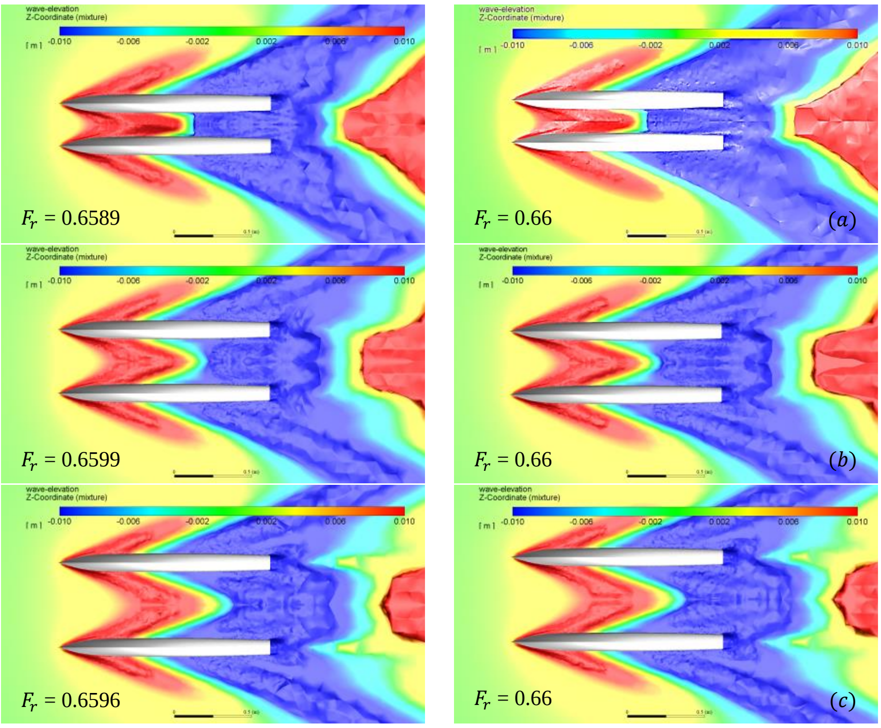

Figure 10. Wave patterns of optimized Fr comparison with (a) S/L = 0.2 (b) S/L = 0.3 (c) S/L = 0.4

C_T for F_r 0.6589 is lower than the C_T for F_r = 0.66 by 0.025%. Referring to Fig. 10(a) for F_r = 0.6589, there is weaker red colour happening in the middle of the two hull compared to F_r = 0.66. Other than that, transversal pressure gradient (dark blue colour) is weaker at the stern for the optimized F_r case.

C_T for F_r = 0.6599 is lower than the C_T for F_r = 0.66 by 0.0015%. Referring to Fig. 10(b) for F_r = 0.6599, there is lower wave crest and the wave scatter more in the middle of two hull compared to F_r = 0.66. Moreover, the wave generated by the stern of ship is lesser for the optimized F_r = 0.66.

C_T for F_r 0.6596 is lower than the C_T for F_r = 0.66 by 0.086%. This means that F_r = 0.6596 had been optimized since its total resistance coefficient is lesser compared to existing F_r = 0.66. Referring to Fig. 10(c) for F_r = 0.6596, the blue wave trough is more scatter compared to F_r = 0.66 astern of the ship hull. Additionally, the wave generated in between the hull for F_r = 0.66 and optimized F_r was almost the same and not much difference.

Table 8. Total resistance coefficient for catamaran at S/L = 0.2 to 0.4 (Fr = 0.56)

S/L	F_r	Total Resistance Coefficient, C_T	Discrepancy of C_T (%)
0.2000	0.56	0.009278935	-
0.2125		0.009203327	-0.81
0.2250		0.009069646	-1.45
0.2375		0.008996420	-0.81
0.2500		0.009073417	0.86
0.2625		0.008917622	-1.72
0.2750		0.008899929	-0.20
0.2875		0.008811081	-1.00
0.3000		0.008772445	-0.44
0.3125		0.008730137	-0.48
0.3250		0.008797172	0.77
0.3375		0.008659397	-1.57
0.3500		0.008600827	-0.68
0.3625		0.008634891	0.40
0.3750		0.008706303	0.83
0.3875		0.008575417	-1.50
0.4000		0.008543530	-0.37

4.4. Optimization of S/L ratio in Fr=0.56 and 0.66

Based on Table 5, it is interesting to note that there is a great reduction of C_T from Froude number 0.56 to 0.66, which is --13.16% for S/L = 0.2, -11.05% for S/L = 0.3 and -10.50% for S/L = 0.4. The wave elevation decreases as shown in three of the cases. There is an interval of S/L where at here resistance remains almost constant or even decreased particularly at F_r = 0.56 and 0.66. It is of great interest to find the optimum S/L ratio happening between these two Froude numbers due to both the cases are of medium speed. The others Froude number are too rough. Design of Experiment (DOE) will be performed from S/L = 0.2 to S/L = 0.3 and also S/L = 0.3 to S/L = 0.4 for 2 of the F_r 0.56 and 0.66. There will be 4 results produced later. The existing S/L will be 0.2, 0.3 and 0.4.

4.4.1. Case Fr=0.56

As viscous resistance interference was found to be relatively independent of speed and hull separation and rather is dependent on demi hull-length-to beam ratio. It is evident that a significant reduction in resistance could be achieved by finding the optimum position of stagger [12].

Table 9 below shows the comparison of total resistance coefficient for the optimized S/L ratio with respect to S/L 0.3 and 0.4. The computed wave patterns for the catamaran with optimized S/L are presented in Fig. 11.

Table 9. Optimized S/L ratio in comparison with S/L 0.3 and 0.4 at Fr = 0.56

S/L	F_r	Total Resistance, R_T	Total Resistance Coefficient, C_T	Discrepancy of C_T (%)
0.29934	0.56	9.21970800	0.008718198	-
0.30000		9.27707560	0.008772445	0.62
0.39885	0.56	9.00577420	0.008515901	-
0.40000		9.03499320	0.008543530	0.32

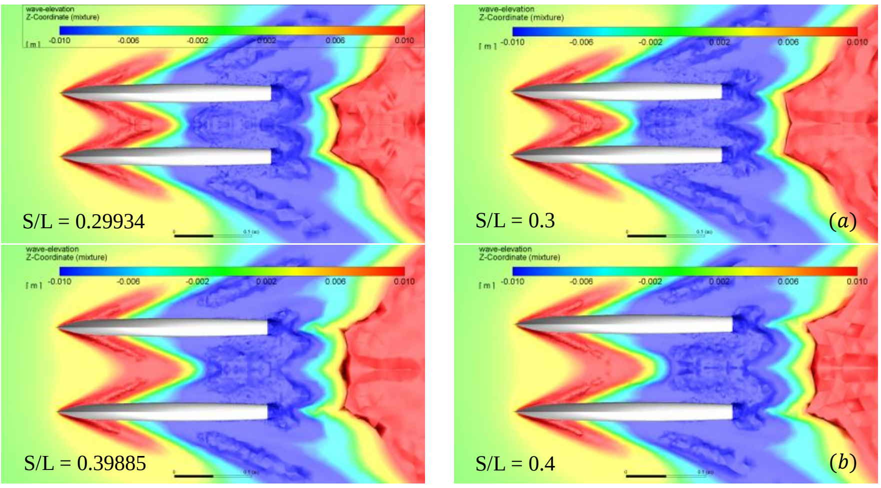

Figure 11. Wave patterns of optimized S/L in comparison with (a) S/L = 0.3 (b) S/L = 0.4

Table 10. Total resistance coefficient for catamaran at S/L = 0.2 to 0.4 (Fr = 0.66)

S/L	F_r	Total Resistance Coefficient, C_T	Discrepancy of C_T (%)
0.2000	0.66	0.008057724	-
0.2125		0.008091421	0.42
0.2250		0.007973133	-1.46
0.2375		0.007948858	-0.30
0.2500		0.007867262	-1.03
0.2625		0.007998523	1.67
0.2750		0.007791769	-2.58
0.2875		0.007806362	0.19
0.3000		0.007803135	-0.04
0.3125		0.007695932	-1.37
0.3250		0.007699001	0.04
0.3375		0.007719823	0.27
0.3500		0.007649308	-0.91
0.3625		0.007745565	1.26
0.3750		0.007620160	-1.62
0.3875		0.007763952	1.89
0.4000		0.007646398	-1.51

Table 11. Optimized S/L ratio in comparison with S/L 0.3 and 0.4 at Fr = 0.66

S/L	F_r	Total Resistance, R_T	Total Resistance Coefficient, C_T	Discrepancy of C_T (%)
0.27500	0.66	11.4462310	0.007792202	-
0.30000		11.4622898	0.007803135	0.14
0.37500	0.66	11.1810715	0.007611691	-
0.40000		11.2320536	0.007646398	0.46

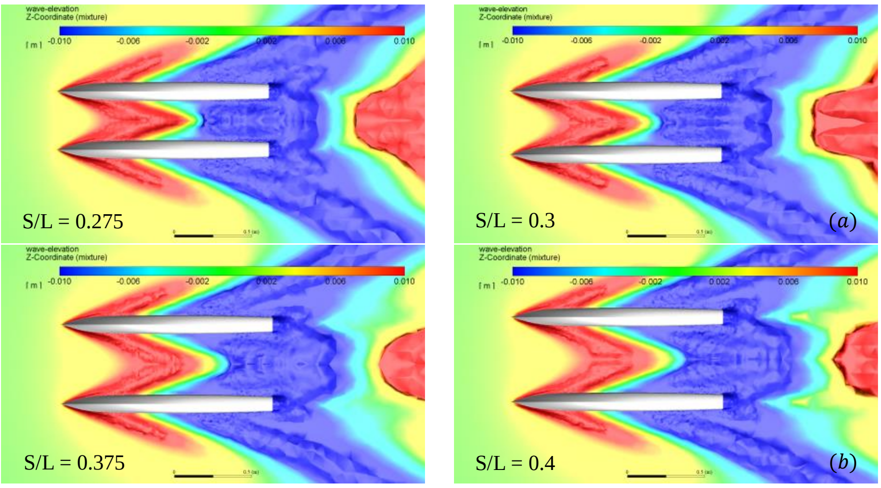

Figure 12. Wave patterns of optimized S/L in comparison with (a) S/L = 0.3 (b) S/L = 0.4

From Table 9, C_T for S/L = 0.29934 is lower than C_T for S/L = 0.3 by 0.62%. Interference will cause wave superposition in the center wave profile of catamaran. But with the optimum distance of separation between the hull, there will be favourable resistance occurring. Figure 11(a) shows the lower wave elevation at ship stern for optimized S/L = 0.2993 compared to S/L = 0.3. Besides that, the blue colour wave trough is lower beside the two ship hull for the While C_T for S/L = 0.3988 is lower than the C_T for S/L = 0.4 by 0.32%. Figure 11(b) shows the lower wave elevation at ship stern for S/L = 0.3988 compared to S/L = 0.4. Higher and darker colour of wave trough beside the two ship hull for S/L = 0.3988 proof that there is lower pressure exerted.

4.4.2. Case Fr 0.66

From Table 10, we can notice that the total resistance coefficient decreased from S/L = 0.2 to 0.4 as general case. At a glance we can notice that C_T for S/L = 0.275 is lower than C_T for S/L = 0.3. C_T for S/L = 0.275 will be 0.007791769 while C_T for S/L = 0.3 is 0.007803135 with a percentage difference of 0.14%. On the other hand, S/L = 0.375 has a lower total resistance coefficient compared to S/L = 0.4. C_T for S/L = 0.375 will be 0.007620160 while C_T for S/L = 0.4 is 0.007646398 with a percentage difference of 0.34%.

To verify it, manual running of ANSYS FLUENT is carried out. Table 11 below shows the comparison of total resistance coefficient for the optimized S/L ratio with respect to S/L 0.3 and 0.4. The computed wave patterns for catamaran with optimized S/L are presented in Fig. 12.

C_T for S/L = 0.275 is lower than the C_T for S/L = 0.3 by 0.14%. Figure 12(a) shows the darker blue colour wave generated in the middle of two ship hull, indicating lower pressure exerted. Also the pattern for red colour wave crest for optimized ratio 0.275 has smaller area.

As a result, the total resistance coefficient of optimized S/L ratio 0.375 is determined after verification. As we can see from Fig. 12(b), the lower wave elevation indicated by darker blue colour around ship stern for S/L = 0.375 compared to S/L = 0.4. Other than that, the yellow wave elevation for optimized S/L ratio 0.375 is lower than that of S/L = 0.4.

5. Conclusion

The Computational Fluid Dynamic investigation on the total resistance coefficients of the rounded catamaran was successfully performed ANSYS FLUENT software. The effects of lateral separation ratios were examined accordingly at a wide range of Froude numbers. Optimization of Froude number with respect to different S/L ratio and optimization S/L ratio is carried out at Froude number 0.56 and 0.66. The computation results are drawn as follows:

- In general, the increase of lateral separation ratio from 0.2 to 0.3 dealt with less total resistance coefficient.
- Fr = 0.65895 is the optimized Fr for S/L = 0.2.
- Fr = 0.65995 is the optimized Fr for S/L = 0.3.
- Fr = 0.6596 is the optimized Fr for S/L = 0.4.
- It is interesting to note that in S/L ≤ 0.3, there is a tendency of optimized S/L ratio in Fr 0.56 and 0.66.
- S/L = 0.29934 is the optimized S/L ratio between 0.2 ≤ S/L ≤ 0.3 for case Fr 0.56.
- S/L = 0.39885 is the optimized S/L ratio between 0.3 ≤ S/L ≤ 0.4 for case Fr 0.56.
- S/L = 0.275 is the optimized S/L ratio between 0.2 ≤ S/L ≤ 0.3 for case Fr 0.66.
- S/L = 0.375 is the optimized S/L ratio between 0.3 ≤ S/L ≤ 0.4 for case Fr 0.66.

References

[1] J. Van Hadler, C. Lee, J. Birmingham, and H. Jones, “Ocean Catamaran Seakeeping Design, based on the Experiments of USNS HAYES,” 1974.

[2] S. Asapana and N. Architecture, “Resistance Prediction for Asymmetrical Configurations of High-Speed Catamaran Hull Forms,” 2015.

[3] K. Kenevissi, M. Atlar, and E. Mesbahi, “A New-generation Motion-control System for Twin-hull Vessels using a Neural Optimal Controller,” *Mar. Technol.*, vol. 40, pp. 168–180, 2003.

[4] S. E. Rollings, “Seakeeping Analysis of Small Displacement High-speed Vessels,” Naval Postgraduate School Monterey Ca., 2003.

[5] A. Fitriadhy, S. A. Azmi, N. A. Mansor, and N. A. Aldin, “Computational Fluid Dynamics Investigation on Total Resistance Coefficient of A High-speed ‘deep-V’ Catamaran in Shallow Water,” 2017.

[6] A. Fitriadhy, N. S. Razali, and N. A. Mansor, “Seakeeping Performance of a Rounded Hull Catamaran in Waves using CFD Approach,” 2017.

[7] M. Insel and A. F. Molland, “An Investigation into the Resistance Components of High-Speed Displacement Catamarans,” *Trans. RINA*, vol. 134, 1991.

[8] A. F. Molland, I. Utama, and D. Buckland, “Power Estimation for High-speed Displacement Catamarans,” in *International Conference on Marine Technology*, 2000.

[9] P. K. Sahoo, L. J. Doctor, and L. Pretlove, “CFD Prediction of the Wave Resistance of a Catamaran with Staggered Demihulls,” in *Procs. of International Conference on Marine Hydrodynamics*, 2006.

[10] A. Fitriadhy, S. P. Lim, and A. Jamaluddin, “CFD Investigation on Total Resistance Coefficient of Symmetrical and Staggered Catamaran Configurations through Quantifying Existence of an Interference Factor,” 2016.

[11] Yanuar, Ibadurrahman, S. Karim, and M. Ichsan, “Experimental study of the interference resistance of pentamaran asymmetric side-hull configurations,” 2017.

[12] S. I. Sohn, D. H. Park, Y. S. Lee, and L. K. Oh, “Hull Separation Optimization of Catamaran Unmanned Surface Vehicle Powered with Hydrogen Fuel Cell,” *Int. J. Phys. Math. Sci.*, vol. 6, no. 3, 2012.

[13] V. Anantha, “Choosing a Cat,” pp. 69–82, 2006.

[14] ANSYS Release 18.1, *Computing Forces, Moments, and the Center of Pressure*. 2018.

[15] W. Froude, “On the Influence of Resistance upon the Rolling of Ship,” *Nav. Sci.*, p. 155, 1872.

[16] ITTC, “Report of the Performance Committee,” 1957.

[17] ANSYS Release 18.1, *Volume Fraction Equation*. 2018.

[18] ANSYS Release 18.1, *Transport Equations for the Standard k-ε Model*. 2018.

[19] K. Svanberg, “Method of Moving Asymptotes—A New Method for Structural Optimization,” *Int. J. Numer. Methods Eng.*, vol. 24, pp. 359–373, 1987.

[20] ANSYS Release 18.1, *Central Composite Design (CCD)*. 2018.

[21] ANSYS Release 18.1, *Genetic Aggregation*. 2018.

[22] ANSYS, *ANSYS Fluent Theory Guide.14.0*. 2011.

[23] C. Janson and L. Larsson, “A Method for the Optimization of Ship Hulls from Resistance Point of View,” in *Proceedings Twenty-First Symposium on Naval Hydrodynamics*, 1997.

[24] A. Papanikolaou and N. Dafnias, “Hydrodynamic Optimization and Design of a Fast Displacement Catamaran Ferry,” in *the 6th International on Marine Design Conference*, 1997.

[25] A. F. Molland, J. F. Wellicome, and P. R. Couser, “Resistance Experiments on a Systematic Series of High Speed Displacement Catamaran Forms: Variation of Length-Displacement Ratio and Breadth-Draught Ratio,” 1994.

[26] V. A. Subramanian and P. Joy, “A Method for Rapid Hull Form Development and Resistance Estimation of Catamarans,” *Trans. Mar. Technol.*, vol. 38, no. 1, pp. 5–11, 2004.

[27] A. Molland, P. Wilson, D. Taunton, S. Chandraprabha, and P. Ghani, “Resistance and Wash Measurements on a Series of High Speed Displacement Monohull and Catamaran Forms in Shallow Water,” *Int. J. Marit. Eng.*, pp. 19–38, 2004.

EPI International Journal of Engineering
Volume 3, Number 1, February 2020, pp. 84-89
DOI: 10.25042/epi-ije.022020.12

*p*ISSN 2615-5109
*e*ISSN 2621-0541

Design and Manufacture of 6 Axis Forces and Moments Transducers for Seaplane Floaters Test in Towing Tank

Nurhadi[a,*], Mochammad Nasir[b], Chandra Permana[c], Endah Suwarni[d]

[a]Laboratory for Hydrodynamics Technology, BPPT. Email: nrhadi@gmail.com
[b]Laboratory for Hydrodynamics Technology, BPPT. Email: nasir08.lhi@gmail.com
[c]Laboratory for Hydrodynamics Technology, BPPT. Email: chandra.pzm@gmail.com
[d]Laboratory for Hydrodynamics Technology, BPPT. Email: endahsuwarni@gmail.com

Abstract

To develop seaplanes as a means of inter-island transportation, it is necessary to have a simulation, testing, and analysis of force measurements that work so that the aircraft can be designed optimally in terms of function and safety. To fulfill one type of test, the seaplane floater model is pulled in the Towing Tank to determine the hydrodynamic forces acting on the floater which include resistance (*Fx*), side force (*Fy*), lift force (*Fz*), and moments in all three axes. A method of measuring the force of 6 axis force and moment or 6 degrees of freedom (6 Degree of Freedom, 6 DOF) was built and designed by combining several single load cells so that these forces can be known optimally. From the results of the 6 DOF transducer design, it is proven that it can be used well in measuring 6 forces and moments with force measurement errors ranging from 1.38%. The distance between the 6 DOF transducer capture point and the floater force capture point will affect the measured moment transformation.

Keywords: 6 degree of freedom; floater; towing tank; transducer design

1. Introduction

One of the proper transportation models developed in Indonesia as an archipelago is a transportation that can be used both on land, air, and water such as seaplanes. Seaplanes are airplanes that can air from land or from the surface of the water and can return to land or to the surface of the water. One type of seaplane is a floatplane or seaplane where the aircraft uses additional components in the form of a floater to float while the fuselage is above the surface of the water. This transportation system will be very flexible because it can cover the land (airstrips), large lakes and rivers, bays, seas, and waters among islands that have calm seas, which allow for takeoff and landing for amphibious aircraft throughout the year. This transportation is much easier and cheaper than building airports in general.

In the design and development of seaplanes, they should not be careless because they are related to safety so an analysis of the forces that work both on the fuselage and the floater is needed. To know the forces, of course, it can be done using simulation [1] and through measurement analysis using force sensors [2].

Seaplanes will run at high speed from start to 60 knots when taking off, especially on the water so that the hydrodynamic forces will work due to the friction of the floater with water. Because of the hydrodynamic forces so it will be important to know the amount of resistance and the amount of lift force of the floater and the moments that work that will facilitate the control of the seaplane. With the existence of these forces, in addition to simulations and aerodynamic tests [3], the simulation and testing of the floater model to determine the hydrodynamic forces are very important to do.

In testing the seaplane floater model in the Towing tank, a measuring instrument should capture the hydrodynamic forces acting on the floater. These forces include resistance (*Fx*), side forces (*Fy*), lift (*Fz*), as well as moments in the three-axis directions. A method of measuring the force of 6 degrees of freedom (6 Degree of Freedom, 6 DOF) requires a special design to obtain an optimal value following their needs [4]. For this reason, it is necessary to design a transducer by utilizing six S type load cells which are arranged in such a way as to form six-component transducers. With six-component transducers, it is expected that the forces of *Fx*, *Fy*, *Fz,* and the moments of *Mx*, *My*,

---

* Corresponding author. Tel.: +62811328567
Jl. Hidrodinamika, Kompleks ITS, Sukolilo, Surabaya, 60111

Mz that occur on the floater when pulled will be known optimally.

2. Literature Review

2.1. Strain and sensors applications

A strain sensor is a passive transducer that uses the concept of changing the electrical resistance in a metal wire to change every pull produced by the force that hits the wire. The concept of this change can be used to measure weight, pressure, and mechanical force. Strain sensors are made of one long wire, folded, and placed on a soft or flexible material [5]. Any force, strain, applied to the area where the strain gauges are attached will cause a change in the length and cross-sectional area of the wire as shown in Fig. 1.

This change will result in a change in the resistance of the wire itself through the connection:

$$R = \frac{\rho . l}{A} \qquad (1)$$

R = wire resistance (Ω)
ρ = wire resistance coefficient (Ω -m)
l = wire length (m)
A = wire cross-sectional area (m^2)

The relationship between strain and force (load) can be calculated by the formula:

$$Strain(\varepsilon) = \frac{change\ of\ wire\ length\ due\ to\ the\ load\ (\partial l)}{wire\ length\ (l)} \qquad (2)$$

Based on the principle of changes in strain values due to forces, by using 4 strain gages which are connected in the full-bridge, the value of a strain that occurs due to changes in force acting can be measured.

In Fig. 2, if the load cell has a force *F*, there will be a strain on the R-value of the strain gages mounted with the change in the value of *R* is:

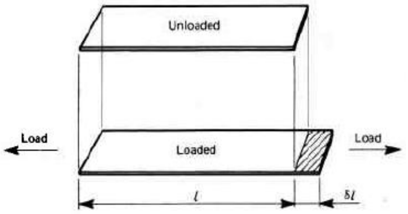

Figure 1. Principle of strain gages sensor [5]

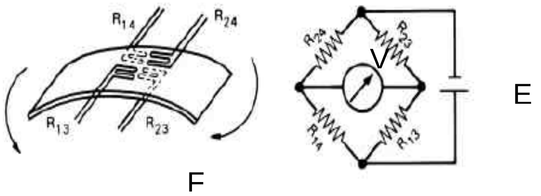

Figure 2. Strain sensor application with the full-bridge relationship [5]

R24 increases to *R* + *δR*
R13 increases to *R* + *δR*
R14 is reduced to *R* - *δR*
R23 is reduced to *R* - *δR*

So that

$$i_{24} = \frac{E}{R_{24}+R_{14}} = \frac{E}{R+\partial R+R-\partial R} = \frac{E}{2R} \qquad (3)$$

$$V_{24} = i_{24.}R_{24} = \frac{E}{2R}(R+\partial R) \qquad (4)$$

$$V = V_{23} - V_{24} = \frac{ER-E\partial R}{2R} - \frac{ER+E\partial R}{2R} \qquad (5)$$

$$V = \pm\frac{E\partial R}{R} \qquad (6)$$

By comparing the output voltage generated due to the forces acting on the load cell will be obtained by a factor as a basis for calculating the forces that occur in the test model.

2.2. The forces acting on the floater test model

The forces acting on the floater are the same as the forces acting on ships that moving on the surface of the water at a certain speed. As a result of water shifting with the floater body, hydrodynamic forces include the drag force (*Fx*), side force (*Fy*), lift (*Fz*), and moments in the *x*, *y*, and *z* directions to the point catch floater. Illustration of these styles can be seen in Fig. 3.

3. Methodology

To solve the problems faced, a method was made to facilitate the design of a measuring instrument 6 degrees of freedom of force and moment. In brief, this method can be seen in the flow chart in Fig. 4.

There are three main stages in the design of buildings measuring 6 DOF. The first is the design phase where at this stage it is necessary to know the range of force and moment measurements that will work on the measuring instrument, the determination, and design of a single load cell, the calculation of the weight of the material used. The second stage is the manufacturing stage of design. At this stage, a material for the spring load cell and a framework for the 6 DOF sensor is made. Single load cell calibration is also

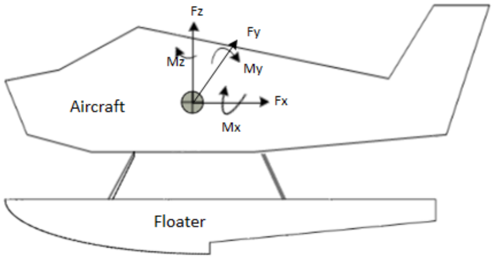

Figure 3. The styles in the floater test model [6]

performed to determine the value of the single load cell calibration and repeatability performance. The last step was assembling the prototype 6 DOF sensor and testing the load force *Fx, Fy, Fz* to determine the accuracy of the signal and the measurement uncertainty that occurred.

Figure 5 shows how the measurement method to be used where 6 channels of 6 DOF sensors will be connected to signal conditioning which functions as a supply of voltage, signal output amplifier, and filter. The output of the signal condition is connected to the NI Data Acquisition which is connected to a PC for recording data and processing the output data from the 6 DOF sensor.

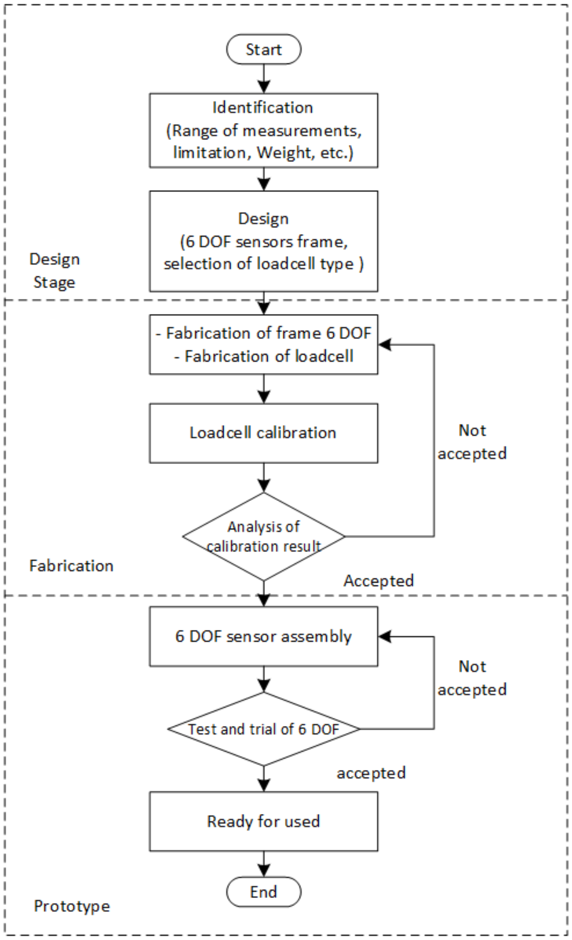

Figure 4. Methodology

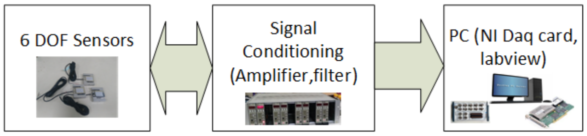

Figure 5. The Measurement method

4. Results and Discussion

4.1. 6 DOF sensor system design

For the 6 DOF load cell design, 6 S type load cells are needed. S type load cells can be made from aluminum alloy material as shown in Fig. 6. For dimensions adjusted to the design of the required load cell capacity. In the calculation of dimensions can be used software ‘Transducers’ made by Marin. Based on the results of the software for 100 N capacity obtained dimensions as in Table 1, the spring element dimensions for load cell type S with a capacity of 100 N, so that if desired can be made according to the required capacity.

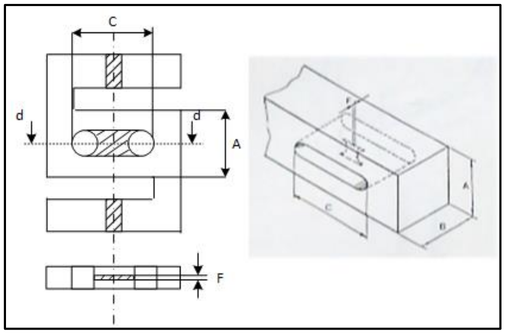

Figure 6. S Type of load cell (shear)

Table 1. The Output of transducers software for 100 N [7]

MATERIAL SENSITIVITY			MEASURING RANGE			ALUMINUM ELECTRICAL OUTPUT		
FX	8.64	uR/N	FX	116	N	FX	17	uV/V/N
FY	8.74	uR/N	FY	114	N	FY	17	uV/V/N
FZ	1.3	uR/N	FZ	797	N	FZ	2	uV/V/N
MX	1747	uR/NM	MX	0.57	NM	MX	3511	uV/V/NM
MY	343	uR/NM	MY	2.91	NM	MY	690	uV/V/NM
MZ	6217	uR/NM	MZ	0.16	NM	MZ	12496	uV/V/NM
MATERIAL MICRO STRAIN			**FULL BRIDGE STRAIN GAGE**					
(Z-AXIS IS LENGTH AXIS)			**INPUT DATA MILLIMETERS**					
HEIGHT IN X-DIRECTION				**A=**		10.00		MM
HEIGHT IN Y-DIRECTION				**B=**		5.00		MM
SLOT LENGTH				**C=**		10.00		MM
THICKNESS SHEAR PLATE				**F=**		2.00		MM
SLOT HEIGHT				**H=**		8.00		MM

The design of manufacture is based on the numerical data of the force to be measured so we need a load cell with a capacity of 2 pieces of 50 N and 4 pieces of 100 N. The capacity of 50 N is used as an *X*-axis load cell so that the maximum *Fx* force can be measured up to 100 N, *Fy* 100 N is being *FZ* to 300 N. Because of the time and capacity considerations of 50 N and 100 N are widely available in the market, for the S type load cell, the manufacturer's Load cell "Dacell", Korean, with the UU model [8].

The calibration process is carried out by individually calibrating both the drag and press of each type S load cell used. Calibration is carried out by giving a load in stages, as shown in Fig. 7, the resulting output is measured so that the calibration factor is known that shows the relationship between the load or force (kg) and the output voltage (volts).

Figure 7. Pull and push calibration of single load cell

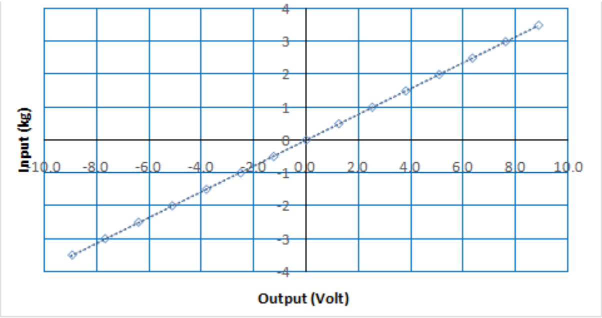

Figure 8. Calibration output of S1 load cell

An example of a calibration graph output can be seen in Fig. 8. The x-axis shows the input load (kg) and the y-axis is the resulting output (volts) so the trend line graph is known as a multiplier factor for the output signal load cell amplifier that read by the data acquisition system.

The mechanical configuration of the 6 DOF sensor system and the design of the 6 DOF sensor frame can be seen in Fig. 9. In Fig. 9 (a). There are 6 load cells arranged in such a way that a 6 DOF (6 degree of freedom) sensor is formed. On the 6 DOF sensor, there are six load cells S1 - S6 which are used to measure the magnitude of the force *Fz, Fy, Fz,* and moments *Mx, My, Mz*. Figure 9 (b) shows the 6 DOF sensor circuit in 3 dimensions, how the placement of load cells S1 - S6 refers to Fig. 9 (a). From the series of Fig. 9 (a), it is known that to measure the Fx force 2 load cells are used, *Fy* 1 load cell and *Fz* 3 load cells are used. From the measurement results of S1 - S6 load cell, then the magnitude of force and moment can be determined by the formula:

$$Fx = S1 + S2 \tag{7}$$

$$Fy = S3 \tag{8}$$

$$Fz = S4 + S5 + S6 \tag{9}$$

$$Mx = \frac{1}{2}c(S6 - S5) \tag{10}$$

$$My = \frac{1}{2}b(S4 - S5 - S6) \tag{11}$$

$$Mz = \frac{1}{2}a(S1 + S2) \tag{12}$$

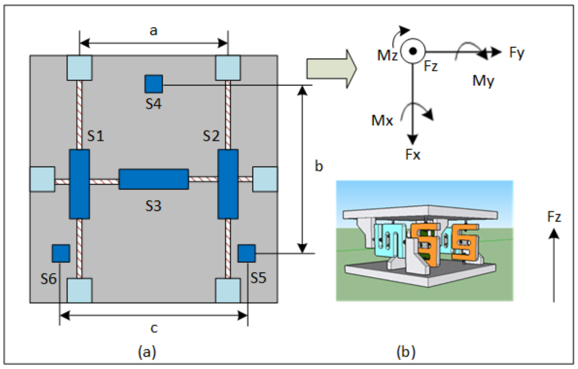

Figure 9. (a) Configuration of 6 DOF (b) Frame design of 6 DOF

4.2. Design measurement model test

To be able to know the magnitudes of the forces and moments caused by the hydrodynamic forces on the amphibious plane floater, the measurement design is made as shown in Fig. 10. In Fig. 10 it is shown that the transformation of the measured force and moment from the 6 DOF sensor axis to the specified measuring point for example, from A to B.

In Fig. 10, the magnitude of the measured force and moment is at point A which is so that it will be given the notation *Fxa*, *Fya*, *Fza*, and *Mxa*, *Mya*, *Mza*. The results of the measured quantities need to be transformed to the desired center point in this case at point B. If the distance between points A and B is equal to m, the formula for force and moment transformation is obtained as follows:

$$Fxb = Fxa \tag{13}$$

$$Fyb = Fya \tag{14}$$

$$Fzb = Fza \tag{15}$$

$$Mxb = Mxa + Fya.m \tag{16}$$

$$Myb = Mya + Fxa.m \tag{17}$$

$$Mzb = Mza \tag{18}$$

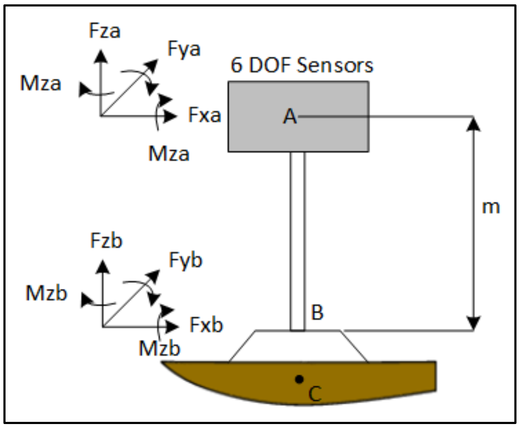

Figure 10. Transformation from point A to B

4.3. Test and measurement results

The model testing was carried out on the floater model which was connected with the 6 DOF measuring device as the measurement design of Figure 10, while the shape of the aircraft was not modeled because the fuselage was not immersed in water. The floater model is made on a certain scale by considering the maximum speed of the tug train in the Towing Tank. In the floater test, the model is pulled with a certain speed, and with the measuring instrument, 6 DOF measured the forces that work so that the influence of hydrodynamic forces on the floater model is known.

Before testing, the measurement is carried out by weighing the measuring instrument 6 DOF of 1300 gr towards the *Z*-axis (*Fz*). The measurement results can be seen in Fig. 11. From Fig. 11 it can be seen that the dominant values are found in the outputs of S4, S5, and S6 as constituents of the *FZ* style [9]. By adding the three in which S4 (345 gr), S5 (387 gr), and S6 (550 gr) the average measured force is 1,282 gr, so there is a difference of 18/1300 or 1.38%.

Model testing is done after testing the DOF 6 gauge and testing the road to find out the performance of the model and the measuring instrument, the floater test model is pulled in several speed points with variations of the draft on the model.

In Fig. 12, the output of one of the seaplane floater models is shown. In the picture, there are 7 channels wherein channel 1 shows the test speed of the floater model, channel 2 (*Fx*), channel 3 (*Fy*), channel 4 (*Fz*), channel 5 (*Mx*), channel 6 (*My*), and channel 7 (*Mz*). These values are obtained by processing the output signal according to the formula [13-18].

On the test graph in Fig. 12, when the condition of the test speed has stabilized on channel 1 (V) it is known that the average test speed is 9.19 m/s. For the magnitude of the force and moment, there are fluctuations in the measurement results that can be caused by the vibration of the floater when pulled. From the Fig. 12, we get the average values of *Fx* (336.21 kg), *Fy* (6.40 kg), *Fz* (583.43 kg), *Mx* (200.64 kg meter), *My* (1013.85 kg meter) and *Mz* (78.12 kg meter) where this value has been multiplied by the scale factor of the model test.

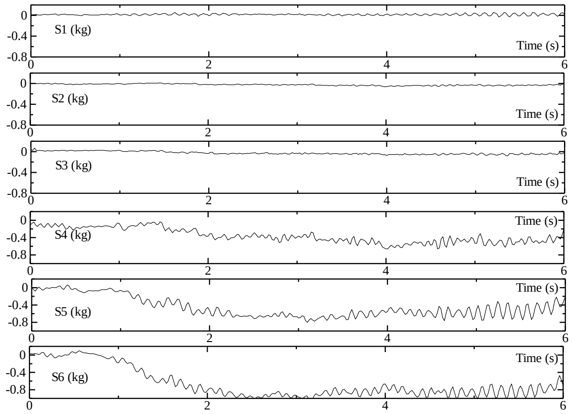

Figure 11. Load test of *Fz* at 6 DOF transducers

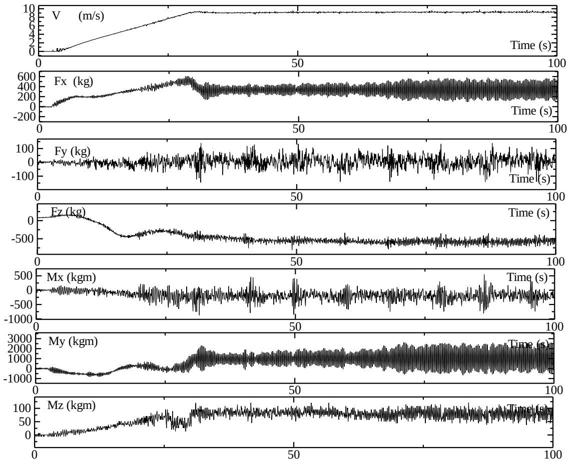

Figure 12. Example force and moment result from the output testing with 6 DOF

5. Conclusion

From the design of the 6 DOF transducer for the measurement of the hydrodynamic forces of the seaplane floater, it can be concluded that:

- 6 DOF transducer can be made from 6 S type load cells which are arranged in such a way that the direction x, y, and z, so that it can be used to measure the force *Fx, Fy, Fz, Mx, My* and *Mz*.
- Load cell calibration and calibration factor values are very important to know correctly because this will affect the accuracy of the measurement results. In testing the measurement of the *Fz* force, an error of 1.38% is obtained so that the sensor is proper to use.
- In testing the hydrodynamic forces using a 6 DOF transducer it is necessary to transform the force and moment produced by the sensor at the desired point, so the distance between that point and the center of the 6 DOF sensor needs to be known.
- To get high accuracy, the capacity of the type S load cell must be adjusted according to the needs according to the prediction of the magnitude of the force to be measured.

References

[1] M. M. Lubis, “Analisis Aerodinamika Airfoil Naca 2412 Pada Sayap Pesawat Model Tipe Glider Dengan Menggunakan Software Berbasis Computional Fluid Dinamic Untuk Memperoleh Gaya Angkat Maksimum,” *J. e-Dinamis*, vol. 2, no. 2, pp. 23–33, 2012.

[2] J. Ma and A. Song, “Fast Estimation of Strains for Cross-Beams Six-Axis Force/Torque Sensors by Mechanical Modeling,” *Sensors Actuators A. Phys*, vol. 13, pp. 6669–6686, 2013.

[3] D. F. Rendra, W. B. Setiawan, and R. Mareta, “Aplikasi Pengukur 3 Derajat Kebebasan Gaya Aerodinamika Pada Water Tunnel,” *J. Sains dan Teknol.*, vol. 6, no. 2, pp. 258–267, 2017.

[4] S. A. Liu and H. L. Tzo, “A Novel Six-component Force Sensor of Good Measurement Isotropy and Sensitivities,” *Sensors Actuators A 100*, pp. 223–230, 2002.

[5] J. Vaughan, *Application of B&K Equipment to Strain Measurement*. Copenhagen: Bruel & Kjaer, 1975.

[6] K. Ito, T. Daenen, Y. Hirakawax, T. Hirayama, and T. Sakurai, "Longitudinal Stability Augmentation of Seaplanes in Planing," *J. Aircr.*, vol. 53, no. 3, pp. 1332–1342, 2016.

[7] "Marine Transducers Software," 2008.

[8] "Load Cell." [Online]. Available: http://www.dacell.com/en/load cell/show/view/cno/10/pno/40/page/3/id/748. [Accessed: 22-Nov-2019].

EPI International Journal of Engineering
Volume 3, Number 1, February 2020, pp. 90-94
DOI: 10.25042/epi-ije.022020.13

*p*ISSN 2615-5109
*e*ISSN 2621-0541

Valuation of Environmental Impact Due to Material Construction Mining, Gowa, South Sulawesi

Andi Arjan[a], Arikah Nurhusna Afifah[b], Yubelium Andrew Patila[c], Aryanti Virtanti Anas[d]

[a]Department of Mining Engineering, Faculty of Engineering, Hasanuddin University. Email: andiarjanpm@gmail.com
[b]Department of Environmental Engineering, Faculty of Engineering, Hasanuddin University. Email: arikahna@gmail.com
[c]Department of Mining Engineering, Faculty of Engineering, Hasanuddin University. Email: yubelpatila@mail.com
[d]Department of Mining Engineering, Faculty of Engineering, Hasanuddin University. Email: virtanti@gmail.com

---

Abstract

Sand, river stone, soil excavation, sandstone, and broken stone are the types of construction materials mining in Gowa Regency and many are found in the Jeneberang River. The Jeneberang River is one of the main rivers in South Sulawesi. However, construction materials mining carried out around the Jeneberang River has a negative impact on the surrounding environment. Those negative impacts are erosion, road damage, noise, air pollution, and a decrease in water quality. This research was conducted in Gowa Regency. The method used is the Contingent valuation method (CVM). CVM consists of the desire to pay (Willingness to Pay or WTP) and the desire to accept (Willingness to Accept or WTA. While the social aspect conducts interviews with questionnaire questions to respondents to find out opinions about the surrounding environment. From this study, it is known that WTP and WTA data are inversely proportional. The greater the compensation to be paid, the more societies who want to receive and the fewer companies paid for the compensation.

Keywords: Environmental impact, construction materials, WTA, WTP

---

1. Introduction

1.1. Background

According to Law No.23 of 1997 concerning Environmental Management, the definition of environmental damage is an action that results in direct or indirect changes to its physical and/or biological properties which causes the environment to no longer function in supporting sustainable development. Environmental problems from sand mining activities require proper handling so that environmental damage having been occurred does not get worse. This is also important for the sustainability of construction material mining activities itself. In fact, changes in the face of the earth caused by open mining can affect environmental balance [1].

The Jeneberang River is one of the major and important rivers in the South Sulawesi Province. This is due to the flow of the Jeneberang River through Gowa Regency, Takalar District and Makassar City [2]. The Jeneberang River is a watershed that flows its water to Makassar City towards the lower reaches of the Makassar Strait and originates from the eastern part of Mount Bawakaraeng (2,833 masl). In the flow area of Jeneberang River, there are two main water catchment areas, such as in the city of Bili-bili and Jenelata. Raw water taken from the Jeneberang River is located seven km south of the city, pumped through a closed channel to the Ratulangi Installation. The river is also a supplier of raw water for the supply of clean water in Makassar City and Sungguminasa District, Gowa Regency [2].

Construction material mining has been operating for more than 19 years in the Jeneberang River and based on data from the Department of Energy and Mineral Resources of South Sulawesi Province, there are 35 construction materials mining in Gowa Regency, which cause environmental impacts. Environmental impacts resulting from mining activities can be felt by the local community. The pollution impact occurred is river erosion, a decrease in water quality, noise, air pollution, and road damage. The environmental impact is caused by the lack of attention of mining companies, so that it is necessary to have an environmental valuation and serve as the cost of externality by using the Contingent valuation method (CVM).

1.2. The aim of the research

Construction materials mining located in Gowa Regency is one of the biggest revenues and provides employment for the people of Gowa Regency, but behind

---

*Corresponding author. Tel.: +62-851-4603-5438
Jalan Poros Malino km. 6 Bontomarannu, Gowa
South Sulawesi, Indonesia 92171

that, there has been an environmental impact due to the mining process, those processes include excavation, production and transportation, and therefore this study aims to (1) determine the environmental impacts caused by construction materials mining (2) identify the valuation of the environment of construction materials mining.

2. Literature Review

2.1. Environmental impact

The damage to village roads that were passed by trucks carrying sand/gravel/stone because the construction of village roads was not specifically made for trucks loaded with sand, repairs had been made but sometimes later it had suffered the same damage. Trucks that exceed road tonnage further aggravate the damage to village roads [3].

Soil erosion is an important indicator of environmental quality. Erosion is defined as an event of loss or erosion of land or parts of land from a place that is transported from one place to another. Based on the classification of Erosion Hazard Levels according to the Directorate General of Reforestation and Rehabilitation of Forestry Ministry No.041/Kpts/V/1998, the value of TBE obtained is categorized as moderate and mild. This should be taken into consideration and thought because the magnitude of erosion that occurs results in impacts resulting from the high erosion of the local environment and the environment in the lower regions [4].

There is a dependency between land use and water availability. Good land use in the catchment area benefits downstream in the form of water quality, flow regulation, water supply and flow productivity. The high runoff water on the surface of the land causes low water to seep into the soil so that there is a tendency to reduce ground water. The high rate of erosion causes the high water wasted as surface runoff so that groundwater capacity tends to decrease. This is in line with complaints from some residents who claimed that the water in the pond was shrinking [3]. The slope was cut because the land was used for sand excavation, resulting in the cutting of the grooves of the ground so that ground water appeared on the excavated surface. On the excavated land, running water appears and at the bottom forms a kind of pond. The cutting of the soil grooves so that they appear on the surface has an effect on the reduction of groundwater that is underground, resulting in a reduction in water supply elsewhere. The water should be stored as ground water reserves and appear elsewhere [4].

Stone breakers are one of the most vulnerable locations exposed to chemical pollutant factors such as dust, steam and gas. Dust is a solid particulate produced by humans or nature and is the result of the breakdown process. Dust in these locations can cause reduced comfort in the workplace, visual disturbances, even general poisoning. Dust that is inhaled for a long time and continuously can cause lung damage and fibrosis. Dust less than 1 micron meter is very dangerous for the body because it can enter the alveolus [5].

The Government of Indonesia through the Minister of Environment has established environmental noise regulations through the Decree of the Minister of Environment No. 48/MENLH/11/1996 in 1996 which regulates the noise limits in residential areas or other public facilities. Noise levels in residential areas are set not to exceed 55 dBA. Beside that the government has also set a standard noise threshold in the work area according to the Minister of Manpower Decree No. KEP.55/MEN/1999, that the noise threshold value in the work area is a maximum of 85 dBA with an 8 hour exposure time. Noise level values between 55-65 dBALeq affect psychological disorders including personal comfort disorders, communication disorders, psychological disorders such as complaints and demonstration, disturbances in learning concentration, resting disorders, disturbances in prayer/worship activities, sleep disorders and other disorders, while somatic complaints, temporary deafness, and permanent deafnesses are many considered impacts of noise in the work environment /industry [6].

2.2. Environmental valuation

One of the methods used in environmental valuation is the Contingent valuation method (CVM). CVM consists of the desire to pay (Willingness to Pay or WTP) and the desire to accept (Willingness to Accept or WTA). WTP is the willingness of a person to make payments for environmental services from an ecosystem that is maintained without pollution and/or partial or total damage or the maximum number of people willing to pay to avoid a decrease in environmental quality or the ability to pay people to obtain goods and services. WTA is the willingness to accept payments for environmental losses that may arise due to pollution and/or damage to an ecosystem or the minimum amount of compensation that someone wants to receive to accept a decrease in environmental quality [7], [8].

In the WTA / WTP method, the respondents will be given questions about willingness to pay to get the value of benefits or the willingness to get compensation for costs for goods and services. Surveys are designed to ask hypothetical questions related to how willing they are to pay or receive compensation to maintain the quality of resources [9].

3. Research Methodology

The method used in this study is Willingness to Pay or WTP and Willingness to Accept or WTA through the distribution of WTP questionnaires to construction material mining companies and WTA questionnaires to the people of Gowa Regency who are in the vicinity of construction material mining.

Data collection will be carried out in several ways, as follows:

1) Determine the number of respondents (n) using the random sampling method with Slovin formula:

$$n = \frac{N}{1 + Ne^2} \tag{1}$$

where,

n = number of samples
N = population Parangloe sub-district (household)
e = error rate (10%)

Table 1. Types and origin of data sources

No.	Type of Data	Data source
1.	Material type Amount of material production Material prices	Department of Energy and Mineral Resources Mining companies
2.	Bidding variable	Department of Energy and Mineral Resources Central Bureau of Statistics Mining companies
3.	Request variable (economic and infrastructure data)	Central Bureau of Statistics of South Sulawesi

Table 2. Types and origin of data sources

Respondent Category	The Way of Respondents Selection	Type of Data	Method
Community around the mining area	*Random Sampling*	Socio-cultural conditions Public perception of mining Large environmental costs who wants to be accepted	Questionnaire Interview
Mining companies	*PuIDRosive Sampling*	The amount of environmental cost that wanted to be paid Environmental impacts caused	Questionnaire Interview

2) Observation and survey of mining companies in the Jeneberang River area to find out the type of material produced, the amount of production, market location, and permits owned.
3) Divide the questionnaire to find out the minimum compensation value as an environmental cost which is the value that the company wants to pay (WTP) and which wants to be accepted by the community (WTA).
4) Determine the mean value of the average WTA and WTP as the price balance using the inteIDRolation method with the formula:

$$Me = \frac{\bar{M}_{wta} + \bar{M}_{wtp}}{2} \tag{2}$$

where,

Me = the median value of the average price of WTA and WTP

$\bar{M}$ wta = average WTA price

$\bar{M}$ wtp = average of WTP price

5) Processing and data analysis:
   a. Building a hypothetical market, which is a decrease in environmental quality due to mining activities.
   b. Obtain the offer value by using the referendum method, which is by giving a number of price options to the respondents then given the question of agreeing or not.
   c. Calculate the frequency number of each bid value chosen by the respondent.
   d. Make WTA and WTP graphs from the bid value and number of respondents frequency.

4. Results and Discussion

The data collected is the result of the distribution of WTA and WTP questionnaires. The number of respondents from the WTA questionnaire were 99 respondents and WTP as many as 8 respondents. The WTA questionnaire was distributed by random sampling method in the area around construction materials mining and each household was given 1 WTA questionnaire. The WTP questionnaire was distributed using a puIDRosive sampling method with the target of the company being close to residential and public roads. Data from the literature study and questionnaire distribution had been analyzed with the following results:

1) Environmental impacts felt by the local society

a. Erosion

Mining activities carried out along the Jeneberang River cause erosion. Continuous dredging of sand on the riverside causes it to be easily eroded by water currents. This results in widening the river area as happened in Fig. 1.

b. Road damage

To transport raw construction materials from sand mining along the river, adequate transportation is needed. As a result of sand mining activities, many roads were damaged. This damage is caused by trucks passing every day while the roads made are not designed for everyday trucks crossed. One example of road damage due to sand transport trucks can be seen in Fig. 2.

c. Air pollution and noise

Air pollution produced in sand mining is dust. Dust is generated from rock crusher or crushers. Another source that produces dust is the activity of trucks carrying sand that has been destroyed. When sand is transferred into the truck, dust of sand will carry over and spread to the surrounding air can be seen in Fig. 3. In addition to air pollution, there is also a noise or noise pollution in sand mining activities the main source of noise in the sand mining area is the sound produced from the crusher.

d. Decrease in quality and quantity of clean water

The sand mining activities carried out on the Jeneberang River have damaged the clean water reserves of the local residents. River water becomes dirty and mixed with mud as shown in Fig. 4. Local residents use the river as the main water source for their daily needs. In addition to the decline in the quality of clean water, due to mining activities, residents have become short of clean water reserves. Dredging of sand causes surface water to emerge.

Figure 1. Erosion on the Jeneberang River due to mining activities

Figure 2. Road damage due to trucks that often pass

Figure 3. Dust of sand from mining activities loaded by sand transport trucks

Figure 4. The polluted water of Jeneberang River

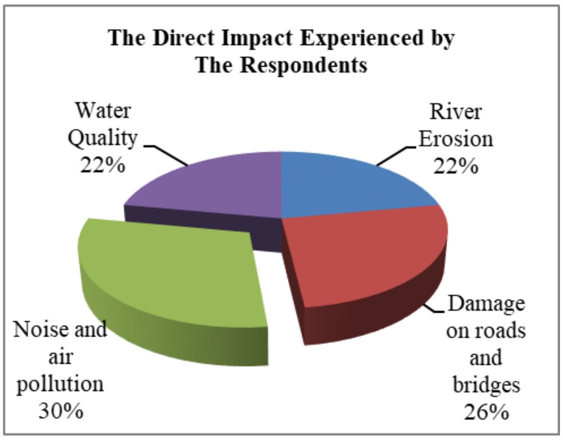

Figure 5. The negative impacts percentage on the environment felt by society

Based on the graph information in Fig. 5, there are 4 environmental impacts caused by the construction material mining in Gowa Regency, based on the questionnaire data have been obtained from the respondents the results show that the noise and air pollution are the dominant environmental impact that felt by the society that is amount of 30%.

e. Environmental valuation

Based on the graph information in Fig. 6, which was made from the results of the WTA questionnaire, the greater the compensation costs offered, the more societies want to receive compensation from the company.

Based on the graph information in Fig. 7, which was made from the WTA questionnaire results, the smaller the compensation costs offered, the more companies want to provide compensation for local societies.

Determine the average price of WTA and WTP and determine the price of balance. The average price of WTA is IDR. 17,303.03 and the average price of WTP is IDR. 13,375.00. Based on the average of WTA and WTP, the balance price obtained is IDR 15,339.02 as summarized in Fig. 8.

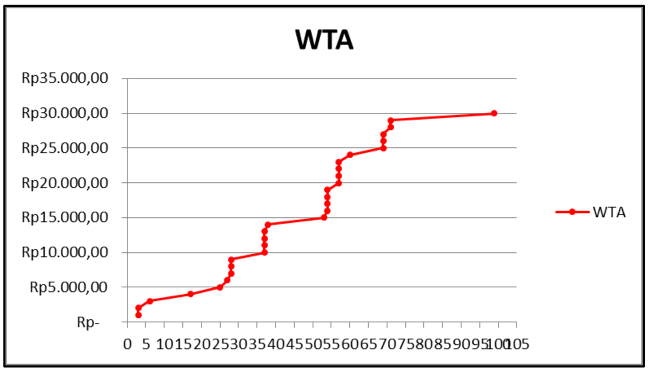

Figure 6. WTA results

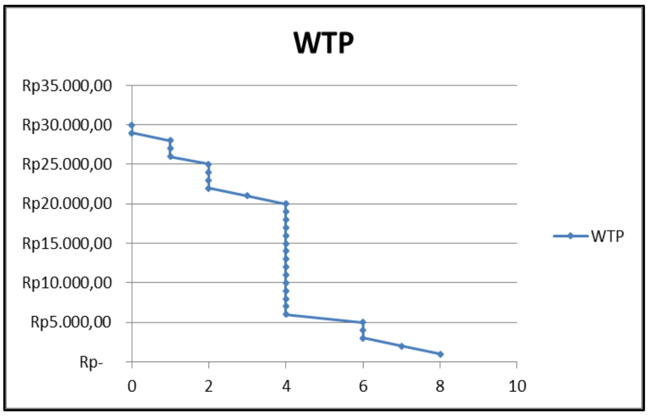

Figure 7. WTP results

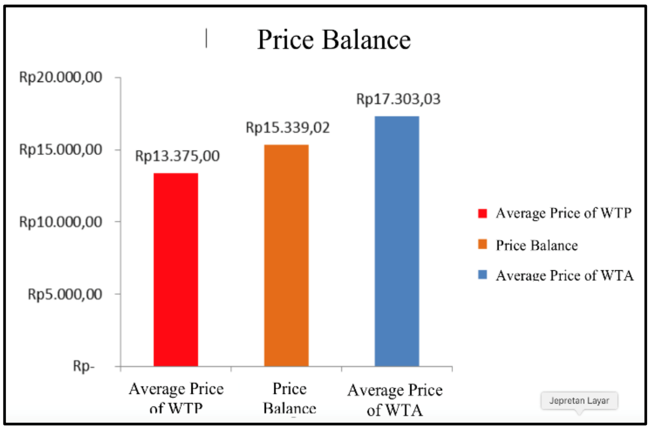

Figure 8. WTA and WTP Price Balance

5. Conclusions

Mining of construction materials in Gowa Regency caused environmental impacts such as road damage, river erosion, decrease in water quality and quantity, and pollution of the air and noise, these environmental impacts can occur due to mining of construction materials, mining processes of construction materials which is excavation, production and transportation. Existing environmental impacts can be minimized by the presence of externality costs from environmental valuation, the willingness of the community to accept shows that the greater the compensation costs offered, the more societies want to receive the compensation from the company while the willingness of companies to pay shows the smaller compensation costs offered, the more companies want to provide compensation for local society. The distribution of existing WTP questionnaires shows the average results is IDR. 13,375.00 and the average results of WTA is IDR. 17,303.03, from the results of WTA and WTP, it is then provide a balance price as much as IDR. 15,339.02.

Acknowledgments

Thanks to the Ministry of Technology and the Higher Education Republic of Indonesia (KEMENRISTEKDIKTI) for providing a forum for Indonesian students to create and work through the Student Creativity Program (PKM), because of this program this research was able to be implemented and completed. Our thanks also go to the people of Gowa Regency who have helped and were willing to provide the information needed, construction material mining companies who were willing to provide the information needed, and to Government of Gowa Regency who has given permission to carry out this research in Gowa Regency.

References

[1] M. K. Abdurrahman, “Inventarisasi Tumbuhan Pada Ketinggian yang Berbeda Pasca Letusan Gunung Merapi Jalur Pendakian Balerante Kecamatan Kemalang Kabupaten Klaten,” Universitas Muhammadiyah Surakarta, 2012.

[2] A. Rifani, “Kajian Kerusakan Lingkungan pada Perairan Sungai Jeneberang Kabupaten Gowa Provinsi Sulawesi Selatan akibat Aktivitas Pertambangan Pasir sebagai Dasar Pengelolaan Lingkungan,” Universitas Gadjah Mada., 2017.

[3] I. N. Dyahwanti, “Kajian Dampak Lingkungan Kegiatan Penambangan Pasir pada Daerah Sabuk Hijau Gunung Sumbing di Kabupaten Temanggung,” Universitas Diponegoro, 2007.

[4] Yudhistira, W. K. Hidayat, and A. Hadiyarto, “Kajian Dampak Kerusakan Lingkungan akibat Kegiatan Penambangan Pasir di Desa Keningar Daerah Kawasan Gunung Merapi,” *J. Ilmu Lingkung.*, vol. 9, no. 2, pp. 76–84, 2011.

[5] K. Ardan, “Hubungan Paparan Debu dan Lama Paparan dengan Gangguan Faal Paru Pekerja Overhaul Power Plant,” *Indones. J. Occup. Saf. Heal.*, vol. 4, pp. 155–166, 2015.

[6] S. Hidayat, Purwanto, and G. Hardiman, “Kajian Kebisingan dan Persepsi Ketergangguan Masyarakat akibat Penambangan Batu Andesit di Desa Jeladri, Kecamatan Winongan, Kabupaten Pasuruan Jawa Timur,” *J. Ilmu Lingkung.*, vol. 10, no. 2, pp. 95–99, 2012.

[7] A. Fauzi, *Ekonomi dan Sumber Daya Alam dan Lingkungan, Teori dan Aplikasi*. Jakarta: Gramedia Pustaka Utama, 2004.

[8] Ministry of Environment and Forestry, *Ganti Kerugian akibat Pencemaran dan/atau Kerusakan Lingkungan Hidup*. Indonesia: Peraturan Menteri Negara Lingkungan Hidup No. 3, 2011.

[9] L. Venkatachalam, “The Contingent Valuation Method: A Review,” *Environ. Impact Assess. Rev.*, no. 24, pp. 89–124, 2004.